Solar Gasification of Biomass:
Design and Characterization of a Molten Salt Gasification Reactor

A DISSERTATION
SUBMITTED TO THE FACULTY OF THE GRADUATE SCHOOL OF THE
UNIVERSITY OF MINNESOTA
BY

Brandon Jay Hathaway

IN PARTIAL FULFILLMENT OF THE REQUIREMENTS
FOR THE DEGREE OF
DOCTOR OF PHILOSOPHY

Dr. Jane H. Davidson
Dr. David B. Kittelson

December 2013

Acknowledgements

I would like to acknowledge the contributions from the many people and organizations that helped in the completion of this dissertation. Funding for this project was supplied through the Initiative for Renewable Energy and the Environment and the Univesity of Minnesota Graduate School through both the Doctoral Dissertation Fellowship and the Interdisciplinary Doctoral Fellowship (co-funded with the University of Minnesota Institute on the Environment).

I'd like to recognize my academic advisors, Jane Davidson and David Kittelson, who cannot be thanked enough for their endless guidance as we developed this solar gasification project from scratch, allowing me to experience the full range of research project management and what's involved in keeping everything on track.

Professors Pat Ferro and Howard MacLean at the Rose-Hulman Institute of Technology and Paul Strykowski at the University of Minnesota first introduced me to the rewards of experimental research and encouraged me to consider pursuing a graduate degree while also completing numerous letters of recommendation for many applications.

My fellow researchers in the Combustion Control Group, Thomas Shepard and Michael Hallberg helped me set up my first round of experimental research. Anil Bika and Luke Franklin in the engines group were always willing to discuss issues with myself and others in the Solar Lab. Many professors helped me transition to the graduate environment including Professors Sue Mantell, Ephraim Sparrow, Steve Girshick, Francis Kulacki, and Terrance Simon. The staff of the ME department has been endlessly helpful, including advising from John Gardner, and assistance with about all aspects of the department from the Jacks-of-all-Trades Jennifer Dahal and Holly Edgett, not to forget the attention of our office custodian Mike. Our many fabrications and reactors made by the professional shop employees, including Bob Nelson, Robin Russell, Mike Jensen, and also Peter Zimmerman for assistance in the student shop and Mark Erickson for no-nonsense advice on finding the right tools for almost any job.

Lastly, I acknowledge the support and friendship of my colleagues in the Solar Lab, including: Julia Haltiwanger, Joshua Quinell, Luke Venstrom, Peter Krenzke, Aaron Wade, Katie Krueger, Masanori Honda, and Amey Kawale.

Dedication

This dissertation is dedicated to my parents and sister, who have done so much to allow me to achieve my goals. From my mother, Sandie, who always encouraged me to try new things, and first pushed me to explore engineering at a summer program at Rose-Hulman Institute of Technology. To my father, Mel Jay, who inspired my curiosity in the realm of mechanics and manufacturing through endless help with school and scouting projects, vehicle repair, and visits to his manufacturing shop, not to mention influencing my habit of casually perusing encyclopedias to constantly broaden my knowledge. Lastly my sister Nicole, who took the time to teach me to read well before it seemed rational to, and always encouraged me to set higher goals and improve myself.

I'd also like to thank Lindsay, for being my source of relief and the light at the end of each week's tunnel. You were always there to listen to my nerdy rants about exciting results and upcoming milestones during the good times and to let me vent and keep my mind on the better things in life during the busy times.

It's been a long road getting to this point, with many adventures and difficulties along the way, and I'm eternally thankful for you all sticking by me and always being there when needed, even if I seemed to disappear for months at a time, buried in research!

Abstract

The design and implementation of a prototype molten salt solar reactor for gasification of biomass is a significant milestone in the development of a solar gasification process. Solar gasification of biomass stores solar energy in a chemical form and improves the yield compared to conventional gasification. The use of molten salts provides faster reaction rates by 2-10 times, enhances heat transfer, and allows continuous operation through solar transients, including 24-hour operation at a commercial 100 MW_{th} scale with 10 GJ/K of thermal storage. The reactor developed in this work allows for 3 kW_{th} operation with an average aperture flux of 1530 suns at salt temperatures of 1200 K with pneumatic injection of ground or powdered dry biomass feedstocks directly into the salt melt.

Laboratory scale experiments in an electrically heated reactor demonstrate the benefits of molten salt and the data was evaluated to determine the kinetics of pyrolysis and gasification of biomass or carbon in molten salt. In the presence of molten salt overall gas yields are increased by up to 22%; pyrolysis rates double due to improved heat transfer, while carbon gasification rates increase by an order of magnitude. Existing kinetic models for cellulose pyrolysis fit the data well, while carbon gasification in molten salt follows kinetics modeled with a 2/3 order shrinking-grain model with a pre-exponential factor of $1.5 \cdot 10^6$ min^{-1} and activation energy of 158 kJ/mol.

A reactor concept is developed based around a concentric cylinder geometry with a cavity-style solar receiver immersed within a volume of molten carbonate salt. Concentrated radiation delivered to the cavity is absorbed in the cavity walls and transferred via convection to the salt volume. Feedstock is delivered into the molten salt volume where biomass gasification reactions will be carried out producing the desired product gas. The features of the cavity receiver/reactor concept are optimized based on modeling of the key physical processes. The cavity absorber geometry is optimized according to a parametric survey of radiative exchange using a Monte Carlo ray tracing model, resulting in a cavity design that achieves absorption efficiencies of 80%-90%. A parametric survey coupling the radiative exchange simulations to a CFD model of molten salt natural convection is used to size the annulus containing the molten salt to maximize

utilization of absorbed solar energy, resulting in a predicted utilization efficiency of 70%. Finite element analysis was used to finalize the mechanical design to achieve acceptable thermal stresses less than 34.5 MPa to avoid material creep.

Initial shakedown tests of the reactor are conducted at reduced power settings to evaluate structural and operational performance. Testing is restricted to 1150 K for about 3.5 minutes due to a pressure buildup in the reactor resulting from excess char deposition on the downstream filters. During this time, feedstock is converted to a CO rich product gas with an average calculated solar efficiency of $\eta_{\text{solar}} = 32 \pm 2.3\%$ and a cold gas efficiency of $\eta_{\text{CG}} = 70.5 \pm 1.7\%$. Recommendations to reduce char production and boost performance through the addition of steam, increased incident power, and higher initial operating temperature are presented.

A scale-up analysis is presented to estimate the performance of a 100 MW_{th} system and to explore the use of hybridization and thermal storage to provide a synthesis gas stream suitable to supply a downstream power or fuel production process. The simulations show that a moderately hybridized facility achieving a solar fraction of $f_{\text{solar}} = 50\%$ can produce synthesis gas with low output variation using only 1 GJ/K of thermal storage resulting in a specific yield of 115 GJ/ha and thermal efficiency of 77%. A more aggressive facility achieving $f_{\text{solar}} = 65\%$ would require 21 GJ/K of thermal storage, but would benefit from an increased specific yield of 128 GJ/ha and thermal efficiency of 80%.

Table of Contents

List of Tables

List of Figures

Nomenclature

A	Area [m^2]
a	Absorption coefficient [-]
$\dot{B}$	Exergy transfer [W]
b	Specific exergy [kJ/kg]
C	Heat capacity [kJ/K], or specific heat [kJ/kg-K], or Solar concentration [suns], or calibration constant [W/m^2]
D	Cavity to aperture diameter ratio. [-]
DA	Annulus diameter ratio [-]
d	Diameter dimension [m]
E	Reaction activation energy [kJ/mol] or blackbody emissive power [W/m^2]
F	View factor [-], or Force [F]
$\vec{F}$	Body force vector [N]
f	Objective function [-], or fractional function [-]
G	Gibbs free energy [J], or turbulent kinetic energy source [W/m^3], or Incident radiation per unit volume [W/m^3]
$\vec{g}$	Gravity acceleration vector [m/s^2]
ΔH	Mass specific enthalpy of reaction [kJ/kg]
H	Insolation incident on enclosure surface [W/m^2], or enthalpy [J]
Δh	Molar specific enthalpy of reaction [kJ/mol]
h	Mass specific enthalpy [kJ/kg], or convection coefficient [W/m^2-K]
I	Standard solar insolation = 1 [kW/m^2], or signal intensity [amps]
$\bar{\bar{I}}$	Identity tensor [-]
J	Radiosity [W/m^2]
K	Drag law proportionality constant [N-s/m]
k	Reaction rate [1/min], [1/sec] or Thermal conductivity [W/m-K]
L	Cavity aspect ratio (length to diameter) [-]
l	Length dimension [m]
LHV	Lower Heating Value of combustion [kJ/kg]
M	Molar mass [g/mol]
m	Mass [g],[kg]
$\dot{m}$	Mass flow rate [kg/s]
N	Number of ray tracing rays [-]
Nu	Nusselt number [-]
n	Moles [mol]
$\dot{n}$	Molar flow rate [mol/s]
P	Pressure [atm], or random uncertainty [various units]
Pr	Prandtl number [-]
$\dot{Q}$	Heat transfer rate [W]
$\dot{q}$	Power per ray for ray tracing calculations[W]
$\dot{q}''$	Heat flux [W/m^2]
$\dot{q}'''$	Volumetric heat source/sink [W/m^3]
$\dot{R}$	Specific reaction rate [kg/m^3-s]

R	Universal gas constant, 8.314 [J/mol-K] , or dimensionless radial coordinate [-], or interphase drag force [N]
Ra	Rayleigh number [-]
RF	Calibrated response factor [-]
r	Radial coordinate position [m]
$\Re$	Random number [-]
S	Specific yield [-]
s	Specific entropy [kJ/kg-K]
T	Temperature [K]
t	Time [sec],[min], or thickness [m]
U	Overall heat transfer coefficient [W/K], [W/m^2-K]
u	Velocity [m/s]
$\dot{V}$	Volumetric flow rate [m^3/s],[std L/min]
V	Volume [m^3]
v	Velocity [m/s]
w	Total uncertainty [various units], or elasticity tensor [Pa]
X	Extent of conversion [-]
x	X-coordinate position [m], or mass fraction [-]
Y	Biomass yield [kg/ha]
y	Y-coordinate position [m], or molar/gas volume fraction [-]
Z	Dimensionless axial coordinate position [-]
z	Axial coordinate position [m]

Greek

α	Volume fraction [-], or absorptivity [-]
β	Volumetric expansion coefficient [1/K], or exergy coefficient [-]
γ	Molar steam to feedstock ratio [-]
δ	Fraction of rated power [-], or small deviation [various units]
ε	Total hemispherical emissivity [-], or strain [-]
η	Efficiency [-]
θ	Angular coordinate [rad]
λ	Wavelength [μm] or volume viscosity [Pa-s]
μ	Mean value [various units], or absolute viscosity [Pa-s], or chemical potential [J/mol]
ν	Dynamic viscosity [m^2/s], or stoichiometric coefficient [-]
ρ	Density [kg/m^3], or reflectivity [-]
σ	Standard deviation [various units], or stress [Pa], or Stefan Boltzmann constant [W/m^2-K^4]
$\bar{\bar{\tau}}$	Strain tensor [-], or time constant [1/s]
ϕ	Porosity [-], or mass steam to feedstock ratio [-], or angular coordinate [rad]
Ω	Solid angle [sr]
ω	Relaxation parameter [-], or angular velocity [rad/s]

Subscripts

0	Pre-exponential term or initial value

a	Absorbed ray, annulus
abs	Absorbed portion
ap	Aperture
app	Apparent value
Ar	Argon
assist	Assist heating value for hybridization
b	Blackbody value
bd	Beam-down reflector
C	Carbon
c	Pertaining to the absorber cavity, or cone angle
CG	Cold gas efficiency
CO	Carbon Monoxide
CO_2	Carbon Dioxide
CH_4	Methane
cell	Cellulose
ch	Chemical component
coll	Solar collection field value
cond	Conductive component
conv	Convective component
CSGS	Compressed Synthesis Gas Storage
e	Emitted
eff	Effective value
energy	Pertaining to an energy balance
exergy, ex	Pertaining to an exergy balance
ext	External reactor body dimension
f	Formation value, or flange, or collection field value
fit	Pertaining to the fit of simulated data
feed	Pertaining to the feedstock
GM	Shrinking grain model of carbon gasification
(g)	Gaseous phase
g	Pertaining to the carbon gasification reaction
gas	Pertaining to the product gases of gasification/pyrolysis
i	Inner surface value
inco	Pertaining to Inconel alloy
ins	Pertaining to insulation
L	Based on length scale '*L*'
loss	Energy lost to the ambient environment
MC	Resulting from a Monte Carlo ray tracing simulation
max	Maximum mass of carbon possible from complete pyrolysis of delivered cellulose feedstock
model	Value obtained from a simulation model
net	Net value of heat transfer across a surface
o	Originating from an external source or outer dimension
obj	Objective function for optimization routine
p	Pertaining to the pyrolysis reaction, or constant pressure value
ph	Physical component

prod	Produced or product gas value
q	Pertaining to the heat flux on a surface
quench	Energy lost from cooling of product gas
r	Radial coordinate direction, or reaction term
rad	Radiation component
ray	Pertaining to rays from ray-tracing simulations
react	Pertaining to the reactor
reflect	Energy reflected from the cavity absorber
reread	Energy radiated from the cavity absorber
recycle	Pertaining to the recycle flow of product gas from the outlet to the inlet of the reactor.
rxn	Pertaining to the reaction zone of the reactor
(s)	Solid phase
s	Mass-specific value
salt	Pertaining to the annular salt volume
solar	Pertaining to the incident solar radiation
steam	Pertaining to steam reactant
stoich	Stoichiometric value
std	Standard flow conditions of 1 [atm], 273.15 [K]
target	Target value of parameter during iterative solution method
t	Turbulence term
th	Thermal energy term
tot	Combining effects of convection and radiation
u	Universal gas constant, or useful portion
wall, w	Pertaining to the wall of the reactor housing the molten salt
z	Axial coordinate direction
θ	Angular term
λ	Wavelength specific term
∞	Far-fluid property value

1 Introduction

One of the most pressing concerns for the near future is keeping up with the ever increasing demand for energy while avoiding excessive environmental degradation. The world demand for energy is projected to increase by 40% over the course of the next 20 years and double by 2050. Liquid fuels derived from petroleum supply the largest share (37%) of energy consumption, the majority due to transportation [1]. Additionally, status quo fossil fuel consumption has led to unprecedented levels of carbon dioxide emissions which the scientific community has deemed a driving factor for accelerated global climate change [2]. Thus it is critical to develop alternate means of liquid fuel production with neutral to negative lifecycle greenhouse gas emissions.

The use of biomass as a feedstock for production of biofuels is one of the potential options for sustainable, low carbon fuels to replace fossil fuels. Current biofuels such as corn ethanol and soybean biodiesel have been criticized for their low life cycle net energy return as well as for competing with food production for agricultural land [3]. Low-input biomass (also referred to as cellulosic or second generation), such as mixed perennials, agricultural byproducts, or conservation reserve program (CRP) cuttings, are suited for production that does not compete with food crops while offering the potential to produce life cycle carbon negative fuels [3].

Methods for utilizing these low-input feedstocks consist of both biochemical (fermentation, anaerobic digestion) and thermochemical (gasification, pyrolysis) processes. Compared to biochemical processes, gasification is typically amendable to a wider variety of feedstock and operates with higher rates of conversion; however, obtaining the thermal energy at a sufficient temperature and rate to drive the process conventionally requires wasteful combustion of the feedstock or reliance on carbon intensive fossil energy sources. The partial combustion of feedstock typically consumes from 20% to 30% of the original energy content [4]. Avoiding combustion is critical for maximizing the yield of biofuel per unit biomass consumed. To better understand gasification and how it may be improved upon, an over of the process of gasification is presented.

1.1 Gasification

Gasification converts solid biomass to gaseous fuels. In this process, the feedstock is heated to sufficient temperatures to drive off all volatile components and break the biopolymer structures (pyrolysis) leaving behind a carbonaceous char. The char is further converted by exposure to a gasifying agent, most commonly steam or carbon dioxide, which produces carbon monoxide and (in the case of steam gasification) hydrogen. The resultant hydrogen and carbon monoxide rich product gas is commonly referred to as "synthesis gas" due to the wide variety of synthetic fuels and chemicals which may be produced from it (including methane, methanol, Fisher Tropsch gasoline or diesel, or monomers for polymer production). The chemical equation describing overall steam gasification process for cellulose, representative of most biomass feedstock, is

$$\mathrm{C_6H_{10}O_{5,(s)}} + \mathrm{H_2O_{(g)}} + \text{heat} \longrightarrow 6 \cdot \left(\mathrm{CO_{(g)}} + \mathrm{H_{2,(g)}}\right) \tag{1.1}$$

The process of biomass gasification may be further broken down into the two steps of pyrolysis and carbon gasification. Considering cellulose as a representative biomass material again, the pyrolysis reaction is given by:

$$\mathrm{C_6H_{10}O_{5,(s)}} \longrightarrow \mathrm{C_{(s)}} + 5 \cdot \left(\mathrm{H_{2,(g)}} + \mathrm{CO_{(g)}}\right) \qquad \Delta h_\mathrm{p} = 128 \frac{\mathrm{kJ}}{\mathrm{mol}} \tag{1.2}$$

The gasification of carbon, in this case using steam as the oxidizing agent, is given by:

$$\mathrm{C_{(s)}} + \mathrm{H_2O_{(g)}} \longrightarrow \mathrm{H_{2,(g)}} + \mathrm{CO_{(g)}} \qquad \Delta h_\mathrm{g} = 144 \frac{\mathrm{kJ}}{\mathrm{mol}} \tag{1.3}$$

Carbon dioxide could also be used as the oxidizing agent in eq. (1.3) in place of steam, with the products containing no hydrogen and two moles of carbon monoxide per mole of carbon. In most practical biomass gasification systems, these steps occur simultaneously with the pyrolysis reaction of eq. (1.2) supplying the char to be consumed by the gasification reaction of eq. (1.3).

The differences between conventional combustion based gasification methods and an externally heated process such as solar gasification are illustrated in Fig. 1.1. The conventional approach to biomass gasification involves carrying out reactions (1.2) and (1.3) under autothermal conditions. Supplying sufficient energy to achieve autothermal operation requires that 20 to 30% of the feedstock be combusted within the gasifier to generate the heat that drives the gasification and pyrolysis reactions. This partial

combustion limits the energetic yield, dilutes the product gas with combustion byproducts, and often requires a dedicated oxygen facility [5].

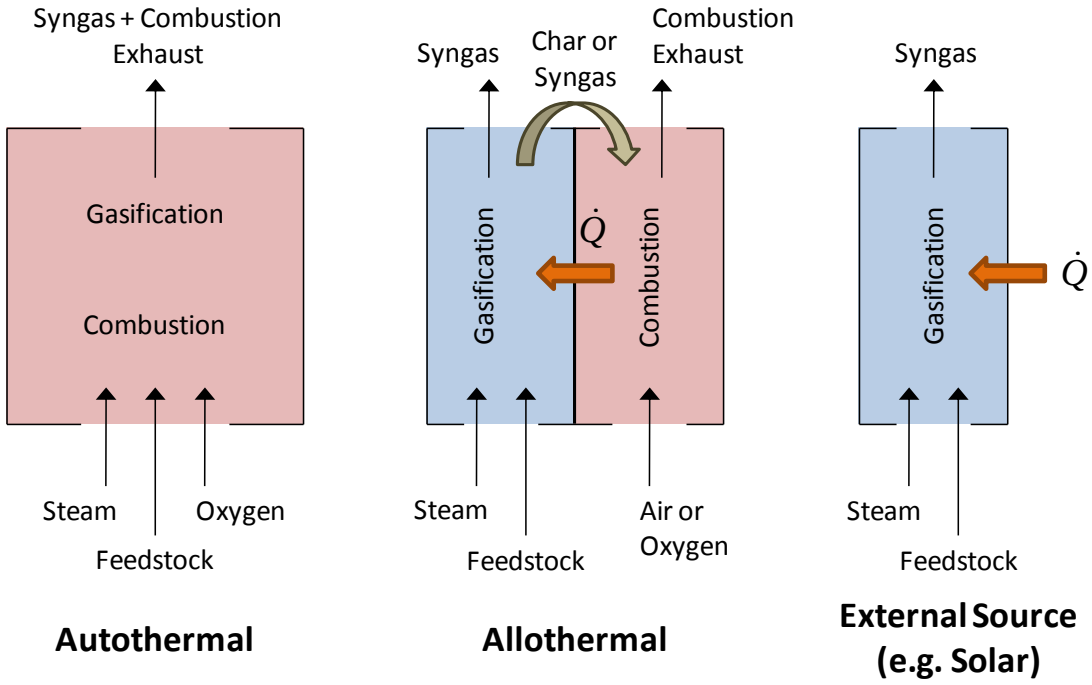

Fig. 1.1 Illustration of gasification processes according to method of supplying reaction energy. The use of solar energy eliminates combustion of feedstock or product syngas.

Improved biomass gasification processes utilize allothermal conditions, where heat is supplied by carrying out combustion of a portion of the feedstock or product gas in an external reactor. This approach avoids dilution of the product stream and the need for an oxygen facility. The energetic yield per unit feedstock is still limited, however, due to consumption of a portion of the feedstock, char, or product gas to drive the biomass gasification reactions [6].

The third case allows yields to be maximized by eliminating combustion from the process altogether. Instead, the process heat from some external source capable of achieving the temperatures and heat transfer rates required to drive the gasification process to the desired equilibrium.

1.2 Solar driven gasification

Concentrated solar energy fits the requirements of a heat source for an externally heated gasification process. In this arrangement, not only are the products of combustion

eliminated and the cost of an oxygen plant avoided, but all of the available feedstock is conserved for upgrading into synthesis gas.

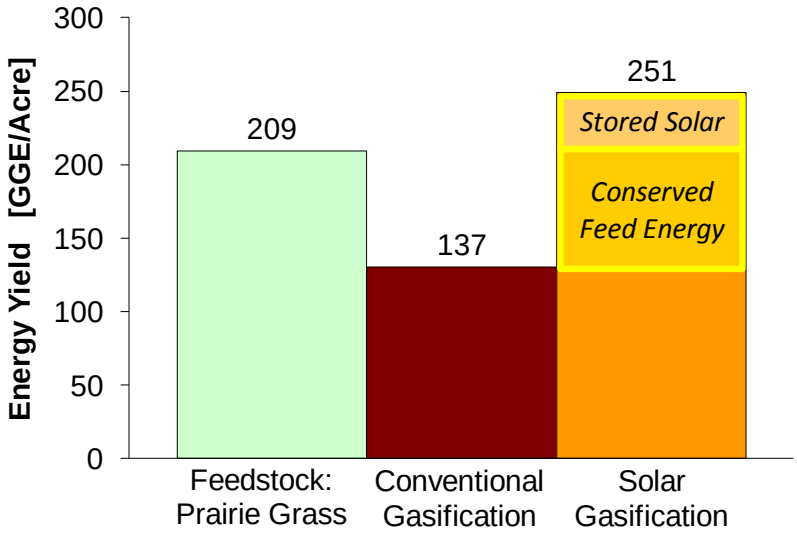

Fig. 1.2 Chemical energy content available from an acre of prairie grass feedstock (*Panicum virgatum*) compared to the yield in synthesis gas produced from the same amount of feedstock using conventional or solar gasification methods. Energy in units of gallons of gasoline equivalent (GGE).

To illustrate the potential benefits of using solar thermal energy as the heat source for gasification, consider the energy yields predicted by ideal equilibrium thermodynamics for both conventional and solar gasification. The energy content (in terms of the lower heating value in units of gasoline gallon equivalents [GGE]) of one acre of prairie grass (*Panicum virgatum*) feedstock or the product gas from said feedstock for both a conventional partial-combustion and a solar gasification process is given in Fig. 1.2. To create this figure, equilibrium thermodynamic calculations were made for (1) a stoichiometric blend of steam and prairie grass at a fixed temperature of 1200 K for the solar process and (2) an isenthalpic blend of feedstock with sufficient oxygen to achieve the same 1200 K temperature and a stoichiometric amount of steam to convert the remaining carbon for the conventional process. The stoichiometery is selected to achieve a final product gas composition with a 2:1 ratio of H_2:CO as desired for a Fischer-Tropsch fuel synthesis process in both the solar and conventional cases. Some notable features of this plot include the reduction in available energy from 209 GGE/Acre for the raw feedstock down to 137 GGE/Acre for the conventional process. On the other hand,

in the solar process there is an increase in available energy compared to the feedstock, with 251 GGE/Acre available. The energy reduction for the conventional process is due to the partial combustion of the feed material, while the gain for the solar process is due to both the avoidance of partial combustion and the storage of solar energy within the product via the endothermic gasification/pyrolysis reactions. By utilizing solar energy as the heat of reaction, there is potential to nearly double the yield of synthetic fuel per acre of biomass harvested.

Concentrated solar energy has shown great potential for use in driving thermochemical processes [7-20]. Very high temperatures, exceeding those possible from combustion or nuclear based heat sources, may be obtained and are constrained only by the magnitude of solar concentration[1] and the receiver materials. Temperatures of 1200 to 1500 K are ideal for rapid pyrolysis and gasification processes and do not require combustion of feedstock. Supplying the high-temperature process heat with concentrated solar energy has numerous advantages over conventional gasification [19, 21, 22]:

- The need for partial combustion is eliminated, allowing all of the feed material to be upgraded into useful synthesis gas.
- The product gas is not diluted by excess CO_2 and N_2 nor contaminated by other combustion by-products.
- There is no need for an economically and energetically expensive oxygen plant that otherwise is necessary for oxygen-based partial combustion.
- The energetic value of the product is *greater* than that of the feedstock—the difference is equal to the amount of solar energy stored in the chemical form.
- Fuel yield per mass of feedstock can be nearly doubled.
- The solar energy, when stored in chemical form, may be transported and consumed on demand in the same manner as any traditional fossil fuel.

The previous work on solar gasification has demonstrated many of these benefits, however issues related to poor heat transfer and production of secondary products such as char and tars have been persistent motivating the search for an improved approach to solar gasification [10]. One approach is the use of molten carbonate salts as a heat

[1] Solar concentration is a measure of the intensity of radiative flux at a receiving surface and is commonly reported in units of "suns" where 1 sun = 1 kW/m^2.

transfer medium and catalyst. This approach is discussed by Epstein [23] and demonstrated in non-solar gasification processes [24-27] with promising results.

In the proposed process, concentrated solar energy is used to drive the thermochemical conversion of low-input biomass feedstock via pyrolysis and gasification reactions in the presence of molten alkali carbonate salts. Fig. 1.3 shows the new concept for a receiver/reactor for solar-driven molten salt gasification of biomass developed in the present research. Concentrated sunlight enters the receiver through an aperture and is absorbed within the cavity and transferred via conduction and convection into the molten salt. Biomass and steam are delivered to the reactor where pyrolysis and gasification reactions take place. The product of these reactions is a blend of CO and H_2 (synthesis gas) which can be used in several existing processes for production of renewable, carbon-neutral synthetic fuels and chemicals typically obtained from petroleum or natural gas.

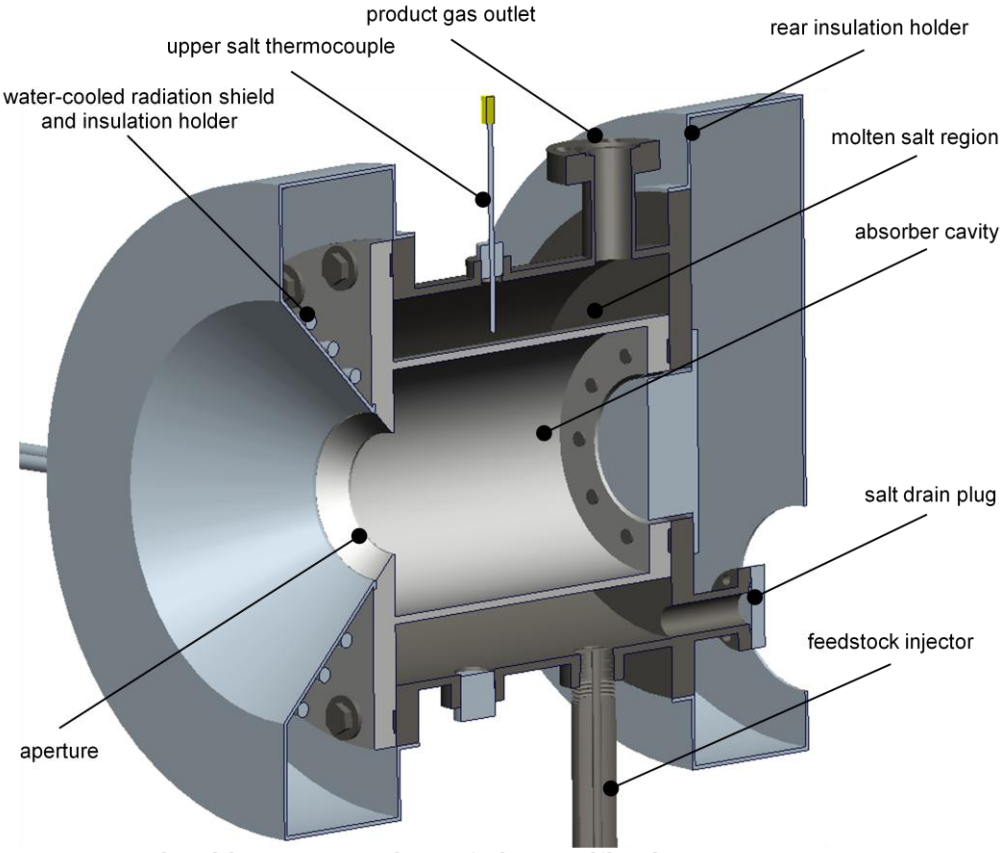

Fig. 1.3 Isometric side-cutaway view of the gasification reactor concept. Insulation material placed within these shields and around the midsection of the reactor core is not shown. Concentrated radiation enters from the left into the absorber (center cylinder). The annular gap between the absorber and housing would be filled with molten salt. Feed is delivered from the bottom and product gas from the top.

1.3 Research objectives

The overarching goal of this project is to demonstrate a molten salt solar gasification process in a 3 kW_{th} laboratory-scale reactor.

The key challenges in developing any solar thermochemical process are maximizing the utilization of solar energy within the reactor and designing a structurally sound device to operate at the elevated temperatures required. The utilization of solar energy is improved by maximizing absorption of incident radiation while minimizing losses to the environment via thermal emission from the cavity or convection and radiation from the other surfaces of the reactor. Planning for operation also require a thorough understanding of thermodynamics and kinetics of biomass gasification in a molten salt environment. Because there are no existing solar reactors of this design, comprehensive modeling of the radiative exchange and convective heat transfer will be required in the design process. Additionally, the impact of molten salt on the chemistry of biomass gasification is not well studied and it is not known if existing kinetic models are applicable or if new models must be formulated to describe reaction rates.

In addition to matching the energetic of the process, the mechanical design of the reactor and considerations of the performance of the process at a commercial scale. The operation of the reactor at high temperatures and with large variation in temperature throughout the reactor in the presence of a liquid carbonate salt presents issues related to differential thermal expansion, material compatibility, sealing, and feedstock delivery that the mechanical design must address. For future commercialization of a solar gasification process, the impact of the inherent intermittence of solar energy on downstream processes must be considered along with how thermal storage and hybridization might be used to help alleviate said impacts.

To address the scientific and engineering challenges associated with the development and demonstration of a solar gasification process, the following objectives are met.

1. To understand the energy requirements of gasification and impact of molten salt on yields, anticipated product yields are predicted using thermodynamics and compared to measured data from gasification reactions carried out at bench scale. Gaseous and secondary product distributions and specific yields

are predicted for cellulose, carbon, switchgrass, corn stover, and low-input high-diversity perennial blends in the presence of molten salt.

2. Chemical kinetic models are developed for pyrolysis and carbon gasification in the presence of molten salt.
3. A 3 kW_{th} prototype reactor for solar gasification of biomass is designed. Numerical analyses are carried out for both the thermochemical and structural design.
4. The prototype reactor is fabricated and tested in the University of Minnesota High Flux Solar Simulator (HFSS).
5. A simulation estimating the scaled-up operation of an on-sun gasification facility is made to explore the impact of hybridization and thermal storage. The outcome is parametric plots demonstrating the expected thermal efficiency, solar fraction, variation in syngas output rate, and specific yield for various plant configurations.

The thesis is structured to guide the reader through the process that was used to meet these objectives and demonstrate the solar gasification process. Chapter 2 is a literature review covering initial studies of the economic impacts of using solar energy for gasification, followed by previously considered solar gasification reactor designs. The limitations of those designs are discussed leading to the introduction of molten salts as a potential route to overcome existing problems. Chapter 3 presents an ideal thermodynamic analysis of the process of solar driven steam gasification of cellulose in terms of both first and second law approaches ending with predictions of performance for a 3 kW_{th} scale process. Chapter 4 presents a study of the chemistry of biomass gasification reactions in a molten salt environment. This study includes development of kinetic models for both cellulose pyrolysis as well as carbon gasification reactions within molten salts. Also included are results describing the yield, yield rate, and product distribution of biomass gasification for a broad range of potential feedstock materials in the presence of molten salt. Chapter 5 next details the design process for the prototype scale reactor, beginning with the design specifications and a reactor concept along with associated design parameters. Several numerical parametric studies follow in order to select values for the design parameters based on radiative exchange, convection heat

transfer, and mechanical stress requirements. Chapter 0 covers the characterization of the prototype reactor through laboratory scale testing, the initial testing results, and suggestions for how to move forward with future operation of the reactor. Chapter 7 contains a study on means of using thermal storage and hybridization to tune the output of a commercial scale gasification process. Lastly, Chapter 8 concludes the dissertation with a summary of the findings and recommendations for future work.

2 Literature Review

In this chapter, the early work which first motivated interest in solar gasification is reviewed, followed by an overview of previously tested reactors and their successes and limitations, and ending with details about the specific approach of using molten carbonate salts as a reaction medium for gasification and the associated benefits and concerns.

2.1 Solar Gasification Economics

Analyses of the economic and land-use aspects of potential solar and conventional gasification facilities have indicated that the primary capital costs are either the cost of the optics for the solar facility or the oxygen separation plant for the conventional facility [19, 21]. Considering coal gasified by the commercial Lurgi process as well as solar coal gasification, Gregg et al. [21] report that despite a 13% increase in capital expense for a solar facility, the lifetime cost for synthesis gas from the solar process would be 12% lower, at $4.47/GJ as compared to $5.12/GJ for the conventional Lurgi system. Mathur et al. considered solar gasification of coal with coal-assisted heating hybridization for nighttime operation to produce synthetic natural gas (SNG) and found that for facilities of 40 MMSCFT/day (million standard cubic feet per day) or larger capacity, gas cost would be below $10/MMBTU (million BTU) [8]. This cost would have been competitive at 2005-2008 natural gas prices; however, the recent collapse of the price of natural gas would limit commercial pursuit of such a process. In a later study, Hertwich et al. [19] consider conventional and solar biomass gasification processes as a means of meeting 10% of our transportation fuel needs by the year 2020 and examine the associated land use. They found that despite the larger facility footprint, a solar process would typically require less land at 25-54 million hectares (Mha) compared to 44-130 Mha for a conventional process. The difference is primarily due to the near-doubling of yield for the solar process.

2.2 Reactor Designs for Solar Gasification

Of the several reactor designs considered for solar gasification, most fall within four general categories: packed bed, fluidized bed, entrained flow, and most recently a drop-tube style design. Fig. 2.1 depicts solar reactors based on these designs. Although the prior work has successfully demonstrated many aspects of the solar gasification process, there is still need for improvement in the areas of heat transfer, secondary product (tars,

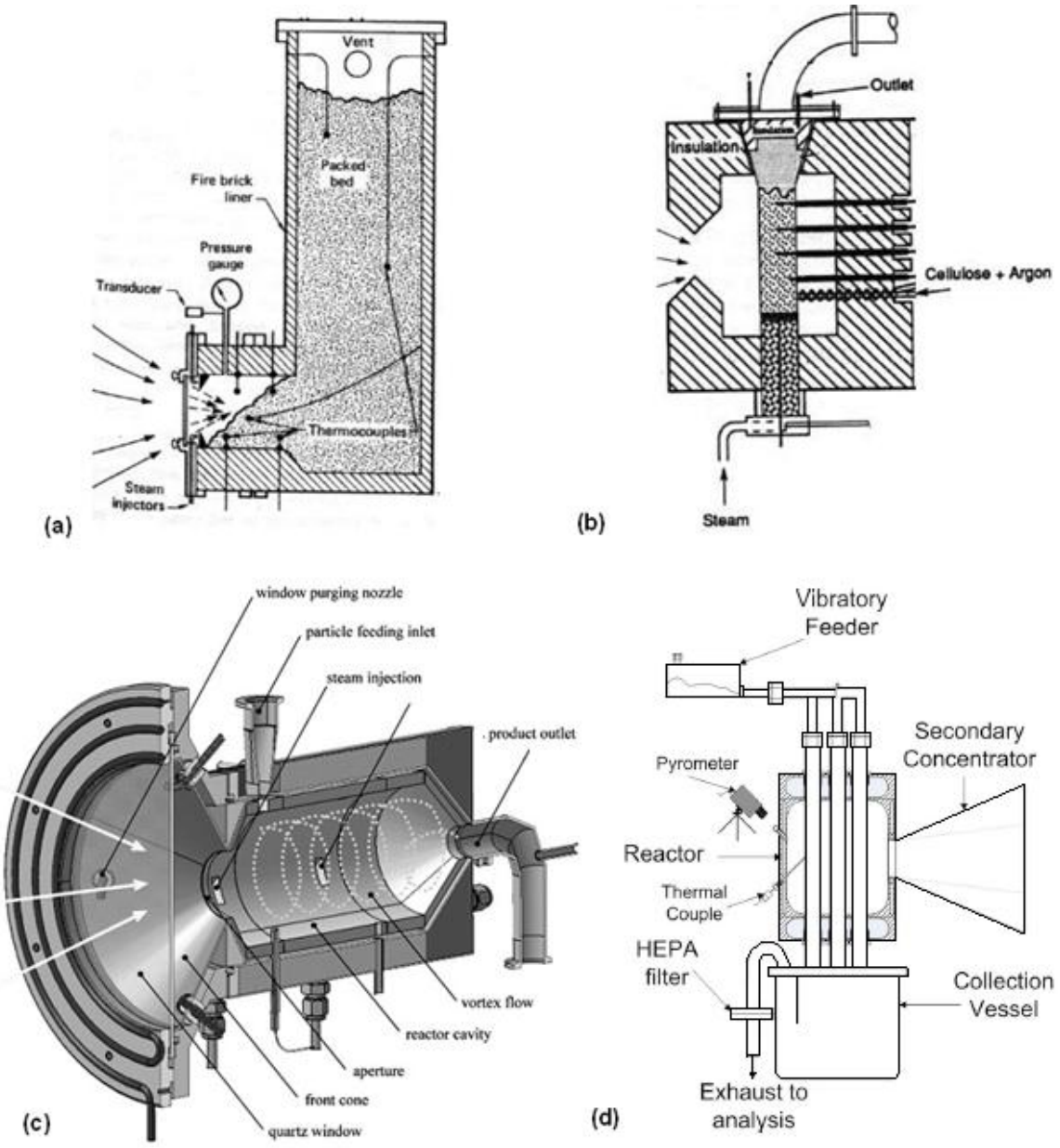

Fig. 2.1 Examples of solar reactors for gasification: (a) packed bed [7], (b) fluidized bed [11], (c) entrained flow [16], and (d) drop-tube [28]**.**

ash) formation, and process stability during solar transients. In most conventional gasification reactors, heat is supplied at the reaction site from the partial combustion of the feed, and so while removing ash is a concern, the ash does not inhibit heat transfer to the reaction. With solar gasification systems, the heat is supplied externally and must be transported to the reacting material, and as such the buildup of ash can reduce radiative heat transfer and insulate the reaction zone, strongly inhibiting the reaction progress [7, 17, 29-31].

In the packed bed design considered by Gregg et al. [7], the feedstock is loaded into a windowed reactor so that the material appears in the focus of the concentrated radiation just behind the window Fig. 2.1(a). Steam jets located around the interior of the window keep the window clear and supply the gasifying agent to the feedstock. As the material is gasified, the bed collapses in a manner that brings fresh feedstock into focus, allowing the process to continue. Alternatively, the window may be replaced by an absorber/emitter surface to avoid issues with the window by heating the feedstock with re-radiated energy [30]. Some studies have experienced the crystallization of windows due to high temperature exposure both with and without buildup of tarry condensate on the window [29, 32]. This crystallization is a significant concern as it halts the process and permanently obscures the window. In several initial studies of packed beds of coal and coal/biomass blends exposed to concentrated solar radiation and steam, solar to chemical energy conversion efficiencies of 30 to 48% were achieved [7, 12, 29]. Packed beds are especially prone to periods of significant higher hydrocarbon and tar production due to longer startup periods [7, 30] and significantly nonuniform temperature distributions caused by poor conduction in the biomass [7, 29, 30]. The tar content typically makes up 10 to 20% by weight of the overall yield [5]. Tar can also condense on windows and thus inhibit heat transfer [7, 12, 33] with tar buildup in some cases leading to the destruction of window surfaces [29].

Fluidized bed designs like the one shown in Fig. 2.1(b) [11] require that the feedstock is ground to fine particles of less than 150 μm mean diameter. The feedstock is then delivered to a vertical column where it is “fluidized” by passing inert gas and reactant steam up through the reactor. Concentrated radiation is focused on the column (which may either be opaque or transparent) to heat the bed. The size of the column and delivery

rate of fluidizing gases are controlled to maintain the feed particles within the reaction zone of the column. Transparent-walled designs have demonstrated slow absorption of radiation by biomass [11, 32] while poor conduction in biomass materials has resulted in temperature differences of up to 300 K over 20 mm of distance within the reaction zone of the bed. Slow heat transfer coupled with the necessary high flow rates of fluidizing gas has led to low solar to chemical conversion efficiencies of typically 8-10%, low feed conversion, and products more akin to slow pyrolysis than gasification reactions [11]. Potential to produce low-tar gas at temperatures as low as 1200 K was only demonstrated with the use of a crushed catalyst bed material or by operating above 1500 K without the catalyst [11]. The presence of crushed automotive catalyst reduced the observed tars by 30%, but due to poor contact between the tars and catalyst surfaces in this arrangement, significant condensate was still collected downstream [11].

Entrained flow reactors are similar to fluidized beds in that they require fine feed particles and rely on the flow of a gas to carry the particles. In entrained flow designs, however, the particles are much smaller, with mean diameters ideally less than 35 μm to ensure the feedstock is fully entrained by the flow and carried through the reactor. The reactor must be designed to allow sufficient residence time for complete reaction of the feed material and generally only works well with feedstocks that are highly absorbing in the solar spectrum. In the design considered by Z'Graggen et al. [16] shown in Fig. 2.1(c), a series of tangential jets about the interior of a cylindrical cavity create a vortex flow path of inert gas and reactant steam, into which feed particles are delivered. The feed reacts with the steam as it travels through the irradiated cavity for the residence time required to achieve full conversion. Recent studies using vacuum residue, petroleum coke or coal slurry feedstocks have exhibited rapid reactions achieving 87% feed conversion with a ~1 second residence time at temperatures up to 1800 K [16, 34, 35]. While direct irradiation in entrained flow reactors has been successful for these highly absorbing feedstocks, similar operation with biomass is not expected given the inherent low absorptivity of most biomass materials [15, 16]. Additionally, the large amounts of sweep gas required to entrain the feedstock will inherently drive down efficiencies without a means of recovering the sensible heat of the product stream.

The drop-tube reactor depicted in Fig. 2.1(d) uses gravity to deliver feedstock through an array of tubes heated in a cavity receiver, which requires less sweep gas than the fluidized bed or entrained flow designs resulting in improved efficiency. The use of opaque tubes as absorber/emitter surfaces exposes the feesdstock to radiation in the IR spectrum where biomass is typically more absorbing compared to the solar spectrum and avoids the requirement of a window. The specific design shown achieved 70-98% conversion of cellulose and grass into low-tar synthesis gas during testing by reaching very high temperatures of ~1500 K [17, 28]. This approach succeeded in reducing tars to 1 to 2% of the feedstock mass at design conditions [28]. Deviation from design conditions (a drop in temperature to 1273 K) led to rapid tar production and clogging of a downstream filter requiring the system to be shut down, illustrating the sensitivity of this approach to solar transients [17]. A different drop-tube design incorporated a fritted insert to prevent unreacted material from exiting the reactor which increased conversion to >84%, however ash buildup would prevent such a design from operating continuously long term [31].

Aside from the reactors shown, a few groups have recently began work on solar gasification processes based on supercritical water (SCW) gasification. These studies have shown that SCW conditions of $T \geq 647$ K and $P \geq 22$ MPa allow high specific syngas yields of up to 110%wt (the additional 10% mass due to hydrogen and oxygen from the water which were converted to H_2 and CO during the gasification process) [36, 37]. While operating at much lower temperatures, this approach requires very finely sized feedstocks and new methods of feeding solids into and removing ash from a high pressure environment while avoiding flow blockages at high throughput.

Several works examined the impacts of variation of the reactants for use in solar gasification and the findings tend to agree on two main points. Biomass tends to be more reactive (and thus easier to gasify) than coals or cokes, resulting in higher reaction rates and higher extents of conversion for the same operating conditions [21, 29]. With respect to the choice of steam or carbon dioxide as the gasifying agent, the use of steam results in a gas with a higher energetic yield and sufficient hydrogen to allow the gas to be used as a synthesis gas [21]. Additionally, steam gasification reaction rates are known to be an order of magnitude faster than those for CO_2 gasification in the same conditions [5].

Issues pertaining to avoidance of secondary products and achieving stable heat transfer are persistent in the solar gasification literature. In their review of several of these studies, Epstein et al. [10] note control of tar as well as problems operating steadily under transient solar conditions as being significant barriers to progress. Lede's [13] review also notes that condensable tar, ash, and particulate production are of primary concern with respect to solar gasification technologies. Both authors discuss crystallization of windows used in many reactors [29, 32] and sensitivity to the solar transients (e.g. passing clouds) as recurring themes amongst studies using windowed reactors. Methods of overcoming each of the problems discussed above will be necessary components of a successful solar gasification reactor design.

2.3 Molten carbonate salts for solar gasification

Based on the reported performance of previous gasification reactor designs, overcoming secondary product issues is one of the critical concerns for the development of gasification processes. An ideal process retains the condensed phase byproducts, such as ash and tar while cracking the tar portion into product gas. Ensuring stable operation is necessary for commercial implementation, and will be discussed in Chapter 7.

A promising technology with potential to resolve the issues of poor heat transfer, transient sensitivity, and secondary product contamination is the use of molten carbonate salts as a combined heat transfer media and catalyst within the reactor. The benefits of these salts arise from their relatively high thermal conductivity and heat capacity compared to a gaseous or fluidized particle environment, as well as the reported catalytic activity of the alkali metal cations lithium, sodium, and potassium.

Molten salt oxidation systems were utilized initially as a means of safely disposing of hazardous wastes as they allowed the synthesis gas derived from the hydrocarbon components of the waste to be collected while retaining the ashes, metals, and hazardous components in the salt melt, which can be reformed at a later time [38]. The benefits of these salts for gasification were recognized in the late 1970s and a 1-ton per hour molten sodium carbonate coal gasification pilot plant was constructed and operated from 1978 to 1981 utilizing air/oxygen partial combustion methods [39, 40]. Operation verified that salt cleanup can be carried out using existing process technology (carbonate salts are

placed into aqueous solution and processed to remove ash and sulfur as part of green liquor cleanup in the pulp and papermaking industry, which was adapted for use with this reactor) and that molten salts can yield a clean synthesis gas by cracking residual tars into gaseous products and capturing sulfur as soluble sulfide compounds in the melt. The project also demonstrated that molten salt gasification is remarkably insensitive to the presence of ash byproduct by operating with a melt that at times contained 20% coal ash by mass. By taking ash into solution and setting an effectively infinite solids residence time, the process was robust to feed size, operating at nearly complete conversion with feed sizes up to 7 mm in diameter. Despite the successful pilot testing, molten salt coal gasification was not pursued at an increased scale, perhaps due to either the moderate energetic value of gas produced via the partial combustion process, or the ease and low cost associated with using coal in Rankine cycle plants at that time. However the project established the feasibility of many features that will be important for eventual commercialization of molten salt gasification technologies, including: salt storage and regeneration, equipment material compatibility, ash and tar control, and limited product gas CO_2 capture.

In addition to prior use for gasification, molten salts have been used as a thermal storage medium in concentrated solar power systems for electricity production. Solar Two, a tower style concentrating collector, operated a Rankine cycle for power generation using molten nitrate salt as a heat transfer medium from 1994 to 1999 [41]. Corrosion issues required the use of low carbon materials and specialty bearing for pump components immersed in the flow. Startup and shutdown procedures were developed to purge salt from the system after operation and to avoid freezing during the initiation of flow. The use of molten salts allowed the system to continue operation for several hours after sunset. Thermal storage in nitrate salts has appeared in several commercial facilities since, including the Solana Generating Station in the US and the Andasol, Extresol, and Torresol facilities in Spain. The largest planned facility using molten nitrate salts is currently under construction by SolarReserve in Tonopah, NV, USA [42].

In the last decade there has been a revival of molten salt gasification research with interest in pairing the process with solar thermal input. Several groups have performed laboratory bench scale experiments using molten salts to gasify coal [43-45] and

biomasses [24-27] using carbon dioxide as the gasifying agent. The amount and composition of salts has been shown to influence the gasification reactions. The alkali metal carbonates that have been explored are pure sodium carbonate [24, 26], sodium and potassium carbonate [24, 26, 43-45], lithium and potassium carbonate [27], and the ternary blend of lithium, potassium, and sodium carbonates [24, 26]. The eutectic composition is typically chosen for the intermixed salts as this composition ensures the lowest possible melting point for the combination of any number of salts. One parametric survey of the efficacy of blended salts over a pure salt reported that the peak rates of the gasification reactions in a sodium-potassium and sodium-potassium-lithium carbonate blend were seven and eight times higher than that of gasification in pure sodium carbonate [26]. The authors suggest the enhancement may be from avoiding local freezing of the salt, a result of the decreased melting point for these blends. Additionally, the mass ratio of salt to feed was surveyed, and it was found for each of the salts that the rate of reaction achieves a constant maximum for ratios greater than 10:1 (salt:feed). This result is likely due to thermal rather than chemical limitations. Considering these results, we may expect optimum performance from a ternary salt blend at salt to mass ratios greater than ten.

Evidence of the catalytic effect of alkali carbonate salts on pyrolysis and gasification as well as in the conversion of tars into gaseous products exists in several studies. The catalysis of pyrolysis reactions is established in [25] by supplying feedstock without a gasifying agent (such as steam or carbon dioxide) to a heated reactor with and without salt present. An increase in the rate of product yield by 20% was observed with salt present. It was suggested that the alkali metals catalyze pyrolysis by assisting in breakage of the β(1,4)-glycosidic bonds between individual monomers [26]. Yoshida et al. and Matsunami et al. [44, 45] established catalysis for carbon gasification reactions by using activated carbon or char. Gasification of activated carbon with carbon dioxide showed a rate increase of 150% when salt was present. Concerning the catalysis of tar conversion, it has been observed that for conditions that would normally result in 18% mass residual tar product, the presence of molten salt reduces the tar present to undetectable levels [25].

The catalysis observed in these studies may not take place in a flash-pyrolysis reaction because of poor contact between the salt and the feed material during pyrolysis. Two of these prior studies were conducted in a manner that involves slowly heating the reactant material and salt together in the reactor [24, 26]. This method allows the salt to permeate the materials before pyrolysis began. Additionally, the work by Adinberg et al. [25] delivered feed to a salt mass less than 10 times the feed delivery mass, which likely resulted in the salt temperature dropping significantly during the run.

A few challenges have been encountered with molten salt gasification systems. The distribution of the feedstock within the salt has been observed to strongly affect the gasification rate. Yoshida et al. [44] observe that char and activated carbon particles tend to sink to the bottom of an unagitated melt due to their higher density and remain unreacted until removed. In a follow up work, the gasification agent (in this case carbon dioxide) was introduced beneath the surface of the melt. This modification was sufficient to agitate the melt and keep the particles suspended, nearly doubling the gas evolution rate [45]. Second, the ash present in feedstock tends to react with and deactivate the catalytic behavior of the carbonate salt, forming glassy alkali silicate species that are inert to the gasification process. Thus far, however, salt melts containing up to 20% by weight of ash have not shown decreases in the rate of gasification or the overall syngas yield [39, 40]. Though the molten carbonate salts desired for this process tend to be corrosive to many materials, compatibility investigations, driven by the desire to utilize molten salts in Molten Carbonate Fuel Cells (MCFCs), have been conducted [46]. The result of these investigations is that most ceramics, especially alumina, appear to be inert to the salts, and a number of steel alloys have been found to sufficiently resist attack from the heated salts. The metals include Inconel 600, 316L stainless steel, and Hastelloy, with Inconel 600 demonstrating the most corrosion resistance.

There is evidence that molten salts would have even greater benefit in steam gasification compared to carbon dioxide gasification. In all of the published literature on molten salt gasification, carbon dioxide has been used as a gasifying agent. The carbon monoxide product has medium to low energetic value and typically contains more than 30% inert carbon dioxide. One study suggested steam gasification be investigated after noting that the presence of moisture increased the solubility of sulfur compounds in the

melt, reduced the observed soot produced, and also resulted in nearly double the biomass conversion rates [27]. Also, for the production of liquid fuels and chemicals, a synthesis gas with significant hydrogen content is desired, and as such steam gasification is typically preferred due to the increased hydrogen content of the product gas.

One concern about steam gasification in molten salts, is the reaction of steam with the salt. Maund and Earp [47] found that carbonate salts could be reformed into hydroxide salts by exposing the melt to steam, thereby also releasing carbon dioxide. The reverse reaction, reforming of hydroxides into carbonates by absorbing carbon dioxide, also readily occurs. The reversible reaction describing these interactions is given by

$$H_2O + M_2CO_3 \rightleftarrows 2 \cdot MOH + CO_2 \tag{2.1}$$

This behavior presents both the challenge of excess carbon dioxide production as well as the possibility of carbon dioxide capture using the carbonate-depleted melt or an aqueous solution thereof. For instance, the previously mentioned pilot molten salt gasification facility demonstrated that an aqueous solution of the used melt could be sprayed through the product gas to re-absorb a portion of the carbon dioxide [39].

The works reviewed here have established many benefits of using molten salts as a catalyst and heat transfer media; however there are several gaps in the existing literature. The reactions of pyrolysis and steam gasification do not have suitable kinetic models for use in estimating the performance of a molten salt gasification reactor. The pyrolysis reaction needs to be studied in a situation where the salt is heated to the temperature of interest before feed is introduced, and there must be a sufficient mass of salt to avoid large temperature deviation upon delivery in order to be representative of a continuous process. The impact of molten salt on the resulting product distribution under these heating conditions is also not known. The design of a receiver/reactor for a molten salt solar gasification process has never been carried out. The reactor will need to efficiently absorb incident concentrated radiation and deliver it to the salt melt in a manner that creates a relatively uniform and well controlled temperature field to overcome the issues described for other solar gasifier designs.

The work carried out in the following chapters answers these remaining questions paving the way for the manufacture and testing of a prototype molten salt solar

gasification process and consideration of how a scaled-up process might operate at the commercial scale.

3 Thermodynamics of Gasification

In this chapter, the chemical and physical thermodynamics of solar gasification are explored. First, the chemical thermodynamics of gasification and resulting selection of operating conditions are presented. Thereafter, a first and second law thermodynamic analysis of the process of solar gasification was carried out in order to determine estimates of feestock throughput, solar efficiency, cold gas efficiency, exergy efficiency, and to explore the sources of exergy loss throughout the gasification process.

The desired range of operating temperatures may be estimated by calculating the thermodynamically favored products for the equilibrium products of the reactants given in eq. (1.1). The method of Gibbs free energy minimization was used while considering potential products of $C_{(s)}$, O_2, CO, CO_2, CH_4, H_2, and H_2O for a stoichiometric mix of cellulose and steam over temperatures from 400 K to 1500 K. The resulting products are reported in Fig. 3.1, which shows that carbon conversion increases rapidly as the temperature approaches 1150 to 1200 K, above which >98% complete conversion to gaseous species is favored. Because we desire to produce a synthesis gas consisting of only hydrogen and carbon monoxide, which maximizes molar yield of gases, the reactions ought to occur at temperatures of 1200 K and above and at atmospheric pressure, where carbon conversion is essentially complete and the products are a 1:1 ratio of hydrogen and carbon monoxide with only small concentrations of other species present.

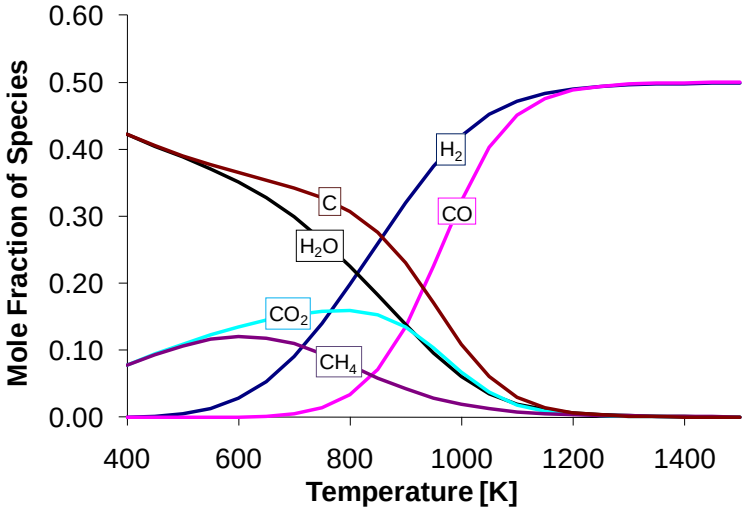

Fig. 3.1 Equilibrium composition for the stoichiometric steam gasification of cellulose (1 atm total pressure, obtained via Gibbs free energy minimization).

To predict the performance of the process, four different measures of performance or efficiency are considered. The cold gas efficiency represents the energy available in the product gas stream as a fraction of the energy present in the original feedstock (in terms of lower heat values) and is a function of the final syngas composition and extent of reaction.

$$\eta_{\mathrm{CG}} = \frac{\dot{m}_{\mathrm{gas}} \mathrm{LHV}_{\mathrm{gas}}}{\dot{m}_{\mathrm{feed}} \mathrm{LHV}_{\mathrm{feed}}} \tag{3.1}$$

The solar-to-chemical efficiency is the fraction of the incident solar power used to upgrade the energetic content of the feed material to that of the product synthesis gas.

$$\eta_{\mathrm{solar}} = \frac{\dot{m}_{\mathrm{gas}}\ \mathrm{LHV}_{\mathrm{gas}} - \dot{m}_{\mathrm{feed}}\ \mathrm{LHV}_{\mathrm{feed}}}{\dot{Q}_{\mathrm{solar}}} \tag{3.2}$$

The energy efficiency is simply the ratio of energy output (in terms of lower heat values) of the product syngas to the solar power and solid feedstock energy inputs, and relates to overall system performance rather than specifically utilization of the solar input.

$$\eta_{\mathrm{energy}} = \frac{\dot{m}_{\mathrm{gas}}\ \mathrm{LHV}_{\mathrm{gas}}}{\dot{Q}_{\mathrm{solar}} + \ \dot{m}_{\mathrm{feed}}\ \mathrm{LHV}_{\mathrm{feed}}} \tag{3.3}$$

Lastly, the exergy efficiency, also known as the "degree of perfection," describes how close the system is to an ideal fully reversible, adiabatic, process by reporting the fraction of the input exergy (primarily from the feedstock and the solar input) that is present in the output syngas stream.

$$\eta_{\mathrm{exergy}} = \frac{\dot{B}_{\mathrm{syngas},T_0}}{\dot{B}_{\mathrm{feed}} + \dot{Q}_{\mathrm{solar}} \cdot \left(\frac{b_{\mathrm{solar}}}{h_{\mathrm{solar}}}\right)} \tag{3.4}$$

The ratio $b_{\mathrm{solar}}/h_{\mathrm{solar}}$ is an exergy to thermal energy ratio defined for solar radiation [48]. The exergy of the syngas and feed in eq. (3.4) consist of both a physical and chemical exergy component.

$$\dot{B}_{\iota} = \dot{n}_i\ (b_{i,\mathrm{ph}} + b_{i,\mathrm{ch}}) \tag{3.5}$$

The physical exergy is based on the enthalpy and entropy of a material in its current state relative to at a base state and represents the potential from work via change of state.

$$b_{i,\mathrm{ph}} = \left(\bar{h}_i - \bar{h}_{i,0}\right) - T_0\ (\bar{s}_i - \bar{s}_{i,0}) \tag{3.6}$$

The chemical exergy, however, is based on reference values of potential for work from chemical interactions and species concentration. For a mix of gases or a single gas, the specific molar chemical exergy is

$$b_{i,\mathrm{ch}} = \sum_j y_j \, b_{j,0} + R_u \, T_0 \sum_j y_j \ln (y_j) \tag{3.7}$$

The standard chemical exergy, $b_{j,0}$ is tabulated for various species in the texts by Szargut [48] and Moran and Shapiro [49]. For a solid fuel containing primarily carbon, hydrogen, and oxygen such as cellulosic biomasses, the chemical exergy is given by

$$b_{\mathrm{feed,ch}} = \mathrm{LHV}_{\mathrm{feed}} \, M_{\mathrm{feed}} \, \beta_{\mathrm{ex}} \tag{3.8}$$

$$\beta_{\mathrm{ex}} = \frac{1 - 0414 + 0.0177 \cdot \left(\frac{\nu_{\mathrm{H}}}{\nu_{\mathrm{C}}}\right) - 0.3328 \cdot \left(\frac{\nu_{\mathrm{O}}}{\nu_{\mathrm{C}}}\right) \cdot \left[1 + 0.0537 \cdot \frac{\nu_{\mathrm{H}}}{\nu_{\mathrm{C}}}\right]}{1 - 0.4021 \cdot \frac{\nu_{\mathrm{O}}}{\nu_{\mathrm{C}}}} \tag{3.9}$$

The molar mass of the feedstock, M_{feed}, accounts for ash and moisture content of the fuel as needed for mass to mole conversion. The equation for β_{ex} is a function of ratios of the elemental composition of the fuel where ν_i is the number of atoms of element *i* in a single molecule of the fuel.

The general solar gasification process being considered is illustrated in Fig. 3.2. The absorber is directly in contact with the reactor, but to allow the exergy loss due to heat transfer to be calculated, they are shown as separate systems here. For an indirectly heated gasification reactor, solar power arrives at an opaque absorber surface where a portion is reflected and lost to the environment and the rest is absorbed. The hot absorber also loses energy to the environment via re-radiation, while the net absorbed power is transferred to the reactor. Steam and pure cellulose feedstock are supplied to the reactor where the net absorbed power provides the heat to drive the pyrolysis and gasification reactions. The additional heat losses from the system exterior are grouped as a general heat loss rate subtracted from the reactor's operating energy balance. Because the stoichiometric amount of steam needed for gasification is small compared to the product gas yield, there is an opportunity to recover a portion of the heat from the product gas by producing steam from an incoming ambient water stream in a heat-recovery steam generator (HRSG). The remaining thermal energy of the product gas stream is removed by quenching the products to the ambient temperature.

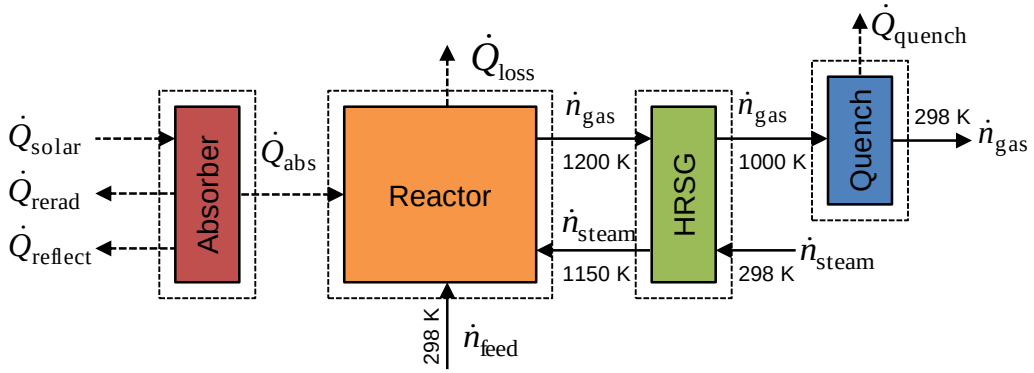

Fig. 3.2 Schematic diagram of the solar biomass gasification system used for initial thermodynamic calculations. The boxes represent the various components of the system and the arrows represent flows of energy or materials. The dotted lines indicated system boundaries for the various components. The temperatures of the flows between devices used in the analysis are indicated above the solid arrows.

To begin the analysis, consider the system of the cavity absorber. The cavity acts to absorb the incident concentrated solar radiation for use within the reactor while emitting reflected and re-radiated thermal energy. The steady state energy balance yields

$$0 = \dot{Q}_{\text{solar}} - \dot{Q}_{\text{abs}} - \dot{Q}_{\text{rerad}} - \dot{Q}_{\text{reflect}} \tag{3.10}$$

For a simplified grey model of the cavity, the various heat transfer terms are

$$\dot{Q}_{\text{solar}} = I \cdot C \cdot A_{\text{a}} \tag{3.11}$$

$$\dot{Q}_{\text{rerad}} = \sigma \cdot \epsilon_{\text{a}} \cdot T_{\text{abs}}^4 \cdot A_{\text{a}} \tag{3.12}$$

$$\dot{Q}_{\text{reflect}} = \dot{Q}_{\text{solar}} \cdot (1 - \epsilon_{\text{a}}) \tag{3.13}$$

Dividing the remaining terms by the incident solar power and solving for the ratio of absorbed to incident power, yields an expression for the absorption efficiency.

$$\frac{\dot{Q}_{\text{abs}}}{\dot{Q}_{\text{solar}}} = 1 - \epsilon_{\text{a}} \cdot \frac{\sigma \cdot T_{\text{abs}}^4}{I \cdot C} - (1 - \epsilon_{\text{a}}) = \epsilon_{\text{a}} \cdot \left(1 - \frac{\sigma \cdot T_{\text{abs}}^4}{I \cdot C}\right) = \eta_{\text{abs}} \tag{3.14}$$

The performance of the cavity is a function of geometry and surface properties, encompassed by the apparent emissivity ϵ_a, as well as operating conditions of the reactor, specifically the absorber surface temperature T_{abs} and the solar facility concentration C (where the insolation I is constant with a value of 1 kW/m^2). To determine the loss of exergy due to heat transfer through the absorber, exergy accounting is applied.

$$\delta \dot{B}_{\text{cavity}} = \left(\dot{Q}_{\text{solar}} - \dot{Q}_{\text{reflect}}\right) \cdot \frac{b_{\text{solar}}}{h_{\text{solar}}} - (\dot{Q}_{\text{rerad}} + \dot{Q}_{\text{abs}}) \cdot \frac{T_{\text{abs}} - T_0}{T_{\text{abs}}} \tag{3.15}$$

Here the term on the left hand side is the rate of exergy destruction in the cavity absorber.

The absorbed portion of the radiation is transported from the cavity surface to the molten salt. Here a portion of this heat drives the gasification reactions while the rest is lost to the ambient surroundings. An energy balance for the reactor system yields

$$0 = \dot{Q}_{\text{abs}} - \dot{Q}_{\text{loss}} - \dot{n}_{\text{feed}}\, d\bar{h}_{\text{rxn}} \tag{3.16}$$

The equation of exergy accounting yields

$$\delta\dot{B}_{\text{reactor}} = \dot{Q}_{\text{abs}} \cdot \frac{T_{\text{abs}} - T_0}{T_{\text{abs}}} + \dot{B}_{\text{feed}} - \dot{B}_{\text{syngas},\, T_{\text{rxn}}} \tag{3.17}$$

The heat loss term does not appear explicitly on the right side of eq. (3.17) because the system boundary includes the exterior of the reactor which is nearly at ambient temperature. There is negligible exergy in the loss stream at this boundary, as it has already been lost within the reactor as the heat was conducted to the surface and is thus embodied by the reactor exergy loss rate. For an initial analysis, we may approximate the magnitude of the heat loss rate with the term

$$\dot{Q}_{loss} = \delta_{loss} \cdot \dot{Q}_{solar} \tag{3.18}$$

Based on research for similar sized reactors operating at similar temperatures, the thermal losses are estimated as 20-30% of the rated solar input power. This loss estimate was calculated by considering 0.2 m of Fiberfrax insulation around a 1250 K reactor in conditions ranging from still to a 40 MPH crosswind. For a conservative base-case, we will assume a 25% loss of the rated thermal input. The enthalpy of reaction per unit feed in the energy balance includes heat consumed for both pyrolysis and carbon gasification, yielding only gaseous products from the initial feedstock and steam.

$$d\bar{h}_{rxn} = \bar{h}_{prod} - \bar{h}_{react} \tag{3.19}$$

$$\bar{h}_{react} = \bar{h}_{f,feed} + \gamma \cdot \left[\bar{h}_{f,H_2O} + \left(\bar{h}_{H_2O,T_s} - \bar{h}^o_{H_2O}\right)\right] \tag{3.20}$$

$$\begin{aligned} \bar{h}_{prod} = {} & a \cdot \left[\bar{h}_{f,H_2} + \left(\bar{h}_{H_2,T_{rxn}} - \bar{h}^o_{H_2}\right)\right] + \\ & b \cdot \left[\bar{h}_{f,CO} + \left(\bar{h}_{CO,T_{rxn}} - \bar{h}^o_{CO}\right)\right] + \\ & c \cdot \left[\bar{h}_{f,CO_2} + \left(\bar{h}_{CO_2,T_{rxn}} - \bar{h}^o_{CO_2}\right)\right] + \\ & d \cdot \left[\bar{h}_{f,CH_4} + \left(\bar{h}_{CH_4,T_{rxn}} - \bar{h}^o_{CH_4}\right)\right] + \\ & e \cdot \left[\bar{h}_{f,H_2O} + \left(\bar{h}_{H_2O,T_{rxn}} - \bar{h}^o_{H_2O}\right)\right] \end{aligned} \tag{3.21}$$

The term γ in eq. (3.20) is the molar ratio of steam to feedstock, which for stoichiometric gasification is given by

$$\gamma = \frac{\dot{n}_{steam}}{\dot{n}_{feed}} = \nu_C - \nu_O \tag{3.22}$$

The molar gas production per mole of feedstock is simply the sum of coefficients from the right hand side of eq. (3.21).

$$n_{gas} = a + b + c + d + e \tag{3.23}$$

Mass balances for each element (carbon, hydrogen, and oxygen) may be written.

C: $$\nu_C = b + c + d \tag{3.24}$$

H: $$\nu_H + 2 \cdot \gamma = 2 \cdot a + 4 \cdot d + 2 \cdot e \tag{3.25}$$

O: $$\nu_O + \gamma = b + 2 \cdot c + e \tag{3.26}$$

The above three equations partially define the five product composition terms (a – e), leaving room for two additional constitutive relations to fix the composition. Synthesis gas composition is often described by two "quality ratios": the ratio of hydrogen to carbon monoxide, and the ratio of carbon dioxide to carbon monoxide. Equilibrium thermodynamics based on Gibbs free energy minimization predicts an ideal yield at 1200 K and above corresponding to

$$\frac{a}{b} = \frac{n_{H_2}}{n_{CO}} = 1 \tag{3.27}$$

$$\frac{c}{b} = \frac{n_{CO_2}}{n_{CO}} = 0 \tag{3.28}$$

These form the base case values for the analysis; however non-equilibrium composition are expected from actual operation, with data from initial pyrolysis/gasification runs resulting in observed values of $a/b = 0.82$ and $c/b = 0.098$.

The hot product gas exits the reactor at T_{rxn} with a significant amount of sensible energy, so a heat recovery steam generator is included in the design to recuperate this energy. For a stoichiometric amount of steam, the syngas would only need to be cooled by ~200 K to T_g in order to boil and superheat the incoming water from ambient conditions to within 100 K of the reactor temperature, T_s. The energy balance for such a device is given by

$$0 = \dot{n}_{feed} \left(n_{gas} \cdot \sum_i y_i \cdot \left(\bar{h}_{i,T_{rxn}} - \bar{h}_{i,T_g} \right) + \gamma \cdot \left(\bar{h}^o_{H_2O} - \bar{h}_{H_2O,\,T_s} \right) \right) \tag{3.29}$$

For the summation, $i = \{\mathrm{H_2}, \mathrm{CO}, \mathrm{CO_2}, \mathrm{CH_4}, \mathrm{H_2O}\}$. The heat recovery steam generator is assumed adiabatic with steam being produced at a fixed temperature of $T_s = T_{rxn} - 100\ \mathrm{K} \approx 1150\ \mathrm{K}$, allowing the synthesis gas outlet temperature to vary as needed to close the energy balance. The exergy accounting equation for this device includes the in and outflow terms for both streams and the exergy destruction rate only.

$$\delta \dot{B}_{HRSG} = \dot{B}_{syngas,\,T_{rxn}} - \dot{B}_{syndas,T_g} + \dot{B}^0_{water} - \dot{B}_{water,T_s} \tag{3.30}$$

Following the heat recovery, the product gas is discharged to a downstream source. Because the sensible thermal content of the gas will most likely not be used and because the gas will likely be compressed prior to piping or usage, a final quench process is included to cool the synthesis gas to ambient condition of $T_0 = 298.15\ \mathrm{K}$. The energy balance for this quench cooling step yields

$$0 = \dot{n}_{\mathrm{feed}}\, n_{\mathrm{gas}} \cdot \sum_i y_i \cdot \left(\bar{h}_{i,T_\mathrm{g}} - \bar{h}_{i,T_0}\right) - \dot{Q}_{\mathrm{quench}} \tag{3.31}$$

The exergy accounting equation similarly produces

$$\delta \dot{B}_{\mathrm{quench}} = \dot{B}_{\mathrm{syngas},\,T_\mathrm{g}} - \dot{B}_{\mathrm{syngas},\,T_0} \tag{3.32}$$

Here again, similar to the exergy balance for the reactor, the heat loss term is not included as the system boundary includes just outside of the quench device, thus the interface temperature is nearly ambient. Essentially the exergy destruction rate includes the effects of the quenched or lost thermal exergy for both situations.

The above equations form a closed description of the prototype biomass gasification reactor with six variable parameters of interest. These variables are the apparent emissivity of the cavity, ϵ_a, the concentration of the incident solar flux, C, the portion of the rated power lost by conduction and convection to ambient conditions, δ_{loss}, the temperature of the absorber/reactor, T_{rxn}, and the two quality ratios describing the product gas composition, $a/b = \mathrm{H_2/CO}$, and $c/b = \mathrm{CO_2/CO}$.

The base case values of these parameters are given in Table 3.1 along with a range of values to be explored for each parameter. The apparent emissivity is varied from the value of unity (a rational value for base-case geometry described in Chapter 5) to 0.2 at which point absorption efficiency reaches zero when all other parameters are fixed at the base values. For the concentration, the range is from 510 suns, corresponding to a single lamp out of 7 in use within our concentrated solar simulator, to the base case of 1530

suns for 3 of 7 lamps, to a maximum of 3600 suns corresponding to the full design flux of the solar simulator. These values also correspond to the range of concentration ratios available from parabolic trough systems on the low 500 suns range, current flat-mirror tower systems around the 1500 suns range, and parabolic-mirror tower or parabolic dish systems at the high end 3600 sun concentrations. As previously mentioned the thermal loss as a fraction of rated power may vary from 0-30% with 25% being the conservative base case. The reactor is designed to operate at a nominal temperature of 1200 K, though we explore the effect on performance for variation from 1300 K to 1100 K (a minimum at which point the pyrolysis reaction begins to significantly slow) and up to 1500 K, beyond which the yield strength drops off for Inconel 601. For the composition of the product gas, we keep the base case given by equilibrium thermodynamics given the similar observed results from actual experimental data.

Table 3.1 Parametric ranges for 1st and 2no law analysis.

Parameter	*Base Case*	*Range*
ϵ_a	1	0.2 – 1
C	1530	510 – 3600
δ_{loss}	0.25	0 – 0.3
T_{rxn}	1200 K	1100 – 1300 K
a/b	1	*Not varied*
c/b	0	*Not varied*

The equations were solved using Engineering Equation Solver (EES) for base and parametric cases. At the base-case set of values for each parameter, the reactor system performance can be quantified with the efficiencies found in Table 3.2.

Table 3.2 Base-case performance quantities

Performance Indicator	*Base Case Value*
η_{abs}	91%
η_{CGE}	122%
η_{solar}	53%
η_{energy}	79%
η_{exergy}	69%

With selection of a cavity geometry that approaches black behavior, the absorption of solar energy with this design can be quite efficient, resulting in 91% of the incident

power being delivered to the salt melt within the reactor as indicated by the absorption efficiency. The energetic content of the feedstock is significantly increased, with a cold gas efficiency of 122% implying that with 22% of the energy content was derived from the solar input. In traditional partial-combustion based gasification processes, the cold gas efficiency is inherently limited to a maximum of 100% and typically only 60-75% is achieved in practice. The predicted utilization of solar energy at an efficiency of 53% is fairly high compared to values reported for previous solar gasification reactors, and indicates this design should be competitive with previous reactors. For a visual

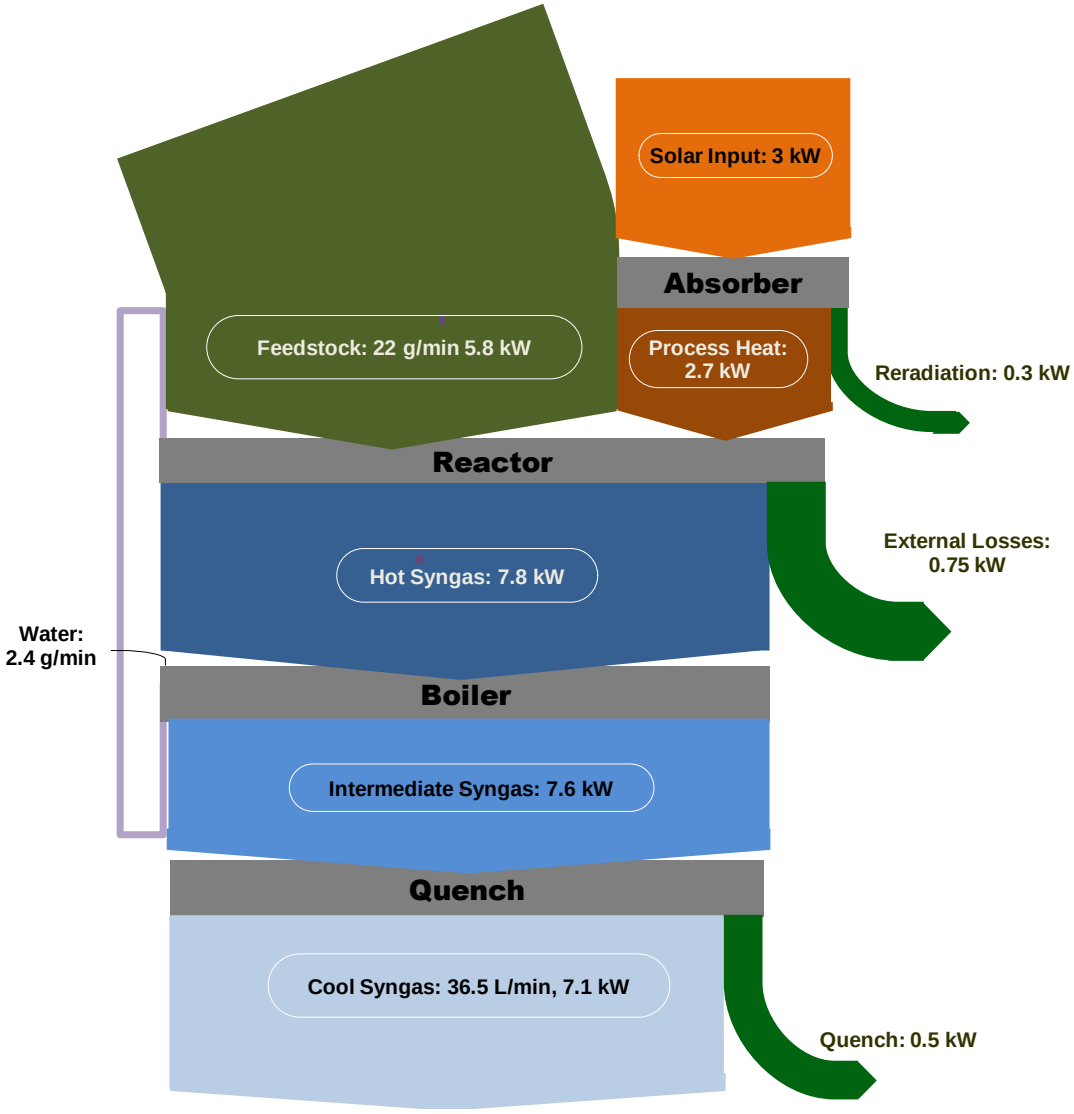

Fig. 3.3 The energy flows throughout the solar biomass gasification system as calculated from the base case of the thermodynamic analysis are shown in Sankey diagram form. The widths of the arrows are proportional to the magnitude of the energy flows.

representation of the outcome of the energy analysis, a Sankey diagram of the energetic flows to and from each component in the system is shown in Fig. 3.3. In this diagram, the thickness of the arrows is proportional to the magnitude of the flows. The primary loss mechanism is conduction through the insulation and convection and radiation from the insulation to the ambient environment. Re-radiation from the absorber is the second most important loss, followed by the quenching of sensible heat from the warm product gas. Improvement to the system should focus on reducing these losses.

The results of the parametric survey are shown in the series of plots in Fig. 3.4. With respect to the apparent emissivity of the cavity the solar efficiency scales linearly from the baseline value for a near-black cavity to zero near a value of 0.25. This behavior supports the assertion that a cavity design, rather than a non-enclosed absorber design, is critical for our application as cavities allow the use of surfaces that are far from black while still achieving near-black apparent emissivities (or absorption efficiencies). This result is further elucidated in the cavity radiation analysis of section 5.2.4. The exergy efficiency parallels this behavior for high (greater than 0.6) apparent emissivities, but

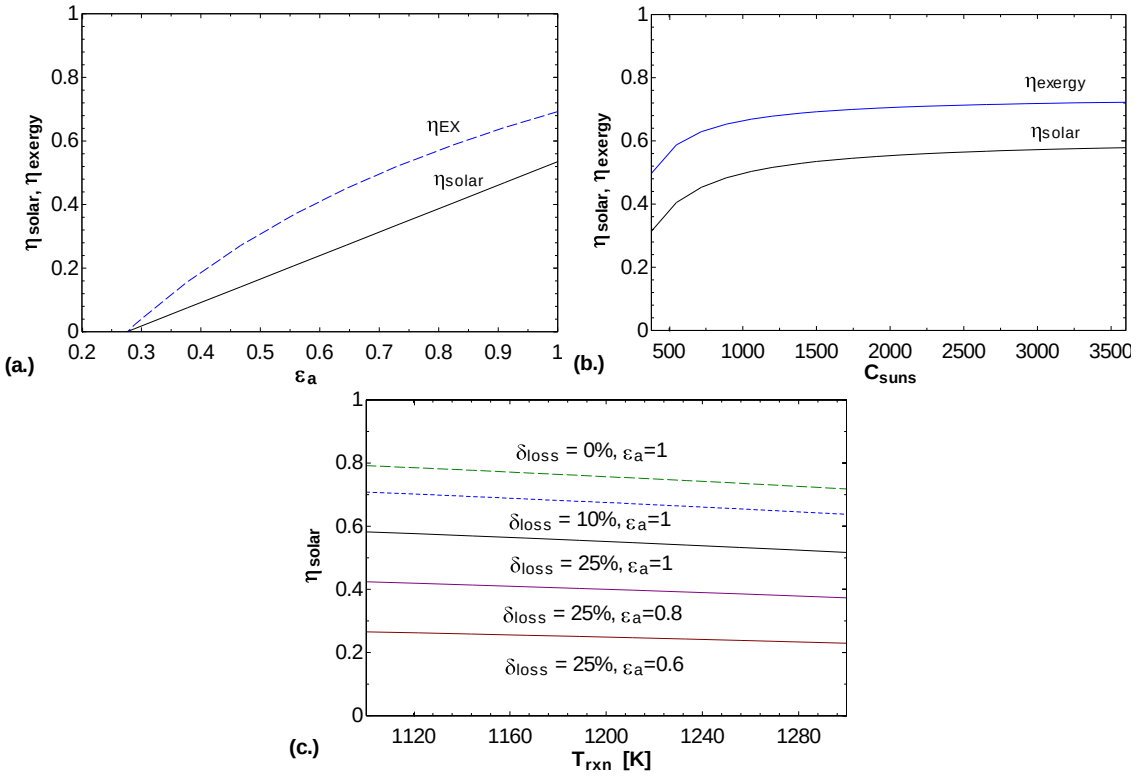

Fig. 3.4 Parametric plots exhibiting the variation in reaction performance parameters with respect to the key operating variables described in Table 3.1.

collapses towards the solar efficiency curve at lower values. This result implies that for high apparent emissivities, the variation of the solar and exergy efficiencies are similar and tell the same story. This is backed up by the plot (b.) which demonstrates again parallel behavior between the two efficiencies when considering varied flux concentrations. There is a knee in the plot around 750 suns, and above 1000 suns both efficiencies level out near their base case. All of the planned operating concentrations are 1200 suns and higher which will keep us far from the knee of the curve. In plot (c.) the focus is on solar efficiency across a range of target reactor temperature from 1100 K to 1300 K. The solar efficiency is relatively stable with respect to temperature, varying about 8% within this range. The effect of varied thermal losses or apparent emissivity is more pronounced as a 25% change in thermal loss fraction or 20% loss in apparent emissivity corresponds to a 20% drop in solar efficiency. These features again highlight the importance of reducing the reactor losses to ambient and achieving a near-black cavity, which are key issues to be addressed in the design work.

4 Biomass Pyrolysis & Carbon Gasification in a Molten Salt Environment

The chemical kinetics and reaction rates of biomass pyrolysis and steam gasification of carbon in a molten salt environment are studied. As of yet, steam gasification reactions within an alkali carbonate salt melt have not been adequately quantified, and kinetic models are only available for concentrations of alkali carbonate catalyst up to a few weight percent of the feedstock mass [50]. The findings of these initial studies demonstrate an initial decrease in activation energy for gasification at low alkali carbonate doping levels, followed by relatively unchanging activation energy but continually increasing pre-exponential factors as the doping level is increased. This finding indicates carbon sites are becoming available as more catalyst is added, however they do not see saturation of carbon sites at the low concentrations considered, so at the salt-rich conditions of the proposed process, the existing kinetic model are unlikely to apply. Additionally, existing catalytic models may not be appropriate for the rapid reaction of flash pyrolysis of biomass in molten salts due to a lack of contact between the feed and the melt. A fluoroscopic study of the devolatilization of coal in a molten medium revealed the formation of a bubble of product gas separating the immersed sample from the melt [51]. Similar behavior can be expected for flash pyrolysis of biomass suddenly exposed to molten salt.

In the present study, we examine both flash pyrolysis of cellulose and steam gasification of carbon in a molten blend of sodium, potassium, and lithium carbonate salts from 1124 to 1235 K. To obtain kinetic models, pyrolysis and steam gasification reactions are carried out with salt as well as within an inert gas/steam environment. For the pyrolysis reaction, which is a heat transfer rate limited reaction, direct parameter extraction is not possible, so a numerical model of the process is used in conjunction with the yield rate data to obtain kinetic parameters.

4.1 Experimental facility and methods

During steam gasification of biomass materials, two separate chemical reactions are taking place simultaneously. Biomass material first undergoes pyrolysis as described in the reaction of eq. (1.2) producing gases and a carbon char. Once produced, the carbon

char then begins to react with a gasifying agent in a gasification reaction as described in eq. (1.3). Obtaining parameters for the kinetics of both of these reactions is required to form an accurate model of biomass gasification.

To examine pyrolysis and gasification independently, two feedstocks were studied. For pyrolysis, the feedstock is microcrystalline cellulose (ARCOS Organics, 50 μm particle size). The cellulose powder was compressed into 8 mm and 10 mm diameter tablets with corresponding thicknesses of 3.2 mm and 4.7 mm. The cellulose powder was mixed with distilled water to obtain 20%wt moisture to aid stability while forming the tablets. The tablets were dried in a vacuum oven at 390 K and 0.2 atm to 7 to 10%wt moisture. Based on a cellulose density of 1.2 to 1.4 g/cm3, the estimated porosity of the tablets is 20 to 45%.

For gasification reactions, the feedstock is activated wood charcoal powder (Fluka Analytical, <40 μm particle size, ~700 m2/g specific surface) with a 40%wt paraffin wax binder (McMaster-Carr 1085K991). The powder was formed into 8 mm diameter by 3.4 mm thick tablets. The tablets are 91% carbon by mass with an initial porosity of 37% based on a density of 2.2 g/cm3 for charcoal and 0.9 g/cm3 for paraffin wax ($C_{30}H_{62}$).

Carbonate salts are preferred to chlorides or fluorides to avoid the production of chlorine or fluorine gas [44]. A ternary eutectic blend containing lithium, potassium, and sodium carbonate was selected for several reasons including the reduced melting point (670 K as compared to 970 K without lithium carbonate), reduced corrosion of stainless steel surfaces when lithium is present [46], and evidence of lithium carbonate enhancing gasification performance beyond that observed for any single or binary carbonate salt blend without lithium [26]. The properties of the molten salt blend are listed in Table 4.1.

Table 4.1 Composition and properties of ternary eutectic alkali carbonate salt blend at 1200 K.

Composition [%wt]	32% Li_2CO_3 33% Na_2CO_3 35% K_2CO_3
Thermal Conductivity	0.75 [W/m-K]
Specific Heat Capacity	1842 [J/kg-K]
Melting Point	670 [K]
Density	1680 [kg/m^3]

A schematic of the facility used to obtain kinetic data is shown in Fig. 4.1. Argon and steam are supplied to the reactor via mass flow controllers capable of 0-100 std mL/min or 0-500 std mL/min respectively. A bypass stream of argon, controlled by a separate 0-8000 std mL/min flow controller, dilutes the outlet products prior to analysis via mass spectroscopy. This dilution stream prevents secondary reactions in the product gas, speeds transit time to the mass spectrometer and (along with the argon stream into the reactor) provides a reference flow from which the product gas yield rates were calculated. All mass flow controllers (MKS 1790 for argon and MKS 1153A for steam) were calibrated to an accuracy of ±1% of the reading.

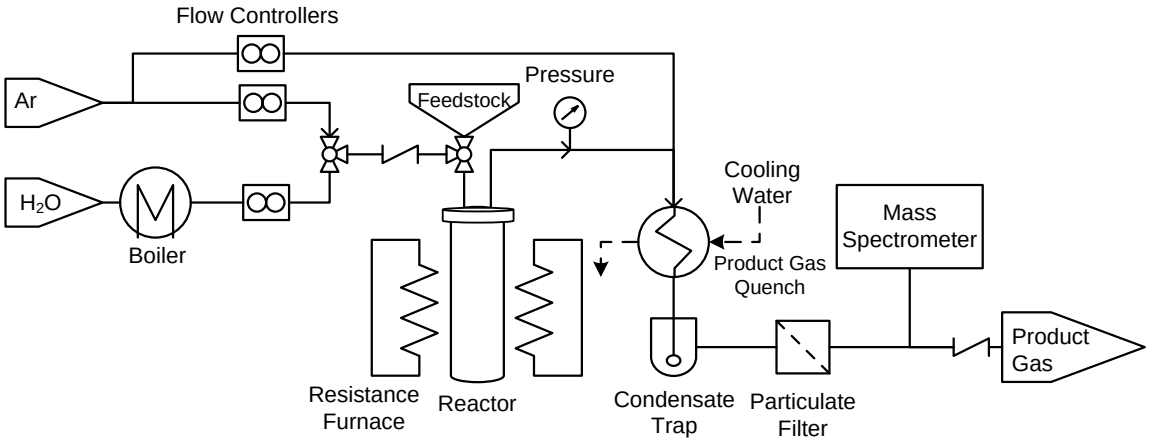

Fig. 4.1 Flow diagram of the system used to carry out the gasification and pyrolysis reactions.

The reactor, shown in Fig. 4.2, is a 64 mm diameter by 178 mm long cylindrical alumina crucible which is positioned vertically within a stainless steel enclosure and sealed with a flange containing connections for feedstock delivery, gas extraction, and temperature sensors. Heating was provided by a 2.5 kW crucible furnace capable of temperatures up to 1573 K. The furnace power level was controlled to achieve the desired set point based on the temperature indicated by two type-K thermocouples (±9 K accuracy) located just beneath the salt level.

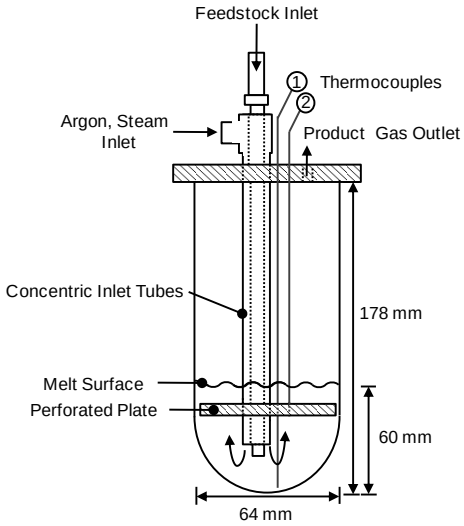

Fig. 4.2 Detail cross-section diagram of the reactor assembly.

The feedstock tablets were fed through the inner of two concentric tubes which make up the feedstock/reactant delivery assembly by a manual plunger. Steam and argon were fed through the annulus of the same assembly. The outlet of both tubes is located mid-depth of the salt melt (30 mm from the surface), and 20 mm beneath a perforated stainless steel plate that ensures the feedstock is submerged during reactions with salt present. Product gases leaving the reactor were passed first through a condenser at 270 K, followed by a condensate trap and a HEPA filter. A portion of the product gas stream was sampled by an Inficion Transpector CPM mass spectrometer/residual gas analyzer to detect CO, H_2, CO_2, CH_4, C_2H_2, and C_2H_4 as well as Ar and H_2O.

During experimental runs, the reactor was supplied with a 200 std mL/min reactant flow containing a molar steam concentration of 60% in argon. The reactor pressure was maintained at ~105 kPa while the temperature varied from 1124 to 1235 K. The product gas stream was diluted with argon at 1800 std mL/min prior to analysis via mass spectrometry. Initial tests determined these flow conditions are sufficient to achieve zeroth order (with respect to steam) reaction behavior and avoid mass transfer limitations. These conditions result in a molar steam to carbon ratio of 6.6 to 1 at the peak of the gasification reaction rate. Prior to each run with salt present, the alumina crucible was loaded with 280 g of the salt. Air was purged from the system by pulling a -5 psig vacuum followed by increasing pressure 20 psig with argon for five cycles.

For each run, the reactor was heated with only the inert gas flow until the temperature at the bottom of the reactor reached the desired set point. The steam flow was then initiated. Once the mass spectrometer signals for the gases of interest were stable, the signals from the mass spectrometer as well as the gas flow rates, pressure and temperature were recorded every 1.6 seconds. Feed was delivered in batches of roughly 1 gram of material in the form of seven of the 8mm diameter tablets or three of the 10mm diameter tablets. Each run progressed until concentrations of hydrogen and carbon monoxide were within 5% of the levels prior to introduction of feedstock (typically 7-30 minutes for pyrolysis or 20-300 minutes for gasification reactions). Data were acquired for each tablet size and feedstock for temperatures of 1124, 1149, 1176, 1205 and 1235 K. Duplicate data were obtained to ensure repeatability.

In the runs with salt, the melt releases carbon dioxide due to thermal dissociation and interaction with steam, forming alkali metal oxides and hydroxide salts [52]. To ensure a consistent salt composition, after each run the salt melt was exposed to a 200 std mL/min flow of 60% carbon dioxide in argon to reform the carbonate salt.

The primary data collected from each run are transient reactor temperatures, inert and reactant gas flow rates, mass of feedstock supplied, and mass spectrometer signal intensities for the product gas species. The data were analyzed to obtain product gas flow rates in terms of volume at standard conditions (273 K, 1 atm) as well as the extent of carbon conversion. The calculations utilize the internal standardization method for gas flow rate determination. With this method, a constant of proportionality, the response factor, is established during calibration by dividing the flow ratio of two gas species by the corresponding mass spectrometer signal ratio [53]. To obtain volumetric gas flows by this method, the calculation proceeds according to

$$\dot{V} = \frac{I_i}{I_{\mathrm{Ar}}} \cdot RF_i \cdot \dot{V}_{\mathrm{Ar}} \tag{4.1}$$

The total mass-normalized gas yield rate reported for the pyrolysis runs is the sum of the flow rates of H_2, CO, CO_2, and CH_4 divided by the mass of feedstock delivered. Higher hydrocarbon production was found to be below the threshold of statistical significance.

The extent of carbon conversion is determined by integrating the moles of carbon present in the product gas from the start of the reaction to time '*t*' according to

$$X_{\mathrm{C}}(t) = \frac{\int_0^t \left(\dot{V}_{\mathrm{CO}} + \dot{V}_{\mathrm{CO_2}} + \dot{V}_{\mathrm{CH_4}}\right)\mathrm{d}t}{m_{\mathrm{C}}^0 / M_{\mathrm{C}}} \cdot \left(\frac{P_{\mathrm{std}}}{R \cdot T_{\mathrm{std}}}\right) \tag{4.2}$$

To correct for carbon dioxide released from the carbonate melt, the yield rate of carbon dioxide during the stabilization period prior to feed delivery is modeled according to an exponentially decaying function. The mass balance of carbon based on observed residues on the downstream portion of the reactor system and the corrected carbon conversion was closed to within +2/-5%.

4.2 Data analysis

Two methods of analysis were used to obtain kinetic models for the pyrolysis and steam gasification reactions with and without molten salt. For gasification, kinetically controlled conditions were obtained, allowing for direct extraction of kinetic parameters from the data. For pyrolysis, heat transfer limits the rate of reaction. Thus, a numerical model of the combined pyrolysis and gasification of cellulose was formulated and the pyrolysis reaction parameters were obtained from a best fit of the rate data.

A simple means of describing the rate of either of these processes is the reactivity index. The intent of the reactivity index is to quickly gauge the change in reaction rates for a given reaction with and without salt. This index is defined as the inverse of twice the time needed to reach 50% conversion and gives an estimate of the overall rate for complete conversion of the reactant material.

$$\tau = (2 \cdot t_{50\%})^{-1} \tag{4.3}$$

4.2.1 Steam gasification

The kinetics of steam gasification reactions are often represented using a single step model given by

$$\frac{\mathrm{d}X_{\mathrm{C}}}{\mathrm{d}t} = k_i \cdot (1 - X_{\mathrm{C}})^n \tag{4.4}$$

where X_C is the extent of carbon conversion defined by eq. (4.2), n is the order of the reaction with respect to carbon, and k is the rate constant. The rate constant is assumed to follow an Arrhenius expression:

$$k_i = k_{0,i} \cdot \exp\left(\frac{-E_g}{R \cdot T}\right) \tag{4.5}$$

Two commonly used variants of this model are the volumetric model (VM) and grain model (GM). The volumetric model assumes the reaction takes place homogeneously within the particle; the reaction surface area decreases linearly with conversion and the order of the reaction is given by n=1 [53]. On the other hand, the grain model assumes the reaction takes place at the surface of a collection of shrinking spherical grains, resulting in reaction of order n=2/3 [54]. For gasification, the grain model is applied because it includes surface area growth and has been shown to result in a better fit to data in prior studies of various chars [55].

The product of the rate constant and elapsed time as a function of the extent of carbon conversion, X_C, for the grain model is

$$k_{GM} \cdot t = 3 \cdot \left(1 - (1 - X_C)^{1/3}\right) \tag{4.6}$$

By plotting the carbon conversion function shown on the right hand side of eq. (4.6) with respect to time, the slope of a linear regression of the data yields the rate constant at each temperature. After obtaining the kinetic rate parameters from the data over the temperature range of interest, an Arrhenius model for the temperature dependence of the kinetic rate is determined according to the expression of eq. (4.5).

4.2.2 Cellulose pyrolysis

To extract kinetic parameters from the pyrolysis data, a two-dimensional numerical model of the reacting tablets was developed. The finite-volume model includes the chemical reaction terms governing pyrolysis and gasification rates and energy consumption, release of product gas, and transport of heat and gases through the tablet. The computational domain is shown in Fig. 4.3. This volume represents one half of a tablet, with the mid-plane located at the origin of the z-axis.

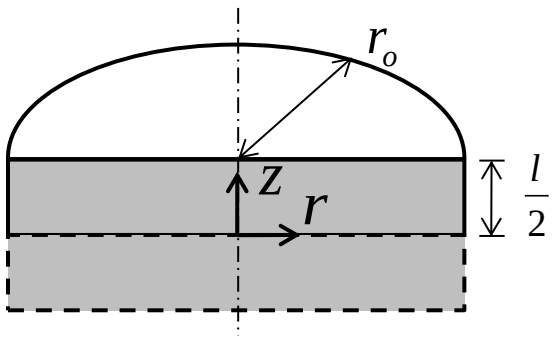

Fig. 4.3 Computation domain representing the cross section through the mid-plane of the feed tablet. The half outlined with a dashed line was not modeled due to assumed symmetric behavior.

The pyrolysis reaction is modeled as a single-step first-order reaction with respect to cellulose mass, based on the volumetric model of eq. (4.5) where n=1.

$$\dot{R}_{\mathrm{p}} = k_{\mathrm{p}} \cdot \frac{m_{\mathrm{cell}}}{V} \tag{4.7}$$

Without salt, the activation energy, E_{p}, is set at 238 kJ/mol, which is the value found to apply to the pyrolysis of a wide variety of cellulosic materials [56]. The pre-exponential factor is established by minimizing the error associated with a regression of the data from control runs carried out without molten salt. In the case where molten salt is present, the activation energy is determined from a regression analysis of the data while the pre-exponential factor is maintained at the value previously established by regression of the salt-free data.

This procedure is sometimes employed for determining cellulose pyrolysis kinetics to avoid complications related to the "compensation effect". The compensation effect describes the observed behavior of pyrolysis kinetic parameters, whereby reported values of the pre-exponential factor and the activation energy for uncatalyzed pyrolysis occupy a wide range of values that form a linear relationship[57]. As a result, changes in the operating conditions may result in a change of obtained kinetic parameters even though catalytic behavior may not be present. By fixing the pre-exponential factor based on uncatalyzed (no salt) data, any catalytic behavior will be evidenced by a decrease in the activation energy.

The gasification reaction is modeled similarly using the chemical kinetic model and parameters determined for carbon gasification. The volumetric reaction rate is related to the rate of change of carbon conversion by:

$$\dot{R}_{\mathrm{g}} = \frac{\mathrm{d}X_{\mathrm{C}}}{\mathrm{d}t} \cdot \frac{m_{\mathrm{C,max}}}{V} \tag{4.8}$$

Substituting the differential equation for the rate of change of the extent of carbon conversion from eq. (4.4) into this equation yields:

$$\dot{R}_{\mathrm{g}} = k_{\mathrm{GM}} \cdot (1 - X_{\mathrm{C}})^{2/3} \cdot \frac{m_{\mathrm{C,max}}}{V} \tag{4.9}$$

The extent of conversion, X_{C}, can be defined in terms of the initial (or maximum) mass of carbon delivered to the system and the current mass of carbon present according to:

$$X_{\mathrm{C}} = 1 - \frac{m_{\mathrm{C}}}{m_{\mathrm{C,max}}} \tag{4.10}$$

Replacing the extent of conversion in the volumetric rate equation then leads to the final form of the volumetric reaction rate:

$$\dot{R}_{\mathrm{g}} = k_{\mathrm{GM}} \cdot \left(\frac{m_{\mathrm{C}}}{m_{\mathrm{C,max}}}\right)^{2/3} \cdot \frac{m_{\mathrm{C,max}}}{V} = k_{\mathrm{GM}} \cdot \frac{m_{\mathrm{C}}^{2/3}}{V} \cdot m_{\mathrm{C,max}}^{1/3} \tag{4.11}$$

The differential energy equation for an axisymmetric, isotropic porous cylindrical solid undergoing a chemical reaction and considering convection due to product gases is given by:

$$\begin{aligned} &\left(\phi\, C_{\mathrm{g}} + (1-\phi)\, C_{\mathrm{s}}\right)\frac{\partial T}{\partial t} + \phi\, C_{\mathrm{g}} \left(u_r \frac{\partial T}{\partial r} + u_z \frac{\partial T}{\partial z}\right) \\ &\qquad = \left(\frac{1}{r}\frac{\partial}{\partial r}\left(r\, k_{\mathrm{eff}} \frac{\partial T}{\partial r}\right) + k_{\mathrm{eff}} \frac{\partial^2 T}{\partial z^2}\right) - \dot{R}_{\mathrm{p}}\, \Delta H_{\mathrm{R,p}} - \dot{R}_{\mathrm{g}}\, \Delta H_{\mathrm{R,g}} \end{aligned} \tag{4.12}$$

The volumetric heat capacities are separated into gas and solid components which are combined according to the porosity of the region of interest to establish an effective volumetric heat capacity [58]. The effective thermal conductivity is calculated according to the method of Yagi and Kunii [59] for combined conduction and radiation within high temperature porous structures. The heat capacity and thermal conductivity of the product gas were established considering a well-mixed blend of average product gas components over an applicable range of temperatures.

The flow of the gases through the cellulose tablet is governed by the continuity equation.

$$\frac{\partial \phi}{\partial t} + \frac{1}{r}\frac{\partial (r\,\phi\,u_r)}{\partial r} + \frac{\partial (\phi\,u_z)}{\partial z} = \frac{\dot{R}_\mathrm{p}}{\rho} + \frac{\dot{R}_\mathrm{g}}{\rho} \tag{4.13}$$

The gases are considered incompressible with a density corresponding to standard conditions at 1 atm and 273 K. As the gases are produced from within the reacting volumes, local thermal equilibrium is assumed. Because of this assumption, the effect of convective heat transport through the tablet is determined by the mass flux of gas alone and the assumption of constant density does not influence the behavior of the model.

The initial conditions of the simulation are uniform ambient temperature and porosity throughout the tablet.

$$T(r,z,0) = 300\ \mathrm{K}, \qquad \phi(r,z,0) = \phi_0 \tag{4.14}$$

In the radial direction, boundary conditions consist of a symmetry condition at the centerline of the cylindrical axis of the tablet,

$$\frac{\partial T}{\partial r}(0,z,t) = 0, \qquad u_r(0,z,t) = 0 \tag{4.15}$$

as well as a convective heat transfer condition at the perimeter of the tablet,

$$k_\mathrm{eff}\,\frac{\partial T}{\partial r}(r_0,z,t) = h_\mathrm{tot}\left(T_\infty - T(r_0,z,t)\right) \tag{4.16}$$

The heat transfer coefficient, h_tot, includes the effects of radiative exchange with the gray-diffuse walls of the reactor in the cases without salt.

Without salt, the convective heat transfer term is set to 22 W/m^2-K, which corresponds to the tablets behaving like spheres exposed to a bulk gas velocity of 10 cm/s, the calculated velocity at which the feed gases exit the delivery annulus within the reactor at 1200 K conditions, according to the correlation of Whitaker [60].

With salt, the correlation of Whitaker is not acceptable because the Prandtl number of ~0.07 is outside of the applicable range. In addition, the flow field is unknown. Thus, the regression was optimized to determine this value starting from an initial estimate of 400 W/m^2-K in addition to the activation energy. This estimate corresponds to a Nusselt number of 2 for an 8mm tablet in a lightly agitated salt melt.

The radiative exchange was assumed to take place between a small convex object within a large cavity as described in [61]. This behavior can be represented as a heat transfer coefficient according to

$$h_\mathrm{rad} = \sigma\,\varepsilon\left(T_\infty^2 + T^2(r_0,z,t)\right)\cdot\left(T_\infty + T(r_0,z,t)\right) \tag{4.17}$$

In the z-direction, similar boundary conditions are imposed, with symmetry conditions along the mid-plane of the tablet

$$\frac{\partial T}{\partial z}(r,0,t) = 0, \qquad u_z(r,0,t) = 0 \tag{4.18}$$

and a convective heat transfer condition along the upper boundary of the tablet

$$k_{\text{eff}} \frac{\partial T}{\partial z}(r,z_0,t) = h_{\text{tot}} \left(T_\infty - T(r,z_0,t)\right) \tag{4.19}$$

The governing equations along with initial and boundary conditions were solved using an explicit finite-volume program written in FORTRAN 90 and compiled using the *GNU Fortran* compiler. The computational domain of Fig. 4.3 was discretized into twenty radial and ten axial divisions, creating a total of 200 volumes. The model was verified with an analytical solution for transient conduction in a finite cylinder with equivalent thermal diffusivity. The maximum deviation between the analytical and numerical solution was less than 1%.

The continuity equation was solved using an upwind method moving from the coordinate origin outwards while assuming the average velocity leaving both downwind faces of any given volume is uniform.

In the gaseous environment the tablets sit directly against the bottom of the crucible, so a change in boundary conditions was explored by doubling the thickness of the domain to include the full tablet and setting a fixed temperature condition at the lower surface. Negligible change in the predicted gas yield behavior was observed.

Regression of the simulated and measured mass-normalized volume yield rates was achieved by adjusting the convective heat transfer coefficient as well as either the activation energy or the pre-exponential factor to achieve minimization of a root-mean-square objective error function.

$$f_{\text{fit}} = \sqrt{\frac{1}{N}\sum_{i=1}^{N}\left(\frac{V_i}{m_0} - \frac{V_{\text{model},i}}{m_{\text{model}}}\right)^2} \tag{4.20}$$

The minimization of the error function was achieved with the use of the *GenOpt* numerical optimization program's implementation of the *Hooke-Jeeves* global parameter search algorithm. This algorithm searches for a global minimum in the error function while optimizing any number of parameters. As a minima is approached, step size is

decreased until the minima is located with a step size of <0.5% of the magnitude of the parameters of interest.

4.3 Results: Establishing Kinetic Models

4.3.1 Steam Gasification

The measured and predicted carbon conversions for each temperature are shown in Fig. 4.4 as a function of reaction time. The data without salt are shown in Fig. 4.4(a) while Fig. 4.4(b) shows the data with salt. At each temperature, the conversion rises rapidly to ~20% initially due to the release of carbonaceous gases during initial pyrolysis of the wax binder. When adjusted for this initial release, the shrinking grain model fits the data well both with and without salt. The average error in the predicted conversion is ±1.1% without salt and ±1.9% with salt.

The rate constants obtained in the present study are shown on an Arrhenius plot in Fig. 4.5. For comparison, the figure includes kinetic models from prior studies of steam gasification of a variety of carbonaceous chars without salt. The data from Fermoso et al. [55] are for petroleum coke char. DeGroot and Richards [62] utilized cellulose char, and Huhn et al. [50] examined coal. The linear model fits the obtained values for the reaction across all temperatures, implying uniform kinetics in the temperature range of interest. The no-salt data fall within the range of the prior work. The higher reaction rates with salt are evidence of catalysis. Steam mass transfer limitations were avoided by ensuring

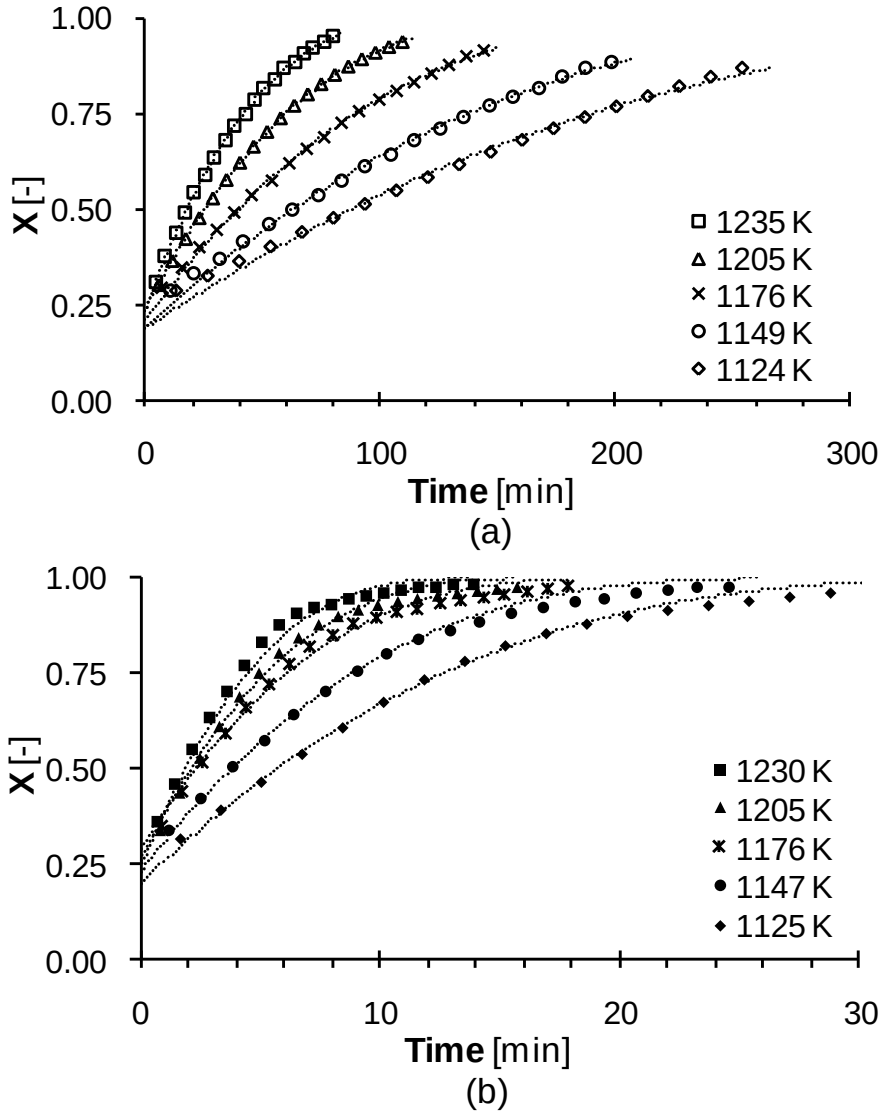

Fig. 4.4 Extent of carbon conversion for steam gasification reactions at various temperatures in (a) gaseous and (b) molten salt environments. The dashed lines represent the conversion predicted by the optimized shrinking grain reaction model.

steady reaction rates despite increases in steam flow as described in the experimental methods section.

Table 4.2 lists the kinetic parameters that were obtained by linear regression of the data of Fig. 4.5. There is a significant impact of the salt on the pre-exponential factor. Without salt, $k_{GM} = 5.9 \cdot 10^4$ 1/min. With salt, the pre-exponential factor increases over an order of magnitude to $1.5 \cdot 10^6$ 1/min. These results along with the slight increase in activation energy suggest that catalysis of the carbon gasification reaction is due to a

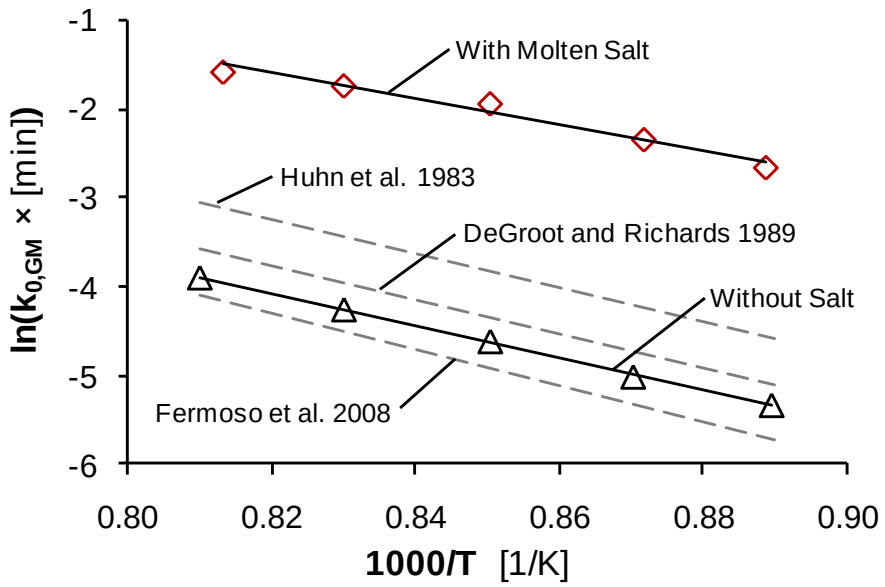

Fig. 4.5 Arrhenius plot of steam gasification data with and without molten alkali carbonate salt.

change in the reaction pathway as suggested by [63]. This pathway, predicted for high concentrations of alkali carbonate salt, calls for the formation of metal-oxygen surface complexes along the edges of the aromatic carbon surface, allowing gasification to take place on all exposed carbon surfaces rather than only free carbon sites or breaks in the aromatic ring structure as is the case with uncatalyzed steam gasification. The increase in number of reaction sites, sometimes described as the active sites becoming *mobile*, is suggested to be the reason for the significant increase in the pre-exponential factor.

Table 4.2 Kinetic parameters obtained for the steam gasification of carbon using the shrinking-grain model.

Conditions	$k_{0,GM}$ [1/min]	E_g [kJ/mol]
Without Salt	$5.9 \cdot 10^4$	152
With Salt	$1.5 \cdot 10^6$	158

The presence of molten salt increases the reactivity of the carbon gasification reaction by more than an order of magnitude from an average reactivity of 0.9 1/hour to 11.4 1/hour. Char generated during biomass gasification would be consumed over 10 times faster in a molten salt environment. This finding is a very important factor when one

considers the time needed to achieve steady-state operation of a solar gasification system, as this time period is limited by the slowest reaction involved, and thus depends on the time it takes to consume the char produced by the pyrolysis reaction. With the molten carbonate salt present, a much more responsive system is achieved, obtaining steady state in 20 minutes as compared to 200 minutes.

To obtain kinetically limited reaction rates, an excess of steam was delivered during the gasification runs, resulting in product gas compositions strongly skewed by the water gas shift reaction. These compositions are not pertinent for this model of the gasification reaction and the reader is referred to the composition of the pyrolysis product gas as representative of typical biomass gasification reactions. Additionally, tars were not a significant byproduct of the carbon gasification reaction based on the lack of filter or condenser residues.

4.3.2 Cellulose Pyrolysis

The average product gas yield per unit cellulose for the pyrolysis reactions at temperatures above 1200 K is given in Fig. 4.6. In the presence of molten salt, the yield of the primary products, hydrogen and carbon monoxide, increased by 29% while the corrected carbon dioxide yield decreased by 62%. The increased synthesis gas production is attributed to a combination of reduced carbon dioxide production, and cracking of retained tars. Methane production was unaffected by the presence of salt. With molten salt, the presence of tars in the HEPA filter and condenser was reduced from 7 to 12% of the feedstock mass to less than 1% of the feedstock mass. The tar appeared as a sooty black deposit on the condenser walls and filter material.

Data and the best fit model for pyrolysis of cellulose tablets at 1235 K are shown in Fig. 4.7. Data for other temperatures and tablet sizes show similar trends. The reported yield rates have a propagated uncertainty of ±0.09 std L/min-g, primarily due to the uncertainty of the reference argon gas flow rate. The predicted yield rates are in excellent agreement with the data with average error of 0.1 std L/min-g between the simulations and data.

Three important findings are demonstrated in Fig. 4.7. First, the presence of molten salt provides a faster rise to the peak yield rate. For the 10mm tablets at 1235 K, the maximum yield rate is 2 std L/min-g reached in 15 seconds. Without salt, the maximum

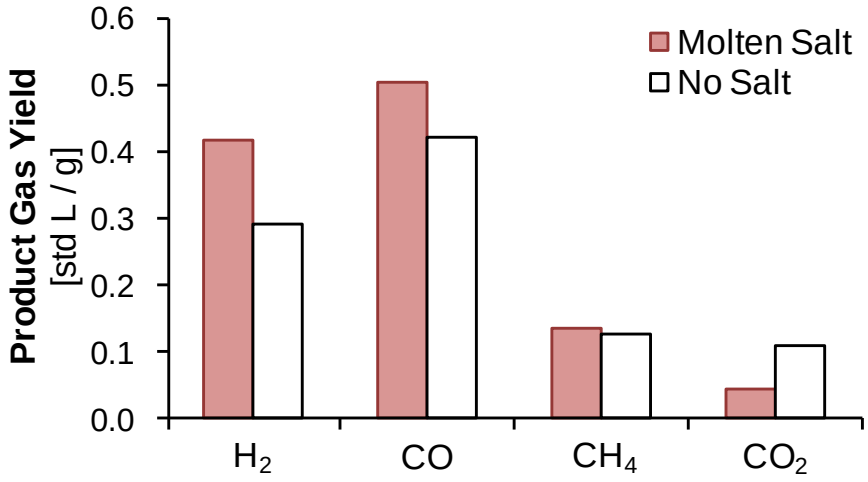

Fig. 4.6 Average measured product gas yield for cellulose tablets undergoing flash pyrolysis at 1200 K and above with and without molten salt present.

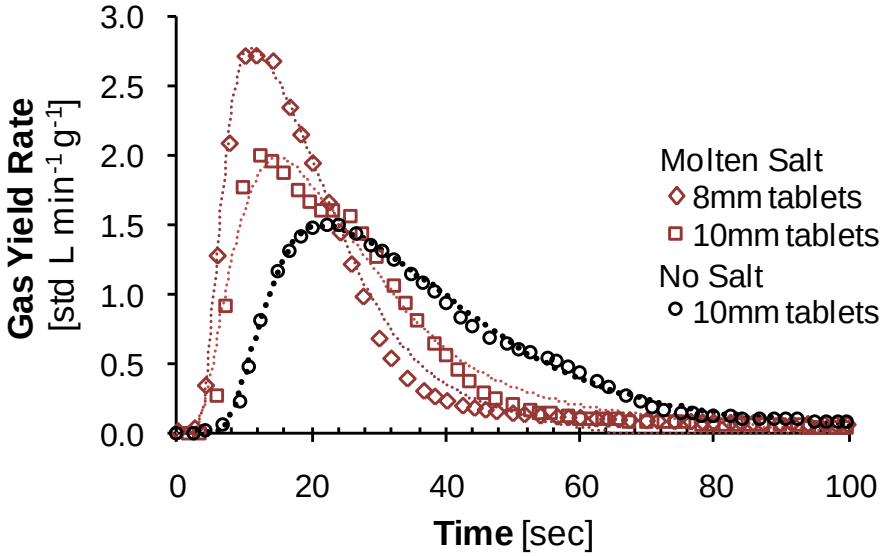

Fig. 4.7 Data and simulations of pyrolysis of cellulose tablets at 1235 K with and without molten salt present.

rate is 1.5 std L/min-g after 25 seconds. Second, a carbon conversion of 95% is achieved in 50 seconds with salt as compared to 80 seconds without salt. This rate corresponds to a 74% increase in the reactivity index from a value of 0.94 1/min to 1.6 1/min. As predicted by the model, the benefits of the salt are due to the enhanced convective heat transfer. Third, the figure compares the yield rates obtained for two different tablet sizes in the case with salt present. The 8mm tablet exhibits a faster reaction as expected for a heat transfer limited process. The reaction model predicts the data for both tablet sizes

indicating that the kinetic parameters determined for the pyrolysis reaction in molten salt are decoupled from the heat transfer behavior. The plot of Fig. 4.8 further illustrates the increase in reaction rate by displaying the cumulative extent of carbon conversion, *X*, for pyrolysis of 10 mm diameter cellulose tablets at 1235 K. The time lag between the two reactions grows from around 10 seconds at low conversion to a maximum of 30 seconds as the reaction completes.

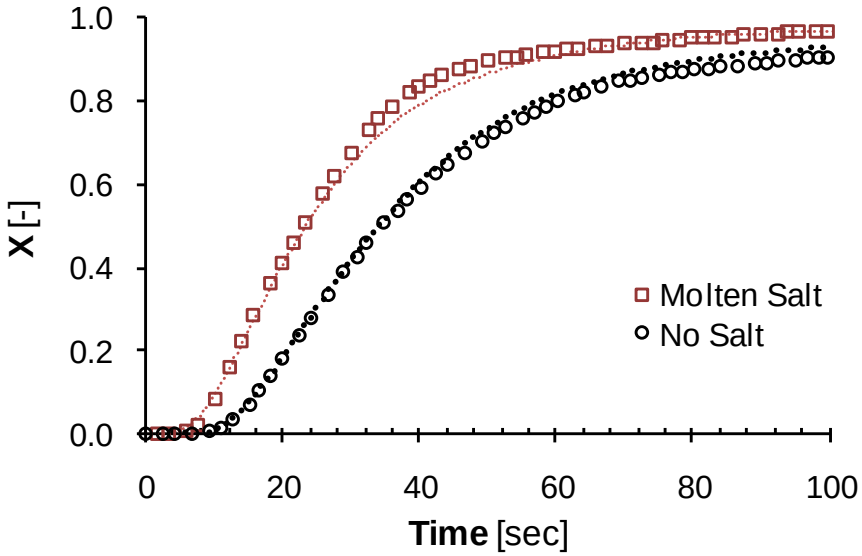

Fig. 4.8 Cumulative extent of conversion for 10 mm diameter cellulose tablets undergoing pyrolysis at 1235 K with and without molten salt present.

The kinetic parameters are listed in Table 4.3. The data are well represented by the uncatalyzed reaction parameters. This result suggests that the increased rates of flash pyrolysis with molten salt are due to enhanced heat transfer and not catalysis. The enhanced heat transfer in the presence of the salt results in data best represented by convective heat transfer coefficients of 424 and 480 W/m^2-K for the 10 mm and 8 mm tablets respectively, somewhat larger than the initial estimated value of 400 W/m^2-K. This result is in agreement with a previous fluoroscopic study that reports the formation of a product gas layer separating high temperature melts and solids undergoing devolatilization/pyrolysis [51]. This separation may prevent sufficient contact between the solid and melt for catalysis to occur. Thus catalysis of the pyrolysis reaction is only expected when the feedstock is heated slowly within the salt or when the salt is impregnated into the feedstock as was the case of a previous study claiming catalysis [50].

Table 4.3 Average and standard deviation of parameters obtained for flash pyrolysis of cellulose by optimization of the numerical model. Grey boxed values were fixed.

Conditions		ln($k_{0,p}$ x [sec])	E_p [kJ/mol]	h_{conv} [W/m^2-K]
Without Salt	*8 mm*	**26 ±1**	*238*	*22*
	10 mm			
With Salt	*8 mm*	*26*	**238 ±4**	480 ±10
	10 mm			424 ±8

The key conclusion is that the molten salt increases the rate of pyrolysis by 74% and increases gasification rates by more than an order of magnitude while promoting a product gas composition nearer to thermodynamic equilibrium predictions. Though alkali metal carbonates have been found to catalyze pyrolysis reactions in studies where there is sufficient contact time between the melt and the feedstock, catalysis was not observed in the present study in which pyrolysis was extremely rapid. The increase in reaction rate is instead due to enhanced heat transfer within the salt. On the other hand, the data support a catalytic effect during steam gasification of carbon in the molten salt. The catalysis is reflected in an increase in the pre-exponential factor from $5.9 \cdot 10^4$ to $1.5 \cdot 10^6$ 1/min and an increase in the activation energy from 152 kJ/mol to 158 kJ/mol with salt present.

The present study provides strong justification for using molten carbonate salts as a combined catalyst and heat transfer media for solar gasification. The advantages of the molten salt are compelling. Because the molten salt improves heat transfer to the biomass and catalyzes the reaction, one can operate at lower temperature, and thus higher solar efficiency while avoiding the production of tars. The increase in the rate of catalyzed char gasification also allows for improved reactor control at these temperatures as steady state operation can be achieved in a shorter period of time.

4.4 Results: Comparing Candidate Feedstock Materials

Given the relatively slow rate of carbon gasification reactions compared to pyrolysis, increased char production will inherently result in longer overall conversion times for plant biomass. Thus, the molten salt's ability to catalyze the gasification of carbon is anticipated to yield greater improvements in the overall conversion rates for plant biomass than those observed with pure cellulose. In addition to the potential for high

char production, plant biomass also contains moderate levels of ash, consisting primarily of calcium, potassium, and magnesium oxides. Chemical thermodynamics predicts that, in the presence of molten salt, the ash may form liquid phase compounds with the salt melt, thus avoiding formation of solid slag within the gasifier.

To test these hypotheses, an extended study was undertaken considering steam gasification of representative biomass feedstocks in a eutectic blend of molten of lithium, potassium, and sodium carbonate salts at 1200 K. Biomass gasification experiments were carried out for each feedstock in a batch reactor heated by an electric furnace. Measurements of product gas yield rate, composition, and total yield of both gaseous and secondary products are presented and compared between runs with and without salt present. The data quantify the influence of molten salt on the reaction kinetics, product gas composition, and production of tar.

The crop biomass materials were obtained from test plots managed by the University of Minnesota. The blend of perennial plants consists of 32 different species native to the state of Minnesota. Both switchgrass (*Panicum Virgatum*) and the perennial blend are selected for study due to their widespread adoptability, moderate to high yields, and ability to grow on marginal lands and thus avoid competition with traditional food production agriculture [3]. Corn stover is an agricultural residue consisting of corn stalks and cobs left on the field after harvest. Cellulose is used as a control against which the performance of these candidate feedstocks is compared. Each feedstock material was

Table 4.4 Ultimate and Proximate analyses of feedstock materials

Ultimate Analysis	Cellulose	32 Species	Corn Stover	Switch grass
C [%wt]	44.16	48.21	45.701	47.04
H [%wt]	6.37	5.83	5.70	6.04
O [%wt]	49.44	41.62	42.36	41.15
N [%wt]	0.02	0.64	0.92	0.84
S [%wt]	0.01	0.04	0.06	0.09
Proximate Analysis				
Ash [%wt]	<0.01	3.66	5.26	4.84
Volatiles [%wt]	87.10	77.36	75.03	76.10
Fixed Carbon [%wt]	12.90	18.98	19.71	18.98

characterized according to the standard test method ASTM E-870 for proximate and ultimate (elemental) analyses [64]. The results of these analyses are listed in Table 4.4 as well as for cellulose.

The plant feedstock was ground to a particle size of less than 450 μm using a blade grinder and sieve, while the cellulose powder was utilized as-received with a reported average particle size of 50 μm. Each feedstock, including the cellulose powder, was compressed into cylindrical tablets with 8 mm diameter and 4 mm thickness to ensure uniformity between runs. The tablets were dried in a vacuum oven at 390 K and 0.2 atm to 4% wt moisture, determined by measurement of the mass loss during drying. Based on an estimated average true density of 1.45 g/cm^3 for cellulose and the other biopolymers, the porosity of the tablets was 15% for cellulose and 40% for the plant biomass.

During experiments, the reactor was supplied with a 200 std mL/min reactant flow containing a molar steam concentration of 60% with the balance argon. The absolute pressure within the reactor remains constant at ~120 kPa for the given flow conditions. Immediately after exiting the reactor, the product gas stream was diluted with argon at 7000 std mL/min. All data were acquired at a target temperature of 1200 K. The experiment was repeated four times for each feedstock with and without salt. The mass balance of carbon based on the product gas composition and the measured mass of any residual char and tar was closed to within ±5% for all experiments. Following each run, the salt melt was exposed to a 200 std mL/min stream of 60% carbon dioxide in argon to reform the carbonate salt. Results are presented in terms of the specific yield rate, extent of carbon conversion as defined in eq. (4.2) and the reactivity index, defined in eq. (4.3).

The total gas production rate from the reactor during the first minute of gasification of each feedstock is shown in Fig. 4.9 for both gaseous and molten salt environments. The reported gas production rates have a maximum propagated uncertainty of ±0.07 mol/min/mol-carbon primarily due to the uncertainty in the reference flow rate of argon.

Considering the data for runs without salt (dashed lines), the peak gas production rate during pyrolysis was higher with cellulose (Fig. 4.9a) than for any of the other feedstocks. The maximum gas production rate for cellulose is 3.2 mol/mol-C/min while the other feedstocks produce gas at rates less than 1.7 mol/mol-C/min with corn stover (Fig. 4.9c)

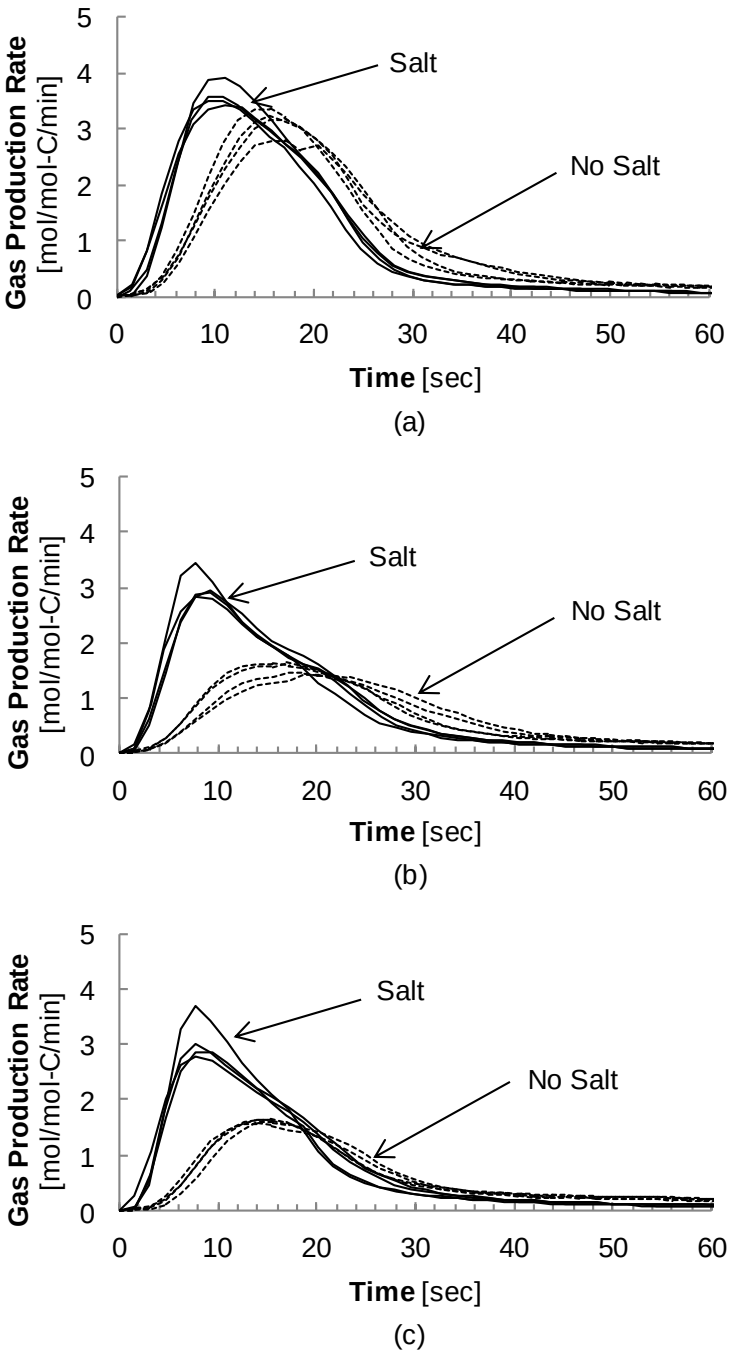

Fig. 4.9 Molar gas production rates for the combined pyrolysis and steam gasification of (a) cellulose (b) perennial blend of grasses (c) corn stover and (d) switchgrass at 1200 K with and without salt.

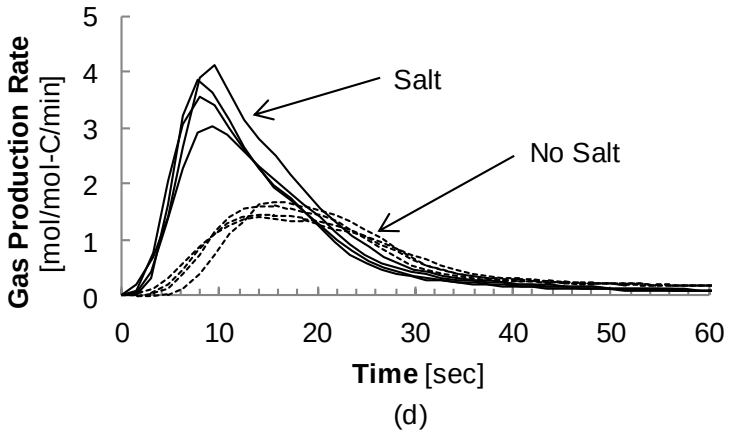

(d)

Fig. 4.9 cont. Molar gas production rates for the combined pyrolysis and steam gasification of (a) cellulose (b) perennial blend of grasses (c) corn stover and (d) switchgrass at 1200 K with and without salt.

having the slowest rate of gas production of all the feeds. This difference in gas production rate was due to both slower pyrolysis of the more complex and thermally stable biopolymers as well as the lower volatile content of the complex feeds (as listed in the proximate analysis in Table 4.4).

Considering the effect of molten salt, the data show that in all cases molten salt increases the gas production rate by a statistically significant degree. The maximum gas productions rate for cellulose was 4.0 mol/mol-C/min (Fig. 4.9a), while maximum rates for the complex feeds are 2.9 to 4.1 mol/mol-C/min. Additionally, the peak rates occur with salt present, around 10 seconds after feed delivery compared to 15 seconds without salt. Compared to without salt, the differences between the rate of gas production from cellulose and the complex feeds are much less significant when molten salt is present. Given the heat transfer rate limited nature of pyrolysis, the comparative results demonstrate the benefit of enhanced heat transfer to the feedstock offered by the molten salt. After approximately 50 seconds with salt and 80 seconds without salt, pyrolysis is complete and the gas production rate slows as steam gasification of the remaining char becomes the dominant reaction. Although not shown in these plots, char gasification requires on average another 20 minutes for the cellulose runs and 30 minutes for the other feeds to reach completion. The first 60 seconds of the reaction are presented because the majority of the product gas (70-94%) is produced and the effect of salt is most pronounced during the initial pyrolysis reaction. This yield estimate is based on the

"volatile fraction" reported for each feedstock which predicts well the pyrolysis only yield. Direct measurement of the yield during pyrolysis alone is difficult due to confounding contributions from the simultaneous gasification reactions.

To quantify the average reaction rates, the reactivity index for each feedstock is shown in Fig. 4.10. The molten salt increases the reactivity index of cellulose from 1.2 min^{-1} to 1.6 min^{-1}. For the plant biomasses, the molten salt increases the reactivity indices from 0.5, 0.2, and 0.4 min^{-1} to 1.3, 1.4, and 1.4 min^{-1} for the perennial blend, corn stover, and switchgrass feedstocks respectively. The largest relative gain in reactivity index is for corn stover, which has a 600% faster reactivity index in the presence of molten salt. When salt is present, the reactivity indices from gasification of the plant feedstocks are comparable to that of cellulose.

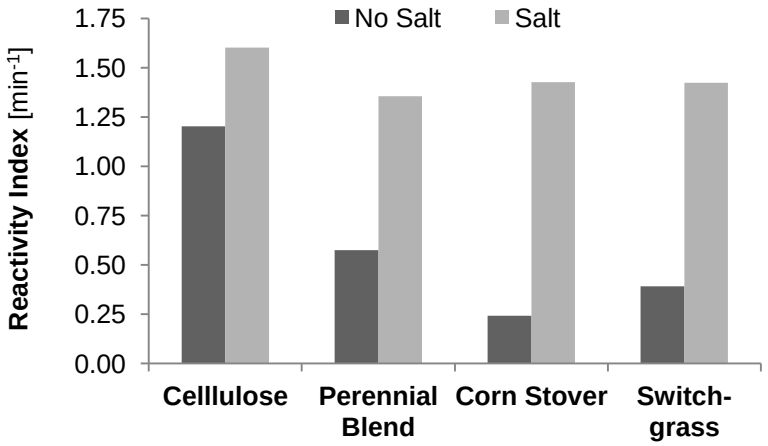

Fig. 4.10 Reactivity index for gasification of each feedstock with and without salt.

The average product gas yield per unit mole of carbon in the feedstock delivered is shown in Fig. 4.11 and listed in Table 4.5. With molten salt, the useful syngas ($CO + H_2$) production increases for all of the feedstock considered. For cellulose (Fig. 4.11a) the gain is a 9% increase, from 0.94 mol/mol-C without salt to 1.02 mol/mol-C of useful syngas with salt. For the perennial blend (Fig. 4.11b) and corn stover (Fig. 4.11c) feeds, a 20% increase in useful syngas is observed with salt. Switchgrass shows the largest relative increase in useful syngas production at 30%.

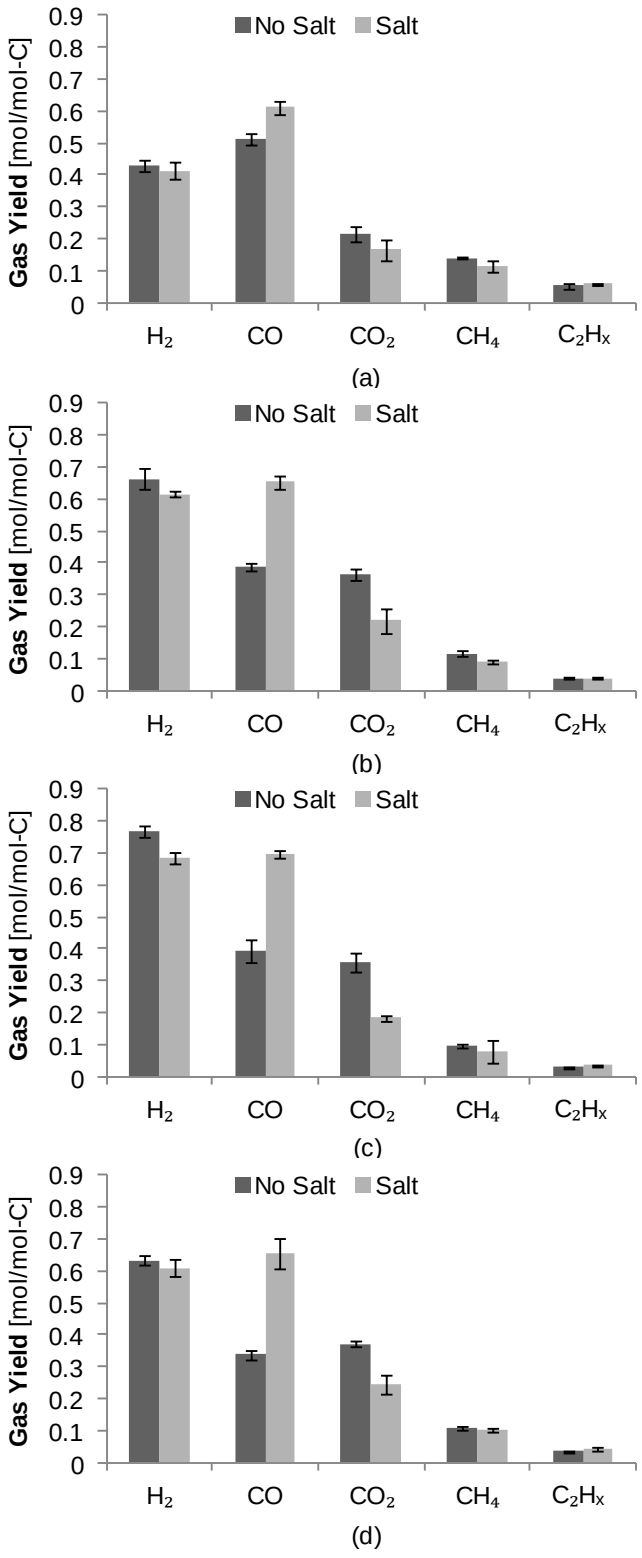

Fig. 4.11 Molar gas yield for the combined pyrolysis and steam gasification of (a) cellulose (b) perennial blend of grasses (c) corn stover and (d) switchgrass at 1200 K with and without salt.

This increase is primarily due to reduced production of secondary products such as tar as well as reduced net production of non-useful carbon dioxide gas. The larger gain for switchgrass may be due to the fact that the ash in the switchgrass feedstock builds up on the unreacted char and inhibits gasification without salt present. This behavior is suggested based on an observation, unique to the switchgrass feedstock, of grey-black spheres which remained in the reactor following gasification runs. Because these spheres contained carbonaceous material and because they were not observed in the runs with salt present, we suspect that they contained unreacted material that was able to be fully reacted with salt present, giving switchgrass the largest relative production increase. The total product gas produced from cellulose is less than that for the plant biomass due to the higher ratio of carbon to oxygen for the plant biomass, as seen in Table 4.5. This behavior is consistent with reactions (1.2) and (1.3); as feedstock oxygen content approaches zero, total hydrogen and carbon monoxide yield is maximized. Another notable but less important feature is the large H_2/CO ratio when salt is not present due to the unreacted steam in the reactor favoring the forward water-gas shift reaction

$$CO + H_2O \leftrightarrow H_2 + CO_2 \tag{4.21}$$

which results in less carbon monoxide and more hydrogen in the product gas. With salt present, this ratio is closer to the near unity H_2/CO ratio predicted by the equilibrium analysis as some of the unreacted steam interacts with the salt producing carbon dioxide which counteracts the forcing effect of steam on the water-gas shift reaction. The change in production of methane and other hydrocarbons when salt is present is not statistically significant.

Table 4.5 The impact of molten salt on syngas production from gasification.

Feedstock	Relative increase in syngas yield with molten salt (% vol)
Cellulose	5.8
Perennial Blend	15.9
Corn Stover	15.9
Switchgrass	25.7

To compare the energetic yields of the process, Fig. 4.12 shows the mass normalized lower heating value (LHV) of both the product gas with and without molten salt as well as the feedstock itself. As expected, the LHV of the gas from the molten salt environment is greater than that without the salt, with a 3% increase in energy content for cellulose, 10% increase for the perennial blend, 14% increase for corn stover and 30% for the switchgrass. These increases are due primarily to the increased overall gas yield previously discussed; however, there is also a small boost in energetic content with salt present due to carbon monoxide being favored over hydrogen and carbon monoxide having a higher molar LHV than hydrogen

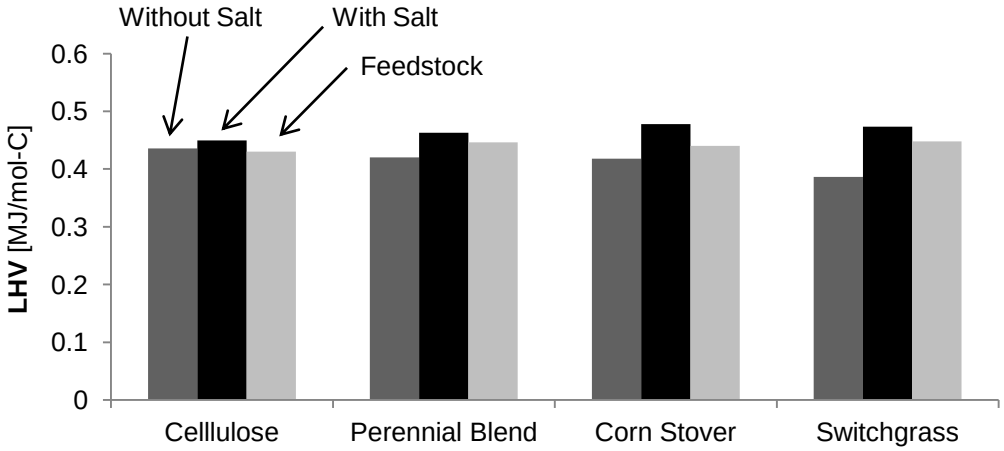

Fig. 4.12 Molar lower heating value (LHV) of the product gas and the feedstock.

Secondary products in the form of condensable liquid tar or solid unreacted char are collected in and downstream of the reactor and on the HEPA filter. Without molten salt, much of the collected material is an oily tar, which represents about 4.2%wt of the total feedstock mass. For the switchgrass, 5.4% of the mass remains in the reactor in the form of a mixture of ash and the unreacted char spheres mentioned previously. Based on visual observation in an optical microscope (100x magnification), ash appears to have formed a slag barrier that prevented the remaining char from reacting with the steam. For the perennial blend and corn stover, the ash forms a solid slag at the bottom of the crucible with no visible carbon retained within. This slag could not be removed with solvents or mild detergent, but was removed after heating the crucible to 1200K with salt

present, confirming our earlier prediction that the ash may not remain solid when salt is present.

With molten salt, there are no noticeable oily tar deposits and no unreacted char remaining in the reactor. Tar collected on the HEPA filter was reduced in the presence of molten salt to only 0.8% of the total mass delivered into the reactor. The ash present in the feed material enters into solution or forms secondary products with the melt thus no slag was found in the reactor following runs with salt. The presence of ash within the melt is not expected to affect the reaction behavior based on results of testing of a pilot scale molten salt coal gasifier where ash in quantities up to 20% of the salt mass were maintained during continuous operation [40].

The primary objective of the present study is to quantify the ability of molten carbonate salts to enhance the overall conversion of various cellulosic feedstocks into synthesis gas via the process of gasification. A comparison of gas production rates and total yields is presented along with an analysis of the secondary products formed during the gasification process.

The results demonstrate that the presence of molten salt greatly enhances the rate and extent of conversion of switchgrass, blended perennials, and corn stover as gasification feedstocks. The overall rate of gasification increases by up to 600% for the plant biomass, allowing more structurally complex feedstock to be consumed at rates comparable to that of simple cellulose. The rates of conversion of the candidate feedstocks are also much more uniform in a molten salt environment. In addition to faster reactions, the useful syngas yield for plant biomass is increased by up to 30% while overall energetic yield per unit feedstock (based on the LHV of product gas) are increased by up to 22%. These production gains are primarily due to reduced secondary product formation. Specifically, liquid tar deposits on the filter are reduced by 77% along with the elimination of ash or unreacted ash/carbon material in the reactor following runs. These are all indications that complete conversion of plant biomass to synthesis gas is improved with molten salt.The results point to the ability of a solar gasification process using molten salts to handle a wide variety of feedstock without major process adjustments required for changing feedstocks, a powerful benefit for flexibility of larger scale gasification operations.

5 Design Process

In this chapter the design of the prototype reactor is presented. Specifications and operational constraints are presented, followed by presentation of the reactor concept and the key design parameters. Following the overview, a series of studies are presented. These studies include numerical simulation of radiative exchange in a cavity receiver, heat transfer in the annular cavity containing the molten salt, and thermal stresses.

5.1 Concept Overview

The prototype solar gasification reactor was designed to meet requirements consisting of specifications for the operation and performance of the reactor and constraints based on the available facilities for characterization.

5.1.1 Design Specifications and Constraints

The specifications that govern the reactor design are as follows. (*i*) The reactor is intended to operate at a nominal 3 kW_{th} input power. (*ii*) The average flux at the aperture must be (*a*) achievable with the UMN 45 kW_e High Flux Solar Simulator (HFSS) and (*b*) representative of tower-style solar concentrating systems, typically 1000 to 1500 suns [42]. The design of the HFSS allows for seven discrete levels of concentrations based on the number of lamps in place, with three lamps resulting in a flux of 1530 suns on average over a 5cm diameter target area. Thus, the final design specification for average flux at the aperture is 1530 suns. Details on this choice are presented in Appendix B. (*iii*) The reactor must be capable of feeding solid feedstock materials, including powdered cellulose and ground dry plant matter. (*iv*) Reactants must be fed at steady rates up to 22 g/min for feedstock on a dry ash-free (DAF) basis and 2 SLPM for steam or CO_2 as a gasifying agent. This decision is based on the max throughput predicted in the thermodynamic analysis of Chapter 3. (*v*) The reactor system must contain downstream gas cleanup and filtration as needed to ensure that no solid byproducts, salt, condensable tars, nor condensed water vapor may reach gas analysis equipment. (*vi*) The reactor must include features to allow mounting to a test stand structure with the mounting interface achieving a temperature of no more than the 520 K, above which the yield strength rapidly falls for Aluminum alloy 6061 (which is the composition of the testing stand structure). (*vii*) The reactor must contain means by which the molten salt can be drained

from the reactor following operation. (*viii*) The reactor structure must be capable of sustained operation at temperatures up to 1250 K, based on the desired operating salt temperature of 1200 K as determined by kinetic calculations and thermodynamic equilibrium and allowing for up to a 50 K increase for temperature rises due to conductive resistance or localized hot-spots. (*ix*) The reactor will be unpressurized, operating as close to atmospheric pressure as practicable and economical in order to favor the production of light gaseous products and for design simplicity. (*x*) The solar simulator testing enclosure has a rectangular footprint 3.81 m wide and 2.74 m long, with a ceiling 3.12 m high. The reactor and all ancillary equipment directly connected to the reactor must fit within this space. Additionally, the doorway used to move reactors into the enclosure is 3.12 m wide, setting the maximum dimension on any fixed feature on the reactor. (*xi*) The traverse/test stand has a 50 kg limit for the combined weight of the reactor, salt, feed, and associated equipment.

5.1.2 Reactor Concept

A concept of the geometry of the molten salt reactor was developed after considering several possible configurations. For high temperature processes utilizing concentrated solar power, a cavity receiver is preferred over a flat or open receiver to maximize the incident radiation that is absorbed within the cavity and to minimize energy lost due to thermal emission from the hot cavity walls. In some processes, the cavity itself is where the chemical reactions take place; this approach delivers radiation directly to the reaction site [7]. For molten salt gasification, the high thermal emissivity of the salt melt (absorption coefficient around 8900 1/m for a 1200 K blackbody emission spectrum) and the incompatibility of the materials available for windows preclude such a design. Therefore, the energy delivered to the cavity receiver must be absorbed through opaque walls and delivered to a surrounding salt melt.

The reactor concept is shown in Fig. 5.1. The inner cylinder is a cavity receiver with an open aperture on one end to allow concentrated radiation to enter the receiver. The incident radiation is absorbed along the walls of the cylinder and transferred to the annular region between the two cylinders which contains the molten salt heat transfer and reaction medium. Conduction through the cavity wall followed by convection and radiation between the wall and the salt transfers the thermal energy into the salt region.

The feedstock is delivered into this salt region where it undergoes pyrolysis and gasification resulting in a product gas that exits the reactor.

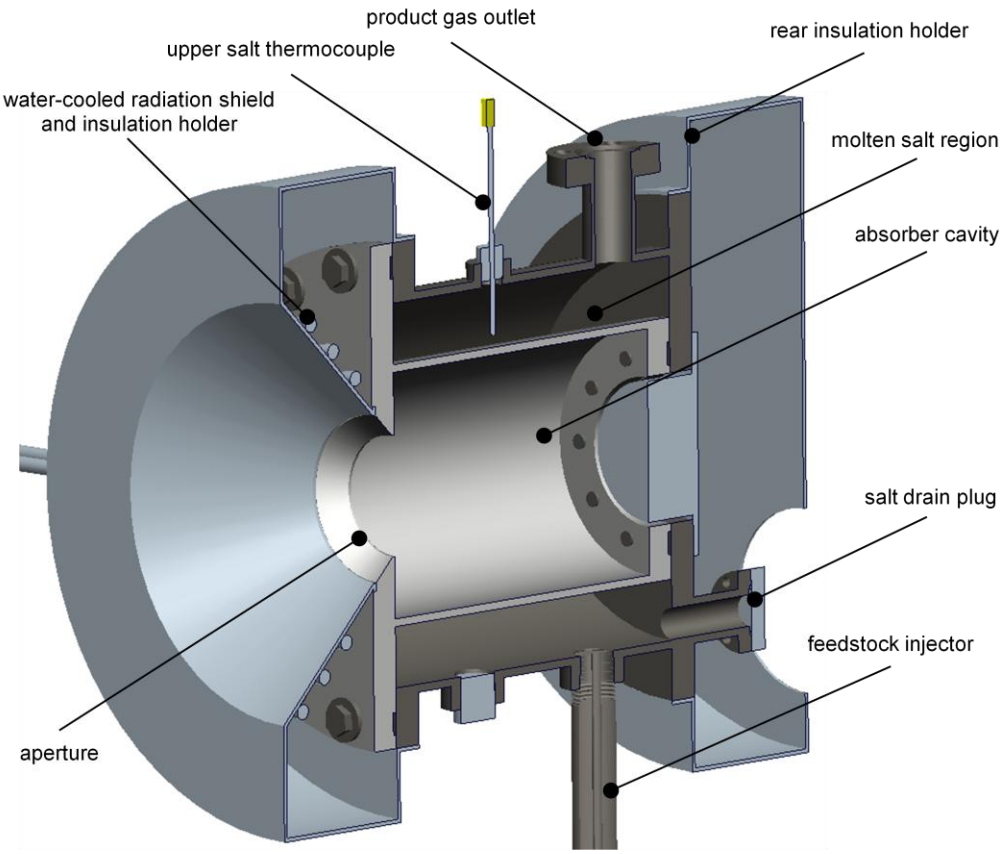

Fig. 5.1 Isometric side-cutaway view of the gasification reactor concept. Insulation material placed within these shields and around the midsection of the reactor core is not shown. Concentrated radiation enters from the left into the absorber (center cylinder). The annular gap between the absorber and housing would be filled with molten salt. Feed is delivered from the bottom and product gas from the top.

For the initial design studies of sections 5.2 and 5.3, the geometry of the reactor is simplified into the form shown in Fig. 5.2, with the pertinent dimensions and their simplified dimensionless terms shown. This simplified representation allows modeling of heat transfer without the added complexity of the detailed design features. In this figure, the side view takes advantage of axis-symmetry, and the front view displays the hidden lines marking the edges of the walls with dashed lines.

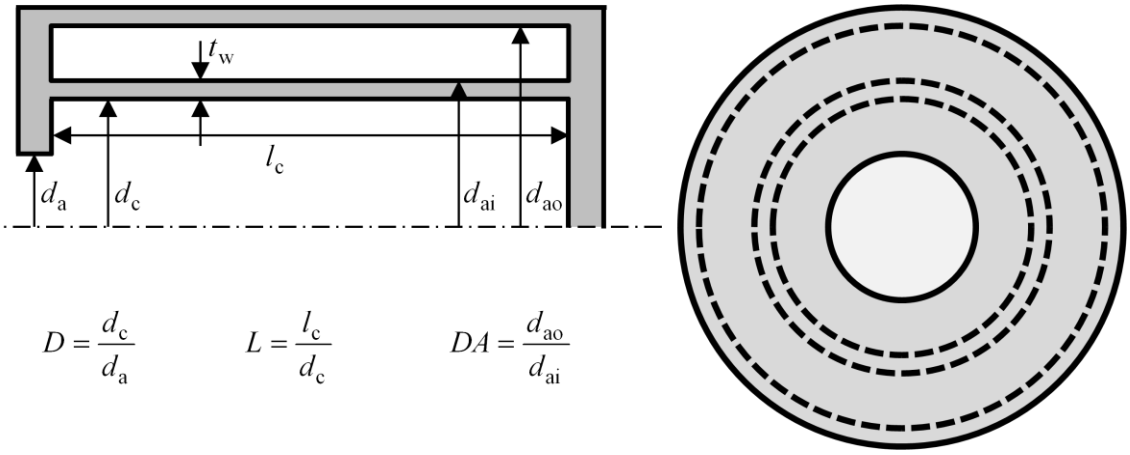

Fig. 5.2 Side cross-section (left) and front (right) views of the generalized geometry of the molten salt solar gasification reactor as used for heat transfer studies. Key dimensions and their ratios are shown.

Mechanical design of the reactor in section 5.4 requires a more detailed model geometry as shown in Fig. 5.3 for modeling of the stresses in the walls, flange, and fasteners of the reactor. This geometry represents a manufacturable assembly of separate parts, better approximating the final form of the reactor components.

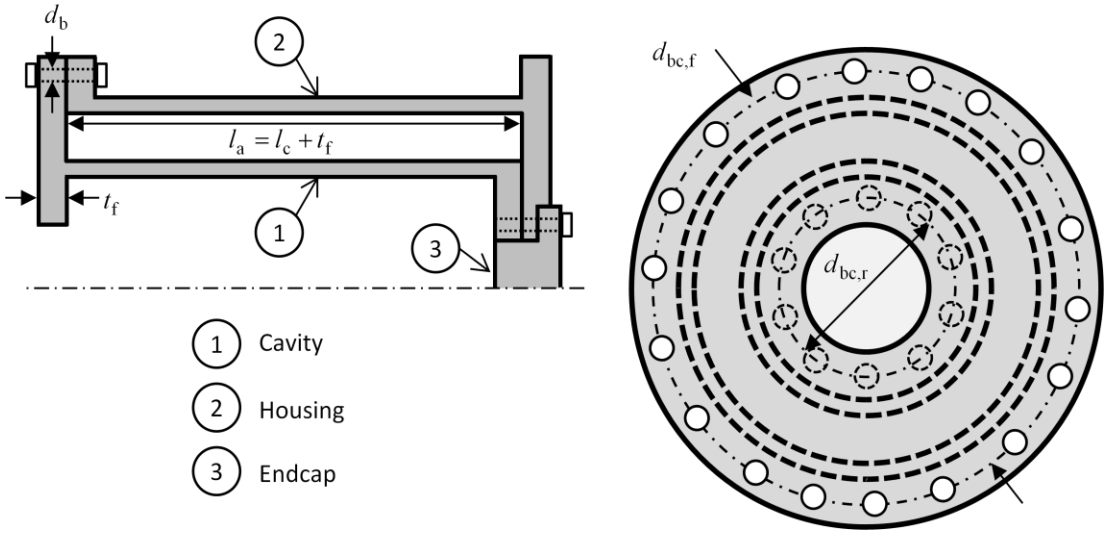

Fig. 5.3 Sketch of the assembly geometry of the molten salt solar gasification reactor as used for mechanical studies with the three primary components labeled. Only new dimensions beyond those of Fig. 5.2 are shown.

The reactor is made in three parts which are assembled into the final reactor structure: (1) the cavity absorber and outer front flange, (2) the housing with inner front flange and the rear flange, and (3) the end cap. The cavity, part (1), includes a large flange with the

aperture and a smaller rear flange with a port for the end-cap to close the rear of the cavity. The housing, part (2), includes a flange that mates with a bolted seal to the rear of the front flange of part (1), and a rear flange that is used for attaching the reactor to a support structure and for sealing against the rear flange of part (1). The end cap, part (3), passes through both the rear flange and the rear portion of the cavity absorber and also acts as a bearing surface for bolts which pass through all three parts in order to mate with threads within the rear flange of part (1) to seal parts (1) and (2) together. Final interfacing features, such as inlets, outlets, and sensor interface ports are introduced in the final design as presented in section 5.5.

5.1.3 Design Parameters

The design parameters to be established include the dimensions shown Fig. 5.2 and Fig. 5.3. The inner cylinder has inner diameter d_c and length l_c with an aperture of diameter d_a. The annulus region is bounded by the outer wall of the cavity on the inside, d_{ai}, and the inner wall of the housing on the outside, d_{ao}. The thickness of the cavity and housing walls is t_w, while all flanges have thickness t_f. The actual length of the annulus is slightly longer than the cavity by one flange thickness, $l_a = l_c + t_f$. In dimensionless terms, the cavity geometry is described by the geometric ratios $D = d_c/d_a$ and $L = l_c/d_c$. The annulus geometry is described by the annulus diameter ratio, $DA = d_{ao}/d_{ai}$. The bolts used to seal the components together are of diameter d_b and placed about a bolt circle of diameter $d_{bc,f}$ on the front flange and $d_{bc,r}$ on the rear inner flange. The inner annulus diameter is related to the inner cavity diameter by the cavity wall thickness such that $d_{ai} = d_c + 2 \cdot t_w$. The bolt circles are placed 1.5 bolt diameters away from the nearest surface for clearance according to $d_{bc,f} = d_{ao} + 2 \cdot t_w + 3 \cdot d_b$ and $d_{bc,r} = d_c - 3 \cdot d_b$.

The geometry can be fully defined by the set of seven free parameters: the aperture diameter d_a, the cavity-aperture diameter ratio *D*, the cavity aspect ratio *L*, the annulus diameter ratio *DA*, the wall thickness t_w, flange thickness t_f, and bolt diameter d_b.

In addition to the geometric parameters, the reactor design is governed by the operation parameters: $\dot{Q}_{solar} = 3\ kW_{th}$, C = 1530 suns, and the average salt temperature T_{salt} = 1200 K.

The aperture diameter is selected to achieve the desired nominal solar power based on the average concentration. The nominal solar power is defined in terms of the aperture diameter as:

$$Q_{\text{solar}} = CI\frac{\pi}{4}d_{\text{a}}^2 \tag{5.1}$$

For a 3 kW_{th} nominal power the design aperture size is $d_{\text{a}} = 5$ cm with an average concentration of 1530 suns. Details on aperture sizing are given in Appendix B. The values of D and L for the receiver cavity are selected in section 5.2 based on a parametric study of radiative exchange between the HFSS and the cavity. The annulus diameter ratio DA is selected in section 5.3 based on a computational fluid dynamic (CFD) study of natural convection heat transfer in the molten salt. The mechanical design is explained in section 5.4 based on a parametric study of the thermal stresses developed in the reactor.

5.2 Cavity Receiver Design

In this section, the impacts of the cavity design parameters and the choice of cavity surface material on absorption efficiency and the distribution of temperature or flux along the surfaces of the cavity are evaluated.

5.2.1 Blackbody cavity receivers

Most high temperature solar thermochemical processes utilize a cavity style receiver to maximize the net absorption of concentrated radiation. The net absorption of concentrated radiation can be quantified by the absorption efficiency,

$$\eta_{\text{abs}} \equiv \frac{\dot{Q}_{\text{solar}} - \dot{Q}_{\text{ref}} - \dot{Q}_{\text{rerad}}}{\dot{Q}_{\text{solar}}} = \alpha_{\text{app}} - \varepsilon_{\text{app}}\frac{\sigma T^4}{I\,C} \tag{5.2}$$

where $\dot{Q}_{\text{solar}}$ is the incident solar power at the aperture, $\dot{Q}_{\text{ref}}$ is the reflected portion of the incident power, and $\dot{Q}_{\text{rerad}}$ is the power emitted thermally from the cavity. The solar concentration ratio is defined as

$$C \equiv \frac{\dot{q}_{\text{solar}}}{I} \tag{5.3}$$

where $\dot{q}_{\text{solar}}$ is the average incident solar flux at the aperture of the cavity and a reference insolation value, $I = 1\ \text{kW/m}^2$. The temperature distribution throughout the cavity is an important consideration because the surface temperature can impact both the long-term durability of the material and the efficiency of the planned energy conversion process.

Normally, a uniform temperature distribution is preferred to avoid stresses generated from differential thermal expansion of receiver components, hot spots, and non-uniform performance. Both absorption efficiency and temperature distribution depend on the spatial and spectral distribution of the incident radiation, the spectral radiative properties of the surface of the cavity, and the boundary conditions.

Early work on the design of cavities for radiation heat transfer focused on the use of isothermal cavities for the calibration of optical devices against known emission spectra, *e.g.* [65]. These studies reveal that the key to approaching blackbody behavior is to maximize the cavity surface area to aperture area ratio, but they do not provide insight into how geometry affects the distribution of net flux or temperature on the inner walls of the cavity. A more recent analysis of the concept of a two-cavity solar receiver found similarly that the absorption efficiency is maximized for increasing values of the cavity surface area to aperture area ratio [66]. Other analyses of cavities specifically for solar processes, including concentrating solar power [67] and solar thermochemistry [68, 69], show that the geometry of the cavity has a significant impact on the distribution of radiative flux and/or temperature within the cavity. All of these studies were restricted to a single cavity material.

The present analysis considers the design of a cylindrical cavity intended for solar gasification of biomass in a molten carbonate salt, but the concept is suitable to other solar thermochemical processes in which the reactants are heated indirectly [25, 70]. A numerical study on heat transfer in a cylindrical cavity having opaque walls, exposed to direct high-flux irradiation and surrounded by a convecting fluid is presented. The model is based on the steady state-energy equation formulated for the cavity walls, which is solved by applying the finite volume method (FVM). The Monte Carlo ray tracing (MCRT) method is applied to solve for radiative transfer from the aperture to the cavity walls and the radiative exchange in the cavity and, consequently, to determine the boundary conditions for the energy equation at the internal cavity wall. An iterative procedure for solving for temperatures and radiative transfer is employed to compute the steady-state temperature distribution in the cavity.

5.2.2 Problem statement

A more detailed depiction of the cavity geometry is given in Fig. 5.4, illustrating the geometry of a cylindrical cavity receiver considered in the present study. Concentrated solar radiation enters the cavity through an aperture of diameter d_a. The coordinate origin is located in the plane of the aperture along the cylinder centerline. The geometry of the cavity, specifically the aspect ratio $L = l/d$, and the diameter ratio $D = d/d_a$, the convective film coefficient, h, and the cavity surface material, for which Inconel and alumina are considered, are the critical parameters affecting performance. A schematic representation of the problem of radiative heat transfer to a right cylindrical cavity is given in Fig. 5.5, which shows the computational domain and boundary conditions for the present study.

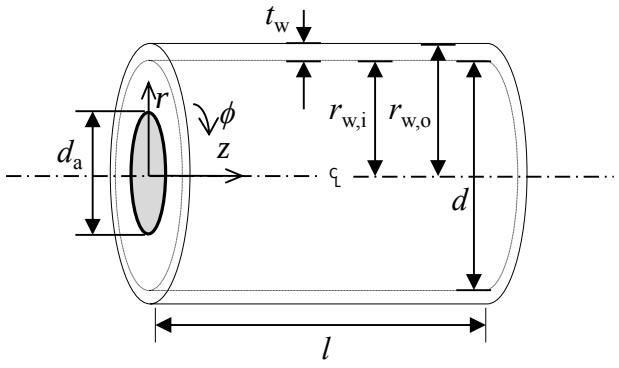

Fig. 5.4 Diagram of the geometry of a right cylindrical cavity receiver. The aperture is located on the left end with the coordinate origin placed along the centerline of the cylinder in the plane of the aperture.

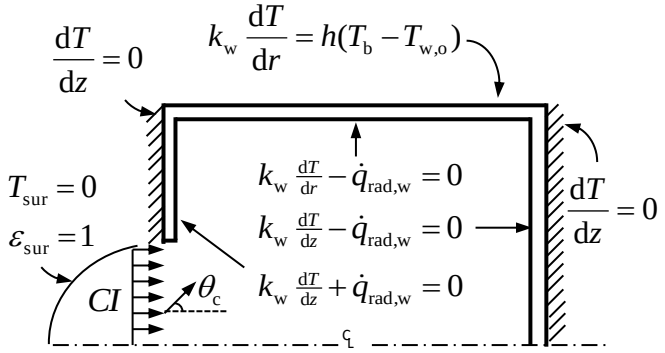

Fig. 5.5 Schematic diagram of the cavity receiver problem under investigation including boundary conditions. All boundary conditions are circumferentially symmetric.

In the present work, the aperture diameter is fixed at $d_{\mathrm{a}} = 0.05$ m commensurate with an input power of 3 kW. The incident radiation at the aperture is assumed to have a uniform flux distribution at an average concentration ratio of $C = 1530$. The concentration ratio was selected to match the concentrating characteristics of a typical tower style concentrating solar receiver. The directional distribution of the incoming radiation is considered to be uniformly distributed within a cone angle of $\theta_{\mathrm{c}} = 37°$ measured from the horizontal centerline, approximating the directionality of incident sunlight for a tower style concentrating receiver and equal to the cone angle of the indoor solar concentrator at the University of Minnesota [71]. The spectral distribution of the incident light is assumed to be equivalent to that of a blackbody at the effective temperature of the sun, 5777 K. For radiation incident from within the cavity on the aperture, the aperture is assumed to be black. The front and back ends of the cavity are assumed to be well insulated and in the model are treated as adiabatic surfaces. The boundary condition along the circumference of the outer wall is described by a uniform convective heat transfer film coefficient h to the molten salt. The cavity wall is of thickness t_{w} and thermal conductivity k_{w}. The walls are assumed to be thin, and thus conduction is assumed to be in the radial direction. This assumption is justified by initial calculations which demonstrate that the spatial gradient of temperature in the radial direction is typically 10 to 100 times larger than in the axial direction. Note that the assumption of 1-D conduction produces a temperature discontinuity where the cylindrical wall meets the front and back ends of the cavity which are treated as an adiabatic surface.

The outer circumferential wall of the cavity is assumed to be immersed in molten salt with a bulk temperature $T_{\mathrm{b}} = 1200$ K. The temperature of the salt was selected to favor complete conversion of biomass feedstock to gaseous products based on chemical thermodynamics [70]. In order to explore the impact of the value of h on the results, convective film coefficients encompassing natural and forced convection in a ternary eutectic alkali carbonate salt [72] were modeled. The values of h were bounded at the lower end by the appropriate correlation for either natural convection from the inner cylinder of an annulus [73] and at the upper end by the correlation for forced convection for a cylinder in cross flow [74].

5.2.3 Materials

Inconel was selected as the basic structural material for the reactor due to its resistance to corrosion from molten salts [46] and high-temperature strength, maintaining a yield strength exceeding 20 MPa at temperatures up to 1300 K [75]. The thermal conductivity is assumed to remain constant at the value of 27 W/m-K. An alumina surface coating is considered to help reduce thermal stresses due to uneven surface temperature distributions and to avoid localized temperatures in excess of design limits. Both materials are assumed to have diffusely reflecting, emitting, and absorbing surfaces.

Spectral hemispherical emissivity and thermal conductivity of these materials were obtained from a database of measured values [76, 77]. The properties are assumed to be directionally independent. The spectral hemispherical emissivity of the two surfaces considered is shown in Fig. 5.6, with the closed circles and solid line representing the data and piecewise polynomial model respectively for Inconel and the open squares and dashed line representing the same for a plasma sprayed thin film alumina coating on an Inconel substrate. Inconel has high emissivity near 0.9 in the short wavelengths from 0.1 μm to 1 μm, corresponding to high absorptance of solar radiation. The emissivity in the infrared band from 2 μm to 12 μm is approximately 0.5, reducing emission from the heated cavity as compared to a blackbody cavity of the same geometry. The spectral properties of Inconel are anticipated to result in stronger variation in the cavity temperature and a higher overall absorption efficiency than alumina. Alumina has an emissivity of approximately 0.25 from 0.1 μm to 1 μm, and a rising emissivity in the

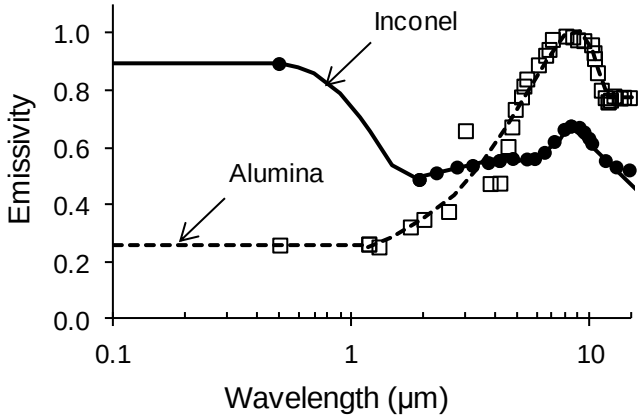

Fig. 5.6 Data and piecewise polynomial model of the spectral emissivity of Inconel or an alumina coating on Inconel substrate.

longer wavelengths above 2 μm, reaching $\varepsilon_\lambda \sim 1$ near $\lambda = 6$ μm. This distribution would physically correspond with many reflections of incident solar radiation along with signification re-radiation within the cavity. More uniform distributions of flux and temperature but lower absorption efficiency than a receiver with an Inconel surface are expected.

5.2.4 Methodology

Governing equations

The energy conservation equation is formulated for the solid cavity walls without volumetric heat sources/sinks.

$$\rho c \frac{\partial T}{\partial t} = -\nabla \cdot \vec{\mathbf{q}} \tag{5.4}$$

where $\vec{\mathbf{q}} = \vec{\mathbf{q}}_{\text{rad}} + \vec{\mathbf{q}}_{\text{cond}}$ is the total heat flux. The conductive heat flux is computed using Fourier's law,

$$\vec{\mathbf{q}}_{\text{cond}} = -k_{\text{w}} \vec{\nabla} T \tag{5.5}$$

Steady-state and, 1-D conduction are assumed. Furthermore, the cavity walls are assumed to be non-porous and opaque as justified by the selection of materials listed in Section 5.2.2. Hence, $\vec{\mathbf{q}}_{\text{rad}} = 0$, and for the cylindrical wall, where $0 \le z \le l$ and $r_{\text{w,i}} \le r \le r_{\text{w,o}}$, eq. (5.4) reduces to:

$$k_{\text{w}} \frac{\text{d}}{\text{d}r}\left(r \frac{\text{d}T}{\text{d}r}\right) = 0 \tag{5.6}$$

The boundary condition at the inner cylindrical wall surface, $r = r_{\text{w,i}} = d/2$, and $0 < z < l$ is:

$$k_{\text{w}} \left.\frac{\text{d}T}{\text{d}r}\right|_{r=r_{\text{w,i}}} = \dot{q}_{\text{rad,w}} \tag{5.7}$$

For the outer cylindrical wall surface, $r = r_{\text{w,o}} = r_{\text{w,i}} + t_{\text{w}}$ and $0 < z < l$, we have instead

$$k_{\text{w}} \left.\frac{\text{d}T}{\text{d}r}\right|_{r=r_{\text{w,o}}} = h(T_{\text{b}} - T_{\text{w,o}}) \tag{5.8}$$

For the front and back disks, where $z = 0, l$ and $d_{\text{a}}/2 \le r \le r_{\text{w,i}}$ or $0 \le r \le r_{\text{w,i}}$, eq. (3) reduces to:

$$\frac{\mathrm{d}^2T}{\mathrm{d}z^2} = 0 \tag{5.9}$$

The boundary condition at the inner surface of the front annular disk, $d_a/2 < r < r_{w,i}$ and $z = 0$ is:

$$-k_w \frac{\mathrm{d}T}{\mathrm{d}z}\bigg|_{z=0} = \dot{q}_{rad,w} \tag{5.10}$$

For the inner surface of the back circular disk, $0 < r < r_{w,i}$ and $z = l$, we have

$$k_w \frac{\mathrm{d}T}{\mathrm{d}z}\bigg|_{z=l} = \dot{q}_{rad,w} \tag{5.11}$$

For the insulated outer surface of either the front or back of the cavity, the boundary conditions are:

$$\frac{\mathrm{d}T}{\mathrm{d}z}\bigg|_{z=-t_w} = \frac{\mathrm{d}T}{\mathrm{d}z}\bigg|_{z=l+t_w} = 0 \tag{5.12}$$
$$\tag{5.13}$$

In eqs. (5.7), (5.10) and (5.11), the net radiative flux from the surface is:

$$\dot{q}_{rad,w} = E - \alpha H = J - H = \int_{\lambda=0}^{\infty} \int_{\Omega=0}^{2\pi} (\varepsilon_\lambda E'_{b\lambda} - \alpha_\lambda H'_\lambda)\, \mathrm{d}\Omega\ \mathrm{d}\lambda \tag{5.14}$$

To determine the temperature profiles within the wall, the finite volume method is applied to elements of arbitrary surface area and a thickness of $t_w$to solve eq. (5.6) and eq. (5.9) subject to their boundary conditions. The solutions to eq. (5.6) relate the inner and outer surface temperatures of the cylinder wall to the radiative flux and the convective heat transfer. These relations are given by

$$T_{w,o} = \frac{r_{w,i}\, \dot{q}_{rad,w}}{k_w} \ln\left(\frac{r_{w,o}}{r_{w,i}}\right) + T_{w,i} \tag{5.15}$$

$$T_{w,i} = \frac{r_{w,o}\, h}{k_w} (T_b - T_{w,o}) \ln\left(\frac{r_{w,i}}{r_{w,o}}\right) + T_{w,o} \tag{5.16}$$

The system of eqs. (5.15)-(5.16) describing the cylinder wall are combined to eliminate the unknown temperature of the outer cavity wall. For wall elements on the ends of the cavity, the solution to eq. (5.9) is trivial due to the adiabatic boundary conditions, which result in a constant temperature across the wall thickness, and leads to the condition of surface radiative equilibrium at cavity ends. Consequently, the radiative flux at any location at the internal cavity wall surface can be expressed as:

$$\dot{q}_{\mathrm{rad,w}} = \begin{cases} -\dfrac{T_{\mathrm{w,i}} - T_{\mathrm{b}}}{\dfrac{r_{\mathrm{w,i}}}{h\, r_{\mathrm{w,o}}} - \ln\left(\dfrac{r_{\mathrm{w,i}}}{r_{\mathrm{w,o}}}\right)\dfrac{r_{\mathrm{w,i}}}{k_{\mathrm{w}}}} & \text{for cylindrical wall} \\ 0 & \text{for cavity ends} \end{cases} \tag{5.17}$$

According to the above equation, the net surface radiative flux has to be determined first to compute the temperature distribution in the cavity. This flux, in turn, depends on the unknown inner surface temperature through the emissive power and radiative properties as given by eq. (5.14). An iterative procedure using MCRT is employed to solve for the temperature distribution on the inner cavity wall surfaces as elaborated in the next section.

Solution technique

The cylindrical cavity is divided into discrete volume elements. A structured grid with 16 circumferential divisions on the cylindrical wall, 9 radial divisions on either disk at the ends of the cavity, and 30 axial divisions is employed. The temperature difference across the wall thickness is known from eq. (5.15) and eq. (5.16).

The solution method utilized to solve eq. (5.17) for all volume elements of the cavity is iterative based on estimates of the inner wall temperature, $T_{\mathrm{w,i}}$. At iteration level *n*, the net surface radiative flux, eq. (5.14), is approximately found for all faces of the discrete volumes by applying MCRT:

$$\dot{q}^{n}_{\mathrm{rad,MC}} \approx \varepsilon^{n} \sigma \left(T^{n}_{\mathrm{w,i}}\right)^{4} - N^{n}_{\mathrm{abs}} \dot{q}^{n}_{\mathrm{ray}} \tag{5.18}$$

where N^{n}_{abs} is the number of stochastic rays absorbed at a face of a given discrete volume and $\dot{q}^{n}_{\mathrm{ray}}$ is radiative power carried by a single stochastic ray.

The new temperature distribution is calculated by combining eqs. (5.17) and (5.18). Applying successive under relaxation with the relaxation parameter $\omega < 1$, one obtains:

$$T^{n+1}_{\mathrm{w,i}} = \omega \left(\frac{\dot{q}^{n}_{\mathrm{rad,w}} - \dot{q}^{n}_{\mathrm{rad,MC}}}{\sigma\, \varepsilon^{n}} + T^{n\ 4}_{\mathrm{w,i}} \right)^{\frac{1}{4}} + (1 - \omega)\, T^{n}_{\mathrm{w,i}} \tag{5.19}$$

The temperature of a given cylinder wall surface element is considered converged when the computed flux meets the following error criterion. This criterion is derived by solving eq. (5.17) for the inner wall temperature based on the net flux provided by the MCRT method and then computing the absolute difference between this temperature and the current wall temperature estimate at iteration *n*.

$$\left| T_{\mathrm{w,i}}^{n} - \left(T_{\mathrm{b}} + \dot{q}_{\mathrm{rad,MC}}^{n} \left(\frac{r_{\mathrm{w,i}}}{h\, r_{\mathrm{w,o}}} - \ln\left(\frac{r_{\mathrm{w,i}}}{r_{\mathrm{w,o}}} \right) \frac{r_{\mathrm{w,i}}}{k_{\mathrm{w}}} \right) \right) \right| < 0.5 \text{ K} \tag{5.20}$$

For the cylinder ends, there is no predicted temperature to compare to, so convergence is simply determined by the size of predicted change in temperature between iterations.

$$|T_{\mathrm{w,i}}^{n} - T_{\mathrm{w,i}}^{n+1}| < 0.5 \text{ K} \tag{5.21}$$

Once the final temperature distribution across all surface elements has converged, the absorption efficiency, defined in eq. (5.2), is calculated by the ratio of the sum of net heat transfer through all surface elements j to the incident radiation at the aperture.

$$\eta_{\mathrm{abs}} \approx \frac{4}{\pi\, d_{\mathrm{a}}^{2}\, C\, I} \sum_{j=1}^{N} -A_j\, \dot{q}_{\mathrm{rad},j} \tag{5.22}$$

The MCRT method without energy partitioning is utilized to solve for the net flux absorbed by each area element as a function of the surface temperature of the element. The resultant net flux is then used in the iterative calculations described above until the temperature of every element converges within the error threshold defined in eq. (5.21). The details of the MCRT method are well known [78] so only the relations that deviate from the standard relations for diffusely reflecting, emitting, and absorbing surfaces are described here. The methods used to account for the spectral distribution of the rays as well as the cone angle of incident rays are specific to this study. The random number relation for location of a given emitted ray on a surface element is calculated according to standard MCRT relations for a diffuse, isothermal surface.

The probability of a ray generated at the aperture or wall having a certain wavelength is determined by setting the irradiation term, H_{λ}', to zero in eq. (5.14) and then evaluating the equation for the full integral limits with respect to direction but only to a wavelength upper limit of λ, and then dividing by the total emissive power for the location. This procedure yields a random number relation for wavelength given by

$$\Re_{\lambda} = \frac{\int_{0}^{\lambda} f_{\mathrm{T},\lambda}\, \varepsilon_{\lambda}\, d\lambda}{\varepsilon_{T}} \tag{5.23}$$

For a random real number R_{λ}, the corresponding wavelength is determined by numerical integration of the right hand side of eq. (5.23) over discreet wavelength intervals no larger than $\Delta\lambda = 5$ nm until the equality yields the value closest to the random number for the given wavelength interval size. The random number relation for the azimuth

direction, ψ, is determined by standard MCRT relations. The random number relation for the cone angle θ of an incident ray with respect to the centerline of the cavity is determined by the ratio of the emissive power from the surface element from a cone angle of 0 to θ to the total emissive power within the maximum cone angle of the incident light, θ_c.

$$\Re_\lambda = \frac{\int_0^\lambda f_{T,\lambda}\, \varepsilon_\lambda \, d\lambda}{\varepsilon_T} \tag{5.24}$$

The resulting inverted expression for the cone angle θ is

$$\theta = \text{asin}\left(\sin\theta_c \sqrt{\Re_\theta}\right) \tag{5.25}$$

The remaining relations for direction of reflection and absorption criteria are determined by standard MCRT relations for diffusely reflecting and absorbing opaque surfaces.

Solution validation

The numerical code was validated against the analytical solution for absorption efficiency obtained using the radiosity method for an isothermal cavity with gray and diffuse walls and uniform insolation. For the validation case, we used the geometric parameters of $D = 3$ and $L = 2$, a total hemispherical emissivity of 0.8, and a surface temperature of 1250 K. The analytical solution predicts an absorption efficiency given by

$$\eta_{\text{abs}} = \left(1 - \frac{\sigma\, T^4}{I\, C}\right) \times \left(1 + \frac{(1/\varepsilon - 1)}{D^2\,(2 + 4\,L) - 1}\right)^{-1} = 0.907 \tag{5.26}$$

This analytical result is composed of the product of two terms which describe the physics of the system. The first term in the product represents the absorption efficiency of a black body. The second term represents the reduction due to the influence of the geometry and for non-black cavity walls. For an infinitely large cavity with a finite aperture size or for perfectly black walls, the second term becomes unity.

In addition to verifying agreement with the analytical absorption efficiency, the numerical solution was checked for circumferential symmetry because deviation from symmetry implies a lack of ray independence for the temperature distribution. The convergence of the MCRT solution in terms of the absorption efficiency and the relative standard deviation of flux (RSDF) around a circumferential ring of surface elements within the cavity is shown in Fig. 5.7, with the number of rays launched in the MCRT

routine increasing along the abscissa. The absorption efficiency approaches the analytical solution smoothly as the number of rays is increased, with deviations no larger than 1% of the analytical value once 10^5 or more rays are launched. The RSDF converges somewhat slower and achieves a steady value less than 1% with 10^6 or more rays. These results validate the MCRT code against a known analytical solution and show that ray independence is achieved for simulations launching at least 10^6 rays. Results reported here are for simulations with 10^7 rays.

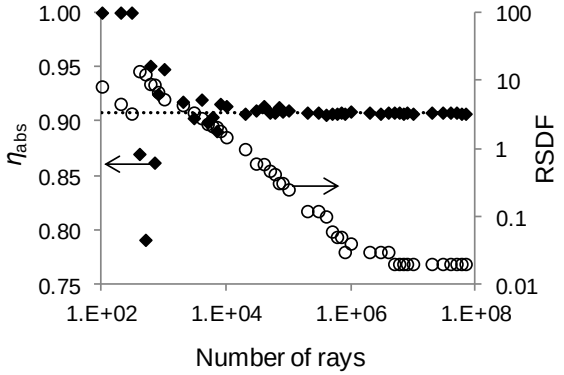

Fig. 5.7 Convergence of absorption efficiency and relative standard deviation of flux (RSDF) in the circumferential direction for increasing numbers of rays traced by the MCRT routine.

5.2.5 Results

The cavity simulation was run for values of the geometric parameters *D* and *L* from 1.25 to 2.5 in increments of 0.25. For surface properties, both Inconel and alumina materials were evaluated. The convective film coefficient values considered were within the range

$$200 \frac{\mathrm{w}}{\mathrm{m}^2\,\mathrm{K}} \leq h \leq 5000 \frac{\mathrm{w}}{\mathrm{m}^2\,\mathrm{K}} \tag{5.27}$$

This range encompasses values representative of both natural and forced convection in gases or liquids. The results for values of 200, 1000 and 5000 W/m^2 K are reported here to bound the maximum range of operation while including the value of 1000 W/m^2 K as the estimated performance point for the previously described biomass gasification reactor. All combinations of the above parameters are evaluated.

The results are reported both in terms of absorption efficiency and temperature along the inner cavity wall. Contour maps are shown in Fig. 5.8 (a) – (f) contain contour maps

of absorption efficiency for each design considered as a function of the geometric parameters D and L. The maps in Fig. 5.8 (a), (c), and e are for cavities with an Inconel surface while Fig. 5.8 b, d, and f are for a cavity with a thin coating of alumina. As the alumina is a thin coating, only the radiative properties of the wall are affected by the choice of surface material. The underlying Inconel determines the wall thermal conductivity and remains the same for both surface material choices. The maps of Fig. 5.8 (a) – (b) are for a film coefficient of $h = 200$ W/m^{2}K, while Fig. 5.8 (c) – (d) are for $h = 1000$ W/m^{2}K, and Fig. 5.8 (e) – (f) are for $h = 5000$ W/m^{2}K. Absorption efficiencies range from 68% to 91%.

The distribution of temperature along the inner cavity wall is plotted in Fig. 5.9 – Fig. 5.11 for both (a) Inconel and (b) alumina. The effect of varying D for L =2 and $h =$ 1000 W/m^{2}K is illustrated in Fig. 5.9, while Fig. 5.10 shows the impact of changing L for D =2, and Fig. 5.11 shows the impact of varying the convective film coefficient for L=D=2. For simplicity, these figures are plotted with normalized coordinates according to

$$R \equiv \frac{r}{r_{\max}} = \frac{r}{d/2} \tag{5.28}$$

$$Z \equiv \frac{z}{z_{\max}} = \frac{z}{l} \tag{5.29}$$

The plots are arranged such that the leftmost section displays the temperature in the radial direction from $0 \leq R \leq 1$ at $Z = 0$ with the center of the aperture at $R = 0$. The middle section displays the axial temperature distribution for $0 \leq Z \leq 1$ at $R = 1$. The rightmost section displays the radial temperature for $0 \leq R \leq 1$ at $Z = 1$. The dashed line represents a temperature limit of 1627 K, which is the highest temperature that favors a stable solid phase for Inconel alloy 600.

Impact of geometry

In this section, the impact of changing the geometry of the cavity, i.e., changing the

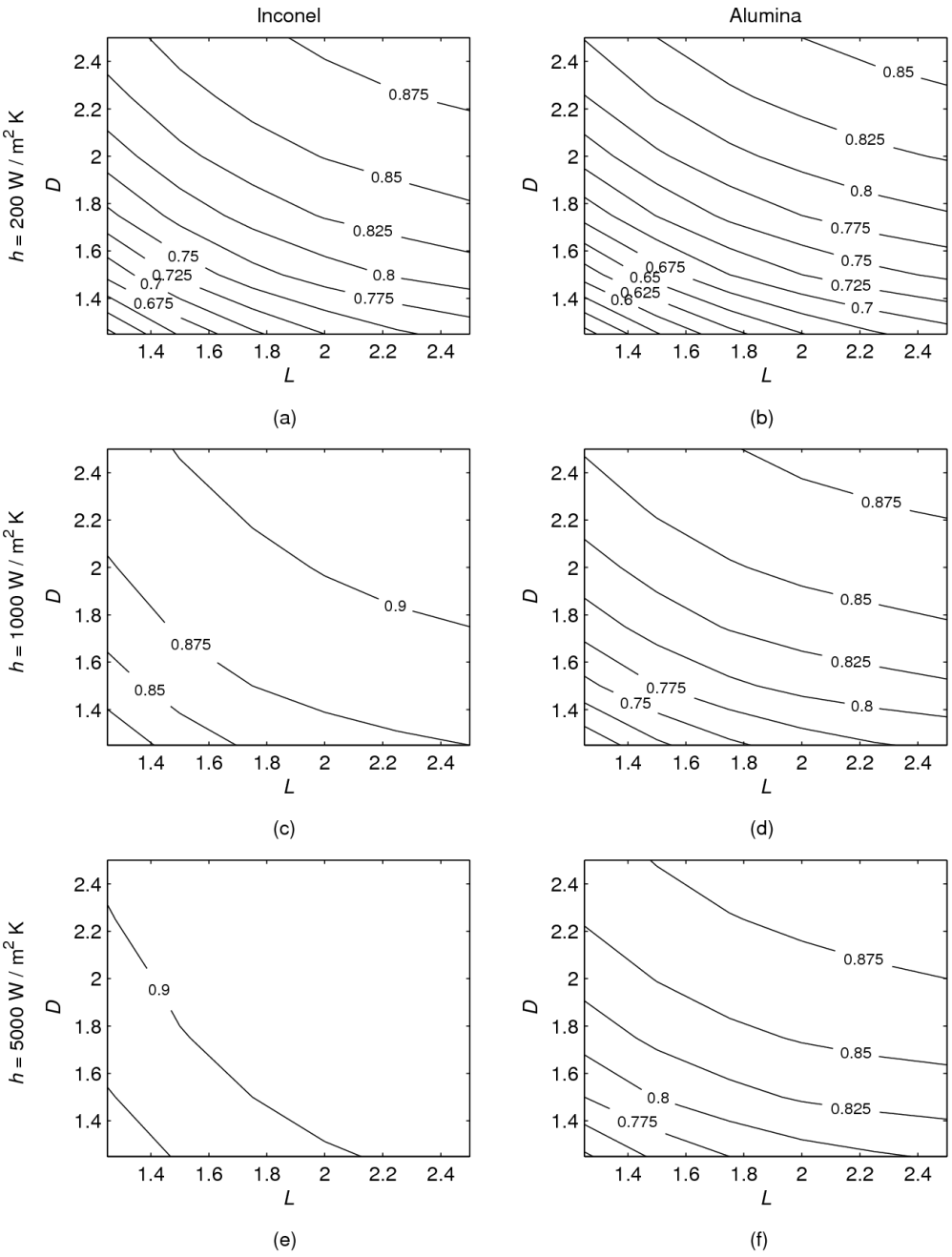

Fig. 5.8 Contour maps of the absorption efficiency as a function of the convective film coefficient h, the dimensionless geometric parameters D, and L. Figures a,c, and e are for a cavity with an Inconel surface while Figs. b, d, and f are for a cavity with an alumina surface. Figures a – b, c – d, and e – f are for film coefficient values of $h = 200, 1000,$ or $5000\ \mathrm{W/m^2K}$ respectively.

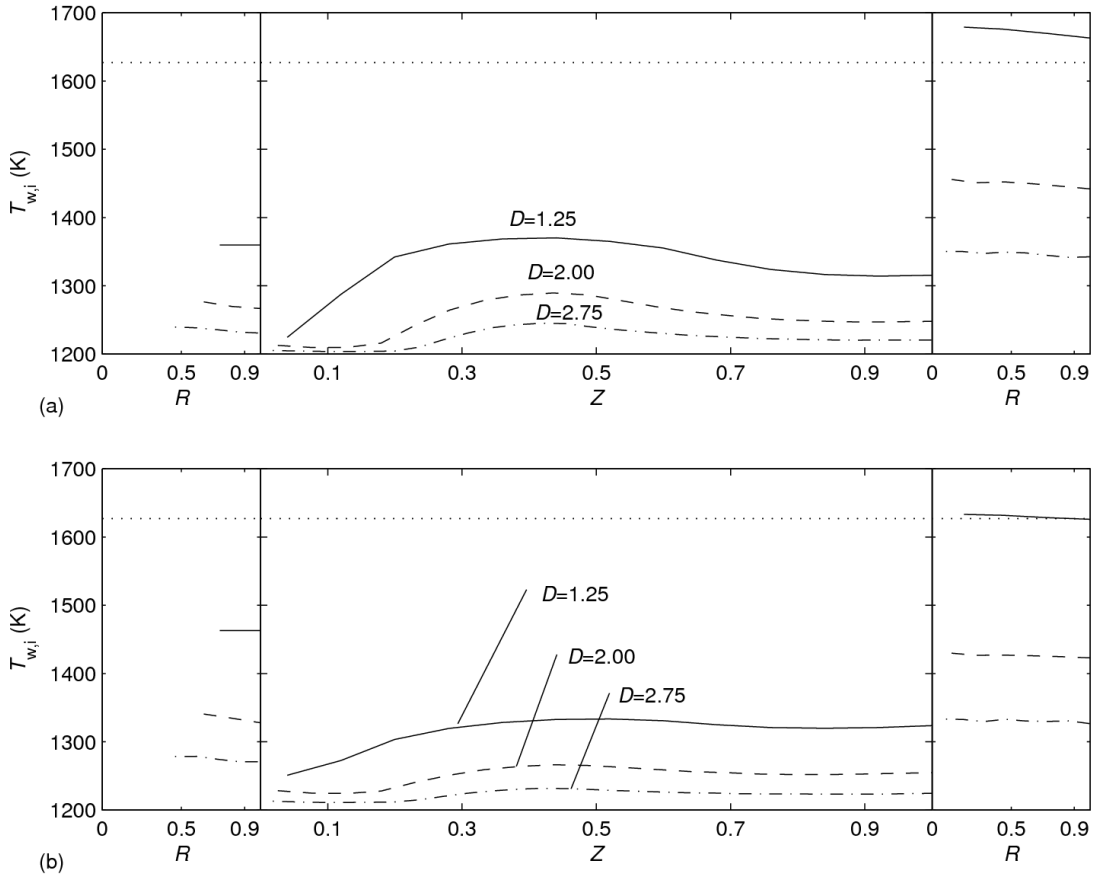

Fig. 5.9 The effect of changes in the aperture diameter ratio D on the distribution of temperature throughout the interior of the cavity for (a) Inconel, and (b) alumina coated surface. L = 2 and $h = 1000\ \mathrm{W/m^2K}$.

cavity/aperture diameter ratio D or cylindrical aspect ratio L, is discussed. First consider changes in D for $L = 2$ and $h = 1000\ \mathrm{W/m^2K}$. As D is increased, the average temperature of the cavity is reduced. As a result of the incident light having a fixed cone angle, the relative location of the peak temperature remains constant. The change in average temperature is attributed to an increase in surface area and concurrent reduction in the incident radiative flux intensity and increase in overall convective losses. Increasing D from 1.25 to 2.75, decreases the average axial cavity temperature from 1320 to 1250 K for the Inconel surface (Fig. 5.9 (a)) and from 1305 to 1240 K for an alumina coated surface (Fig. 5.9 (b)). The combined effects of a lower average temperature and a reduced view factor from the hot walls to the aperture results in a reduction of both emitted and reflected radiation leaving the cavity, and therefore an increase in the

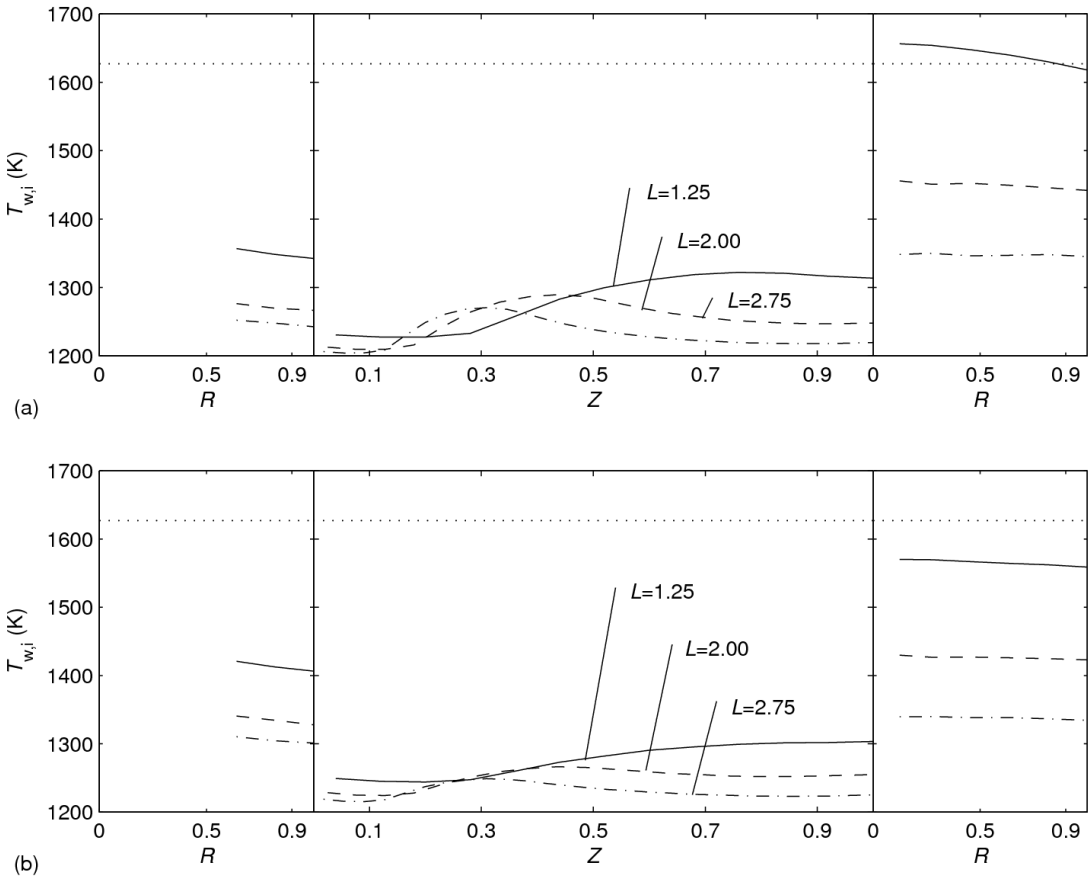

Fig. 5.10 The effect of changes in the cavity aspect ratio *L* on the distribution of temperature throughout the interior of the cavity for (a) Inconel, and (b) alumina coated surface. *D* = 2 and $h = 1000\ \mathrm{W/m^2K}$.

absorption efficiency of the cavity, as demonstrated by Fig. 5.8. Efficiency is increased from 87% to 91% and 76% to 88% for Inconel and alumina respectively.

For $D = 2$, increasing L shifts the relative location of the maximum temperature towards the aperture, as demonstrated in Fig. 5.10. This relative change in location of the maximum wall temperature is due to the fact that the cone angle of incident light intercepts the walls at the same absolute axial location. Again the combined influence of a lower wall-aperture view factor and lower cavity temperatures act to minimize reflected and emitted radiation and boost the absorption efficiency for increasing values of L, as shown by Fig. 5.8.

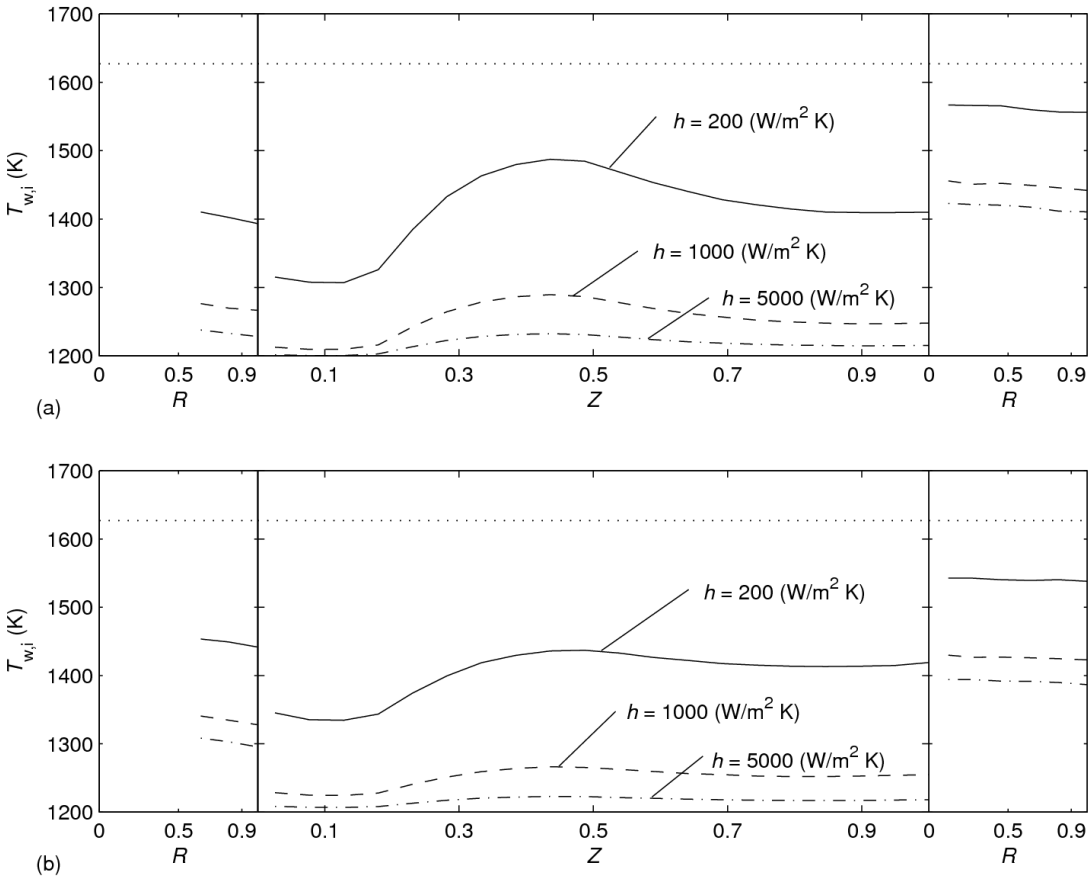

Fig. 5.11 The effect of changes in the convective heat transfer coefficient on the distribution of temperature throughout the interior of the cavity for (a) Inconel, and (b) alumina coated surface. $L = D = 2$.

The absorption efficiency is slightly less sensitive to changes in the cavity aspect ratio, L, than to changes in the cavity-aperture diameter ratio D. For example, as shown in Fig. 5.8 (a), the absorption efficiency varies from 59% to 76% across the range of L for $D = 1.25$. For $L = 1.25$, the absorption efficiency varies from 59% to 84% as D is changed. The impact of changes in geometry on the absorption efficiency is less significant as the cavity is increased in size. For very small cavities with L or D less than 1.5, the rear of the cavity experiences sufficient direct irradiation to reach temperatures close to or above the maximum acceptable for Inconel.

Impact of surface material

The results demonstrate the importance of spectral radiation properties on the performance of a cavity receiver. The Inconel surface has higher emissivity in the short wavelengths and lower emissivity in the long IR wavelength range, corresponding to high

absorption of the incident solar radiation and low emission of thermal radiation. The alumina surface exhibits the opposite trend, favoring higher reflectance for the incident solar radiation and higher thermal emission.

As a result of the differing spectral radiative properties, Inconel provides superior absorption efficiency, typically 5% greater than for the alumina coated surface for all geometries considered. On the other hand, the axial temperature distribution is more uniform for cavities with an alumina coating. For a reference base case of $D = 2$, $L = 2$, and $h = 1000$ W/m^{2}K, the standard deviation of the temperature is 25 K for Inconel and 13 K for alumina. The maximum axial temperature with an alumina coating is typically 20 to 35 K lower than that for Inconel. This trend holds for all cases considered in the present study.

The absorption efficiency of the Inconel surface is less sensitive to changes in geometry than the alumina surface because most of the incident light is absorbed at the first contact and thermal emission is reduced compared to the alumina surface. This trend is apparent when comparing the absorption efficiencies reported for Inconel in Fig. 5.8 (c), which range from 81% to 91%, to those reported for alumina in Fig. 5.8 (d) which range from 68% to 86%. In general the higher absorption efficiency and reduced sensitivity to design changes offered by Inconel make it the preferred surface.

Impact of convection

As expected, the magnitude of the heat transfer coefficient at the outer surface of the cavity impacts the temperature within the cavity which in turn affects emission and absorption efficiency. As h is increased from 200 W/m^{2}K to 1000 W/m^{2}K, the average temperature of the Inconel cavity is reduced from 1413 to 1253 K for $L = 2$, and $D = 2$. The standard deviation of the axial temperature distribution is reduced from 57 to 25 K. For $h = 5000$ W/m^{2}K, the average temperature is 1218 K and the standard deviation of temperature is 10 K. A similar trend is observed for the alumina cavity. The reduction in temperature for increasing convective intensity correlates directly to a reduction in the magnitude of thermal emission from the cavity walls and therefore an increase in the absorption efficiency of the cavity. Corresponding to the behavior observed for temperature, the effect of variation in the convective film coefficient on the absorption efficiency is most pronounced at lower h. For an Inconel cavity with the base

case geometry and $h = 200\ \mathrm{W/m^2K}$, the absorption efficiency is 85%. For $h = 1000\ \mathrm{W/m^2K}$ the absorption efficiency is 90%. At $h = 5000\ \mathrm{W/m^2K}$, the absorption efficiency is 91%. Above $h = 1000\ \mathrm{W/m^2K}$ the performance of the cavity varies little and approaches the result expected from an isothermal outer wall boundary condition. This result is specific for the inner and outer wall radii used in this study. For a larger outer to inner wall radius ratio (or a less conductive material), the insensitivity to changes in film coefficient would occur at even lower values of h, while for smaller outer to inner wall radius ratios (or a more conductive material), this value would be higher

5.2.6 Selection of cavity design

For the prototype gasification reactor, geometric parameter values of $D = 2$ and $L = 1.5$ were selected to obtain a reactor whose absorption efficiency falls in the range of 81%-90% depending on the convective condition, and whose flux distribution results in a peak-flux near the midsection of the cylindrical wall. Keeping the peak flux, and thus the resulting peak temperatures, away from the ends of the cavity prevents end effects from slowing convective salt flows and also allows thermal expansion to take place while minimizing stresses that would be concentrated at the joints between surfaces at either end. The cavity surface material of Inconel was selected for the final prototype design because it provides the highest absorption efficiency and an acceptable flux distribution.

5.3 Numerical Design of Salt Region

The heat transfer and fluid mechanics of a prototype scale solar receiver/reactor are modeled to determine heat transfer within the annulus to establish the annulus diameter ratio $DA = \frac{d_{\mathrm{ao}}}{d_{\mathrm{ai}}}$. The molten salt is contained within the annular region between the outer walls of the cavity receiver and the inner wall of the reactor housing. Selection of DA is an optimization based on two competing trends. A smaller value of DA corresponds to decreased external surface area and thus decreased thermal losses for a fixed operating temperature and insulation thickness. However as DA is decreased, viscous drag from the annulus walls increases, stagnating fluid motion and increasing the resistance to heat transfer from the receiver walls via convection, and thus increasing cavity temperature and emission losses.

The value of DA is selected on the basis of maximizing solar utilization efficiency, which is defined as the ratio of useful power to the solar power delivered at the aperture of the reactor.

$$\eta_{\mathrm{u}} = \frac{\dot{Q}_{\mathrm{useful}}}{\dot{Q}_{\mathrm{solar}}} \tag{5.30}$$

where $\dot{Q}_{\mathrm{useful}}$ includes sensible heating of carrier gases to the reactor temperature and the heat required for the heating and endothermic gasification of feedstock material (both included within the reaction enthalpy, Δh_{rxn}, which is calculated for feedstock initially at ambient temperature). The rate of reaction, $\dot{R}$, may be calculated from eqs. (4.7) and (4.8). The sum of these terms is approximated by a sink term, $\dot{q}'''$, as defined in eq. (5.31).

$$\dot{Q}_{\mathrm{useful}} = \int_{V_{fluid}} \dot{R} \Delta h_{\mathrm{rxn}} \, \mathrm{d}V + \int_{T_\infty}^{T_{\mathrm{salt}}} \dot{m}_{\mathrm{N_2}} \, C_{P,N_2} \mathrm{d}T = \dot{q}''' \, V_{fluid} \tag{5.31}$$

For each geometry considered, the volumetric sink is set at a magnitude that results in steady operation with average salt temperature of 1200 K, allowing the utilization efficiency to be calculated. The use of a uniform sink is most appropriate for modeling slow reactions where the reactants are well distributed before being consumed, such as the gasification of carbon or char [70]. Exploratory simulations of non-reacting carbon particles in molten salt undergoing natural convection have demonstrated that the particles are well entrained by the salt with a volume fraction varying by no more than 10% throughout the salt after a simulated 1 minute of operation, verifying this approximation for carbon gasification reactions. However, cellulosic feedstocks are buoyant in the salt and would require a multiphase modeling approach. Natural convection is assumed to represent a worst case for mixing and heat transfer to the salt.

Prior studies [73, 79-82] have examined natural convection in a horizontal annulus; however the impact of a volumetric energy sink on the natural convection flow has not been studied. The prior work shows that for large annuli where $DA > 4$, the heat transfer along the inner surface of the annulus approaches that of an isolated cylinder in an infinite medium and at the outer surface, equivalent to convection in a cylinder of equivalent outer diameter. As DA is decreased, two convection cells are formed on either half of the annulus and correlations describing the overall Nusselt number as a function of any Rayleigh number for $\mathrm{Pr} > 0.1$ are available [73]. For $DA < \sim 1.75$, the

momentum boundary layers begin to interact and the natural convective flow stagnates resulting in reduced heat transfer approaching conduction. While the impact of a volumetric sink has not been studied, that of a volumetric source has, with results demonstrating that the source causes the boundary layer on the hot surface to grow and the heat transfer rate on that surface to decrease approaching an effectively adiabatic surface with sufficient intensity of a heat source [80]. This results in reduced rising flow velocities along the hot surface and can impact the heat transfer from the other surface negatively as the recirculation in the convection cell is slowed.

Here the effect of variation of the annulus diameter ratio in the presence of a volumetric energy sink on the utilization efficiency of the reactor is explored. The study is conducted to determine the value of DA ratio that maximizes utilization efficiency given the competing effects mentioned in the beginning of this section: increased thermal losses at large values of DA and increased resistance to convective heat transfer from the cavity walls at small values of DA.

5.3.1 Methodology

The three-dimensional numerical domain and boundary conditions used for the present study are illustrated in Fig. 5.12. The domain consists of the annular salt volume and the solid walls of the cavity receiver. A wall thickness of $t_{\mathrm{w}} = 3.175$ mm is assumed, allowing the inner annulus diameter to be fixed at $d_{\mathrm{ai}} = d_{\mathrm{c}} + 2 \cdot t_{\mathrm{w}}$ and leaving only the outer annulus diameter to be selected. Within the fluid region of the numerical domain, the governing equations are of continuity

$$\frac{\partial}{\partial t}(\rho) + \vec{\nabla} \cdot (\rho \vec{u}) = 0 \tag{5.32}$$

conservation of momentum,

$$\frac{\partial}{\partial t}(\rho \vec{u}) + \vec{\nabla} \cdot (\rho \vec{u}\vec{u}) = \vec{\nabla} p + \vec{\nabla} \cdot \bar{\bar{\tau}} + \rho \vec{g} \tag{5.33}$$

and conservation of energy,

$$\frac{\partial}{\partial t}(\rho h) + \nabla \cdot (\rho \vec{u} h) = \frac{\partial p}{\partial t} + \bar{\bar{\tau}} : \nabla \vec{u} - \vec{\nabla} \cdot \vec{q} + \dot{q}''' \tag{5.34}$$

Radiation within the salt is modeled using the gray P1 approximation, with the radiative flux added to the heat flux divergence term in eq. (5.34).

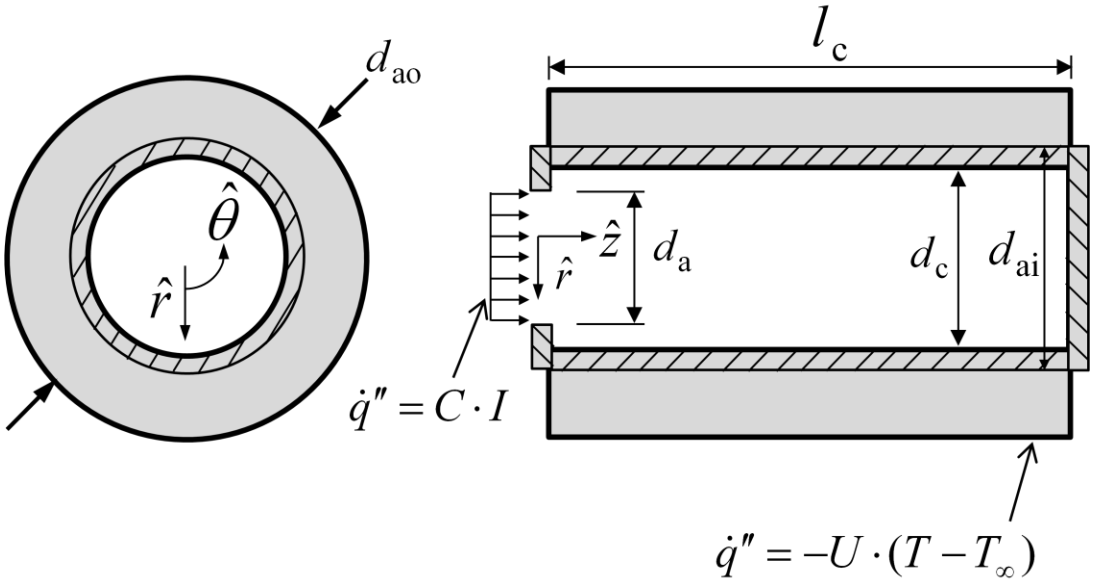

Fig. 5.12 Front (left) and side cross section (right) views of the numerical domain and boundary conditions for the numerical simulation of natural convection within the salt filled annulus region.

The transport equation which is solved for the radiative flux in the P1 model is

$$-\vec{\nabla} \cdot \vec{q}_r = aG + 4an^2\sigma T^4 \tag{5.35}$$

Turbulence is modeled using the realizable variant of the $k-\epsilon$ model with the equation for conservation of turbulent kinetic energy given by

$$\frac{\partial}{\partial t}(\rho k) + \vec{\nabla} \cdot (\rho k \vec{u}) = \vec{\nabla} \cdot \left[\left(\mu + \frac{\mu_t}{\sigma_k}\right)\vec{\nabla} k\right] + G_k + G_b \tag{5.36}$$

and for conservation of the turbulent dissipation rate

$$\frac{\partial}{\partial t}(\rho \epsilon) + \vec{\nabla} \cdot (\rho \epsilon \vec{u}) = \vec{\nabla} \cdot \left[\left(\mu + \frac{\mu_t}{\sigma_\epsilon}\right)\vec{\nabla} \epsilon\right] + \rho C_1 S \epsilon - \rho C_2 \frac{\epsilon^2}{k + \sqrt{\nu \epsilon}} + C_{1\epsilon}\frac{\epsilon}{k} C_{3\epsilon} G_b \tag{5.37}$$

the volumetric source term, $\dot{q}'''$, is a thermal sink representing sensible heating and chemical reactions as described in eq. (5.31). This term is varied to obtain steady operation at the target temperature of 1200 K. Within the solid regions of the cavity absorber, only conservation of energy is solved and the volumetric source term is zero.

The boundary condition at the aperture of the cavity receiver is a specified flux of concentration C relative to the reference insolation $I = 1\ \mathrm{kW/m^2}$ according to

$$\dot{q}''_{\mathrm{ap}} = C\ I \tag{5.38}$$

resulting in an incident solar power of

$$\dot{Q}_{\text{solar}} = \dot{q}''_{\text{ap}} \frac{\pi}{4} d_{\text{a}}^2 \tag{5.39}$$

This flux is assumed to be spatially uniform in intensity over the area of the aperture, and diffusely emitted within a limited diverging cone of 37° half-angle, representing the input from a typical solar concentrating field and the University of Minnesota high flux solar simulator [71]. The radiative exchange between the aperture and the walls of the cavity absorber is modeled using a collision-based Monte Carlo Ray Tracing (MCRT) routine without energy partitioning. The details of this model were described in section 5.2.

All exterior boundaries of the reactor feature a Robin-type thermal boundary condition which represents the loss of energy to the ambient environment via conduction through an 8 cm layer of insulation and subsequent radiation and natural convection to the ambient environment, embodied by an overall heat transfer coefficient U.

$$\dot{q}''_{\text{wall}} = U(T - T_{\infty}) \tag{5.40}$$

In eq. (5.40) the overall heat transfer coefficient U is estimated by

$$U = \frac{1}{A_{\text{o}} R_{\text{tot}}} = \left(A_{\text{o}} \left(R_{\text{cond}} + \left(\frac{1}{R_{\text{conv}}} + \frac{1}{R_{\text{rad}}} \right)^{-1} \right) \right)^{-1} \tag{5.41}$$

The resistance due to conduction through the reactor housing and the insulation is given by

$$R_{\text{cond}} = \frac{1}{l_{\text{a}}\, 2\pi} \left(\frac{\ln(d_{\text{ao}}/d_{\text{oh}})}{k_{\text{inco}}} + \frac{\ln(d_{\text{oh}}/d_{\text{ext}})}{k_{\text{ins}}} \right) \tag{5.42}$$

and the resistance due to convection from the exterior of the reactor to the ambient environment is given by

$$R_{\text{conv}} = \frac{1}{h_{\text{conv}} A_{\text{ext}}} \tag{5.43}$$

where the convection coefficient, h_{conv}, is calculated using the correlation for a hot horizontal cylinder in an infinite medium by Churchill and Chu [83]. The resistance due to radiation from the reactor exterior to the ambient environment is given by

$$R_{\text{rad}} = \frac{1}{(T_{\text{ext}} - T_{\infty})(T_{\text{ext}}^2 - T_{\infty}^2)\sigma \epsilon_{\text{ins}} A_{\text{ext}}} \tag{5.44}$$

For a representative case where the ambient temperature is 300K and the temperature of the salt at the outer wall is 1180K, $U = 4\ \text{W/m}^2 \cdot \text{K}$.

For all surfaces bounding the fluid region an impermeable no-slip condition is imposed.

$$\vec{u} = 0 \tag{5.45}$$

The numerical domain includes two materials. The fluid region consists of the molten ternary eutectic alkali metal carbonate salt while the solid region is an Inconel alloy. The pertinent physical properties of both of these materials as well as the insulation material are listed in Table 5.1 [72, 75, 84]. The density of the salt is modeled as variable using a 2nd order polynomial curve-fit of data with respect to temperature in order to capture buoyant behavior, while all other properties are constant.

$$\rho_{\text{salt}} = 3800 - 2.95T + 0.001T^2 \text{ kg/m}^3 \tag{5.46}$$

The absorption coefficient for the salt is a power averaged value based on the 1200K blackbody emission spectrum [85].

Table 5.1 Physical properties of the materials in the numerical model of the reactor.

Material	**Ternary Eutectic Alkali Metal Carbonate Salt**	**Inconel alloy 600**	**Fiberfrax Insulation**
Thermal Conductivity [W/m-K]	0.75	29.3	0.25
Specific Heat Capacity [J/kg-K]	1842	639	
Melting Point [K]	670	1350	
Density [kg/m^3]	eq. (5.46)	8430	
Viscosity [kg/m-s]	$2.06 \cdot 10^{-3}$		
Absorption Coeff. [m^{-1}]	8890		
Refractive Index	1.4		
Emissivity		eq. (5.39)	0.3

The governing equations and boundary conditions are solved on a grid of 1,868,000 finite volume tetrahedral elements with a maximum edge length of 2mm using ANSYS/FLUENT 14. The density-based fully coupled solver is utilized with an implicit spatial formulation scheme. Spatial discretization of the governing equations is performed using the 3rd order MUSCL scheme with gradients calculated according to the least squares cell-based method.

The solution is approached with iterative adjustment of the volumetric energy sink, $\dot{q}'''$, to obtain the desired criteria of a mass-averaged salt temperature of 1200 K at steady

state. Four cases were considered with values of $DA = \{1.5, 2, 2.5, 3\}$ to bound operation below the typical $DA = 1.75$ value where stagnating effects begin as well as up to a large reactor sizes where the combined mass of the reactor, salt, and ancillary equipment approaches the design constraint requiring the total mass remain under 50 kg for traverse/test stand operability.

5.3.2 Results

The simulation results are presented in terms of the resultant utilization efficiency and the average Nusselt number at the cavity wall, as well as qualitative figures depicting the flow fields and temperature distributions. To quantify the intensity of the natural convection, an average Rayleigh number is calculated. With the outer wall nearly insulated, the primary heat transfer pathway is from the hot cavity to the bulk molten salt. Therefore, the area-averaged absorber wall temperature is used for the hot temperature and the mass-averaged bulk fluid temperature as the cold temperature. For the length scale, the annulus gap length, $L = (d_{\mathrm{ao}} - d_{\mathrm{ai}})/2$, is used.

$$\mathrm{Ra}_L = \frac{g\beta}{\alpha\nu}(\bar{T}_{\mathrm{h}} - \bar{T}_{\infty})L^3 \tag{5.47}$$

The corresponding average Nusselt number for heat transfer from the absorber wall is defined as

$$\mathrm{Nu}_L = \frac{\bar{h} \cdot L}{k_{\mathrm{salt}}} \tag{5.48}$$

where the average convective heat transfer coefficient, h, is an area average

$$\bar{h} = \frac{1}{2\pi l_{\mathrm{c}}} \int_0^{2\pi} \int_0^{l_{\mathrm{c}}} h(z, \theta)\, \mathrm{d}z\, \mathrm{d}\theta \tag{5.49}$$

and the local heat transfer coefficient defined based on the local surface flux and the bulk temperature of the salt from the simulation data.

$$h(z, \theta) = \frac{\dot{q}''(z, \theta)}{(T(z, \theta) - \bar{T}_{\infty})} \tag{5.50}$$

Table 5.2 lists the values of key input and output parameters for the four cases considered. The input parameters are flux concentration, average salt temperature, and the ambient temperature while the remaining parameters are outputs. The reported Nusselt number is an area-averaged value.

Table 5.2 Results of the parametric simulation of annular natural convection.

DA	1.5	2.0	2.5	3.0
$\dot{q}'''$	-844 kW/m^3	-340 kW/m^3	-186 kW/m^3	-118 kW/m^3
η_{u}	70.0%	67.6%	64.7%	62.8%
$\dot{Q}_{useful}$	2.10 kW	2.03 kW	1.94 kW	1.88 kW
$\dot{Q}_{loss}$	461 W	571 W	676 W	791 W
$\mathrm{Ra_L}$	$1.7{\cdot}10^7$	$1.8{\cdot}10^8$	$7.6{\cdot}10^8$	$2.1{\cdot}10^9$
$\mathrm{Nu_{avg}}$	37	60	73	85

The strengths of the volumetric sinks are reasonable given the kinetics of biomass gasification. For the cases considered, the energy sink represents a 2-0.3% volume fraction of reacting biomass within the salt at 1200 K for the smallest and largest cavity sizes respectively. This value was calculated using the kinetics and reaction enthalpy reported in Chapter 3 for cellulose pyrolysis to determine the required volume fraction of feedstock to obtain the above listed volumetric energy sink magnitudes. Thermal losses to the ambient scale roughly with the square root of the external surface area. For a given average temperature, a thicker gap length leads to a decreased surface temperature, which explains why the scaling is not linear with respect to surface area. The cavity absorption stays relatively steady around 2.6-2.7 kW, thus the net result is that $\dot{Q}_{\mathrm{useful}}$ is largest for the smallest cavity design of $DA = 1.5$ resulting in a utilization efficiency of $\eta_{\mathrm{u}} = 70.0\%$. The best fit correlation of Nu and Ra the form of $\mathrm{Nu} = C \cdot \mathrm{Ra}_L^m$ is with $m = 0.18$ and $C = 1.8$, as shown in Fig. 5.13. Based on these results, for maximized performance the smallest annulus size is the preferred design so the selection of geometry is made with $DA = 1.5$.

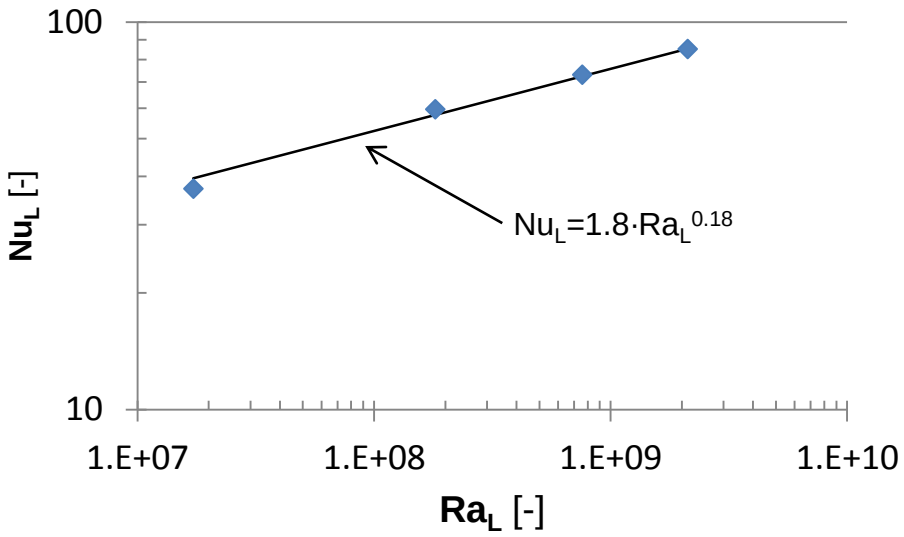

Fig. 5.13 Area averaged Nusselt number as a function of the Rayleigh number based on gap-length *L* for the simulated cases. The solid line is a fitted correlation corresponding to the standard natural convection form of $Nu = C \cdot Ra_L^m$.

The velocity magnitude and temperature distributions for the four cases considered are shown in Fig. 5.14 and Fig. 5.15 respectively. The distributions are shown in a vertical X-Y plane at position $z = 0.5 \cdot l_c$. The velocity contours highlight the regions of primary fluid motion, which consist of the momentum boundary layer along the surface of the absorber wall, the plume of rising fluid where the flow separates from the absorber wall, and the region where the plume impinges on the top of the reactor. In all cases, the boundary layer along the absorber wall is similar in both thickness and growth rate, with no thickening of the layer at even the smallest value of $DA = 1.5$, indicating that stagnation of the flow has not occurred. Looking at the temperature distribution, the upper 2/3^{rds} of the salt region is generally well-mixed for $DA \geq 2.0$ with a temperature differences no greater than 30 K. For the smallest size of $DA = 1.5$ a gradient is more apparent, however the shape of the contours indicate motion in the form of a rising flow along the cavity and a sinking flow along the outer wall despite the gradient. For the other cases of $DA \geq 2.0$ the salt region below the cavity forms gradients that are flat corresponding to a stable density gradient and no significant fluid motion and heat transfer by conduction only. While these planar views give some indication of the general flow behavior, the axially varying flux distribution along the cavity causes the flow field to be significantly three dimensional.

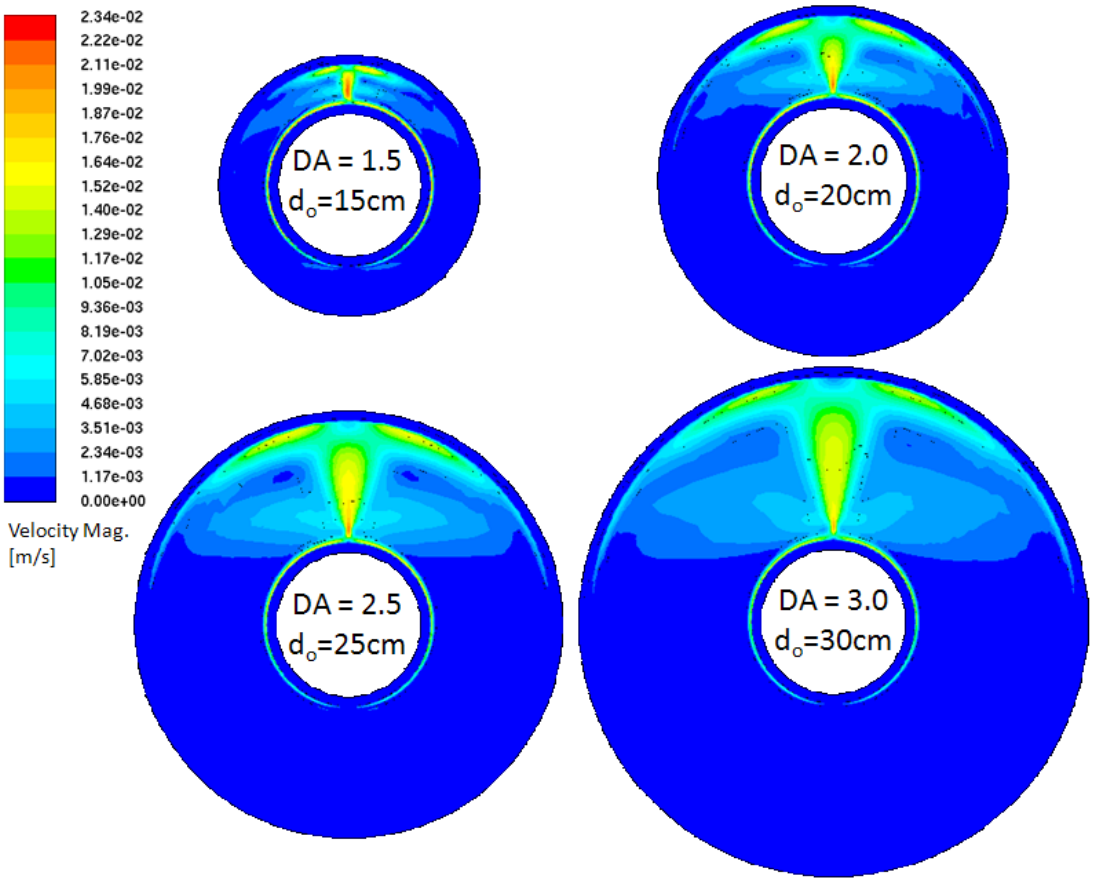

Fig. 5.14 Contours of velocity magnitude for the four geometry cases considered. Key features are the momentum boundary layer which grows as flow moves from the bottom of the absorber to the top, and the plume formed by the flow separating from the absorber.

The three dimensional fluid motion is illustrated for $DA = 1.5$ in Fig. 5.16 with streamlines in the right half of the reactor. The flow field is 3-dimensional, symmetric about a vertical Y-Z plane passing through the center of the reactor, and does not exhibit the planar convection cells found in prior studies with uniformly heated walls and without a volumetric heat sink [73, 79]. The dominant upward flow occurs near the rear ($+\hat{z}$) portion of the cavity with an average velocity of 1 cm/s. This behavior is due to the flux distribution. The front of the cavity is shaded from the direct radiation in the region $Z \leq 0.2$ as evidenced in the flux distributions displayed in section 5.2.5. The peak velocity occurs in the plume above the cavity at 1.45 cm/s. The rising plume in the rear of

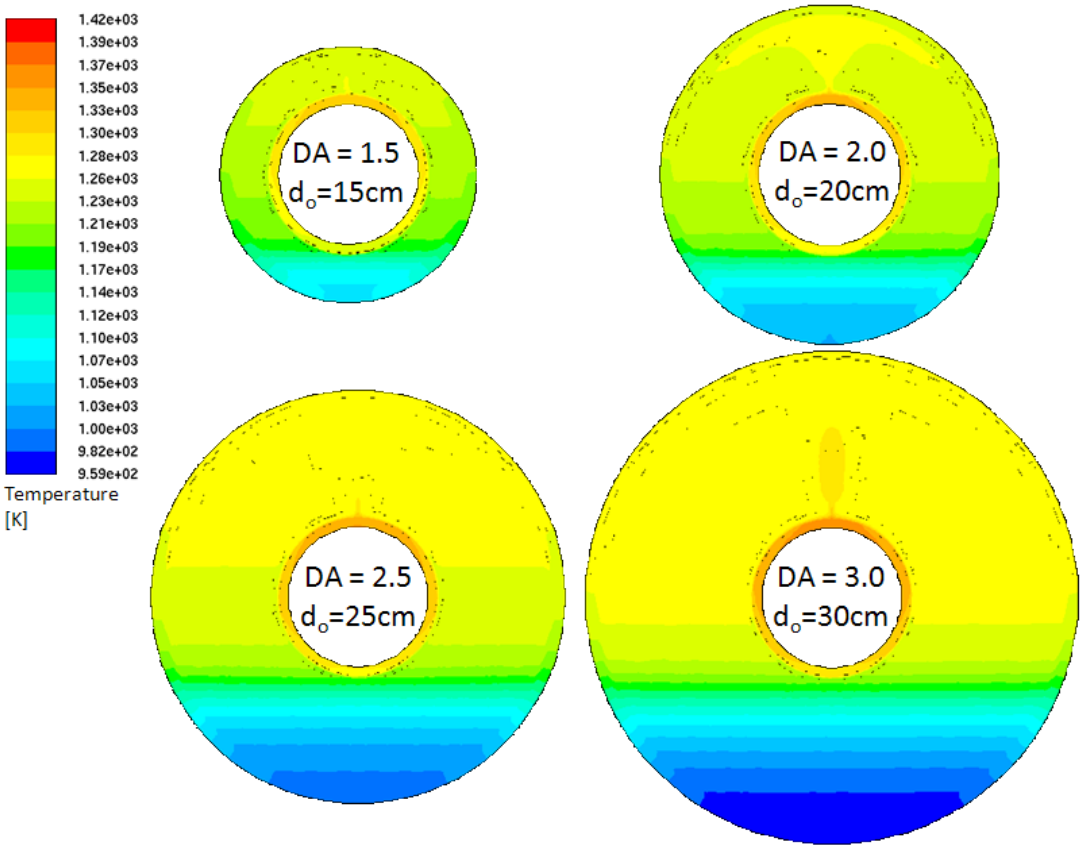

Fig. 5.15 Contours of temperature for the four geometry cases considered. High thermal conductivity and convective heat transfer results in uniform temperature in the upper region, while stagnant fluid at the bottom results in conduction-like temperature gradients.

the reactor forms a counter-rotating eddy as the salt moves forward and then descends from the top of the cavity as it cools. When the flow reaches the front of the reactor it is directed down along the front wall housing wall at 0.4 cm/s until about 45° from vertical at which point the streamlines bend towards the rear of the reactor where the streamlines slow to less than 0.1 cm/s, diverge, descend, and recirculate into the rising flow at various points. Fluid motion is nearly stagnant in the bottom 1/3rd of the cavity. As this is a worst-case scenario for heat transfer analysis, one must keep in mind that with the injection of feedstock and reactant gases, this stagnant region would be entrained by the rising flows and the convection cell would grow to encompass the extent of the salt volume.

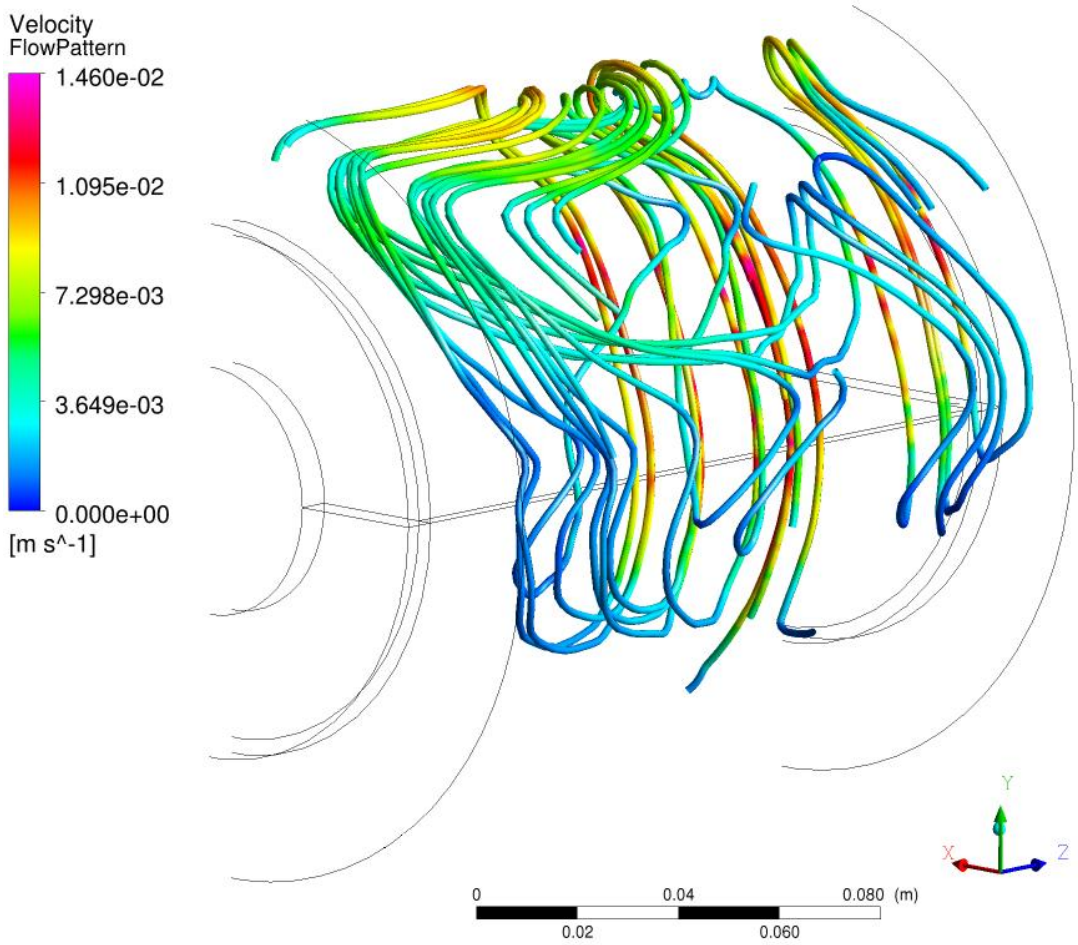

Fig. 5.16 Streamlines showing the three dimensional motion of the circulating molten salt for $DA = 1.5$. Only one half of the domain is shown as the flow is symmetric on either half. The streamlines are colored by velocity magnitude.

5.3.3 Conclusion

Heat transfer and fluid flow in a solar reactor filled with molten salt and in which a volumetric endothermic reaction takes place is modeled using MCRT and 3-D CFD. Four different annulus sizes were considered, corresponding to values of $DA = \{1.5, 2.0, 2.5, 3.0\}$ resulting in utilization efficiencies of $\eta_u = \{70.0\%,\ 67.6\%, 64.7\%, 62.8\%\}$. The general trend is of a monotonic decrease in efficiency with increasing annulus size, corresponding to increasing thermal losses to the ambient with little change in the cavity absorption efficiency. Heat transfer can be described by gap-length Rayleigh numbers on the order of 10^7-10^9 resulting in Nusselt number values from 37-85 which fit well to a correlation of $Nu_L = 1.8 \cdot Ra_L^{0.18}$,

indicating a continuous convection regime in the range of geometries studied and no appreciable stagnation of the convective flow due to viscous drag against the annulus walls, even at the smallest gap length considered. Based on maximizing utilization of the incident solar power, the selected design is of an annulus with diameter ratio $DA = 1.5$.

Qualitatively the flow field is three-dimensional due to the non-uniformity of the flux at the cavity walls resulting in unique flow unlike typical natural convective cells obtained in prior studies with uniform boundary conditions. Based on these simulations, some suggestions on operation of the current reactor design can be made. Specifically, targeting the delivery of reactants towards the rear of the cavity will help ensure the reactants pass through the regions of highest temperature and most effective heat transfer. Also, delivery of buoyant reactants ought to be done from the bottom of the reactor to encourage the existing natural convective flow patterns and enhance heat removal from the cavity receiver while agitating otherwise stagnant fluid that would exist on the bottom portion of the salt volume when only natural convection is present.

Future work with this reactor concept will aim to move beyond general operation to model specific thermochemical processes such as the pyrolysis and gasification of biomass. Means of enhancing heat transfer should also be explored, such as the introduction gaseous jets or agitation.

5.4 Mechanical Design

In this section we specify the remaining design parameters of wall thickness t_{w}, flange thickness t_{f}, and bolt diameter d_{b} as illustrated in Fig. 5.3. The values are determined by examining the stress state of the reactor assembly over a range of values of these parameters. The primary driver of mechanical stress in the reactor is differential thermal expansion resulting from the temperature distribution in the solid components of the reactor. In general, the cavity walls are at a higher temperature than the housing walls, resulting in compressive axial loading of the cavity and tensile axial loading of the housing walls. Flux and temperature distributions obtained from the previous CFD studies were used to set the thermal boundary conditions for the studies.

A two-step modeling approach was utilized to analyze first the inner and outer cylinder walls, and second the front bolted flange connection. The first step used a 2D

axis-symmetric model of the reactor cavity and housing parts, with an assumed perfect connection between the two parts at both front and rear flange connections. The wall thicknesses are varied and the resulting wall stresses and total axial load are obtained. The second step uses a 3D model of an angular segment the front of the reactor including the cavity flange down to the aperture, the bolt connection to the housing flange, and a partial segment of the cavity wall and housing wall. The total axial load from the 2D study is used to set the load condition applied to the cavity and housing wall so the resulting stresses and deformation of the flanges and bolt can be observed. The flange and bolt thicknesses are varied to determine acceptable values of stress and to ensure the bolted connection remains sealed with typical bolt pre-torque values.

5.4.1 Material Selection

The desired material of construction for the reactor was selected prior to the simulations to obtain mechanical properties and stress limits. Previously mentioned studies of corrosion demonstrated that the Inconel series of nickel alloys had superior resistance to corrosion in a molten carbonate salt [46]. Selection of a specific alloy was based on an investigation of the various Inconel alloys for their high temperature properties.

The stand-out material was Inconel alloy X-750 (UNS N07750), which is a similar composition to the common Inconel 600 alloy used in the corrosion study with the addition of aluminum to allow precipitation hardening for high temperature resistance to creep and useful strength up to 1255 K. Precipitation hardening is achieved using a "triple heat treatment" process specified in AMS 5668 which involves an annealing at 1422 K, followed by air cooling down to 1116 K for 24 hours and holding at 978 K for another 20 hours for the final precipitation and growth of the precipitate grains resulting in maximized creep, relaxation, and rupture strength at high temperatures.

Properties of alloy X-750 after a triple heat treatment are available for operation at 1100 K [86]. At these temperatures, the failure mode is not set by the yield strength but instead by creep behavior. This generally allows you to predict the extent and mode of deformation given (1) the stress applied to the material and (2) the length of time held at that stress state. The design strategy used for the reactor is to limit stress to a level where any deformation is purely elastic (recoverable) for an infinite length of time. Based on

this requirement, the maximum allowable stress at any point within the reactor structure is limited to 34.5 MPa. Designing to this limit with a factor of safety of 1 is acceptable given that plastic strain would only begin to occur after 1000 hours at 62.1 MPa and rupture only after 10,000 hours at 62.1 MPa or 1000 hours at 137.9 MPa. The remaining pertinent physical properties of alloy X-750 are presented in table Table 5.3.

Table 5.3 Elevated temperature properties of Inconel alloy X-750 [86].

Property	**Value**
Thermal Conductivity [W/m-K]	29.4
Melting Range [K]	1666 – 1700
Coefficient of Linear Expansion [1/K]	$1.76 \cdot 10^{-5}$
Modulus of Elasticity [GPa]	128
Poisson's Ratio	0.29

5.4.2 2D Simulation

The first simulation was set up using an axis symmetric domain representing a simplified form of the geometry in Fig. 5.3 where the bolts are not directly modeled and the endcap part is not included. The domain of the simulation and boundary conditions as applied are shown in Fig. 5.17. The red boundaries show the only regions where

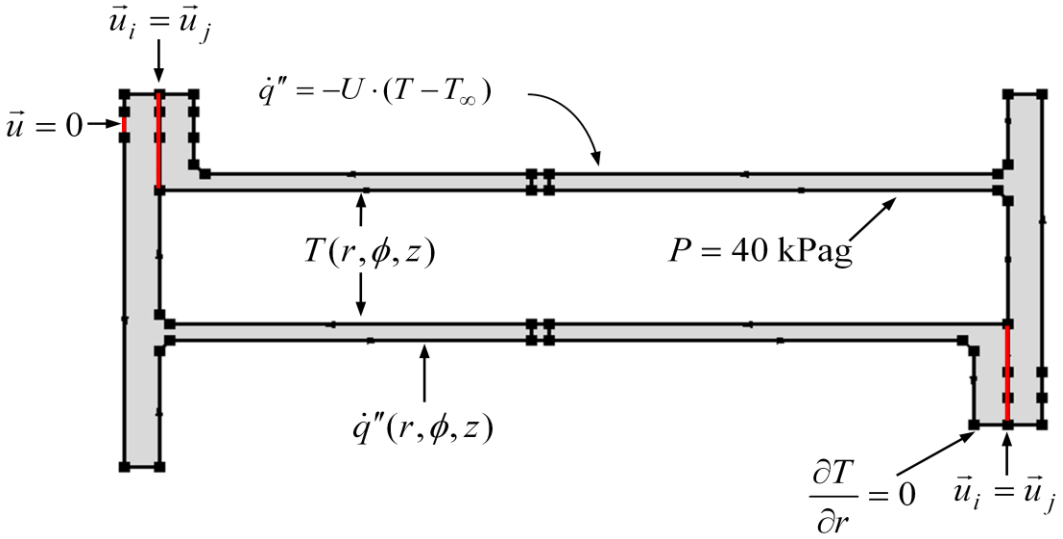

Fig. 5.17 Domain and boundary conditions used for the 2D axis symmetric thermal stress study. The front of the reactor is on the left side and the axis of symmetry is the dot-dashed line along the bottom of the figure. The endcap part is not included.

mechanical boundary conditions were directly applied aside from the pressure within the annulus. The annulus pressure of 40 kPag was applied to all the surfaces of the annulus and represents a worst-case scenario of the combination of the hydrostatic pressure from the salt at the bottom of the annulus and the pressure limit of the relief valve to be installed on the outlet array of the reactor assembly. The remaining mechanical boundary conditions represent a perfect seal between the two flanges at the front and back (total displacement of both surfaces is equal) and a fixed axial ($\hat{z}$) position at the outer flange bolt circle to avoid an unbounded solution.

The thermal boundary conditions were established based on the worst-case temperature distribution of heat transfer by natural convection to the molten salt using the final geometric parameters of $D = 2$, $L = 1.5$, $DA = 1.5$ as established in the prior works and using the coupled CFD and MCRT model described in section 5.3 for a flux concentration of $C = 1530$ suns. The boundary conditions include a flux distribution applied along the inner surfaces of the cavity wall as generated by the MCRT radiation simulation as well as a wall temperature within the annulus region based on the boundary temperatures of the salt volume observed in the CFD model. Because the outer housing wasn't included in the CFD model, the outer surface is not prescribed a flux or temperature distribution directly, but instead a convective boundary condition is applied with the overall heat transfer coefficient set to the same value used in the CFD study, $U = 4$ W/m^2-K, representing conduction through insulation and convection/radiation from the outer surface of the insulation to the ambient. Finally, the surface between the rear flange joint and the end cap is prescribed as adiabatic under the assumption that the end cap is at the same temperature as this surface with negligible net heat transfer.

The governing equations in steady-state form solved within the domain are the static equilibrium form of Newton's second law,

$$-\nabla \cdot \sigma = \boldsymbol{F}_{\mathrm{V}} \tag{5.51}$$

where σ is the stress tensor and F_{V} is the body force per unit volume, and conservation of energy for an isotropic solid,

$$0 = \nabla \cdot (k \nabla T). \tag{5.52}$$

The stress tensor σ can be related to the strain tensor ϵ according to the general form of Hooke's law,

$$\sigma = C : \epsilon \tag{5.53}$$

where C is the fourth order elasticity tensor. Coupling between the thermal and linear elastic deformation models is achieved by defining the total strain as the sum of the elastic and thermal strains.

$$\epsilon = \epsilon_{\mathrm{el}} + \epsilon_{\mathrm{th}} \tag{5.54}$$

where the thermal strain is found from the coefficient of linear expansion and the difference between the current and initial temperature.

$$\epsilon_{\mathrm{th}} = \alpha \cdot (T - T_0) \tag{5.55}$$

Lastly, the strain tensor is related to the displacement vector according to

$$\epsilon = \frac{1}{2}[(\nabla \vec{u})^T + \nabla \vec{u}] \tag{5.56}$$

These governing equations and boundary conditions were applied to a triangular finite element mesh using Lagrange shape functions to develop the weak form of the equations as solved by the *COMSOL Multiphysics* finite element analysis (FEA) software. The element mesh used for these simulations is shown in Fig. 5.18 with the scale in meters and values of $t_{\mathrm{w}} = 3.175$ mm and $t_{\mathrm{f}} = 6.35$ mm.

The FEA equations were solved to obtain a stress and displacement distribution. The principal stress in either the cavity wall or housing wall is in the axial direction. We report the average axial stress in both of these surfaces by averaging across the wall thickness at the locations indicated by the box near the midpoint of either wall as seen in Fig. 5.17 and Fig. 5.18.

$$\overline{\sigma_{z,i}} = \frac{1}{(r_o - r_i)^2} \int_{r_{\mathrm{i}}}^{r_o} \sigma_{\mathrm{z,i}}(r)\, \mathrm{d}r \tag{5.57}$$

where r_i and r_o are the inner and outer radius of the wall of interest. Another result of interest is the closure force, representing the force that the bolted connection at the front flange must maintain in order to hold the seal at that surface.

$$F_{\mathrm{c}} = \pi \int_{r_{\mathrm{i}}}^{r_o} \sigma_{\mathrm{z,i}}(r)\, \mathrm{d}r \tag{5.58}$$

The rear bolted connection is not critical during operation as this joint is in compression,

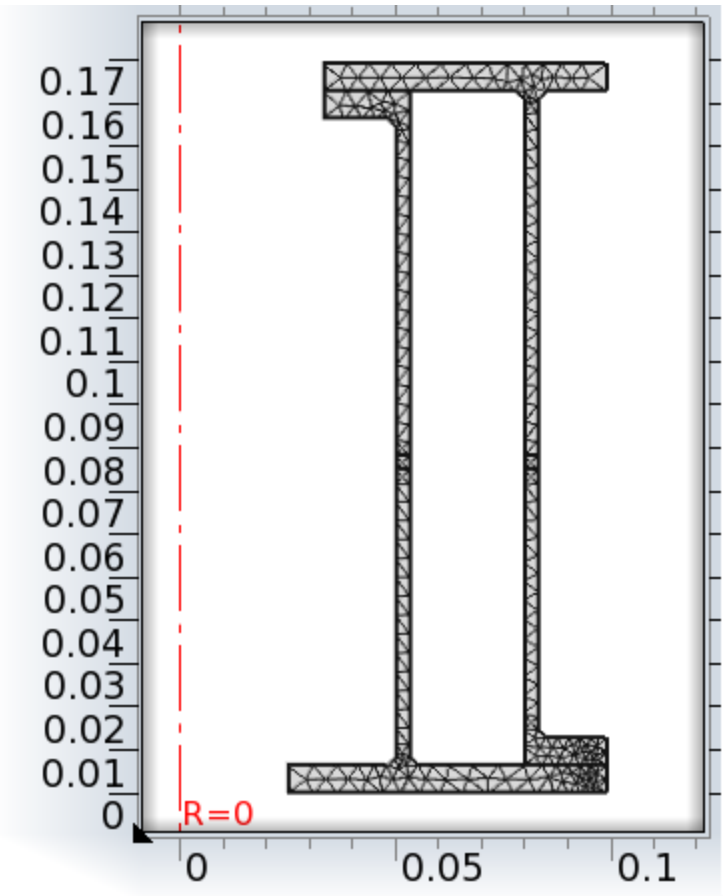

Fig. 5.18 Grid and scale axes for the 2D axis symmetric finite element model of the reactor structure. Dimensions are in meters and the dash red line is the axis of symmetry. The front of the reactor is towards the bottom of the figure.

unloading the bolts with the force transmitted directly from the rear cavity flange to the rear housing flange.

The resulting temperature and stress distribution for the base case of $t_w = 3.175$ mm and $t_f = 6.35$ mm are shown in Fig. 5.19 rotated about the symmetry axis to aid interpretation of the 2D results. The cavity walls are generally around 50 K hotter than the housing walls, which drives the axial stresses. The highest stresses are observed near the ends of either the cavity or housing walls where they meet the flanges. These peak regions are due to localized bending that adds to the total axial stress as well as inherent stress concentration due to the transition between the wall and flange geometry. Another peak compressive region occurs where the corner of the cavity presses into the rear flange causing a stress concentration. The region of peak stress near the front flanges of the reactor is larger in the housing wall than in the cavity wall, however the intensity of the

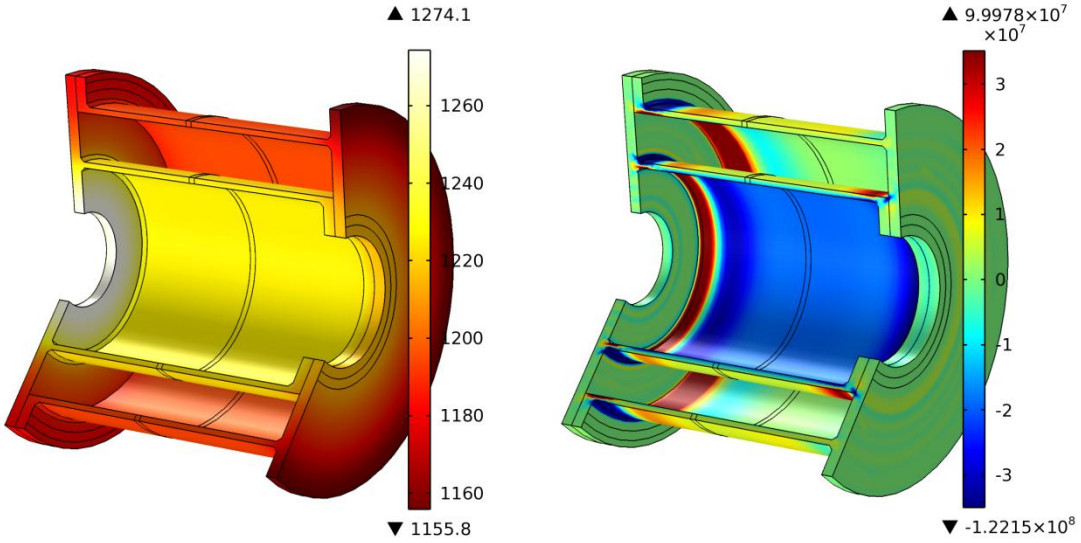

Fig. 5.19 Representative results of the temperature distribution (left, in Kelvin) and axial stress distribution (right, in Pascals) for the base case geometry.

peak stress as well as the average stress is larger in the cavity wall. For this specific case, the average stress in the cavity wall is $\overline{\sigma_{z,\mathrm{c}}} = -7.1$ MPa with the peak occurring in compression on the outer surface of the cavity wall at $\min(\sigma_{z,\mathrm{c}}) = -33.6$ MPa while in the housing wall the average stress is $\overline{\sigma_{z,\mathrm{h}}} = 4.8$ MPa with the peak occurring in tension on the inside surface of the housing wall at $\max(\sigma_{z,\mathrm{h}}) = 32.8$ MPa. The closure force required to hold the front flange closed for this stress state is 7.8 kN.

At these stress levels, no permanent deformation is expected over an infinite lifetime. If the stresses were to increase due to increased loading from increased temperature differences, the failure mode would be localized yielding near the flange-wall connections that would relax the stresses. A rupture of the walls would not be expected from this yielding during a single cycle of operation, but rather from fatigue after several cycles with yielding, so with regular inspection of this region following operation any catastrophic rupture can be avoided.

The solution was repeated for a parametric survey over values of wall thickness of $t_{\mathrm{w}} = \{3.175\ \mathrm{mm},\ 6.35\ \mathrm{mm}\}$ and flange thickness of $t_{\mathrm{f}} = \{3.175\ \mathrm{mm},\ 6.35\ \mathrm{mm},\ 12.7\ \mathrm{mm}\}$ for all combinations where the flange is greater than or equal to the wall thickness. The resulting average and maximum stresses in both walls and required closing force were calculated, as well as an estimate of the average bolt stress based on

an assumed bolt diameter equal to the flange thickness (a general best practice for bolted flange connections). The true maximum bolt stresses cannot be determined from the 2D study as the bolts will experience bending in addition to axial stress, however the estimate of average axial stress still allows for elimination of designs that exceed the material design stress at this phase, as the bolt stresses in the 3D study will only increase with the addition of bending. The results of this parametric survey are presented in Table 5.4 for the various cases considered.

Table 5.4 Results of 2D axis symmetric parametric study of wall and flange thicknesses .

Case	Thin Flange	Base	Thick Flange	Thick Wall	Thick Both
Wall Thickness [mm]	3.175	3.175	3.175	6.35	6.35
Flange Thickness [mm]	3.175	6.35	12.7	6.35	12.7
Housing Stress [MPa]					
Average	1.7	4.8	21.2	4.9	13.2
Max	5.44	32.8	**74.2**	12.8	26.4
Cavity Stress [MPa]					
Average	-2.8	-7.1	**-34.7**	-7.3	-22.5
Max	-8.4	-33.6	**-62.5**	-10.95	**-56.3**
Closing Force [kN]	2.9	7.8	35.3	16.3	48.5
Est. Bolt Stress [MPa]	32.0	21.1	24.0	**44.3**	33.0

The values of stress that exceed the maximum magnitude of 34.5 MPa are displayed in bold. The thin flange and base cases demonstrate acceptable stress levels for both walls , however the bolt stress in the thin flange case is approaching the maximum and the the thin flange is anticipated to result in larger bending stresses in the bolt, so this case is still suspect and the 3D analysis will be required to ensure the bolt stresses are acceptable. The case of a thickened flange and base wall thickness results in an excessive average cavity stress as well as excessive stress peaks on both the cavity and housing walls. The thick wall design generally allows for acceptable stresses and less excessive peak stresses than the base case, however the thick walls result in a large closing force that bolts of 6.35 mm diameter would be unable to withstand without yielding. For the case of both the flange and wall having their thickest value, the average stresses are acceptable, however the peak stress on the cavity wall is excessive and the closure force is quite high, resulting in an estimated bolt stress for 12.7 mm diameter bolts that nearly exceeds the maximum design stress, so with the added bending in the 3D study, the bolts

may still reach failure. Based on these results, we see that the thin flange and base case parameter sets are the currently favored designs.

5.4.3 3D Simulation

The second step in the mechanical analysis is to produce a simulation that models the stresses in the bolted flange connection at the front of the reactor. In order to remove the assumptions of the perfectly sealed flange of the 2D analysis, a 3D model was produced including the outer front flange and cavity wall, the inner front flange and housing wall, and a connecting bolt/washer assembly. This simulation takes place at a fixed temperature of 1200 K in order to simplify the solved system by eliminating the energy equation. The stresses observed in the walls from the 2D simulation are applied as a boundary condition for this simulation to produce the same loads as the differential thermal expansion does without the need to actually simulate the coupled thermal/structural system.

The goal of this simulation is to make the final geometry selection for the structural elements of the reactor design, specifically the wall thickness t_{w}, flange thickness t_{f}, and bolt thickness d_{b}. In addition, the required pre-loading of the bolts is determined for use in the reactor assembly process. Bolt pre-load is needed to ensure that a seal is maintained during operation however excessive pre-loading during assembly can result in stresses during operation that exceed the limits for the bolt material.

The numerical domain, mesh, and associated boundary conditions are depicted in Fig. 5.20. An "undercut flange" design was used where material is removed in a channel around the bolt to increase closure pressure on the sealing faces. Only the front portion of the reactor was modeled as the rear connection is in compression during operation and is not a significant concern. Axial symmetry was utilized to allow only a $1/36^{\mathrm{th}}$ angular segment of the reactor to be modeled (half a bolt and half of the between-bolt region for a 18 bolt connection). The symmetry condition is applied to all surfaces along the angular cut planes that form the angular reactor segment. The housing wall and cavity wall are cut by a ZX plane. The mechanical boundary condition at the housing wall cut is a uniform normal tensile stress equal to the average stress in the housing wall in the 2D study. The boundary condition for the cavity wall cut surface is a "roller" that fixes the position in the axial direction and produces a reaction force to counter the load on the

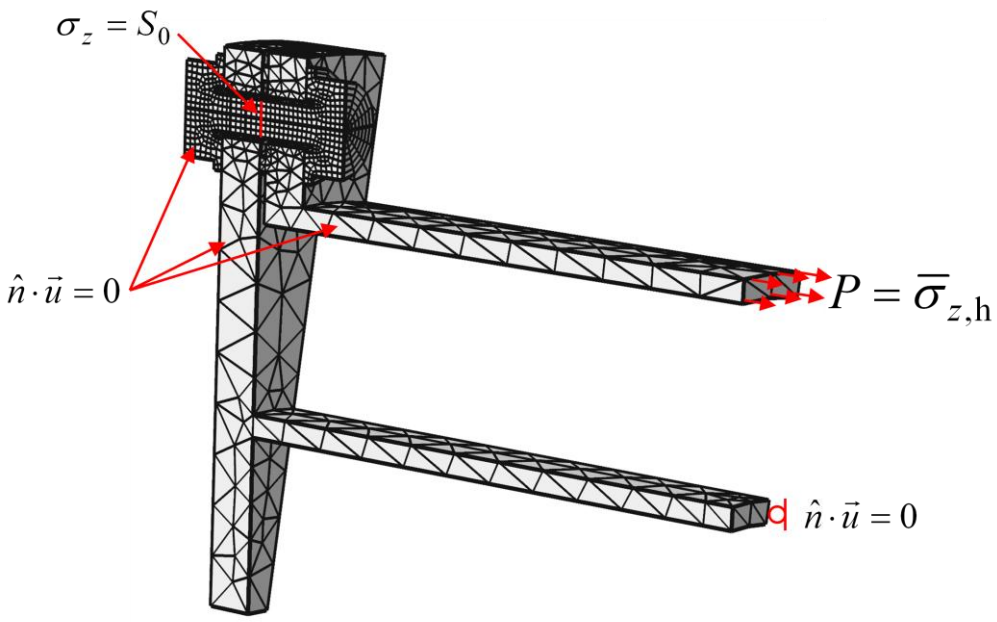

Fig. 5.20 Numerical domain, mesh, and boundary conditions for the 3D simulation using the base-case geometry.

housing wall. Mathematically, the symmetry and roller boundary conditions are the same, setting the dot product of the surface normal vector and the displacement vector to zero. Lastly, an initial condition of an internal tensile stress is applied to the bolt by reducing the bolt length while requiring the washer surfaces to maintain contact with the flanges to simulate the preloading of the bolt with an initial torque applied during assembly.

The governing equations for this simulation are the same except that the energy equation is not solved nor are there any thermal strains. The equation and boundary conditions are applied to a three-dimensional mesh of tetrahedral elements with Lagrangian shape functions to develop the weak-form of the equations as solved by *COMSOL Multiphysics*. Solutions were generated for the thin flange and base case geometries described in Table 5.4. The magnitude of bolt pre-stress was varied to determine a value for each geometry that maintains contact at the seal face under planned loading conditions. For the thin flange case, using a bolt of the same thickness as the flange did not allow for the seal to remain closed without bolt pre-stress exceeding the design maximum, so a bolt of 6.35 mm diameter was used in the analysis for both cases.

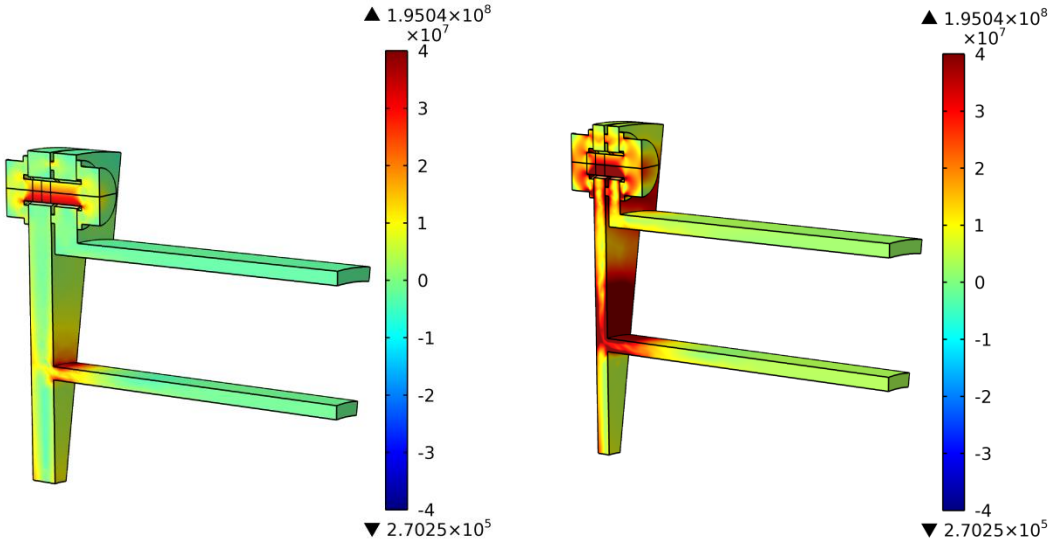

Fig. 5.21 Stress distributions from the 3D analysis of the bolted flange connection for the base case (left) and thin flange (right) configurations. Von Mises stresses are shown in units of Pascals for both figures.

The results of the simulations are shown in Fig. 5.21, illustrating the resulting von Mises stresses in both the thin-flange and base case parameter sets. For the base case, the maximum stress of 33.9 MPa occurs on the lower surface of the bolt due to the combined axial loading and bending loading in the bolt. In the thin flange design, the tendency for the less rigid flange to bend and open at the sealing surface required a larger prestress to be applied to the bolt in order to maintain a seal. This results in a much larger maximum stress observed in the bolt at the lower surface of 38.2 MPa, which just exceeds our maximum stress design criteria for elastic-only deformation over infinite life. Additionally the flange itself exhibits stresses in excess of 35 MPa implying that some plastic deformation would occur during the operating lifetime with the thin flange design. The indicated stresses on the flange are somewhat higher than expected for an actual welded assembly however, as the solid model contains a hard edge where the flange and cavity wall meet. A welded joint here would result in a smoother transition between the surfaces reducing the local stress concentration at this position observed in Fig. 5.21.

Based on these results, it was decided that the base case geometry will be selected for the structural design of the reactor. The final values for the remaining design parameters are thus: $t_{\mathrm{w}} = 3.175$ mm, $t_{\mathrm{f}} = 6.35$ mm, and $d_{\mathrm{b}} = 6.35$ mm.

5.5 Final Design

To summarize the work in this chapter, Table 5.5 presents the selected values of design parameters which define the prototype reactor concept as introduced in section 5.1.

Table 5.5 Final values of prototype reactor design parameters.

Parameter	***Symbol***	***Selected Value***
Salt Temperature	T_{salt}	1200 K
Flux Concentration	C	1530 suns
Aperture Diameter	d_{a}	5 cm
Cavity Diameter Ratio	D	2
Cavity Aspect Ratio	L	1.5
Annulus Diameter Ratio	DA	1.5
Wall Thickness	t_{w}	3.175 mm
Flange Thickness	t_{f}	6.35 mm
Bolt Diameter	d_{b}	6.35 mm

Prior to final manufacture, the reactor features were added to the reactor to allow for interfacing of sensors, the feed delivery, drainage of salt, and gas outlet. The fully featured reactor assembly is show in isometric and cross section views in Fig. 5.22. The new features are six ½" NPT threaded ports on the sides and bottom of the reactor, a ¼" NPT threaded port at the top of the reactor, a 1" flanged port on the top of the reactor for product gas outlet, and a ½" flanged port on the rear flange of the reactor. Tapered thread ports were selected for the interfaces that would likely not be removed frequently (thermocouple probes and feed injector) while mating flanges were selected for the interfaces that will be connected and disconnected for each use (outlet array, salt drainage). In the previous section, the highest stresses were found on the inner cavity wall, while the outer housing wall experienced much lower stresses. Reduced cross section area and stress concentrations in the vicinity of these features result in housing stresses of up to 12 MPa in tension, well below the maximum design stress. The maximum housing stress still occurs near the front flange and is not changed by these added features.

Feedstock is delivered to the reactor using an entrained-flow injector attached to the bottom rear NPT port and fed by a hopper and screw feed conveyer. Details on the

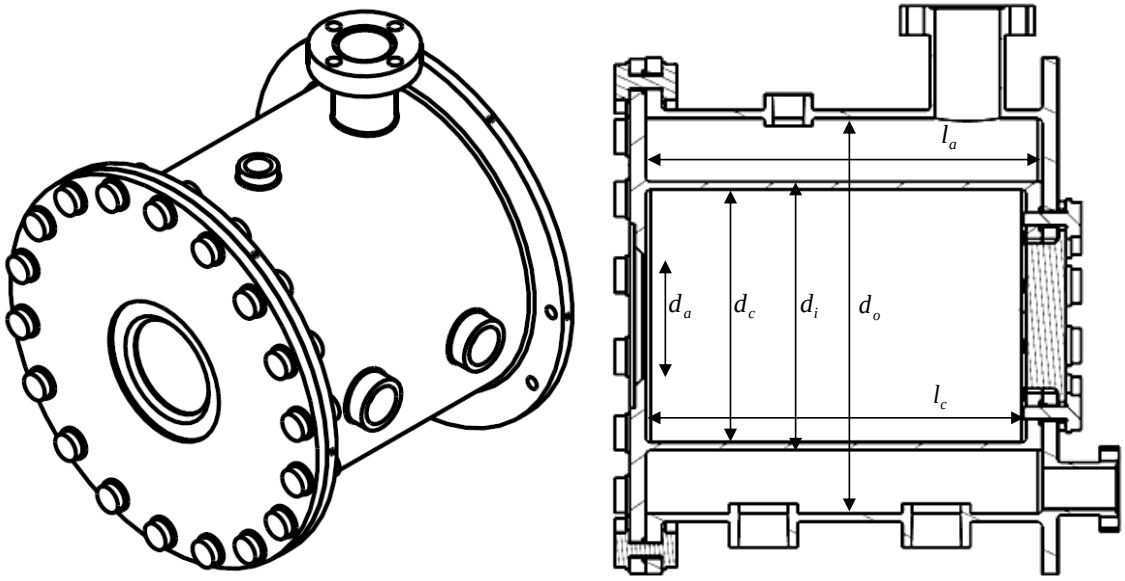

Fig. 5.22 Isometric and side cutaway view of the final featured reactor assembly with inlet, outlet, sensor, and drain ports added to the outer housing.

design testing and calibration of the feed system can be found in another published thesis [87]. The injector is shown in a side cross section view in Fig. 5.23 with dimensions in inches. The injector is threaded into the rear bottom ½" NPT port in a vertical orientation. Reactant and injection gases enter from the right and move through the narrow passage in the center of the injector, picking up feedstock where the feed screw joins the injector through the opening on the bottom of the part.

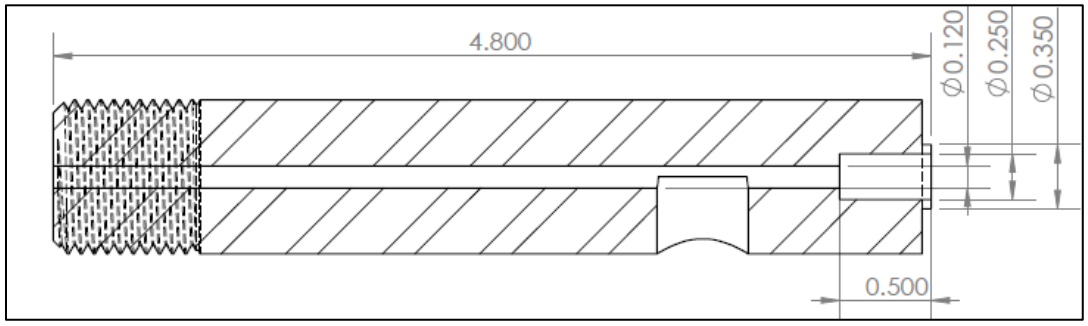

Fig. 5.23 Cross section view of the feedstock injector. The threaded portion on the left mates with the bottom port of the reactor while reactant and injection gases enter the injector from the port on the right. The feed screw from the hopper enters through the passage on the bottom.

Feedstock is stored in a hopper located adjacent to the reactor during operation and is moved from the hopper to the injector using a helical feed screw driven by an electric variable speed motor. A side view of the hopper and feed screw housing tube is shown in Fig. 5.24. The size of the hopper was set to allow for one hour of steady operation at a

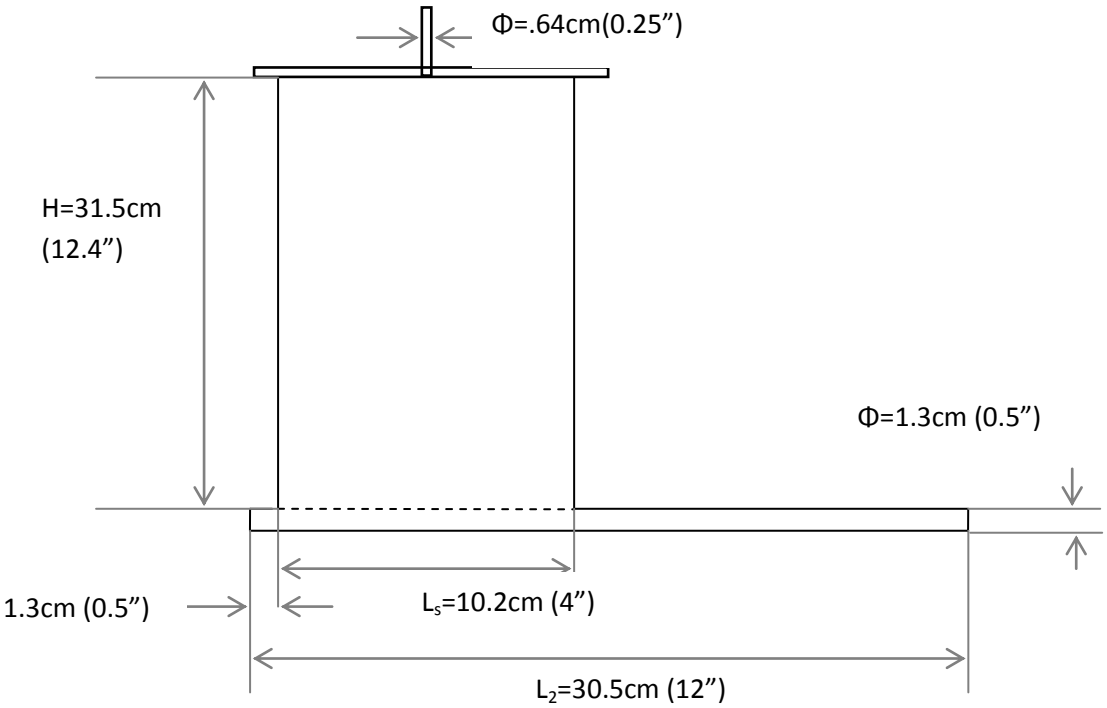

Fig. 5.24 Side view of the hopper and feed screw tube assembly. The feeds crew passes through the tube on the bottom moving feedstock from the hopper to the injector. The port on top of the hopper is used to pressurize the hopper with nitrogen to prevent backflow of gases from the injector.

feedstock delivery rate of 22 g/min of powdered cellulose. The hopper includes sloped sides with an angle of convergence of 40° to avoid buildup of feedstock during feeding and a port for nitrogen to be added to the top of the hopper in order to set up a favorable pressure gradient from the hopper to the injector that will prevent backflow and encourage forward movement of the feedstock. The feed screw itself is a modified deep-hole wood boring bit of helical shaftless design as pictured in Fig. 5.25. This design features a wide flute and shallow pitch well suited for the movement of biomass chips. The feed system was calibrated for delivery of feedstock at rates from 8 - 15 ± 0.04 g/min.

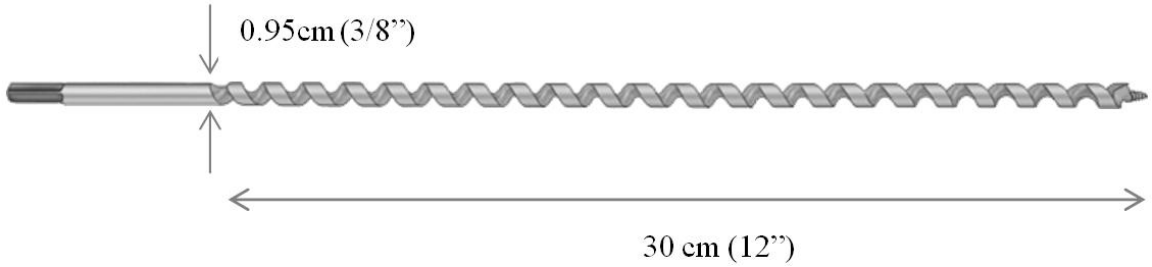

Fig. 5.25 Side view of the wood boring bit utilized as the feed screw in the feed assembly.

6 Characterization of the Prototype Reactor

The prototype reactor was characterized under simulated radiation in the 45 kW_e high flux solar simulator. The goals of the initial testing were to examine the durability and proper operation of the reactor and feed system and make initial measurements of product gas yield, composition, solar efficiency and cold gas efficiency. For these shakedown tests, the reactor was operated at a reduced power of 2.2 kW_{th} for gasification of cellulose using CO_2 as a gasifying agent. Operation with CO_2 and at a reduced incident power allows us to demonstrate basic operation while initially avoiding the complications of steam delivery and reducing the risk of damage from excess thermal stress or localized hot spots. The generalized overall reaction for CO_2 gasification of biomass is given by

$$\mathrm{CH}_x\mathrm{O}_y + (1-y)\cdot \mathrm{CO}_2 \rightarrow (2-y)\cdot \mathrm{CO} + \left(\frac{x}{2}\right)\cdot \mathrm{H}_2 \qquad (6.1)$$

where, for cellulose, $x = 5/3$ and $y = 5/6$, resulting in a carbon-monoxide rich product gas with an equilibrium product distribution as shown in Fig. 6.1.

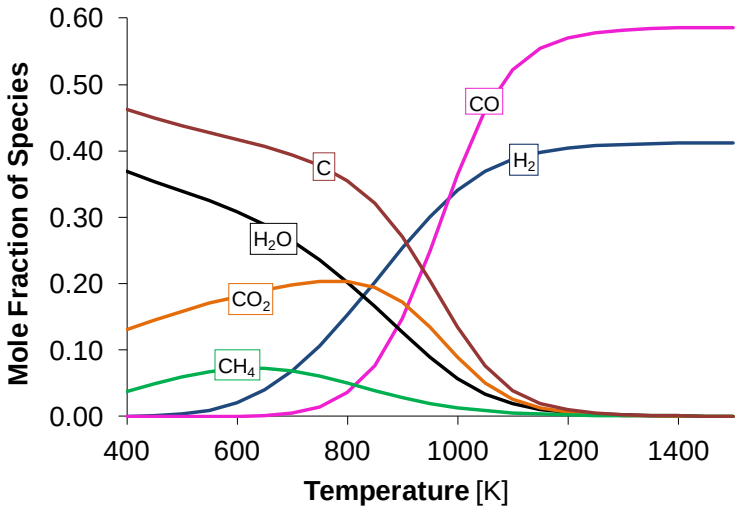

Fig. 6.1 Equilibrium product distribution for stoichiometric CO_2 gasification of cellulose.

6.1 Reactor and Facility

The prototype reactor is shown in Fig. 6.2, which presents an isometric cross-section view. The reactor consists of a central cylindrical cavity receiver 15cm long and 10cm in

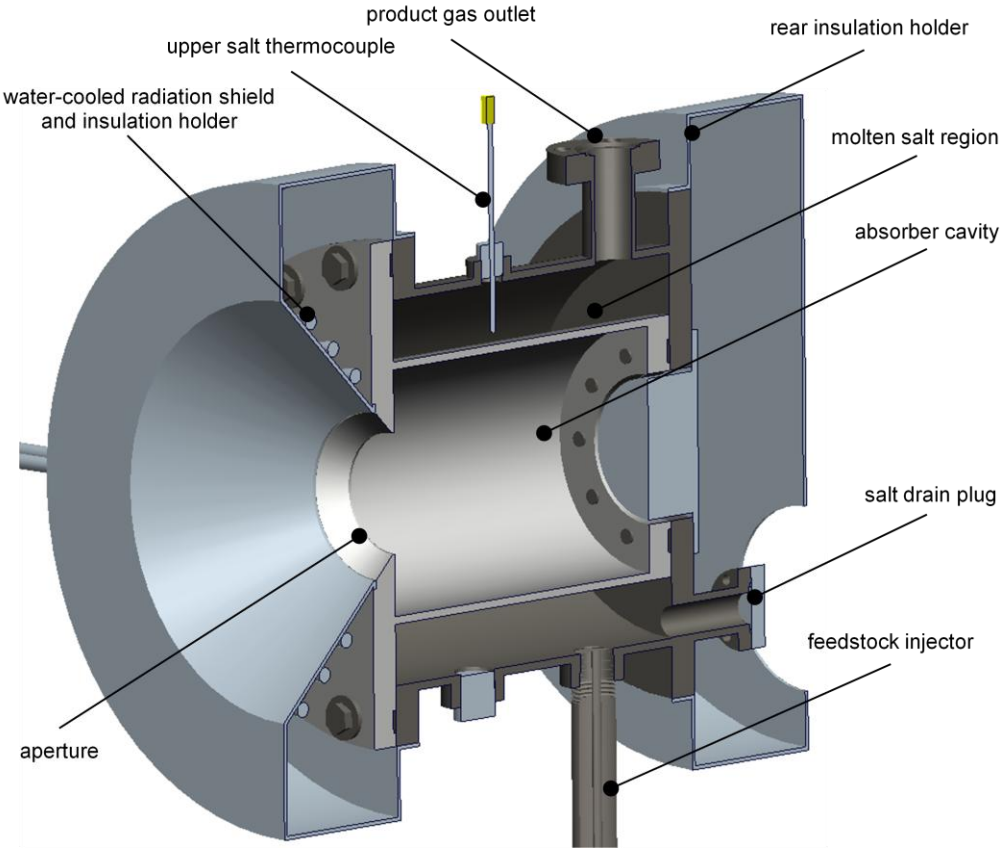

Fig. 6.2 Isometric side-cutaway view of the prototype gasification reactor. Insulation material placed within these shields and around the midsection of the reactor core is not shown. Concentrated radiation enters from the left into the absorber (center cylinder).

diameter with an aperture of 5cm diameter located at one end and a removable end cap closing the other end. The end cap is not exposed to molten salt directly, and so was given a surface coating of optically reflective alumina to reduce absorption of radiation. The cavity is surrounded by a molten salt region bounded by the outer housing with a 15.9cm diameter and 15.6cm length and filled with 2.6 kg of a ternary eutectic alkali metal carbonate salt. All reactor components in contact with the salt were manufactured from Inconel alloy X-750, due to the demonstrated corrosion resistance of Inconel to alkali carbonate salts, and due to the superior high temperature strength of alloy X-750. The front of the reactor is protected from concentrated radiation that arrives outside of the aperture with a water-cooled stainless steel radiation shield. Refractory ceramic insulation (Fiberfrax Durablanket) is placed within this shield and a similar rear insulation holder as well as around the reactor midsection with a typical thickness of 8cm.

Feedstock is delivered to the bottom of the salt region by entraining the feed particles in a flow of N_2 and CO_2. The feedstock and CO_2 react in the salt region producing a product gas that rises out of the salt and exits the reactor through the product gas outlet at the top of the housing. The rear salt drain port is used to remove molten salt following operation.

The temperature of the cavity wall is monitored by two thermocouples placed horizontally through the salt region in the reactor midplane until they contact the cavity wall (not pictured). The thermocouple sheaths pass through the salt and this may lead to a conduction error if the salt and wall temperatures are different. These thermocouples may be viewed as fins attached to the cavity with a reduced base temperature due to this conduction. For an extreme case of a bulk fluid temperature 50 K cooler than the cavity temperature and convection with $h = 1000 \frac{\mathrm{W}}{\mathrm{m^2 - K}}$ around the body of the probe, the junction temperature would be 5 K lower than the wall temperature. The temperature of the salt is monitored with two horizontally orientated thermocouples placed in the middle of the salt region between the cavity wall and housing wall (not shown) as well as a vertical thermocouple placed through the top of the reactor housing with its junction located 1cm above the cavity wall. Additional thermocouples monitor the temperature of the rear of the cavity, the reactor housing, the insulation shield, and the body of the feedstock injector by direct welding of the junction to the surface of interest. All thermocouples are Chromel-Alumel (Type K) with a reported accuracy of ±9 K.

Further details of the facility and instrumentation are illustrated in the diagram of Fig. 6.3, which depicts the upstream and downstream equipment, the path of the feed and product gases, the solar simulator placement, and in the inset portion, detailed placement of the thermocouples including those not shown in Fig. 6.2. The injection and reactant gases are metered by MKS 1179 series mass flow controllers with calibrated accuracy of ±1% and the pressure of the injector gas line is monitored by a pressure transducer with an accuracy of ±1.5 kPa. The injector is supplied with feedstock from a hopper with a 2 kg capacity via a variable speed motor driven feed screw that joins the bottom of the hopper and is designed to obtain feedstock delivery rates up to 22 g/min with a calibrated accuracy of ±2% of the feed rate. The injection gases entrain the feedstock at the end of the feed screw and deliver it to the reactor. The injector body is cooled by two impinging

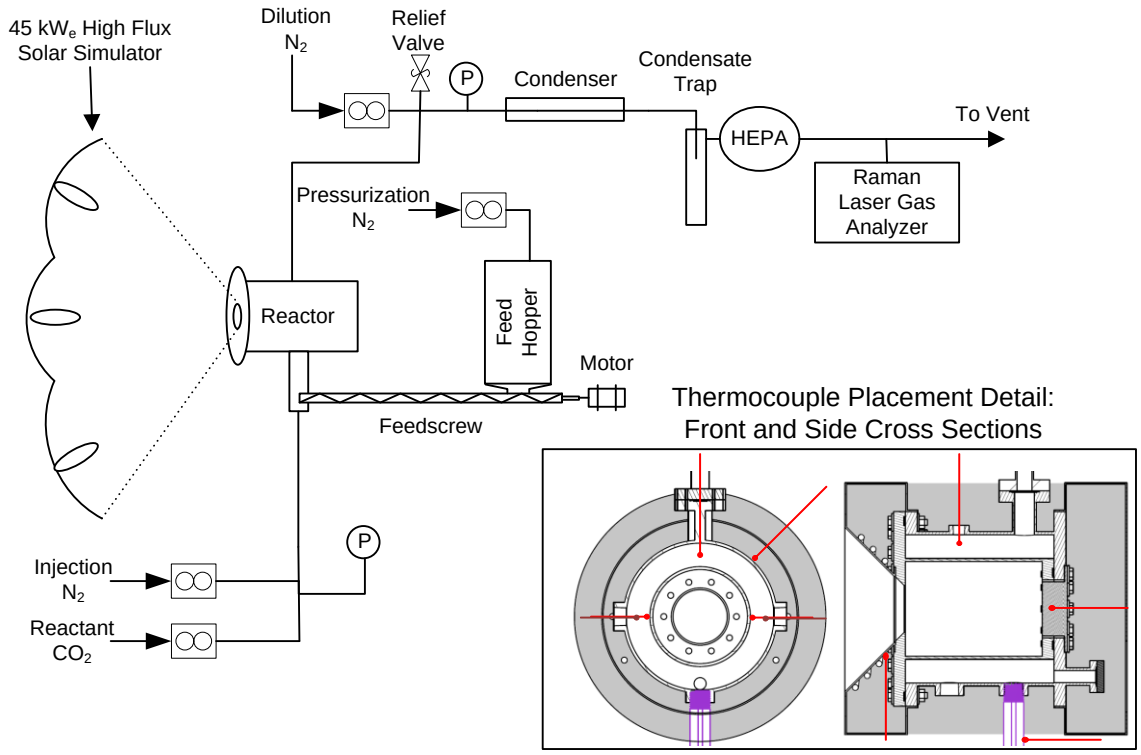

Fig. 6.3 Flow diagram of the reactor and testing facility indicating radiation delivery, gas flows, the feedstock delivery system, and placement sensors throughout the setup. Thermocouple placement internal to the reactor is shown in the detail inset (lower right).

air jets where the feed screw enters to maintain a temperature of no more than 400 K to prevent premature pyrolysis of the feedstock material. The hopper is pressurized with a 100 SCCM flow of N_2 to maintain the hopper at a higher pressure than the injector by ≥5 kPa to eliminate backflow through the feed screw.

After product gases exit the reactor, they are diluted with a flow of N_2 to minimize secondary reactions outside the reactor and to reduce the residence time between the reactor and gas analysis equipment. A 35 kPa(g) relief valve is connected to the outlet passage to prevent pressurization of the reactor and a pressure transducer of ±1.5 kPa accuracy monitors the pressure in the outlet tube during operation. The diluted product gases move though a water cooled condenser which lowers the gas temperature to <300 K. This temperature ensures any water vapor or tars that may be present are condensed to be collected in the condensate trap or HEPA filter along with any entrained solids that may be present. The clean product gas is supplied to an ARI RLGA-8800 series Raman

laser gas analyzer to determine volume fractions of N_2, CO, CO_2, H_2, and CH_4 with an absolute accuracy of ±0.25% for each gas except CH_4 which is accurate to ±0.06%.

Concentrated radiation is delivered to the reactor using the University of Minnesota 45 kW_e High Flux Solar Simulator (HFSS). The HFSS consists of a series of 7 xenon arc lamps placed within truncated-ellipsoidal reflectors that direct the radiation to a common focal point. The reactor is positioned so this focal point is centered within the reactor aperture for testing. Prior to reactor operation, the simulator power output was measured by taking CCD images of the radiation reflected from a Lambertian target using the desired HFSS lamp configurations and converting the image intensities into flux using a calibration method established by Brack et al. [88] and the calibration constant established for our specific setup by Krueger et al. [71, 89]. Due to previous issues with reactor surfaces overheating, the lamps were de-focused by moving their arc out of the focal point by 2.5 mm (away from the reflectors). For our reactor aperture of 5±0.002 cm, the average flux within the aperture was measured in this lamp configuration as 1132±144 suns for three lamps, resulting in delivered power of 2.22±0.28 kW_{th} during final heating and operation. Though not directly measured, a fair approximation of the flux and power during initial heating with 2 lamps can be made as 755 suns and 1.47 kW_{th}. Further details on the flux measurement are found in Appendix B and on uncertainty calculations in Appendix D.

The salt was composed of a ternary eutectic blend of Na_2CO_3, K_2CO_3, and Li_2CO_3 with physical properties as listed in Table 6.1. The feedstock material was ash-free cellulose sieved to a particle diameter range of 0.3mm to 0.5mm. The cellulose material was tested and verified to be ash-free with a chemical composition corresponding to the ideal formula $C_6H_{10}O_5$. The feedstock was dried at 380 K under vacuum until mass remained steady. All gases were reagent grade with purity of greater than 99.9%.

Table 6.1 Properties of ternary eutectic alkali carbonate salt at 1200 K.

Composition [%wt]	32% Li2CO3, 33% Na_2CO_3, 35% K_2CO_3
Thermal Conductivity	0.75 W/m-K
Specific Heat Capacity	1842 J/kg-K
Melting Point	670 K
Density	1680 kg/m^3

6.2 Data Analysis

During feedstock delivery, the composition of the product gas stream is obtained directly from the RLGA in terms of a volume or mole fraction of each species, y_{i}. Knowing the total flow rate of nitrogen supplied to the reactor assembly, individual gas production rates may be calculated.

$$\dot{V}_i = \dot{V}_{\mathrm{N_2}} \cdot \frac{y_i}{y_{\mathrm{N_2}}} \tag{6.2}$$

For CO_2, the reported flow rate is the net flow after subtracting off the flow rate of unreacted CO_2 being delivered to the reactor. The specific yield of useful synthesis gas is a measure of how complete the cellulose gasification reaction is based on the obtained standard flow rates and known density of the product gases at standard conditions (101.3 kPa and 273.15 K). For the stoichiometric gasification of one mole of cellulose ($C_6H_{10}O_5$) with one mole of CO_2, the ideal specific yield is 1.27.

$$S_Y = \frac{\dot{m}_{\mathrm{gas}}}{\dot{m}_{\mathrm{feed}}} = \frac{\sum_i \dot{V}_i \rho_i}{\dot{m}_{\mathrm{feed}}} \text{ for } i = \mathrm{CO}, \mathrm{H_2}, \mathrm{CH_4} \tag{6.3}$$

Given the measurement uncertainty of the gas composition, nitrogen flow rate, and feedstock delivery rate, the specific yield may be calculated with a relative accuracy of ±2.3%, primarily due to the feedstock delivery rate uncertainty. The instantaneous solar efficiency is based on the energetic yield of product gas and the supplied solar power and feedstock energy supply rate, calculated according to

$$\eta_{\mathrm{solar}} = \frac{\sum_{\mathrm{i}} \dot{m}_i \cdot \mathrm{LHV}_i}{\dot{Q}_{\mathrm{solar}} + \dot{m}_{\mathrm{feed}} \cdot \mathrm{LHV}_{\mathrm{feed}}} \tag{6.4}$$

For the solar efficiency, the uncertainty in the solar input dominates, allowing us to report the solar efficiency with a relative accuracy of ±7.2%. The cold gas efficiency is a measure of the energetic upgrade of the feedstock to synthesis gas, and is equal to the ratio of chemical energy of the product gas to the chemical energy of the feedstock as measured by LHV, with a relative accuracy of ±2% the calculated value primarily due to feed delivery rate uncertainty.

$$\eta_{\mathrm{CG}} = \frac{\sum_{\mathrm{i}} \dot{m}_i \cdot \mathrm{LHV}_i}{\dot{m}_{\mathrm{feed}} \cdot \mathrm{LHV}_{\mathrm{feed}}} \tag{6.5}$$

6.3 Procedure

Testing began by heating the reactor using electric tape heaters to achieve a temperature above the melting point of the salt, 670 K, and then adding the crushed salt to the sealed reactor until filled with 2.6 kg of salt, resulting in an estimated total heat capacity of 13.3 kJ/K. After salt addition, the reactor outlet was connected to the outlet tube configured as shown in the flow diagram of Fig. 6.3 and the HFSS was activated. Heating continued initially at 1.47 kW_{th} incident power until the salt temperature indicated 1025 K, at which point the HFSS power was increased to 2.22 kW_{th} for the remainder of the run. The tape heater was turned off once the salt temperature indicated 1125 K, leaving the reactor to be heated only via the HFSS. Once the average salt temperature indicated 1150 K, the feedstock delivery system was turned on and feed was delivered for 3.5 minutes. Feeding was initiated before achieving 1200 K in order to avoid overshooting the target operating temperature, however excess char and tar was produced, clogging the downstream filters and causing a pressure rise that resulted in a reduction in the feed injection system gas flows and clogging of the injector with cellulose after the 3.5 minutes of operation. Following operation of the feed system, the reactor was heated further to the target temperature of 1200 K to verify structural integrity, after which the HFSS was turned off and the reactor was allowed to cool. Salt was drained at 100 K above freezing and solidified on a water-cooled stainless steel pan. A summary of the testing conditions and flow rates is given in Table 6.2.

Table 6.2 Testing conditions during feedstock delivery for the initial characterization of the prototype gasification reactor.

Parameter	Value
Average Flux at Aperture	1132±144 kW/m^2
Incident Power	2.22±0.28 kW
Average Salt Temperature	1150±10 K
Feedstock Delivery Rate	6.9±0.1 g/min
Injection N_2 Flow	3.6±0.04 SLPM
Reactant CO_2 Flow	2±0.02 SLPM
Dilution N_2 Flow	2±0.02 SLPM
Hopper N_2 Flow	100±1 SCCM

6.4 Results

The time history of the testing of the reactor prototype is given in Fig. 6.4 which

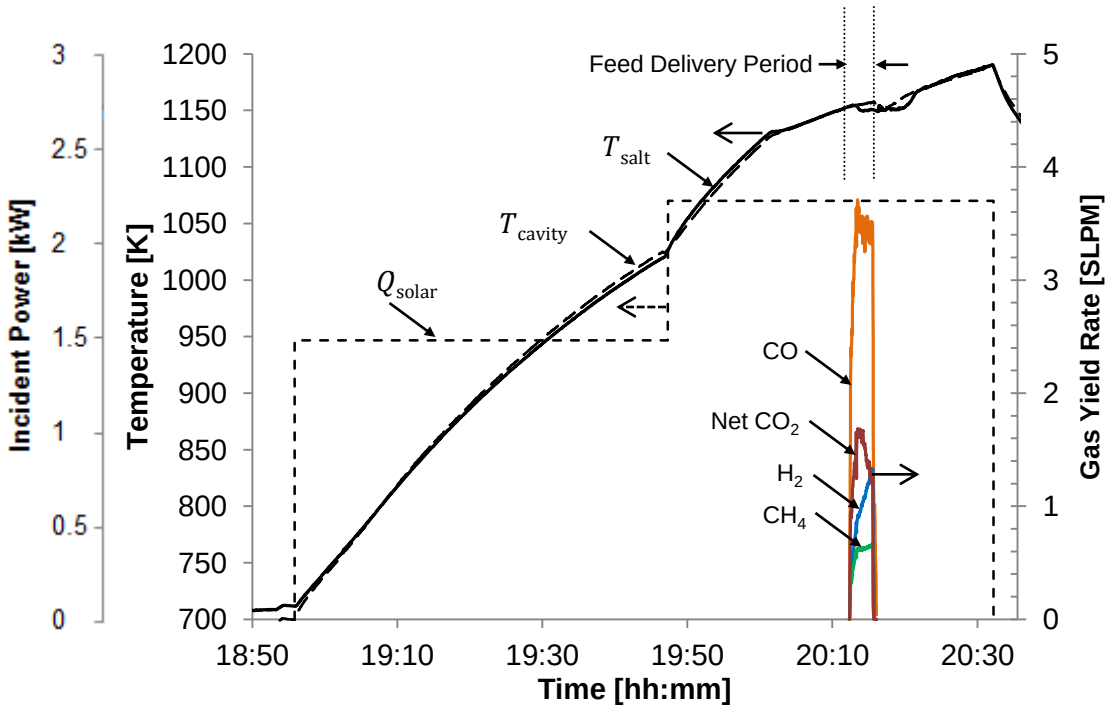

Fig. 6.4 Time history of incident power, average cavity temperature, average salt temperature, and production rates of CO, H_2, CH_4, and CO_2 from the solar gasification reactor test.

displays the incident power, average temperatures of the cavity and the salt, and the product gas yield rates during feedstock delivery. Initial heating at the lower power setting of 1.47 kW_{th} required about 50 minutes, followed by another 25 minutes at 2.22 kW_{th} before the initial feedstock delivery temperature was achieved. The change in slope of the temperature curves during the high-power heating indicates when the tape heaters were turned off. The cavity and salt temperatures remained within 20 K of each other at all times with an average difference of 7 K, indicating strong convective heat transfer between the salt and the cavity wall. Using the previously mentioned estimate of conduction error associated with the wall temperature measurement, the actual cavity wall temperature may be 5 K higher than indicated, or 12 K above the measured salt temperature. Given the ±9K accuracy of the thermocouples the maximum estimated difference between wall and bath temperature is 21 K, indicating strong heat transfer from the salt to the cavity wall.

Upon activation of the feedstock delivery system, a CO rich product gas was quickly generated with a total production rate reaching a maximum of 6.8±0.1 SLPM. For

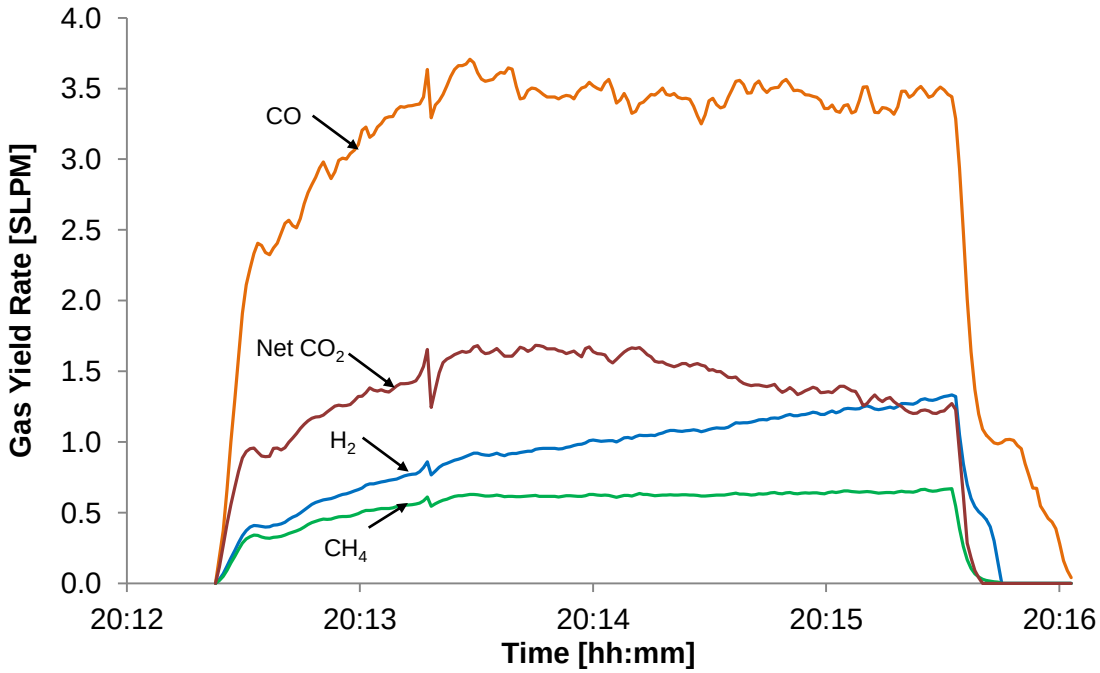

Fig. 6.5 Time history of product gas yield rates. The time range is limited to the period during feedstock delivery.

improved readability, the product gas yield rates during the period of feedstock delivery are shown in Fig. 6.5. After an initial transient lasting roughly one minute after feed delivery was initiated, the yield rates of the gases become fairly steady except for hydrogen, which slowly increases in yield rate during this period. The CH_4 production is a result of the initial pyrolysis reactions, and the steady rate of CH_4 production over the time period of interest indicates a corresponding steady flow of feedstock into the system.

The average measured product gas composition is given in Table 6.3 along with the equilibrium predicted concentrations. A total product gas yield of 18.5±0.4 standard liters was obtained. The product gas is primarily CO, as expected for CO_2 gasification, with significant CO_2 and CH_4. The increased CO_2 production may be due to the lowered operating temperature of 1150 K resulting in increased CO_2 at equilibrium, slowed char gasification kinetics, and production of pyrolytic water that may have reacted with the salt, releasing CO_2 through the reaction of eq. (2.1). The concentration of CH_4 is due to the pyrolysis products exiting the reactor before equilibrium could be established through cracking reactions, which are relatively slow in general due to the chemical stability of CH_4 once it is formed.

Table 6.3 Product gas composition during CO_2 gasification of cellulose at 1150 K. The equilibrium predicted composition at these conditions is included.

Component	Measured Fraction (% vol)	Equilibrium Fraction (% vol)
CO	52±0.5%	56%
CO_2	22±0.8%	1.3%
H_2	16±0.3%	41%
H_2O	N/A	1.1%
CH_4	9±0.06%	0.4%

Downstream of the reactor, the condenser, condensate trap, and filters capture carbonaceous solids equal to roughly 7±0.1% of the mass of delivered feedstock, similar to what would be expected for pyrolysis of cellulose, given the chemical formula of $C_6H_{10}O_5$ and assuming all oxygen is formed into CO leaving 1 mole of carbon per mole of feed. Based on this amount of char, it appears that most of the char was swept from the reactor before significant CO_2 gasification could take place. Based on catalyzed gasification kinetics, a residence time of 5 minutes is required for complete conversion of the produced char. If the char is wetted by the salt, it will remain in the reactor for the required time, however if entrained by the gas flows and not wetted, the particles exit at the gaseous residence time of only 3.8 seconds, far from sufficient to allow complete conversion of the char. The carbonaceous residue obtained downstream of the reactor had a strong organic scent similar to naphtha, indicating that the residue contained tars along with char, with significant hydrogenation. Treating the residue as naptha with a chemical formula C_6H_6, the residue contains 7.7% hydrogen by mass. If the hydrogen embodied by the residue and CH_4 measured were instead converted to H_2 gas, it would measure 3.84±0.12 standard liters and would bring the volume fraction of H_2 up to 39%, much closer to the equilibrium predicted 41%.

The performance parameters described in the data analysis section are calculated based on the average gas yields during the feedstock delivery period. The specific useful (including CO, H_2 and CH_4) yield of synthesis gas under these conditions is 70.3±1.7% of the feedstock mass delivery rate, with the remaining difference making up the CO_2 and char residue obtained. The resulting solar efficiency is $\eta_{\text{solar}} = 31.9 \pm 2.3\%$ while the cold-gas efficiency is $\eta_{\text{CG}} = 70.5 \pm 1.7\%$.

Improvements in yield and efficiency may be obtained through several operational changes. Firstly, operation at a higher incident flux of 1530 suns resulting in 3 kW_{th} at the aperture will reduce the relative magnitude of thermal emission losses. Secondly, operation at 1200 K instead of 1150 K will favor both improved thermodynamics and reaction kinetics. This temperature increase should reduce the production of carbon dioxide during pyrolysis as evidenced by previous pyrolysis experiments, as well as accelerate char gasification, reducing the production of downstream residues. Methane production may be slightly reduced at higher temperatures, but prior work has shown pyrolysis-based methane production to be nearly invariant with temperature in the range 1050 K – 1250 K [70]. Third, operation with steam or a blend of steam and carbon dioxide instead of only carbon dioxide as reactant, while adding operational challenges, generally favors much faster gasification kinetics and an improved chance of converting pyrolytic char before it can leave the reactor. Lastly, it may be necessary to include baffles or other surfaces within the reactor to reduce the entrainment of char in the exiting gases, allowing for longer solids residence times in the reactor and therefore improved conversion of the char/tar residues. Changes that prevent the release of unreacted materials into downstream filters would also prevent the filter-clogging issues that led to the pressure rise and feed-system blockage responsible for the short runtime of only 3.5 mintues during this initial test. With these changes we can expect solar efficiencies closer to 50±7% and cold-gas efficiencies of 122±3% for steam-cellulose gasification.

With regards to the structural performance of the reactor, no sign of localized melting or distortion due to hot-spots was observed on the cavity absorber after disassembly and inspection following the initial tests. None of the fasteners failed and their lengths indicated no creep or plastic yielding had occurred during the test. It was discovered post-operation that the reactor was leaking salt where the cavity and housing surfaces mated due to permeability of the zirconia felt gasket material that had been purchased based on suggestions that the material would not be wetted by the carbonate salt. This leakage saturated regions of the insulation on the bottom of the reactor, leading to a loss in insulating behavior and a thermal short-circuit to the ambient environment that contributed to the reduced solar efficiency. A switch to deformable copper ring gaskets is planned for future work to help eliminate this leakage and minimize thermal losses.

6.5 Conclusion

This initial test has demonstrated the functionality of the reactor and feed delivery system and verified the ability of the reactor to absorb concentrated light. De-focusing to protect the reactor materials resulted in this shakedown test taking place at a reduced power of 2.22±0.25 kW_{th}, and clogging of the downstream filters with unreacted material resulted in a short operation time of only 3.5 minutes and a peak temperature of 1150 K during feeding. The data obtained allowed the calculation of initial baseline values of the performance parameters of product gas composition, specific gas yield, and solar efficiency, and cold gas efficiency. Issues encountered during this test have been analyzed leading to refinement in the operation guidelines for futures tests with the goal to improve yield and selectivity of products while avoiding thermal losses and salt leakage. These guidelines include re-focusing of the simulator lamps to boost flux concentration, the use of steam or a CO_2/steam blend as reactant gas, delaying feedstock delivery until the salt temperature reaches 1200 K, use of baffles or other flow-obstructions to ensure the solid char is wetted by the molten salt, and replacement of ceramic felt gaskets material with copper to prevent salt leakage.

7 Scaled-up reactor performance estimate

This chapter takes a broader look at how the developed reactor might be used in a commercial process. The analysis addresses the ability of a solar gasification facility to supply a downstream fuel or power production process by considering the impact of either thermal storage or hybridization on the performance of the solar gasification facility. Performance is measured in terms of annual averaged factors such as the thermal efficiency or solar fraction as well as instantaneous measures of synthesis gas production.

Chemical synthesis plants for fuel production include numerous reactors and process streams and generally are designed about a single nominal operating point. These processes take significant periods of time to achieve steady state operation and can handle little variation in throughput before product quality is compromised. For power production, a gas turbine engine or combined-cycle generation allows some flexibility in output, but generally performance is optimized about a single preferred operating point, and deviation from that point leads to a reduction in generation efficiency as well as increased production of pollutants such as NO_x. Either of these processes is best paired with a steady supply of synthesis gas.

Direct utilization of intermittent solar energy to drive endothermic gasification reactions would result in a correspondingly intermittent syngas stream unsuitable for most downstream applications. Two approaches for smoothing the output of solar thermal processes are thermal storage and hybridization, minimizing or eliminating the need for on-site storage of syngas as a buffer to downstream processes. With sufficient thermal storage, operation can continue throughout the night and even continuously over the course of a year; however the required storage capacity, and correspondingly the capital cost of the solar facility, increases as the period desired for steady operation increases. Additionally, compared to direct utilization of the thermal energy, thermal storage allows more time for heat loss to the ambient, and therefore the thermal efficiency of a solar facility incorporating thermal storage will be inherently lower than that without. Hybridization supplies thermal energy from a secondary source to assist the solar thermal input. For a solar gasification process, hybridization would most likely occur with either partial combustion of feedstock within the reactor, or post-combustion of the synthesis gas product. The specific yield of syngas as well as the overall thermal

efficiency will be reduced as the degree of hybridization is increased. In summary both options offer means to reduce the intermittence of fuel production at the expense of reduced specific fuel yield, defined in this paper as the energy content of the product gas, on a LHV basis, per hectare of land used to grow the feedstock (annual yield of 6,000 kg/hectare [3]). The extent to which storage or hybridization should be implemented depends on the degree of variation that a downstream process can accommodate and the variation in solar input.

Previous studies of hybridized solar processes have demonstrated both the potential benefits as well as the need for more detailed performance analyses including the effect of varying the amount of storage or degree of hybridization. In an examination of adding solar thermal input to a combined cycle power plant, Kribus et al. found that hybridization through heat addition in the bottoming cycle can reduce the lifecycle cost of electricity by 50% compared to a solar-only facility [90]. Considering the end goal of fuel production, Sudiro and Bertucco determined that hybridizing a traditional coal to liquids (CTL) or gas to liquids (GTL) process with solar input at the gasification/reforming step can boost the annual thermal efficiency of the process by 67% [91]. A study that examined a hybrid solar coal gasification facility close coupled to a Fischer Tropsch plant considered the use of compressed storage of excess syngas to handle output variations. This configuration benefited from a 21% increase in the energy content per unit coal consumed; however, the storage method required that about 50% of the parasitic work of the solar gasification facility went into compression and storage of the gases [92, 93]. A review of research on hybrid solar-fossil fuel power systems found that many of the studies have only considered a single design point time and day when developing process metrics, and that any performance analysis of a solar hybridized process must take into account the variations in solar resource over the course of an entire year to maximize the value of the results [94].

We explore the impacts of both thermal storage and hybridization on the performance of a 100 MW_{th} solar steam gasification facility in an annual process simulation using typical meteorological year (TMY) solar data to assess how both hybridization and storage impact a biomass-hybridized solar process with the goal of fuel or power

production. Thermal storage is provided by molten carbonate salts within the receiver/reactor.

Hybridization allows for combustion of synthesis gas for assisted process heat when solar energy is insufficient to maintain continuous operation. The operation of a solar gasification facility of 100 MW_{th} nominal solar power is explored by parametric variation of the mass of salt, m_{salt}, and thus the thermal storage capacity, C_{eff}, and the minimum nominal syngas yield rate, $\dot{m}_{\mathrm{nom,sg}}$. Solar gasification facility performance is quantified by the annual solar fraction, f_{solar} (indicating degree of hybridization), the specific yield, the annual average thermal efficiency, $\overline{\eta_{\mathrm{th}}}$, and the maximum over-rate ratio, OR (indicating the magnitude of variation in the synthesis gas yield rate). The results guide discussion of feasibility of the solar facility to drive downstream processes within the range of parameters evaluated.

7.1 Reactor Concept

For the purpose of exploring the impact of storage and hybridization on performance, it is not necessary to assume a specific reactor concept; however the mathematical model requires some basic design assumptions. One concept which is under development by the authors is an indirect receiver/reactor comprised of concentric cylinders as depicted in Fig. 5.2.

The details of this design of solar gasification reactor are discussed in the previous chapters, so only the key paramaters used for defining the geometry for the scaled-up reactor are covered here. The cavity geometry is described by the geometric ratios $D = \frac{d_{\mathrm{c}}}{d_{\mathrm{a}}}$ and $L = \frac{l}{d_{\mathrm{c}}}$, which for this analysis are $D = 2$ and $L = 1.5$. The absorption efficiency and the flux distribution in a right cylindrical cavity depend on the flux concentration at the aperture, the wall temperature, and dimensionless ratios of L and D, therefore the selection of these values are independent of the reactor scale. The aperture size is selected to achieve a desired nominal solar power rating according to the relation $\dot{Q}_{\mathrm{solar,nom}} = C \cdot I \cdot \pi \frac{d_a^2}{4}$. The volume of stored salt is varied by changing the annulus diameter ratio, $DA = \frac{d_{\mathrm{o}}}{d_{\mathrm{c}}}$. The reactor concept can be used either in a horizontal orientation for tower-top operation, or in a vertical orientation for a beam-down optical

system. The general geometry described captures the relative scaling of surface area, salt thermal storage volume, and cavity size for the thermal model used in the scale-up analysis.

Several assumptions about the reactor and its performance are made to allow the process to be modeled.

1. The molten salt storage is well-mixed with sufficiently high convection heat transfer between the molten salt and cavity walls to allow for a lumped capacitance thermal model.
2. The pyrolysis and gasification of the feedstock progresses to the complete thermodynamic equilibrium product distribution predicted for the reactor operating temperature and pressure. This assumption is justified by prior work which shows that the kinetics are rapid and, for the salt volumes considered, the biomass particles are completely gasified as they move through the salt. [25, 70].
3. The thermal storage media is a ternary eutectic blend of alkali metal carbonate salts while the reactor is assumed to be manufactured from Inconel, a nickel superalloy with noted resistance to corrosion from the molten carbonate salts [46].
4. The aperture can be blocked when there is insufficient insolation to allow net positive absorption (i.e. more radiation is leaving the cavity than is incident from the heliostat field) to minimize losses from the hot cavity walls until there is sufficient incident radiation to allow for positive net absorption.
5. Hybridization is achieved by combustion of a portion of the synthesis gas in a heater system integral to the reactor. The combustion products are assumed to exit the heater system at the reactor temperature of 1200 K resulting in a combustion efficiency of $\eta_{\mathrm{comb}} = 85\%$ based on the lower heating value (LHV) of syngas.
6. Ash content is assumed to affect neither the gasification reactions nor the reactor energy balance. This assumption is justified given a salt cleanup process similar to that utilized by the Rockgas process is included to

remove ash from the reactor with minimal thermal impact to the system [39].

In a realistic receiver/reactor, the temperature gradients from the cavity to the salt would result in increased thermal emission from the cavity and therefore a reduced absorption efficiency compared to one predicted using lumped capacitance, as discussed by Ben-Zvi et al. [95]. Additionally, a reactor would obtain a product gas composition differing from the ideal equilibrium predictions, resulting in a somewhat lower energetic content synthesis gas stream. These effects do not impact the general trends of output variability with respect to changes in thermal storage and hybridization.

7.2 Scale-up Analysis

The solar facility is configured for a baseline nominal solar power of 100 MW_{th}, requiring an aperture of 8 m diameter for a flux concentration at the reactor aperture of 2000 suns and a field collection efficiency of $\eta_f = 60\%$. This optical arrangement is simulated as a tower and heliostat field with a compound parabolic concentrator (CPC) of acceptance angle θ_c= 35° in place at the reactor aperture as described in a recent article on considerations for the design of solar-thermal chemical processes [96]. The field collection efficiency is fixed at the above value, which was obtained for day 82, solar hour 10 for a latitude 30° N, representing an average time and date for estimating optical performance throughout the year.

The simulated solar facility is located near Phoenix, Arizona, USA which offers beam radiation with measured peaks in excess of 1000 W/m^2, average cloud coverage of less than 20% through the year [97] and abundant biomass. More than 500,000 tons of biomass is available annually in Maricopa county [98]. The solar facility performance is simulated based on hourly data from the TMY3 data set recorded at Phoenix Sky Harbor International Airport weather station [99]. The data include direct normal insolation (a measurement of beam radiation), temperature, dew point, and wind speed.

Due to the large salt mass considered for some cases, a beam-down arrangement, where a secondary reflector directs the radiation from the tower top to the reactor/receiver located near the ground, is the most practical. The beam-down

secondary optics perform with an optical efficiency of $\eta_{\mathrm{bd}} = 93\%$ [100] resulting in an overall collection efficiency

$$\eta_{\mathrm{coll}} = \eta_{\mathrm{f}} \cdot \eta_{\mathrm{bd}} = 56\% \tag{7.1}$$

For a nominal 100 MW_{th} field, the required heliostat area is thus $A_{\mathrm{coll}} = 180{,}700\ \mathrm{m}^2$.

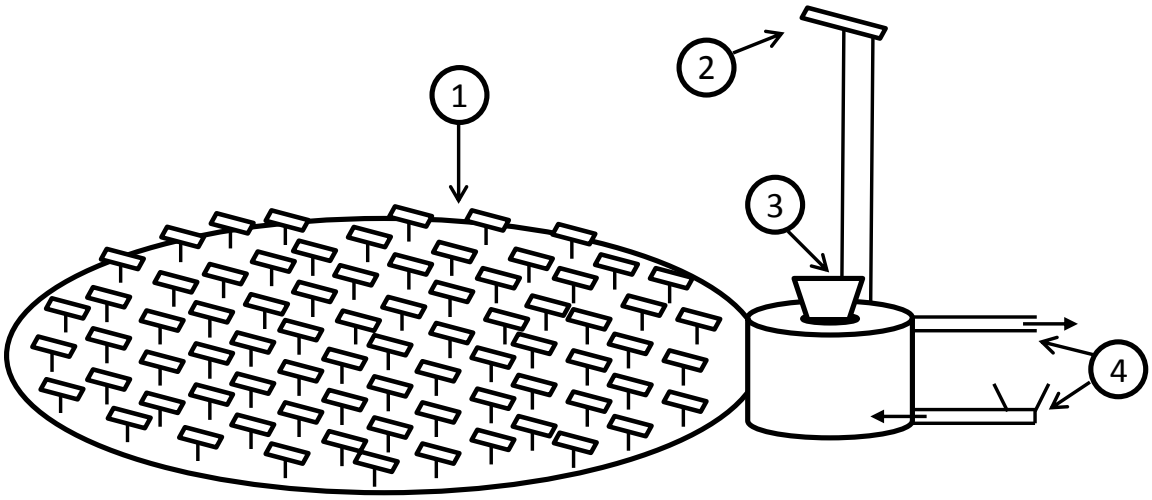

Fig. 7.1 Simplified diagram of a solar gasification facility. (1) Heliostat field (2) Beam-down tower (3) Receiver / reactor (4) Feedstock inlet to reactor and syngas outlet to downstream process.

The model solar gasification facility used to demonstrate the operation at 100 MW_{th} scale is shown in a simple diagram in Fig. 7.1 and as a process flow schematic in Fig. 7.2. The system includes a heliostat field with beam down optics, a cavity receiver with CPC, a reactor with integrated molten salt storage, a process to remove settled ash from the salt, and a syngas-fueled combustion system for assisted heating. Direct normal solar radiation incident on the field, $\dot{I}_{\mathrm{dn}}$ is concentrated and delivered to the receiver at the rate $\dot{Q}_{\mathrm{solar}}$. The cavity receiver reflects a portion of the incident power in addition to the re-radiation due to its elevated temperature at the rate $\dot{Q}_{\mathrm{reread}}$, where the receiver is assumed to be immersed within and thus in equilibrium with the molten salt at T_{rctr}. The reactor loses energy to the ambient environment from its exterior at T_{ext} with convection occurring to the air at T_{∞} and radiation to the sky at T_{sky} at the total rate of $\dot{Q}_{\mathrm{loss}}$.

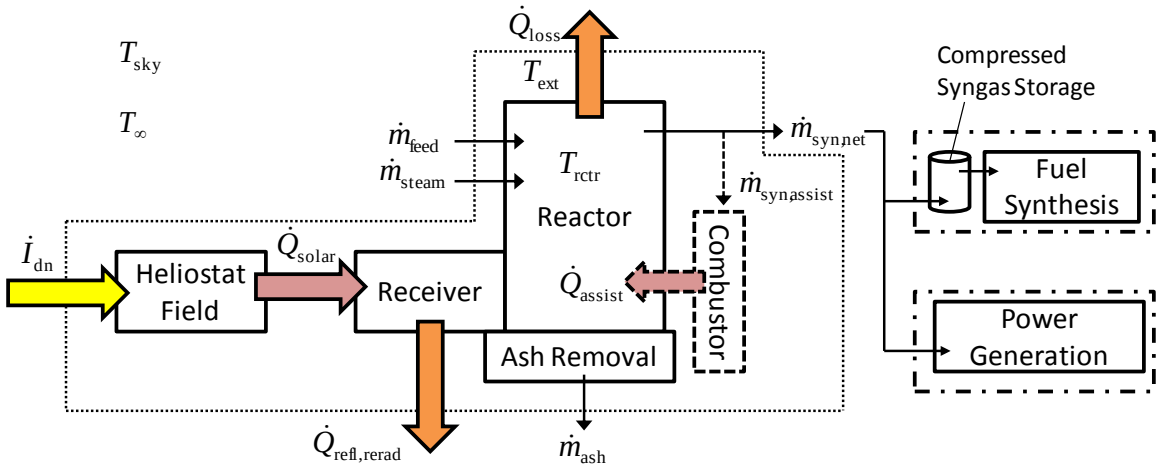

Fig. 7.2 System schematic for the modeled concentrating solar gasification facility. The boundaries of the analysis are represented by the dotted lines. The components and flows with dashed lines are used to assist the solar-driven gasification process when insufficient sunlight is available. Potential downstream processes are shown in the dash-dotted lines at the right.

Feedstock is delivered into the molten salt at the rate $\dot{m}_{\mathrm{feed}}$ along with a stoichiometric amount of steam, $\dot{m}_{\mathrm{steam}}$, producing a product stream of CO and H_2 (synthesis gas) and byproduct ash. All feedstock masses and mass flow rates are reported on a dry, ash-free (DAF) basis. If assisted heating is required, a portion of the synthesis gas produced, $\dot{m}_{\mathrm{assist,sg}}$ is directed to a combustion system to supply heat at the rate $\dot{Q}_{\mathrm{assist}}$. The remaining net stream of synthesis gas leaves the facility at the rate $\dot{m}_{\mathrm{net,sg}}$.

The simulated facility is operated based on the logic of producing a minimum nominal amount of synthesis gas at all times, with increases in syngas production occurring only when the reactor temperature exceeds 1225 K. When the reactor temperature exceeds this value, the feed rate is increased so that the endothermic gasification reactions consume the net energy absorbed, halting heating and maintaining the temperature at this maximum value. When solar radiation is insufficient to maintain the minimum operating temperature of 1200 K, assisted heating from the combustion of synthesis gas is utilized. The combustion products are assumed to exit the heater system at the reactor temperature of 1200K resulting in a combustion efficiency of $\eta_{\mathrm{comb}} = 85\%$ based on the lower heating value (LHV) of syngas. While assisted heating is in use, the feedstock delivery rate is increased to maintain the nominal net syngas production rate at the specified value.

The feedstock in these simulations is a 32 species mixed perennial blend, with properties representative of other region-specific low-input high diversity biomass blends [3]. The blend of species represents high-diversity biomasses that would be available in most regions (the blends will certainly be region-specific, however.) The ultimate and proximate analyses are described in [101]. The pertinent properties for this analysis are the molar ratios of hydrogen to carbon, $x = 1.454$ and oxygen to carbon, $y = 0.6486$ for feedstock with a chemical formula of the form CH_xO_y. For this composition, the stoichiometric steam to biomass mass ratio is $\phi = 0.2654$ and the LHV of the feed is $18.7\ \mathrm{MJ/kg}$, both on a DAF basis. Complete gasification of the feed results in a synthesis gas with a H_2/CO ratio of 1.08 and a LHV of $18\ \mathrm{MJ/kg}$.

The design of the facility is parameterized by two variables: (1) the nominal syngas production rate and (2) the mass of salt within the reactor. For a fixed facility solar power rating, increasing the nominal rate of syngas output (beyond the rate possible from a system utilizing solar input alone) allows for a more uniform gas production rate at the expense of a less efficient conversion of feedstock to synthesis gas due to increased assisted heating, and therefore a lower solar fraction, f_{solar}. Increasing the salt mass and thus the reactor heat capacity, C_{eff}, results in a more uniform gas production rate by smoothing the solar input, but comes at the expense of a larger and more costly facility. We explore the magnitude of these effects by simulating the performance of facilities over a range of effective heat capacities and nominal syngas production rates.

The thermal model of the reactor is based on a lumped thermal capacitance approach, consistent with the assumption that the molten salt is well mixed and in thermal contact with the cavity receiver. The transient energy equation for the reactor is given by

$$C_{\mathrm{eff}}\frac{\mathrm{d}T_{\mathrm{salt}}}{\mathrm{d}t} = \dot{m}_{\mathrm{feed}} \cdot (h_{\mathrm{feed}} + \phi \cdot h_{\mathrm{steam}}) - \dot{m}_{\mathrm{syn}} \cdot h_{\mathrm{syn}} + \dot{Q}_{\mathrm{solar}} + \dot{Q}_{\mathrm{assist}} - \dot{Q}_{\mathrm{rerad}} - \dot{Q}_{\mathrm{loss}} \tag{7.2}$$

The feedstock enters the reactor at ambient conditions, so the feedstock enthalpy is taken to be the standard enthalpy of formation of the feedstock, calculated based on the LHV according to

$$h_{\mathrm{feed}} = \frac{1}{M_{\mathrm{feed}}} \cdot \left(h^0_{\mathrm{f,CO_2}} + \frac{x}{2} h^0_{\mathrm{f,H_2O}} + \mathrm{LHV}_{\mathrm{feed}} \cdot M_{\mathrm{feed}} \right) \tag{7.3}$$

The effective heat capacity of the reactor is based on the estimated mass and specific heat capacity of the reactor structure and the salt within the reactor.

$$C_{\text{eff}} = m_{\text{struct}} \cdot C_{\text{P,i}} + m_{\text{salt}} \cdot C_{\text{P,salt}} \tag{7.4}$$

An estimate of reactor mass is made by assuming the geometry is as described in the Reactor Concept section, with 2.54 cm thick Inconel walls. The annulus diameter ratio is varied in the range $1.020 \leq DA \leq 1.523$ to obtain corresponding effective heat capacities in the range $1\ \text{GJ/K} \leq C_{\text{eff}} \leq 21\ \text{GJ/K}$. The pertinent properties of the carbonate salt blend were given in Chapter 1, Table 4.1.

The incident solar power is calculated based on the collection efficiency, η_{coll}, the direct-normal insolation over the course of each hour found in the TMY3 dataset, I_{dn}, and the area of the heliostat field, A_{coll}.

$$\dot{Q}_{\text{solar}} = \dot{I}_{\text{dn}} \cdot \eta_{\text{coll}} \cdot A_{\text{coll}} \tag{7.5}$$

Where $\dot{I}$ is an average irradiance based on hourly TMY data. When assisted heating is required, the heating power is calculated based on the combustion efficiency for syngas on a LHV basis.

$$\dot{Q}_{\text{assist}} = \eta_{\text{comb}} \cdot \dot{m}_{\text{assist,sg}} \cdot \text{LHV}_{\text{sg}} \tag{7.6}$$

Re-radiation due to thermal emission from the cavity and reflection of the incident solar power is calculated based on the temperature-dependent absorption efficiency of the reactor

$$\dot{Q}_{\text{rerad}} = \dot{Q}_{\text{solar}}(1 - \eta_{\text{abs}}) \tag{7.7}$$

The absorption efficiency is defined as the ratio of energy absorbed by the cavity to the radiation incident at the aperture, the difference being the reflected and emitted radiation leaving the cavity.

$$\eta_{\text{abs}} \equiv \frac{\dot{Q}_{\text{abs}}}{\dot{Q}_{\text{solar}}} = \varepsilon_{\text{eff}} \left(1 - \frac{\sigma T_{\text{salt}}^4}{\dot{I}_{\text{dn}} C}\right) \tag{7.8}$$

In this equation, ε_{eff} is the effective total hemispherical emissivity of the cavity, which is a function of both the cavity geometry and the average emissivity of the Inconel cavity material. Based on the work from section 5.2, we assume $\varepsilon_{\text{eff}} = 0.992$.

The thermal loss term represents the energy conducted through the insulated reactor and lost to the ambient environment via convection and radiation.

$$\dot{Q}_{\text{loss}} = {A_{\text{o}} \cdot (T_{\text{salt}} - T_{\infty})} \Big/ \left(\frac{\Delta x_{\text{i}}}{k_{\text{i}}} + \frac{\Delta x_{\text{ins}}}{k_{\text{ins}}} + \frac{1}{h_{\text{rad}} + h_{\text{conv}}}\right) \tag{7.9}$$

In this equation, A_{o} is the external surface area of the reactor and T_{∞} is the ambient temperature. The reactor is assumed to be insulated with 30.5 cm of fibrous refractory insulation with a thermal conductivity of 0.2 W/m-K. Losses from the external surface via radiation are assumed to be to the sky at a calculated "sky temperature" [102] with the radiative heat transfer coefficient defined by

$$h_{\text{rad}} = \frac{\sigma \varepsilon_{\text{ins}} (T_{\text{o}} + T_{\text{sky}}) \left(T_{\text{o}}^2 + T_{\text{sky}}^2\right) (T_{\text{o}} - T_{\text{sky}})}{T_{\text{o}} - T_{\infty}} \tag{7.10}$$

Convective losses are assumed to be via natural convection when wind speeds are below 4.3 m/s, and forced convection at wind speeds above 4.3 m/s. The reactor is assumed to be a vertical cylinder in form and thus the correlations used to calculate the surface heat transfer coefficients are for a heated vertical plate for the side walls [83] and for the upper surface of a heated horizontal plate for the top surface [103] when considering natural convection and for a cylinder in cross-flow for forced convection [74].

The transient solution to eq. (7.5) is obtained by numerical integration using an explicit Euler method with 1 hour time steps. Because the external insulation surface temperature is used to calculate the rate of heat loss from the reactor, while also being a function of the rate of heat loss from the reactor, an iterative solution process is required.

To simulate performance of the reactor for a year following a previous normal year of operation, the initial salt temperature is set to be equal to the final reactor temperature at the end of the year, providing a "closure condition". An initial guess of 1200 K was used for the initial condition, and then updated. A second round of integration was then carried out with this new initial condition to achieve a closed year-long cycle of typical operation.

Performance of the reactor is quantified according to the annual average thermal efficiency

$$\overline{\eta_{\text{th}}} = \frac{\int \dot{m}_{\text{net,sg}} \cdot \text{LHV}_{\text{sg}} \, \text{d}t}{\int \dot{Q}_{\text{solar}} + \dot{m}_{\text{feed}} \cdot \text{LHV}_{\text{feed}} \, \text{d}t} \tag{7.11}$$

as well as the fraction of the total heating power that is supplied by solar energy, referred to as the annual solar fraction.

$$f_{\text{solar}} = \frac{\int \dot{Q}_{\text{solar}} \mathrm{d}t}{\int \dot{Q}_{\text{solar}} + \dot{Q}_{\text{assist}} \mathrm{d}t} \tag{7.12}$$

The specific yield allows us to compare the utilization of feedstock between solar facility configurations by reporting the useful energy content of synthesis gas produced per unit area used to grow the feedstock. The feedstock material used in this study is capable of a yield of $Y_{\text{feed}} = 6$ tonnes per hectare annually on fertile land [3].

$$S_{\text{y}} = \frac{\int \dot{m}_{\text{net,sg}} \cdot \text{LHV}_{\text{sg}} \mathrm{d}t}{\int \dot{m}_{\text{feed}} \mathrm{d}t} \cdot Y_{\text{feed}} \tag{7.13}$$

Additionally, the instantaneous output of syngas from the facility is reported to demonstrate seasonal differences in operation and to consider the applicability of the facility for use in supplying a close-coupled downstream fuel or power production process. The maximum over-rate is defined as the maximum instantaneous synthesis gas yield rate divided by the nominal synthesis gas yield rate.

$$OR = \frac{\text{MAX}(\dot{m}_{\text{net,sg}})}{\dot{m}_{\text{nom,sg}}} \tag{7.14}$$

For a downstream power generation process, the maximum acceptable overrate value can be equated to the maximum turndown ratio for a close coupled gas turbine engine.

For a downstream fuel production process, the CSGS tank size must be determined. If we assume that the synthesis gas stream behaves like an ideal gas and is pressurized to the typical FT operating pressure of 30 bar, the resulting required CSGS volume for the fuel synthesis plant can be estimated based on the peak mass of syngas stored during the year and the ideal gas law.

$$V_{\text{CSGS}} = \frac{\text{MAX}(m_{\text{CSGS}}) \cdot R_{\text{sg}} \cdot \text{T}_{\infty}}{P_{\text{CSGS}}} \tag{7.15}$$

7.3 Results and Discussion

Transient solutions to eq. (7.2) were solved for a series of scenarios covering all combinations of eleven heat capacities in the range $1 \leq C_{\text{eff}} \leq 21$ GJ/K and eleven nominal syngas yield rates in the range $1.5 \leq \dot{m}_{\text{nom,sg}} \leq 50$ Tonne/hr over the course of a typical year. For a given nominal syngas output rate, assist heat was used when needed to maintain at least the nominal output rate at all times. In situations where the reactor temperature reached the maximum allowed temperature, excess feedstock was supplied such that the total heat of reaction equals the difference between the absorbed solar power

and the thermal losses. This approach holds the reactor temperature at or below the maximum allowed temperature of 1225 K.

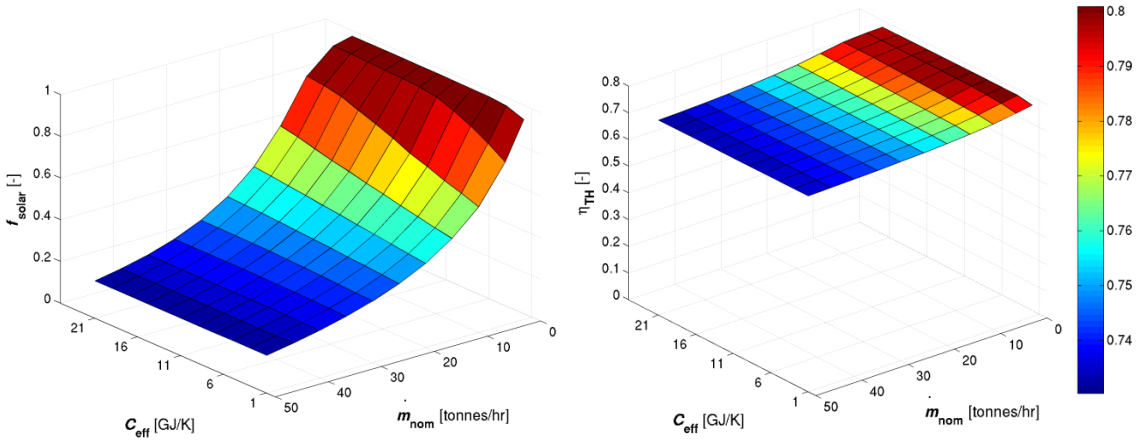

Fig. 7.3 Surface plots of the annual solar fraction (left) and thermal efficiency (right) as a function of the nominal syngas yield rate and heat capacity of the reactor.

7.3.1 Annual performance

The annual solar fraction, defined in eq. (7.12), is shown in the left side of Fig. 7.3 for the various solar facility configurations modeled. The surface plot is presented as a function of the two solar gasification facility design variables of nominal syngas yield rate, $\dot{m}_{\mathrm{nom,sg}}$, and heat capacity, C_{eff}. Values of solar fraction in Fig. 4 vary from 100% for a nominal syngas yield rate of 1.5 tonne/hr and heat capacities greater than or equal to 17 GJ/K (corresponding to salt volumes greater than or equal to 5,300 m^3), to less than 10% for nominal syngas yield rates greater than 50 tonnes/hr. The general trend for a given nominal syngas yield rate is that higher heat capacities buffer the solar input so maintaining the nominal flow rate is possible in the off-sun hours using stored solar heat, thus allowing for a larger solar fraction. For a given heat capacity, the solar fraction is decreased by requiring a larger value of nominal syngas output rate, and thus more frequent usage of assist heating from syngas combustion. At higher nominal syngas yield rates, and therefore lower solar fractions, the difference in possible solar fraction values across the range of heat capacities is smaller due to the reduced dependence on intermittent solar power to drive the gasification process.

The solar fraction is tied into the yield of carbon dioxide per unit fuel produced. While a full mine-to-tank (MTT) or well-to-wheels (WTW) analysis is required to

determine the actual carbon footprint per unit fuel, the difference between a unit of fuel produced in fully-solar operation compared to fully-hybridized can be determined by knowing how much syngas must be combusted to maintain the fuel production rate. Therefore, in the case when the solar fraction $f_{\text{solar}} = 0$, emissions are increased by 59 kg CO_2/GJ compared to the fully solar case where $f_{\text{solar}} = 1$ due to synthesis gas combustion. More detailed analyses of emissions changes associated with hybridized solar fuel production processes are reported in [92, 93].

The annual average thermal efficiency of the solar gasification facility, as defined in eq. (7.11), is shown in the surface plot on the right side of Fig. 7.3 as a function of the nominal syngas yield rate, $\dot{m}_{\text{nom}}$, and the heat capacity, C_{eff}. The average thermal efficiency varies from greater than 79% for nominal syngas yield rates near 1.5 tonnes per hour, which corresponds to a solar fraction greater than 96%, to thermal efficiencies less than 73% for nominal syngas yield rates in excess of 50 tonnes/hr, corresponding to low solar fractions of less than 10%. The surprising insensitivity of efficiency to the parameters investigated is due to the limited variation of thermal losses from the facilities, resulting in similar degrees of utilization of the thermal energy, regardless of if it is derived from solar or hybridized sources. The large increase in specific yield previously discussed better demonstrates the benefits of solar and is responsible for the increase in efficiency observed to follow the same trend as solar fraction though at a lesser magnitude. Variation with respect to heat capacity is less significant than that due to nominal syngas yield rate, with varying behavior depending on the value of the nominal syngas yield rate. At lower nominal yield rates, the increase in heat capacity initially allows for higher solar fractions, and thus the efficiency rises with heat capacity until achieving an optimum near 5 GJ/K at 1.5 tonnes/hr, but shifting closer to 11 GJ/K for a nominal yield rate of 5 tonnes/hr. Increasing heat capacity beyond these values results in the reactor maintaining slightly higher temperatures on average, and thus the higher thermal losses to the ambient decrease thermal efficiency. For nominal syngas yield rates larger than 20 tonnes/hr, when solar fraction is less sensitive to heat capacity, the general trend is for efficiency to decrease for larger values of heat capacity

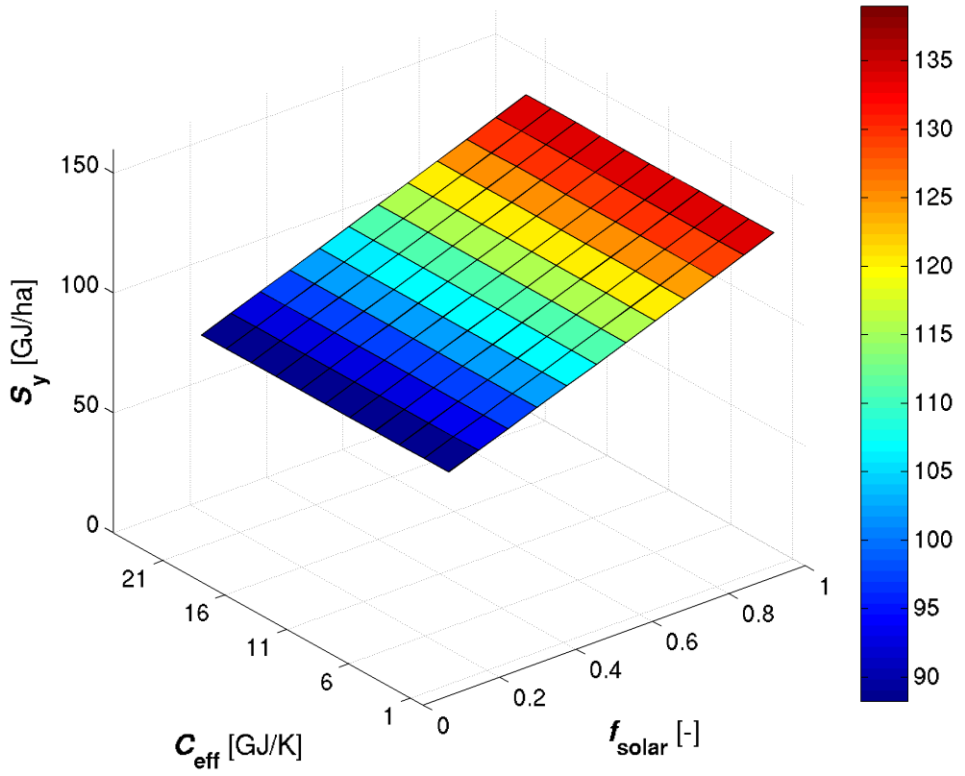

Fig. 7.4 Surface plot of specific yield of synthesis gas for facilities of various heat capacities and annual solar fractions.

The specific yield of synthesis gas is a strong function of the solar fraction while largely insensitive to the amount of thermal storage. This variation is demonstrated in Fig. 7.4. For low solar fractions near 10%, representing highly hybridized operation, specific yields of 88 GJ/ha are achieved. As the solar fraction is increased towards a near-unity value, the specific yield reaches its maximum of around 139 GJ/ha. This variation represents a 57% increase in output, demonstrating the value of using solar energy to drive a gasification process to maximize the yield of synthesis gas production per unit of feedstock crop area.

In summary, the results demonstrate that thermal efficiency, specific syngas yield, and the annual solar fraction are strong functions of the nominal syngas yield rate with much less dependence on the heat capacity. However, the importance of heat capacity should not be overlooked based on these considerations alone. The real importance of thermal storage is the ability to smooth variations in solar gasification facility output.

7.3.2 Instantaneous performance

The impact of heat capacity on the instantaneous output of synthesis gas is demonstrated in Fig. 7.5 for facilities that achieved solar fractions of $f_{\text{solar}} = 50\%$. The strongest variations in output occur during summer, when solar input is most intense, thus Fig. 7.5 highlights the solar input and instantaneous synthesis gas yield rate (as a percentage of the nominal rate) over the course of a typical summer week from July 3rd to

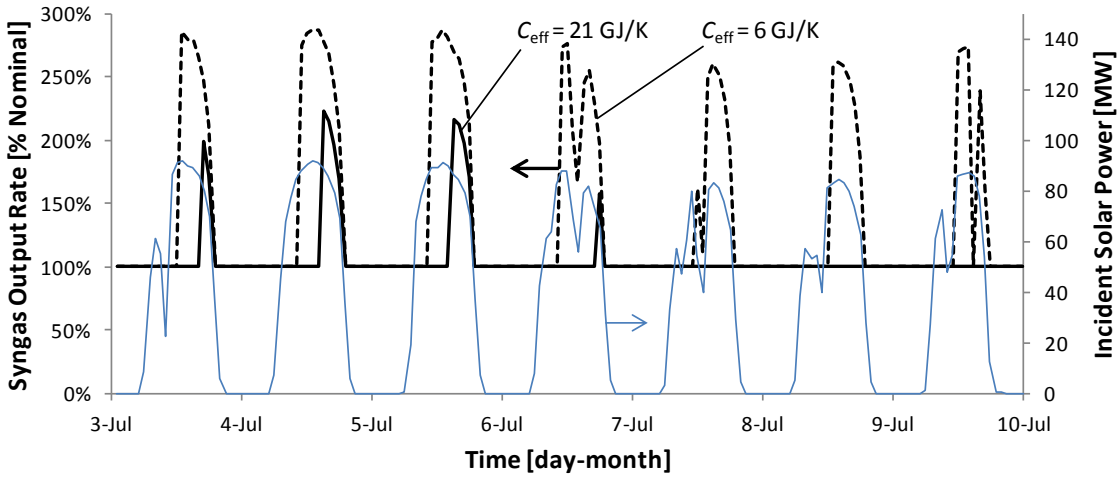

Fig. 7.5 Comparison of normalized syngas yield rate over the course of a typical summer week for a facility achieving a solar fraction of f_{solar}=50% with effective heat capacity values of $C_{\text{eff}} = 6$ GJ/K for the dashed line and $C_{\text{eff}} = 21$ GJ/K for the solid line. The incident solar power is included for reference.

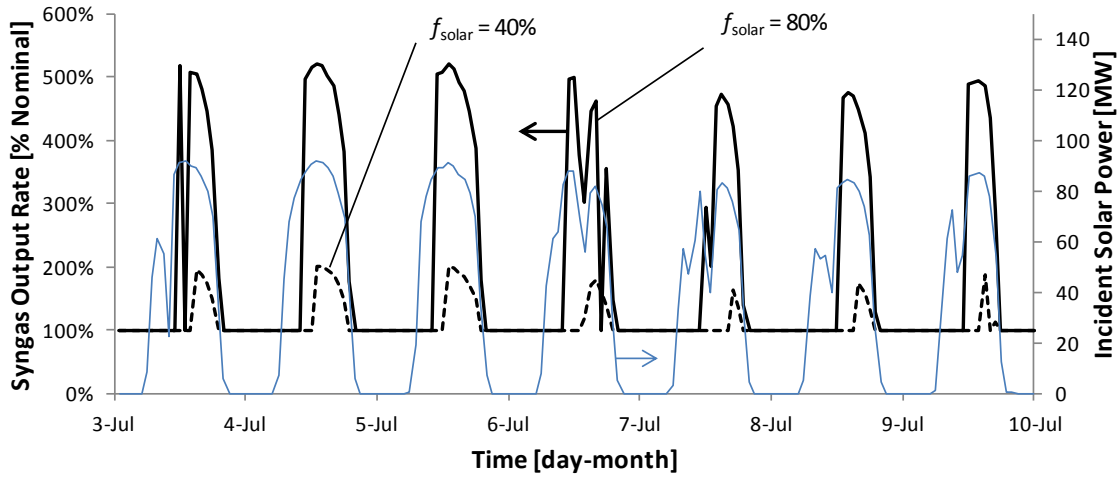

Fig. 7.6 Comparison of normalized syngas yield rate over the course of a typical summer week for a facility with effective heat capacity $C_{\text{eff}} = 11$ GJ/K with nominal feed throughputs resulting in solar fractions of $f_{\text{solar}} = 80\%$ for the solid line and $f_{\text{solar}} = 40\%$ for the dashed line. The incident solar power is included for reference.

July 10th for $C_{\text{eff}} = 21$ GJ/K and 6 GJ/K.

Both scenarios require a ramp-up in production in order to maintain reactor temperatures <1225 K during the first four days of the week; however the magnitude and duration of this ramp-up is much more intense for the low thermal storage case, with peak syngas output reaching 290% and ramped production required for at least a portion of every day of the week. The high thermal storage case requires ramp-up production for a much shorter period of time, and reaches peak production values approximately 210%. In addition, the high storage case runs steadily at the nominal syngas production rate for the final three days of the week when the solar power is broken by cloud cover for portions of the day.

The need for thermal storage to smooth transient operation is also heavily dependent upon the desired solar fraction. If one wishes to rely upon solar energy to drive the majority of the gasification, operation of the solar facility must address the transient nature of solar energy. For a solar gasification facility of a given heat capacity of $C_{\text{eff}} = 11$ GJ/K, the variation in output for the same typical summer week of July 3rd to July 10th is shown in Fig. 7.6 for solar facilities which achieved solar fractions of $f_{\text{solar}} = 40\%$ and 80%. While the moderate amount of thermal storage requires both cases to ramp-up production to some extent every day, the magnitude in this ramp-up is significantly different, with the case targeting an 80% solar fraction requiring syngas production to increase up to 521% in order to control reactor temperature, while the more heavily hybridized case targeting a solar fraction of 40% requires syngas output ramp-ups of no more than 200% of its higher nominal output rate.

7.3.3 Suitability for downstream processes

The variation in output can be a limiting factor in terms of close-coupling a downstream process to the solar gasification facility. We consider two possible scenarios for the utilization of synthesis gas from the modeled facilities: (1) combustion of the synthesis gas for direct power production in a gas turbine engine (GTE) or combined-cycle (CC) power plant, or (2) production of synthetic fuels from a Fischer-Tropsch fuel production plant. For the electricity production scenarios, the output of the solar gasification facility must remain within an acceptable range of operation for the GTE or CC plant. We envision that such a power plant will be sized to handle the maximum

synthesis gas production rate, and thus the ratio of the maximum production rate to the nominal rate as defined in eq. (7.14), must be less than the maximum acceptable turndown ratio for the power plant. Contours of maximum overrate as a function of the solar fraction and the heat capacity on the lower axis or the equivalent volume of molten carbonate salt on the top axis is shown in Fig. 7.7. Acceptable turndown ratios vary depending on specific designs, with one CC power plant requiring operation within a 3.3:1 ratio [104] and some GTE designs allowing up to a 5:1 ratio [105]. If we take a typical limiting turndown ratio to be 4:1, the shaded region of Fig. 9 above the max overrate contour of 4 represents the range of solar gasification facility designs that would be unacceptable for driving a directly coupled power production process. This design requirement would set the limit for maximum solar fraction at 74% for the case with C_{eff} = 21 GJ/K, and a maximum solar fraction of 52% for C_{eff} = 1 GJ/K, corresponding to nominal syngas yield rates of 13 tonnes/hr in both cases.

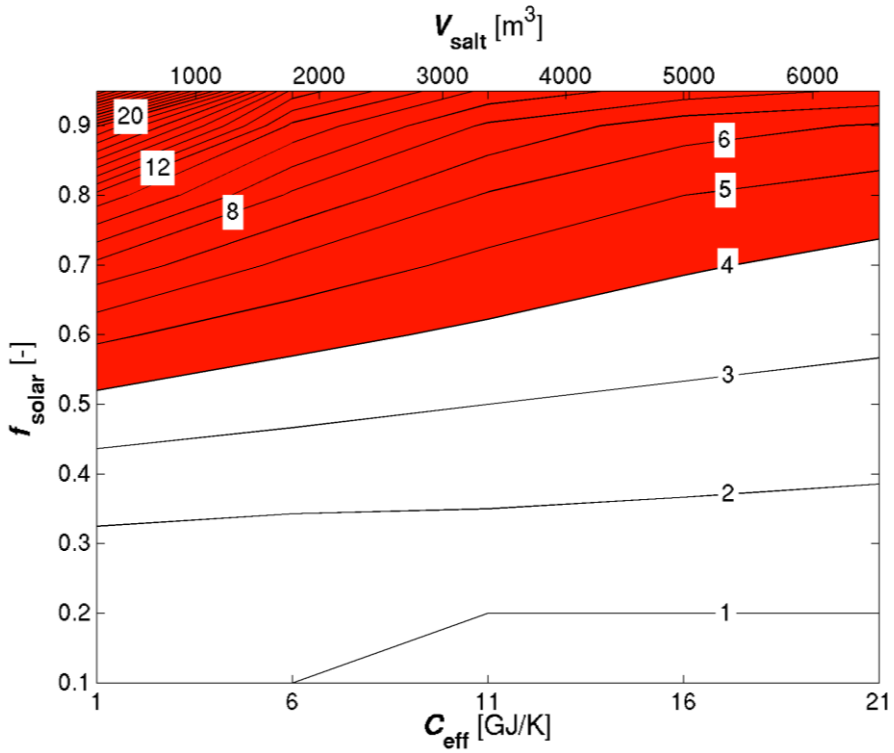

Fig. 7.7 Contours of maximum synthesis gas overrate as a function of the facility effective heat capacity or carbonate salt volume and annual solar fraction. The shaded region indicates a maximum overrate unacceptable for continuously feeding a downstream power production process.

If we consider a continuously operating fuel synthesis plant, consuming the total annual produced syngas at a constant rate, the fuel synthesis plant would need to have a sufficient volume of CSGS available at the process pressure to supply a constant rate of syngas to the downstream fuel synthesis plant throughout the year despite variations in output from the solar gasification facility. For a Fischer-Tropsch fuel production process, an operating pressure of 30 bar is typical. The required volume of CSGS at this pressure is shown in the contour plot of Fig. 7.8 as a function of the solar gasification facility's resultant annual solar fraction and both heat capacity on the lower axis and equivalent volume of molten carbonate salt on the top axis. The required storage volume rises significantly once the solar fraction exceeds 20%, and grows steadily as solar fraction increases. For a given solar fraction, the required volume of CSGS is reduced by increasing reactor heat capacity, exhibiting a trade-off between thermal storage with molten salt and CSGS. This tradeoff can be exploited to attempt to optimize integration

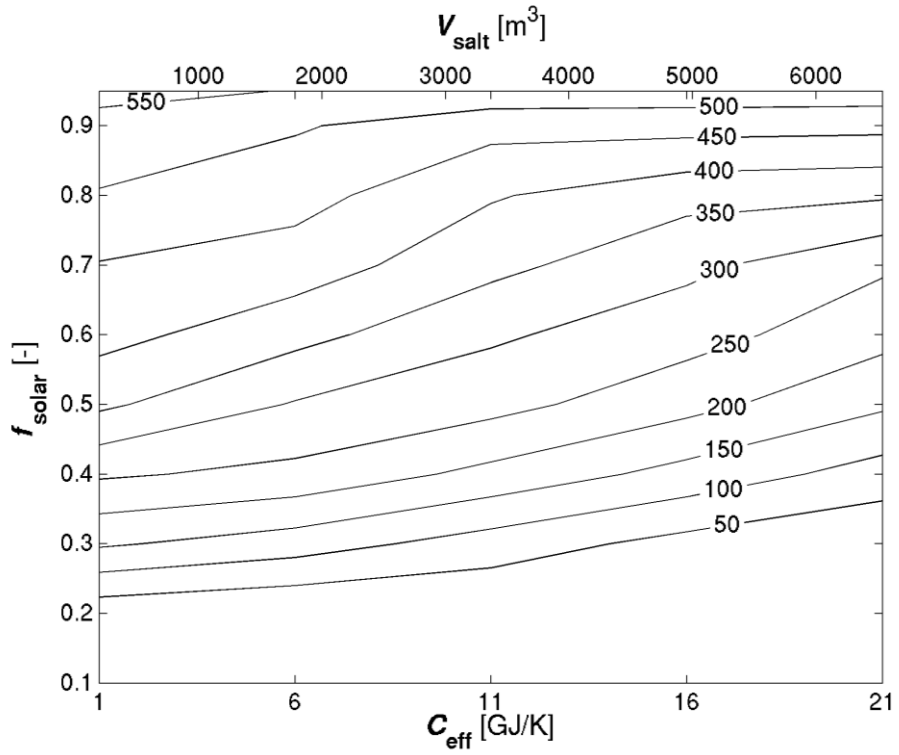

Fig. 7.8 Contours of required syngas storage tank volume in thousands of cubic meters at 30 bar and 300 K to handle synthesis gas yield rate peaks and allow for a steady rate of consumption in a downstream process as a function of the facility heat capacity or carbonate salt volume, and annual solar fraction.

of a fuel synthesis plant based on the difference in cost. CSGS could also be used to smooth GTE operation, however if the GTE fuel lines operate below 30 bar, the work of compression beyond the fuel injection system pressure must be viewed as a parasitic loss.

The impacts of heat capacity and degree of hybridization on the specific yield, efficiency, and variation in synthesis gas output of a 100 MW_{th} solar gasification facility is explored. Targeting high solar fractions by setting a low nominal syngas yield rate achieves maximized specific syngas yield and thermal efficiency of the solar gasification facility. At low nominal syngas yield rates and thus high solar fractions, the average thermal efficiency is 79% and the specific syngas yield peaks at 139 GJ/ha. However, high solar fractions result in high variation of syngas output. For a solar gasification facility with low thermal storage and achieving a 95% solar fraction, this variability can cause peak syngas production rates of greater than 30 times the nominal syngas yield rate. The design of a combined solar gasification facility and power or fuel production plant will require balancing the cost and efficiency impacts of thermal storage and hybridization of the solar power with conventional heat sources in order to achieve an optimum design acceptable for operating a specific process.

8 Conclusions

8.1 Summary

The manufacture and initial testing of a prototype molten salt solar reactor for gasification of biomass is a significant milestone in the development of a solar gasification process. Solar gasification of biomass allows for both improvements in yield compared to conventional gasification and the storage of solar energy in a chemical form. The use of molten salts as both a heat transfer media and catalyst for biomass gasification allows for improvements in reaction rates and avoidance of issues related to solar transients and poor thermal uniformity. The reactor allows for 3 kW_{th} operation with an average aperture flux of 1530 suns at salt temperatures of 1200 K with pneumatic injection of ground or powdered dry biomass feedstocks directly into the salt melt.

The impacts of molten salt on the reactions of biomass pyrolysis and carbon gasification were examined through laboratory bench scale experiments in an electrically heated furnace. The reactions were characterized in terms of reaction rates, and product distributions with and without molten salt present. The mechanisms behind the increase in reaction rates were identified by de-coupling heat transfer and chemical kinetics for both reactions through the use of a numerical simulation of reacting feed tablets. Parameter estimation allowed kinetic models of reaction rates to be produced for both reactions. Parameter estimation was achieved by matching simulation results to data from the laboratory experiments, demonstrating that improved heat transfer in molten salt doubles pyrolysis rates with no signs of catalysis, while catalysis improves the carbon gasification rates by up to 10 times.

The prototype reactor was designed based on a concentric cylinder concept with a cylindrical cavity receiver surrounded by a molten salt volume. The geometry is described by the design parameters of aperture diameter d_a, cavity-aperture diameter ratio D, cavity aspect ratio L, annulus diameter ratio DA, cavity and housing wall thickness t_w, flange thickness t_f, and bolt diameter d_b. The geometric parameters are selected to optimize performance based on the key physical processes involved in operation.

The cavity geometry is selected based on the design power requirement of 3 kW_{th} of solar input and the absorption efficiency of and flux distribution within the cavity. The aperture size of $d_a = 5$ cm results in the desired 3 kW_{th} of intercepted power for the expected flux distribution of the University of Minnesota High Flux Solar Simulator. A numerical simulation of radiative exchange between a concentrated solar source and the hot cavity was developed using Monte Carlo Ray Tracing techniques in order to explore the impact of the remaining cavity design paramaters and the value of a reflective surface coating on the cavity walls. The geometric parameter values of $D = 2$ and $L = 1.5$ are selected as they offer absorption efficiency in the range of 81%-90% for the convection conditions under consideration with the location of the peak flux near the center of the cavity. The cavity material is selected as neat Inconel alloy, without a reflective coating, to maximize absorption efficiency given that predicted wall temperatures were acceptable for the uncoated material.

The salt region geometry is selected to maximize the utilization of solar energy delivered to the cavity. A parametric survey over several values of the annulus diameter ratio DA was performed using finite volume CFD to determine the best geometry in terms of the competing effects of losses to the ambient environment and heat transfer from the hot cavity walls to the molten salt. The value of $DA = 1.5$ results in the highest utilization efficiency by minimizing the external surface area of the reactor while also being sufficiently large to avoid any stagnation of the convective salt flow responsible for removing heat from the cavity absorber walls.

Structural concerns drive the selection of the remaining parameters of wall thickness, flange thickness, and bolt diameter. Numerical finite element simulations of the thermal stresses anticipated during operation based on the temperature distributions from the previous CFD study were used to parametrically explore a range of possible values. A design with stresses not exceeding the infinite life creep stress of 34.5 MPa is selected with values of $t_w = 3.175$ mm, $t_f = 6.35$ mm, and $d_b = 6.35$ mm.

The reactor was given final design features of ports for sensors, feedstock delivery, salt drainage, and product gas removal as well as water cooled surfaces to absorb excess radiation during use. The final design is manufactured out of Inconel alloy X-750 for the primary components of the cavity and housing while 316 stainless steel is used for

attached components including the feedstock injector and feed hopper, radiation shield, and product gas outlet and cooling tubing. The reactor is insulated with a refractory ceramic flexible insulation (Fiberfrax Durablanket).

Testing of the reactor took place at conservative shakedown conditions of a 1132±126 suns average flux and 2.22±0.25 kW_{th} incident power using reactants of cellulose and CO_2. Testing was limited to a salt temperature of 1150 K and a total feed delivery time of 3.5 minutes due to downstream filter clogging during this initial test. A CO rich product gas is produced resulting in an initial solar efficiency of $\eta_{\text{solar}} = 32 \pm 2.3\%$ and a cold gas efficiency of $\eta_{\text{CG}} = 70.5 \pm 1.7\%$. The receiver cavity of the reactor appears mechanically stable following the test at the reduced flux concentration with no signs of deformation, cracking, or localized heat exposure. Initial shakedown results provide guidance for modifications to the reactor prior to future testing to improve performance.

A scale-up analysis was carried out in order to explore the practical considerations for operation of a molten salt solar gasification process at a 100 MW_{th} solar power. Based on requirements for downstream fuel or power production, the use of either hybridization or thermal storage may be used. Hybridization results in decreased specific yield of syngas and decreased energy efficiency while reducing the variation of syngas output due to solar transients. Thermal storage also decreases the sensitivity of syngas yield to solar variation; however it does not significantly impact the specific yield or efficiency compared to hybridization. The design of a combined solar gasification facility and power or fuel production plant will require balancing the cost and efficiency impacts of thermal storage and hybridization of the solar power with conventional feed or syngas combustion heating in order to achieve an optimum design.

In conclusion, the development and testing of the prototype molten salt gasification reactor has demonstrated the value of continued research on the process. The potential benefits of the use of molten salt for biomass gasification reactions were realized during the lab-scale testing which demonstrated increased rates and overall yields as well as reduced secondary product formation. Despite initial testing difficulties, it should be possible for the prototype reactor to achieve similar results, producing high yields of low-tar synthesis gas that is ready to be utilized for downstream processes. The work completed here supports the future development by providing models for the chemical

reactions involved in biomass gasification, thermodynamic predictions of ideal process throughput, measured data of actual yields with candidate feedstocks under ideal conditions, initial characterization of the prototype reactor, and a framework for future testing of the prototype with the key issues encountered during shakedown testing highlighted and suggestions for overcoming these issues provided.

8.2 Contributions

The work reported in this thesis offer several important contributions in terms of gasification chemistry, reactor design, and commercial scale considerations. The reactions of biomass gasification in a molten alkali carbonate salt are better understood based on the results of Chapter 4, which indicate that pyrolysis is accelerated not by catalysis but through improved heat transfer, while carbon gasification is accelerated through chemical catalysis, with new kinetic model parameters calculated to allow modeling of the reaction rates in a molten salt environment. For pyrolysis, a first order volumetric model of the form $\frac{\mathrm{d}X}{\mathrm{d}t} = k_{0,\mathrm{p}} \exp\left(-\frac{E_{\mathrm{a,p}}}{R_{\mathrm{u}} \cdot T}\right)(1 - X)$ with a pre-exponential factor $k_{0,\mathrm{p}} = 1.96 \cdot 10^{11}$ s^{-1} and activation energy $E_{\mathrm{a,p}} = 238$ kJ/mol fits the data, while for carbon gasification, a 2/3rds order shrinking grain model of the form $\frac{\mathrm{d}X}{\mathrm{d}t} = k_{0,\mathrm{g}} \exp\left(-\frac{E_{\mathrm{a,g}}}{R_{\mathrm{u}} \cdot T}\right)(1 - X)^{2/3}$ with a pre-exponential factor $k_{0,\mathrm{g}} = 1.5 \cdot 10^{6}$ min^{-1} and activation energy $E_{\mathrm{a,p}} = 158$ kJ/mol captures the observed rates best.

The design process of Chapter 5 provides a sequential progression towards the final specification of a solar thermochemical reactor in a manner that could be applied similarly for the development of other solar reactors for thermochemical processes. The parametric study of cavity absorber shape in section 5.2 is generally applicable for any receiver cavity with a right cylindrical design and heat transfer by convection from the outer cavity walls, giving insight to cavity design and material selection for a wide variety of potential processes. For arrangements with low convective coefficients of $h < 1000$ W/m^2-K, cavity designs are most sensitive to geometry with absorption efficiencies falling from 90% to 60% as the dimensionless cavity parameters of $D = L = 2.5$ are reduced to $D = L = 1.2$. Boosting the convective intensity to $h \geq 1000$ W/m^2-K

allows for designs less sensitive to geometry, achieving absorption efficiencies from 82.5% to 92.5% over the same range of cavity parameter values.

Lastly the scale-up analysis of Chapter 7 provides insight into the impact of hybridization and thermal storage not just for molten salt solar gasification, but for any endothermic solar reforming/gasification process that may be coupled with thermal storage and hybridized with some conventional heat source in order to meet the needs of a downstream power or fuel production process. The results suggest that hybridization of a solar process resulting in a solar fraction of 50% is sufficient to combat process throughput variations and allow direct coupling to a fuel or power production without thermal storage, while the use of 21 GJ/K of general thermal storage for a 100 MW_{th} nominal facility allows similar throughput variation with less hybridization, achieving solar fractions up to 74%.

8.3 Recommendations

Future research on the process of solar gasification of biomass in a molten salt environment is recommended in the areas of reactor testing, reactor simulation, and understanding the behavior of the molten carbonate salts in reaction conditions.

Based on the results of the initial shakedown testing of the prototype reactor, several suggestions can be made for future testing. First, the primary problems of unreacted char release and salt leakage must be addressed. The release of char can be prevented by ensuring that the reacting particles make contact with and are wetted by the molten salt. Currently bubbles of feed and product gas are given a nearly unobstructed path to the surface of the salt melt, and as such large bubbles may contain significant quantities of charred feed that, upon surfacing release char to be entrained by the injection gases and swept out of the reactor. Providing flow obstruction in the form of baffles or grates within the reactor would act to break up these bubbles/char lumps and expose the char to the salt allowing surface tension to retain the particles, forming a suspension of the char material within the salt until the char is able to complete gasification. The salt leakage issues is due to the use of ceramic felt (Zirconia) material that was thought to not be wetted by carbonate salts. However, at our testing conditions the felt acted to wick the liquid salt to the outside of flange seals and soak into the insulation or drip from the

reactor. In place of the felt material, a deformable metal gasket made of a soft metal such as copper may be used to obtain a better seal. Copper gaskets were used between the drain flange mating surfaces with no leakage or deformation noted during the initial tests, proving that the concept is viable. Second, testing should be expanded to include the use of steam in addition to or in place of CO_2 in order to produce a more H_2 rich product gas amendable to fuel production and to determine if the choice of oxidizing agent has an effect on kinetics of molten salt catalyzed carbon gasification. The move to steam will require overcoming challenges associated with the addition of heated steam delivery lines to the feed injection system as well as predicting and accounting for any gases produced from interaction of steam with the molten salt.

Enhanced numerical simulations of the reactor are recommended in order to determine the conditions within the reactor during operation. These simulations should take a multiphase approach including liquid salt, gaseous reactant and product, and solid feed and char phases in order to fully represent the complex environment within the reactor. The results of the simulations may guide the implementation of reactor design changes such as the implementation of baffles and grates or operational changes such as the choice of injection gas flow rates or the amount of salt the reactor is filled with in order to avoid ejection of materials from the reactor during use.

Finally, the interaction of molten carbonate salts with gases must be understood. The useful product gases of H_2, CO, and CH_4 are not thought to interact with the salt, however there is a phase equilibrium problem that exists between $-CO_3$ and –OH ions within the salt and gaseous CO_2 and H_2O in contact with the salt. Initial testing took place using only CO_2 to avoid these complications; however operation with steam is desired for the reasons mentioned in the testing recommendations above. Studies should aim to determine how the salt composition changes when exposed to various concentrations of CO_2 or H_2O in terms of final composition, the impact of that composition on gasification reactions, and the rate at which that composition is approached. The results will guide the choice of reactant gases during operation and allow for improved accounting of salt-based gas release for improved measurement of product gas yields during gasification processes.

References

[1] U.S. Energy Information Administration 2012, "Annual Energy Outlook 2012," U.S. Energy Information Administration (EIA), DOE/EIA-0383(2012), Washington DC.

[2] Solomon, S., Qin, D., Manning, M., 2007, "Climate Change 2007: Working Group I: The Physical Science Basis," Cambridge University Press, New York, NY, USA, .

[3] Tilman, D., Hill, J., and Lehman, C., 2006, "Carbon-Negative Biofuels from Low-Input High-Diversity Grassland Biomass," Science, **314**(5805) pp. 1598-1600.

[4] Cheng, J., 2010, "Biomass to Renewable Energy Processes,"CRC Press, Boca Raton, FL, USA, pp. 437-489.

[5] Klass, D.L., 2004, "Encyclopedia of Energy,"Elsevier, San Diego, pp. 193-212, Chap. Biomass for Renewable Energy and Fuels.

[6] Iliuta, I., Leclerc, A., and Larachi, F., 2010, "Allothermal Steam Gasification of Biomass in Cyclic Multi-Compartment Bubbling Fluidized-Bed Gasifier/Combustor - New Reactor Concept," Bioresource Technology, **101**(9) pp. 3194-3208.

[7] Gregg, D. W., Taylor, R. W., Campbell, J. H., and Cotton, J. R. T. a. A., 1980, "Solar Gasification of Coal, Activated Carbon, Coke and Coal and Biomass Mixture," Solar Energy, **25**(4) pp. 353-364.

[8] Mathur, V., Breault, R., and Lakshmanan, S., 1983, "Coal Gasification using Solar Energy," Solar Energy, **30**(5) pp. 433-440.

[9] Taylor, R., Berjoan, R., and Coutures, J., 1983, "Solar Gasification of Carbonaceous Materials," Solar Energy, **30**(6) pp. 513-525.

[10] Epstein, M., Spiewak, I., Funken, K., 1994, "Review of the technology for solar gasification of carbonaceous materials," Proc. of ASME Int. Solar Energy Conf. on Solar Engineering, Anonymous San Francisco, CA, USA, pp. 79-91.

[11] Murray, J. P., and Fletcher, E. A., 1994, "Reaction of Steam with Cellulose in a Fluidized Bed using Concentrated Sunlight," Energy, **19**(10) pp. 1083-1098.

[12] Flechsenhar, M., and Sasse, C., 1995, "Solar Gasification of Biomass using Oil Shale and Coal as Candidate Materials," Energy, **20**(8) pp. 803-810.

[13] Lede, J., 1999, "Solar Thermochemical Conversion of Biomass," Solar Energy, **65**(1) pp. 3-13.

[14] Zedtwitz, P. v., and Steinfeld, A., 2003, "The Solar Thermal Gasification of Coal - Energy Conversion Efficiency and CO_2 mitigation Potential," Energy, **28**(5) pp. 441-456.

[15] Trommer, D., Noembrini, F., Fasciana, M., Rodriguez, D., Morales, A., Romero, M., and Steinfeld, A., 2005, "Hydrogen Production by Steam-Gasification of Petroleum Coke using Concentrated Solar Power - I. Thermodynamic and Kinetic Analyses," International Journal of Hydrogen Energy, **30**(6) pp. 605-618.

[16] Z'Graggen, A., Haueter, P., Trommer, D., Romero, M., de Jesus, J. C., and Steinfeld, A., 2006, "Hydrogen Production by Steam-Gasification of Petroleum Coke using Concentrated Solar Power-II Reactor Design, Testing, and Modeling," International Journal of Hydrogen Energy, **31**(6) pp. 797-811.

[17] Perkins, C. M., Woodruff, B., Andrews, L., 2008, "Synthesis gas production by rapid solar thermal gasification of corn stover," CSP SolarPACES, Anonymous Las Vegas, Nevada, pp. 1-8.

[18] Piatkowski, N., and Steinfeld, A., 2008, "Solar-Driven Coal Gasification in a Thermally Irradiated Packed-Bed Reactor," Energy and Fuels, **22**(3) pp. 2043-2052.

[19] Hertwich, E. G., and Zhang, X., 2009, "Concentrating-Solar Biomass Gasification Process for a 3rd Generation Biofuel," Environmental Science and Technology, **43**(11) pp. 4207.

[20] Melchior, T., Perkins, C., Lichty, P., Weimer, A. W., and Steinfeld, A., 2009, "Solar-Driven Biochar Gasification in a Particle-Flow Reactor," Chemical Engineering and Processing: Process Intensification, **48**(8) pp. 1279.

[21] Gregg, D. W., Aiman, W. R., Otsuki, H. H., and Thorsness, C. B., 1980, "Solar Coal Gasification," Solar Energy, **24**(3) pp. 313-321.

[22] Steinfeld, A., and Meier, A., 2004, "Encyclopedia of Energy,"Elsevier, New York, pp. 623-637, Chap. Solar Fuels and Chemicals.

[23] Epstein, M., 1995, "New opportunities for high temperature solar chemistry," International Workshop on High-Temperature Solar Chemistry, Anonymous Paul Scherrer Institut, Switzerland, pp. 85-111.

[24] Iwaki, H., Ye, S., Katagiri, H., and Kitagawa, K., 2004, "Wastepaper Gasification with CO_2 or Steam using Catalysts of Molten Carbonates," Applied Catalysis A: General, **270**(1-2) pp. 237-243.

[25] Adinberg, R., Epstein, M., and Karni, J., 2004, "Solar Gasification of Biomass: A Molten Salt Pyrolysis Study," Journal of Solar Energy Engineering, Transactions of the ASME, **126**(3) pp. 850-857.

[26] Jin, G., Iwaki, H., Arai, N., and Kitagawa, K., 2005, "Study on the Gasification of Wastepaper/Carbon Dioxide Catalyzed by Molten Carbonate Salts," Energy, **30**(7) pp. 1192-1203.

[27] Sugiura, K., Minami, K., Yamauchi, M., Morimitsu, S., and Tanimoto, K., 2007, "Gasification Characteristics of Organic Waste by Molten Salt," Journal of Power Sources, **171**(1) pp. 228-236.

[28] Lichty, P., Perkins, C., Woodruff, B., and Weimer, C. B. a. A., 2010, "Rapid High Temperature Solar Thermal Biomass Gasification in a Prototype Cavity Reactor," Journal of Solar Energy Engineering, **132**(1) pp. 011012.

[29] Taylor, R. W., Berjoan, R., and Coutures, J., 1983, "Solar Gasification of Carbonaceous Materials," Solar Energy, **30**(6) pp. 513.

[30] Piatkowski, N., Wieckert, C., and Steinfeld, A., 2009, "Experimental Investigation of a Packed-Bed Solar Reactor for the Steam-Gasification of Carbonaceous Feedstocks," Fuel Processing Technology, **90**(3) pp. 360.

[31] Kruesi, M., Jovanovic, Z. R., dos Santos, E. C., Yoon, H. C., and Steinfeld, A., 2013, "Solar-Driven Steam-Based Gasification of Sugarcane Bagasse in a Combined Drop-Tube and Fixed-Bed reactor–Thermodynamic, Kinetic, and Experimental Analyses," Biomass and Bioenergy, **52**pp. 173-183.

[32] Kodama, T., Kondoh, Y., Tamagawa, T., Funatoh, A., Shimizu, K. -., and Kitayama, Y., 2002, "Fluidized Bed Coal Gasification with CO₂under Direct Irradiation with Concentrated Visible Light," Energy & Fuels, **16**(5) pp. 1264-1270.

[33] Antal, M. J., Hofmann, L., Moreira, J., Brown, C., and Steenblik, R., 1983, "Design and Operation of a Solar Fired Biomass Flash Pyrolysis Reactor," Solar Energy, **30**(4) pp. 299-312.

[34] Z'Graggen, A., Haueter, P., Maag, G., Vidal, A., and Steinfeld, M. R. a. A., 2007, "Hydrogen Production by Steam-Gasification of Petroleum Coke using Concentrated Solar Power-III. Reactor Experimentation with Slurry Feeding," International Journal of Hydrogen Energy, **32**(8) pp. 992-996.

[35] Z'Graggen, A., Haueter, P., Maag, G., Romero, M., and Steinfeld, A., 2008, "Hydrogen Production by Steam-Gasification of Carbonaceous Materials using Concentrated Solar Energy-IV. Reactor Experimentation with Vacuum Residue," International Journal of Hydrogen Energy, **33**(2) pp. 679-684.

[36] Chen, J., Lu, Y., Guo, L., Zhang, X., and Xiao, P., 2010, "Hydrogen Production by Biomass Gasification in Supercritical Water using Concentrated Solar Energy: System

Development and Proof of Concept," International Journal of Hydrogen Energy, **35**(13) pp. 7134-7141.

[37] Guo, L., Zhao, L., Jing, D., Lu, Y., Yang, H., Bai, B., Zhang, X., Ma, L., and Wu, X., 2009, "Solar Hydrogen Production and its Development in China," Energy, **34**(9) pp. 1073-1090.

[38] Fauth, M. I., 1974, "Non-Polluting Methods for Disposal of Ordnance and Other Hazardous Materials," pp. 504-507.

[39] Kohl, A. L., Harty, R. B., Johanson, J. G., and Naphtali, L. M., 1978, "Molten Salt Coal Gasification Process," Chemical Engineering Progress, **74**(8) pp. 73-79.

[40] Trilling, C. A., and Martin, L. W., 1979, "500-MW combined-cycle power plant fuelled with low-Btu gas produced by the Rock gas molten salt coal gasification process," American Power Conference, Anonymous Chicago, IL, USA, pp. 364-369.

[41] Speidel, P. J., Kelly, B. D., Prairie, M. R., Pacheco, J. E., Gilbert, R. L., and Reilly, H. E., 1999, "Performance of the Solar Two Central Receiver Power Plant," Journal De Physique.IV : JP, **9**(3) pp. Pr3-181 - Pr3-188.

[42] Dunn, R. I., Hearps, P. J., and Wright, M. N., 2012, "Molten-Salt Power Towers: Newly Commercial Concentrating Solar Storage," Proceedings of the IEEE, **100**(2) pp. 504-515.

[43] Tamaura, Y., Tsuji, M., Yoshida, S., Yokota, O., and Sano, T., 1999, "Solar Gasification of Coal using Carbonate Molten Salt Reactor," Journal De Physique.IV, **9**(3) pp. 373-378.

[44] Yoshida, S., Matsunami, J., Hosokawa, Y., Yokota, O., Tamaura, Y., and Kitamura, M., 1999, "Coal/CO_2 gasification System using Molten Carbonate Salt for Solar/Fossil Energy Hybridization," Energy and Fuels, **13**(5) pp. 961-964.

[45] Matsunami, J., Yoshida, S., Oku, Y., Tamaura, O. Y. a. Y., and Kitamura, M., 2000, "Coal Gasification by CO_2 gas Bubbling in Molten Salt for Solar/Fossil Energy Hybridization," Solar Energy, **68**(3) pp. 257-261.

[46] Coyle, R.T., Thomas, T.M., and Schissel, P., 1985, "The Corrosion of Materials in Molten Alkali Carbonate Salt at 900° C," Solar Energy Research Institute, SRI/TR-255-2553, Golden, Colorado.

[47] Maund, J. K., and Earp, D. M., 1989, "Biomass pyrolysis in molten salts for fuel production," Pyrolysis and Gasification, Anonymous Aston Univ, Birmingham, Engl; Publ by Elsevier Science Publ Co Inc, New York, NY, USA, pp. 238.

[48] Szargut, J., Morris, D.R., and Steward, F.R., 1988, "Exergy analysis of thermal, chemical, and metallurgical processes," Hemisphere Publishing Corporation, pp. 332.

[49] Moran, M.J., and Shapiro, H.N., 2004, "Fundamentals of Engineering Thermodynamics,"John Wiley and Sons, Inc., pp. 691-706.

[50] Huhn, F., Klein, J., and Juntgen, H., 1983, "Investigations on the Alkali-Catalysed Steam Gasification of Coal: Kinetics and Interactions of Alkali Catalyst with Carbon," Fuel, **62**(2) pp. 196-199.

[51] Hurt, R. H., Fletcher, T. H., and Sampaio, R. S., 1993, "Heat Transfer from a Molten Phase to an Immersed Coal Particle during Devolatilization," Journal of Heat Transfer, Transactions ASME, **115**(3) pp. 717-723.

[52] White, S. H., and Twardoch, U. M., 1987, "Behavior of Water in Molten Salts," Journal of the Electrochemical Society, **134**(5) pp. 1080-1088.

[53] Ishida, M., and Wen, C. Y., 1971, "Comparison of Zone-Reaction Model and Unreacted-Core Shrinking Model in Solid--Gas Reactions--I Isothermal Analysis," Chemical Engineering Science, **26**(7) pp. 1031.

[54] Szekely, J., and Evans, J. W., 1970, "A Structural Model for Gas--Solid Reactions with a Moving Boundary," Chemical Engineering Science, **25**(6) pp. 1091.

[55] Fermoso, J., Arias, B., Pevida, C., Plaza, M. G., Rubiera, F., and Pis, J. J., 2008, "Kinetic Models Comparison for Steam Gasification of Different Nature Fuel Chars." Journal of Thermal Analysis \& Calorimetry, **91**(3) pp. 779.

[56] Antal, M. J. J., and Varhegyi, G., 1995, "Cellulose Pyrolysis Kinetics: The Current State of Knowledge," Industrial \& Engineering Chemistry Research, **34**(3) pp. 703-717.

[57] Chornet, E., and Roy, C., 1980, "Compensation Effect in the Thermal Decomposition of Cellulosic Materials," Thermochimica Acta, **35**(3) pp. 389.

[58] Dullien, F.A., 1992, "Porous media: fluid transport and pore structure," Academic Press, .

[59] Yagi, S., and Kunii, D., 1957, "Studies on Effective Thermal Conductivities in Packed Beds," Chemical Engineering Progress, **3**(3) pp. 373.

[60] Whitaker, S., 1972, "Forced Convection Heat Transfer Correlations for Flow in Pipes, Past Flat Plates, Single Cylinders, Single Spheres, and for Flow in Packed Beds and Tube Bundles," AICHE Journal, **18**(2) pp. 361-371.

[61] Incropera, F., and DeWitt, D., 2002, "Fundamentals of Heat and Mass Transfer,"John Wiley & Sons, New York, pp. 811, Chap. 13.

[62] DeGroot, W. F., and Richards, G. N., 1989, "Relative Rates of Carbon Gasification in Oxygen, Steam and Carbon Dioxide," Carbon, **27**(2) pp. 247.

[63] Wood, B. J., and Sancier, K. M., 1984, "Mechanism of the Catalytic Gasification of Coal Char: A Critical Review," Catalysis Reviews, **26**(2) pp. 233.

[64] American Society for Testing and Materials, 1982, "Standard Test Methods for Analysis of Wood Fuels," ASTM E870, .

[65] Quinn, T., 1967, "The Calculation of the Emissivity of Cylindrical Cavities Giving Near Black-Body Radiation," British Journal of Applied Physics, **18**(8) pp. 1105.

[66] Wieckert, C., Meier, A., and Steinfeld, A., 2003, "Indirectly Irradiated Solar Receiver-Reactors for High-Temperature Thermochemical Processes," Journal of Solar Energy Engineering, **125**(1) pp. 120-123.

[67] Skocypec, R., and Romero, V., 1989, "Thermal Modeling of Solar Central Receiver Cavities," Journal of Solar Energy Engineering, **111**pp. 117-123.

[68] Hogan, R., Diver, R., and Stine, W. B., 1988, "Comparison of a cavity solar receiver numerical model and experimental data," ASME, Gas Turbine and Aeroengine Congress and Exposition, Anonymous **1,** .

[69] Kräupl, S., and Steinfeld, A., 2005, "Monte Carlo Radiative Transfer Modeling of a Solar Chemical Reactor for the Co-Production of Zinc and Syngas," Journal of Solar Energy Engineering, **127**(1) pp. 102-108.

[70] Hathaway, B. J., Davidson, J. H., and Kittelson, D. B., 2011, "Solar Gasification of Biomass: Kinetics of Pyrolysis and Steam Gasification in Molten Salt," Journal of Solar Energy Engineering, **133**(2) pp. 021011.

[71] Krueger, K. R., Davidson, J. H., and Lipinski, W., 2011, "Design of a New 45 kWe High-Flux Solar Simulator for High-Temperature Solar Thermal and Thermochemical Research," Journal of Solar Energy Engineering, **133**(1) .

[72] Janz, G.J., 1967, "Molten salts handbook," Academic press New York, .

[73] Kuehn, T., and Goldstein, R., 1976, "Correlating Equations for Natural Convection Heat Transfer between Horizontal Circular Cylinders," International Journal of Heat and Mass Transfer, **19**(10) pp. 1127-1134.

[74] Churchill, S., and Bernstein, M., 1977, "A Correlating Equation for Forced Convection from Gases and Liquids to a Circular Cylinder in Crossflow," ASME Transactions Journal of Heat Transfer, **99**(2) pp. 300-306.

[75] Special Metals Corporation, 2008, "Inconel alloy 600," Special Metals Corporation, SMC-027, USA.

[76] Touloukian, Y.S., and DeWitt, D.P., 1979, "Thermophysical Properties of Matter-the TPRC Data Series,"pp. 787-949.

[77] Touloukian, Y.S., and DeWitt, D.P., 1979, "Thermophysical Properties of Matter-the TPRC Data Series,"pp. 1349-1403.

[78] Howell, J., 1998, "The Monte Carlo Method in Radiative Heat Transfer," Transactions-American Society of Mechanical Engineers Journal of Heat Transfer, **120** pp. 547-560.

[79] Kuehn, T., and Goldstein, R., 1976, "An Experimental and Theoretical Study of Natural Convection in the Annulus between Horizontal Concentric Cylinders," Journal of Fluid Mechanics, **74**(4) pp. 695-719.

[80] Shekar, B. C., Vasseur, P., Robillard, L., and Nguyen, T. H., 1984, "Natural Convection in a Heat Generating Fluid Bounded by Two Horizontal Concentric Cylinders," The Canadian Journal of Chemical Engineering, **62**(4) pp. 482-489.

[81] Yasuyuki, T., Kengo, I., Kenji, F., and Shu, H., 1984, "Three-Dimensional Natural Convection in an Inclined Cylindrical Annulus," International Journal of Heat and Mass Transfer, **27**(5) pp. 747-754.

[82] Hamad, F. A., and Khan, M. K., 1998, "Natural Convection Heat Transfer in Horizontal and Inclined Annuli of Different Diameter Ratios," Energy Conversion and Management, **39**(8) pp. 797-807.

[83] Churchill, S. W., and Chu, H. H., 1975, "Correlating Equations for Laminar and Turbulent Free Convection from a Horizontal Cylinder," International Journal of Heat and Mass Transfer, **18**(9) pp. 1049-1053.

[84] Unifrax I LLC, 2010, "Unifrax Product Information Sheet," Unifrax I LLC, C-1421, USA.

[85] Makino, T., Edamura, M., Kato, A., and Yoshida, A., 1992, "Thermal Radiation Properties of Molten Salt (Properties of Alkali Metal Carbonates)," Heat Transfer.Japanese Research, **21**(4) pp. 331-339.

[86] Special Metals Corporation, 2004, "Inconel alloy X-750," Special Metals Corporation, SMC-067, USA.

[87] Kawale, A., 2013, "Design and Fabrication of a Feedstock Delivery System for a 3kW Solar Gasification Reactor," University of Minnesota Graduate School, .

[88] Brack, M., Häberling, P., Wuillemin, D., and Steinfeld, A., 2007, "A Novel 50 kW 11,000 Suns High-Flux Solar Simulator Based on an Array of Xenon Arc Lamps," Journal of Solar Energy Engineering, **129**(4) pp. 405.

[89] Krueger, K. R., 2012, "Design and Characterization of a Concentrating Solar Simulator," University of Minnesota Graduate School.

[90] Kribus, A., Zaibel, R., Carey, D., Segal, A., and Karni, J., 1998, "A Solar-Driven Combined Cycle Power Plant," Solar Energy, **62**(2) pp. 121-129.

[91] Sudiro, M., and Bertucco, A., 2007, "Synthetic Fuels by a Limited CO_2 emission Process which Uses both Fossil and Solar Energy," Energy Fuels, **21**(6) pp. 3668-3675.

[92] Kaniyal, A. A., van Eyk, P. J., Nathan, G. J., Ashman, P. J., and Pincus, J. J., 2013, "Polygeneration of Liquid Fuels and Electricity by the Atmospheric Pressure Hybrid Solar Gasification of Coal." Energy & Fuels, **27**(6) pp. 3538-3555.

[93] Kaniyal, A. A., van Eyk, P. J., and Nathan, G. J., 2013, "Dynamic Modelling of the Co-Production of Liquid Fuels and Electricity from a Hybrid Solar Gasifier with various Fuel Blends." Energy & Fuels, **27**(6) pp. 3556-3569.

[94] Sheu, E. J., Mitsos, A., Eter, A. A., Mokheimer, E., Habib, M. A., and Al-Qutub, A., 2012, "A Review of Hybrid Solar—Fossil Fuel Power Generation Systems and Performance Metrics," Journal of Solar Energy Engineering, **134**(4) pp. 041006.

[95] Ben-Zvi, R., Epstein, M., and Segal, A., 2011, "Coupling solar tower system and molten salt storage for the generation of electricity using the beam-down optics," Proceedings of the 2011 Solar Power and Chemical Energy Systems conference, Anonymous .

[96] Martinek, J., Channel, M., Lewandowski, A., and Weimer, A. W., 2010, "Considerations for the Design of Solar-Thermal Chemical Processes," Journal of Solar Energy Engineering, **132**(3) pp. 1-6.

[97] George, R., and Maxwell, E., 1999, "High-Resolution Maps of Solar Collector Performance Using A Climatological Solar Radiation Model," Proceedings of ASES Annual Conference, B. W. R. Campbell-Howe, ed. American Solar Energy Society, Portland, ME, pp. 243-248.

[98] Milbrandt, A., 2005, "A Geographic Perspective on the Current Biomass Resource Availability in the United States," National Renewable Energy Laboratory, NREL/TP-560-39181, Golden, Colorado.

[99] Wilcox, S., and Marion, W., 2008, "Users Manual for TMY3 Data Sets," National Renewable Energy Laboratory, NREL/TP-581-43156, Golden, Colorado.

[100] Siegel, N. P., Miller, J. E., Ermanoski, I., Diver, R. B., and Stechel, E. B., 2013, "Factors Affecting the Efficiency of Solar Driven Metal Oxide Thermochemical Cycles," Industrial & Engineering Chemistry Research, **52**(9) pp. 3276-3286.

[101] Hathaway, B. J., Honda, M., Kittelson, D. B., and Davidson, J. H., 2012, "Steam Gasification of Plant Biomass using Molten Carbonate Salts," Energy, **49**(1) pp. 211-217.

[102] Berdahl, P., and Martin, M., 1984, "Emissivity of Clear Skies," Solar Energy, **32**(5) pp. 663-664.

[103] McAdams, W.H., 1954, "Heat Transmission,"McGraw-Hill New York, pp. 321, Chap. 7.

[104] Ladwing, M., and Stevens, M., 2011, "KA26 combined cycle power plant as ideal solution to balance load fluctuations," Power Plant Technology Forum-Hannover Messe, Anonymous .

[105] Walsh, P.P., and Fletcher, P., 2004, "Gas turbine performance," Blackwell Science, Limited, Malden, Mass, .

Appendix A: Comparison between solar and conventional gasification

In this appendix, details on comparing the output of solar and conventional gasification are presented. The comparison is based on the requirements that the product stream have a 2:1 ratio of H_2:CO in order to be amendable for the production of fuels through Fisher Tropsch fuel synthesis and that the product stream exits the reactor at 1200 K to ensure complete carbon conversion. Two different approaches are needed for the two processes. For solar gasification, simple equilibrium calculations suffice to determine the amount of steam required per unit feedstock to achieve the desired H_2:CO ratio. For conventional gasification, the process of combustion is inherent to the reaction, and thus both the temperature and composition of the final products depends on the amount of oxygen added for combustion. Therefore, for conventiona gasification, an isenthalpic reaction energy balance is used in conjunction with the equilibrium calculations. Both approaches require some degree of iteration to locate the conditions that result in the desired product gas composition and temperature.

The calculation of equilibrium in both cases takes place at constant pressure and temperature according to the method of Gibbs free energy minimization,

$$\delta G|_{T,P,N} = \sum_i \mu_i \, \delta N_i = 0 \tag{A.1}$$

where μ_i is the chemical potential of species i and N_i is the number of moles of species i. The chemical potentials for each species considered are available from a lookup function included with the equilibrium solver that was used to determine equilibrium compositions, *Chemical Equilibrium with Applications* (*CEA)* provided by NASA Glenn Research Center (grc.nasa.gov/WWW/CEAWeb/).

For both processes, and initial feedstock is first specified. In this case we use the low-input high-diversity perennial blends of Tilman et. al. [3] which have readily available values for yield and energy content. The typical annual yield from non-arable land is 3,682 kg/ha with an average energy content on a LHV basis of 16.87 MJ/kg. This results in an embodied energy yield of 62.1 GJ/ha annually or, in the units found in Fig. 1.2, 209 GGE/Acre. (Gallon Gasoline Equivilent, where 1 GGE = 120 MJ) For chemical

calculations, the feedstock has an average chemical formula $CH_{1.44}O_{0.648}$ based on ultimate analysis.

For the conventional gasification system, the process is considered to be isenthalpic with the requirement

$$H_{\text{reactants}} = H_{\text{products}} \tag{A.2}$$

with the reactant enthalpy given by

$$H_{\text{reactants}} = n_{\text{feed}} \cdot h_{\text{f,feed}} + n_{O_2} \cdot h_{O_2} + n_{H_2O} \cdot h_{H_2O} \tag{A.3}$$

and for the products, a only species with concentrations greater than 10^{-5} were included, limiting the products to H_2, CO, CO_2, H_2O, with the resulting product enthalpy of

$$H_{\text{products}} = n_{H_2} \cdot h_{H_2} + n_{CO} \cdot h_{CO} + n_{CO_2} \cdot h_{CO_2} + n_{H_2O} \cdot h_{H_2O} \tag{A.4}$$

For each species, the specific enthalpy includes the enthalpy of formation and is calculated against a reference temperature of 273.15 K.

$$h_i(T) = h_{\text{f,i}} + \int_{273.15\text{ K}}^{T} C_P \, \mathrm{d}T \tag{A.5}$$

Iterative estimation of the amount of oxygen and steam allowed the two constraints of a final temperature of 1200 K and a 2:1 H_2:CO ratio to be achieved with $\frac{n_{O_2}}{n_{\text{feed}}} = 0.472$ and $\frac{n_{H_2O}}{n_{\text{feed}}} = 1.76$. The specific yield of the useful (only H_2 and CO) product gas was $\frac{n_{H_2}}{n_{\text{feed}}} = 0.753$ and $\frac{n_{CO}}{n_{\text{feed}}} = 0.375$, or on an energetic basis, 12.1 GJ/kg-feed. Given the previously mentioned annual yield of feedstock per acre, potential energetic yield from conventional gasification is 137 GGE/acre.

For solar gasification, iterative estimation of the steam to feedstock led to the constraints being met with $\frac{n_{H_2O}}{n_{\text{feed}}} = 1.52$. The resulting specific yield of useful product gas was $\frac{n_{H_2}}{n_{\text{feed}}} = 1.383$ and $\frac{n_{CO}}{n_{\text{feed}}} = 0.689$, or on an energetic basis, 22.2 GJ/kg-feed, with the potential annual yield on a per acre basis of 251 GGE/acre.

In summary, the potential annual yield of energy per acre land used to grow feedstock, on an LHV basis, is 209 GGE/acre for raw feedstock, 137 GGE/acre after conventional gasification, and 251 GGE/acre for solar gasification. These results are for non-arable land, for feedstock grown on fertile land, increase the yields by a multiplier of 1.63 [3].

Appendix B: Aperture sizing and solar simulator flux / power calculations

In this appendix, the selection of aperture size and calculation of power for the reactor testing is presented. The flux incident at the focal plane of the University of Minnesota high-flux solar simulator (HFSS) is not uniform, but has a roughly Gaussian distribution about the focal point. Therefore, to select an aperture size for the reactor, the flux distribution is integrated over a circular area until an integration radius is found that meets the target value of 3 kW_{th} total power absorbed.

Based on the initial design of the HFSS, it was determined that the solar gasification reactor would be operated using only 3 of the 7 radiation units (lamps) in order to obtain an average flux in the vicinity of 1500 suns. The lamp arrangement is of a hexagonal array of 6 lamps with a centered 7^{th} lamp. Following construction, measurements were made of the actual flux distributions from each lamp according to the method of Brack et al. [88]. The planned method of operating the solar gasification reactor is to use only lamps on the periphery of the HFSS array to avoid directing radiation to the back wall of the cavity, which is not in contact with molten salt. All the peripheral lamps have a similar flux distribution to that of lamp 1 shown in Figure B.1.

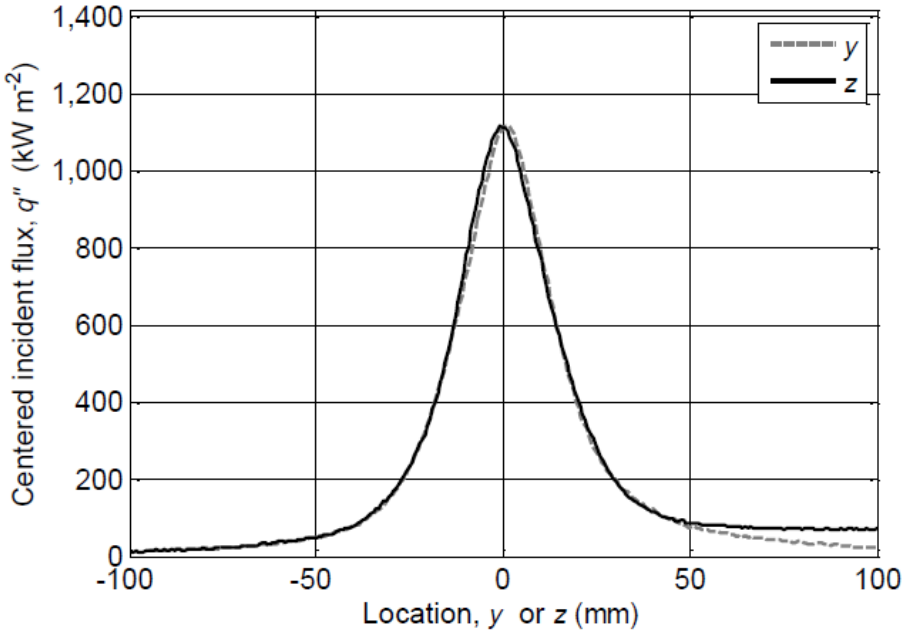

Fig. B.1 Representative flux distribution for a focused peripheral lamp of the UMN HFSS.

In order to obtain an aperture size that intercepts roughly 3 kW_{th} on average for any 3 of the lamps on the periphery of the HFSS array, numerical integration of the flux distributions of all 6 lamps simultaneously was carried out with a target power of 6 kW_{th}.

$$\dot{Q}_{\text{target}} = 6\ \text{kW} = \sum_{i=1}^{6} \int_{0}^{2\pi} \int_{0}^{r_{\text{ap}}} q_i''(r)\, r\, dr\, d\theta \tag{B.1}$$

At an aperture radius of 25 mm, the target power was achieved, with an average flux over the aperture area of 3060 suns. When operating with any combination of 3 of the 6 periphery lamps, the intercepted power will on average be 3 kW_{th} with an average concentration of 1530 suns with a design aperture diameter of $d_{\text{ap}} = 5\text{cm}$.

Prior to testing of the gasification reactor, localized hot-spots resulting in melting were observed in other cavity devices tested within the HFSS. As a precaution, it was decided to de-focus the intended lamps for the first test to reduce the risk of damage from hot-spots and allow the reactor parts to be inspected for signs of deformation due to localized overheating before applying the full design power. Evenly spaced peripheral lamps (units 2, 3, and 7) were adjusted to move the arc 2.5mm forward (away from the reflector) of the focal point.

Following lamp adjustment and prior to reactor testing, the Lambertian reflector

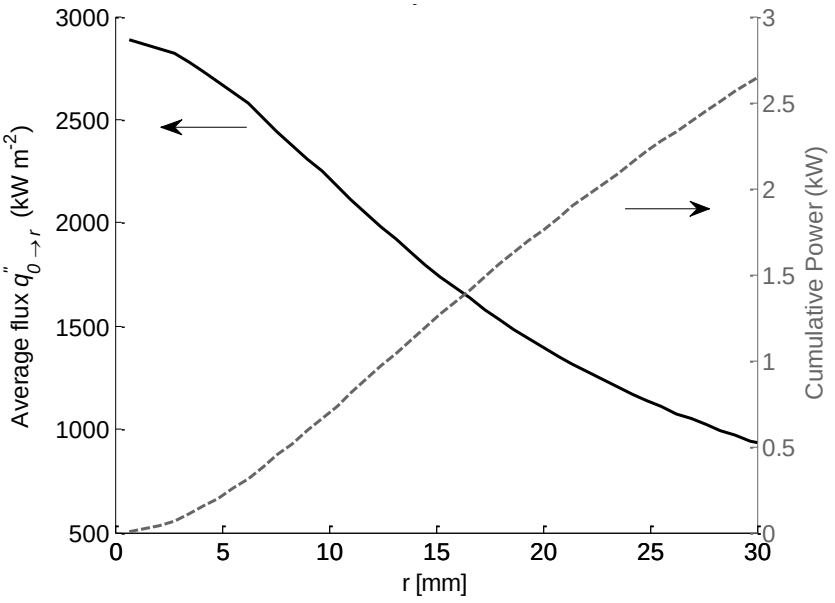

Fig. B.2 Average flux and cumulative power for lamps 2, 3, and 7 in the defocused state used during testing of the solar biomass gasification reactor.

target was co-mounted with the gasification reactor in the same focal plane. The lamps intended for use in the test were then activated and an image of the reflected radiation was obtained. Using the calibration constant established by Krueger [89], the camera intensities were converted to fluxes producing the average fluxes and cumulative power values shown in Fig. B.2 for various aperture sizes. For the biomass gasification reactor's 5 cm diameter, the average flux with propagated uncertainty described in Appendix D was 1132±126 suns and the incident power was 2.22±0.25 $kW_{th.}$

Appendix C: Engineering Drawings

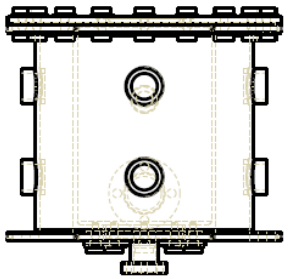

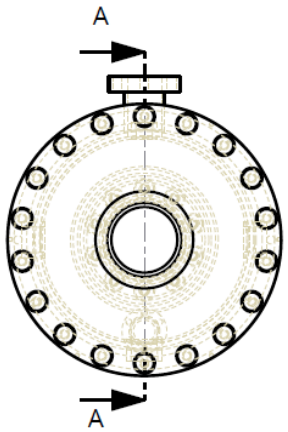

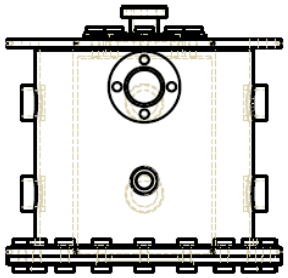

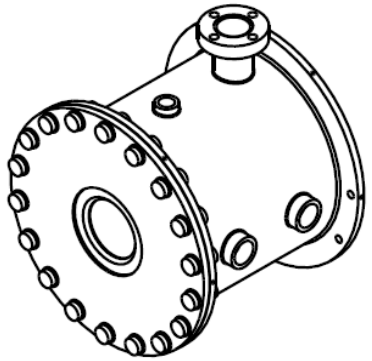

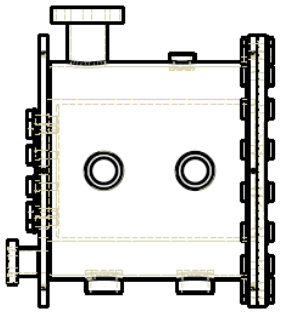

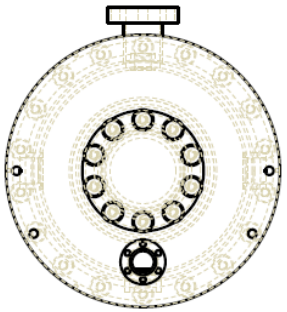

UNIVERSITY OF MINNESOTA		
General Tolerances 0.060in (1.5mm)	Assembly Overview	
Drawn by: B. J. Hathaway Rev: March 10, 2012	Scale: 0.25	DWG: 1/7

#	Part Name	Qty.	Dwg.
1	Outer Housing	1	3,4
2	Cavity	1	5,6
3	Endcap	1	7
4	1/4 - 20UNC - 1" BOLT	18	-
5	1/4 - 20UNC - NUT	18	-
6	1/4 - WSHR	54	-
7	1/4 - 20UNC - 3/4 CAPSCR	10	-
8	1/4 - 20UNC - 1.5" BOLT	4	-
9	#8 - 32UNC - 1" BOLT	6	-
10	#8 - 32UNC - NUT	6	-
11	#8 WSHR	12	-
12	1/4 - NPT PLUG	1	-
13	1/2 - NPT PLUG	6	-

NOTE: All components shall be INCONEL alloy X-750 (or UNS N07750) unless otherwise specified. All X-750 components, including fasteners, require triple heat treatment consisting of 2100° F solution treatment 1550° F stabilization treatment 1300° F precipitation treatment to be completed AFTER any welding.

NOTE: Washers and NPT Plugs may be 316 SS if X-750 unavailable

NOTE: Assembly will experience extreme thermal cycling. Ensure all welds fully penetrate the material and are of high quality.

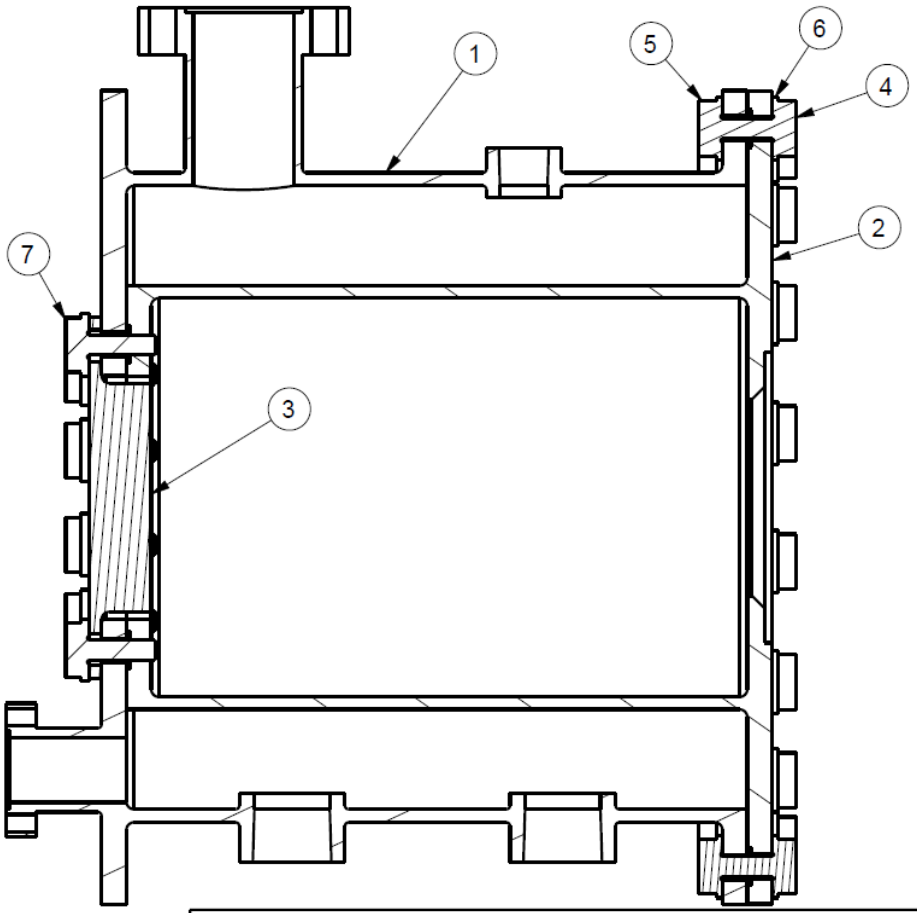

SECTION A-A
SCALE 0.750

UNIVERSITY OF MINNESOTA		
General Tolerances 0.060in (1.5mm)	Assembly Cross-section	
Drawn by: B. J. Hathaway Rev: March 10, 2012	Scale: 0.75	DWG: 2/7

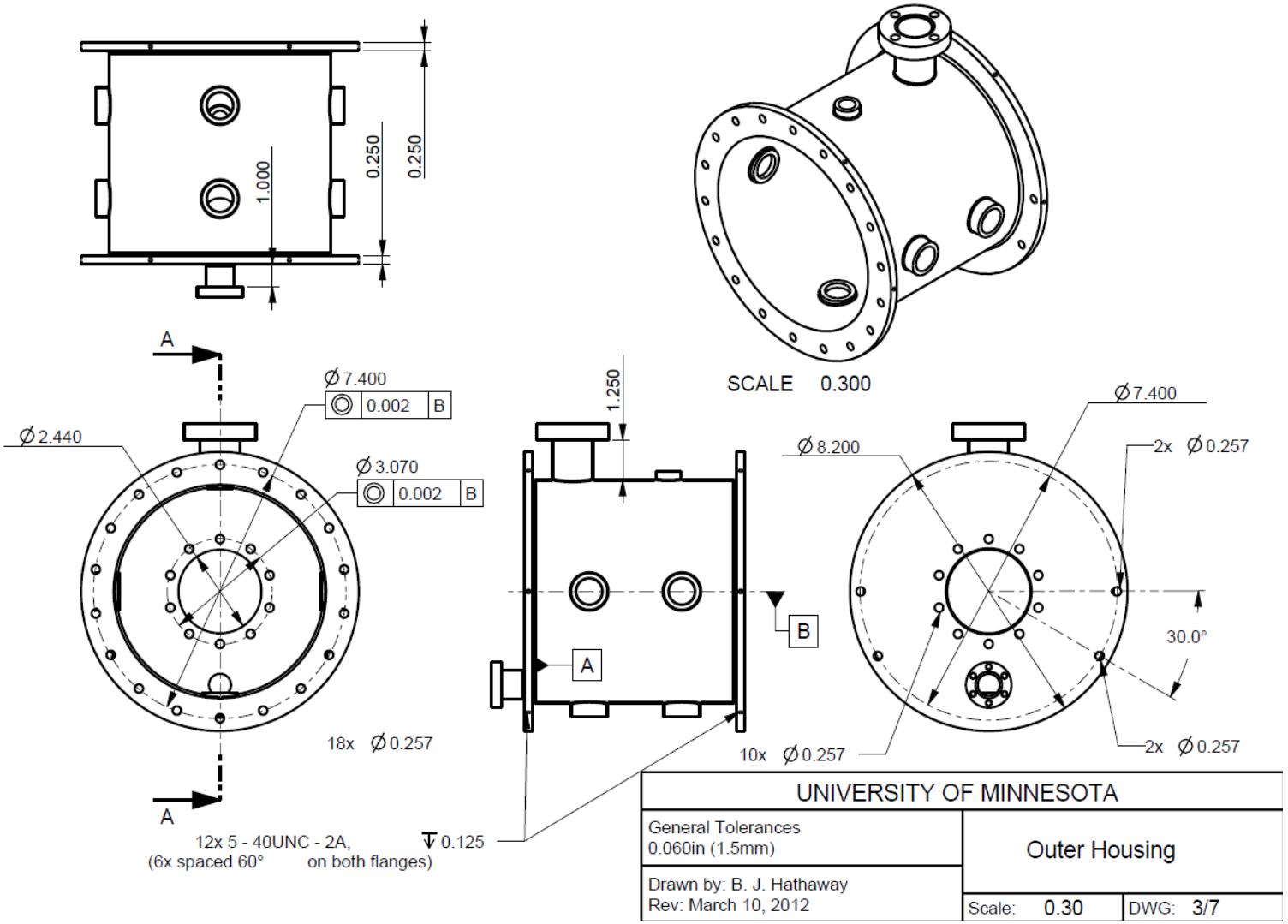

UNIVERSITY OF MINNESOTA		
General Tolerances 0.060in (1.5mm)	Outer Housing	
Drawn by: B. J. Hathaway Rev: March 10, 2012	Scale: 0.30	DWG: 3/7

#	Feature	Description
1	Outlet Flange	2-1/8" CF Flange
2	Drain flange	1-1/3" CF Flange
3	Probe Port	1x 1/4" NPT
4	Feed Ports	6x 1/2" NPT
5	Housing Wall	6.500" OD, 6.240" ID
6	Outlet Tube	1.000" OD, 0.834" ID
7	Drain Tube	0.750" OD, 0.510" ID

NOTE: Flatness tolerance on datum plane "A" may be relaxed outside of regions that will be in direct contact when assembled. (Beyond diameter of 4.25" about datum axis "B".)

NOTE: NPT fitting size and radial placement not specified. Fittings ought to be STD NPT port size and placed for manufacturability while minimizing intrusion into the housing.

NOTE: Drawing lacks design details of the outlet and drain CF flanges. If welding compatability allows, these two flanges may be off the shelf Inconel or 316 SS material CF flanges (e.g. Kurt J Lesker p/n's F0133N075NLN and F0212N000NLN). Otherwise flanges should be manufactured to CF flange specifications for compatability with any same sized CF flanges.

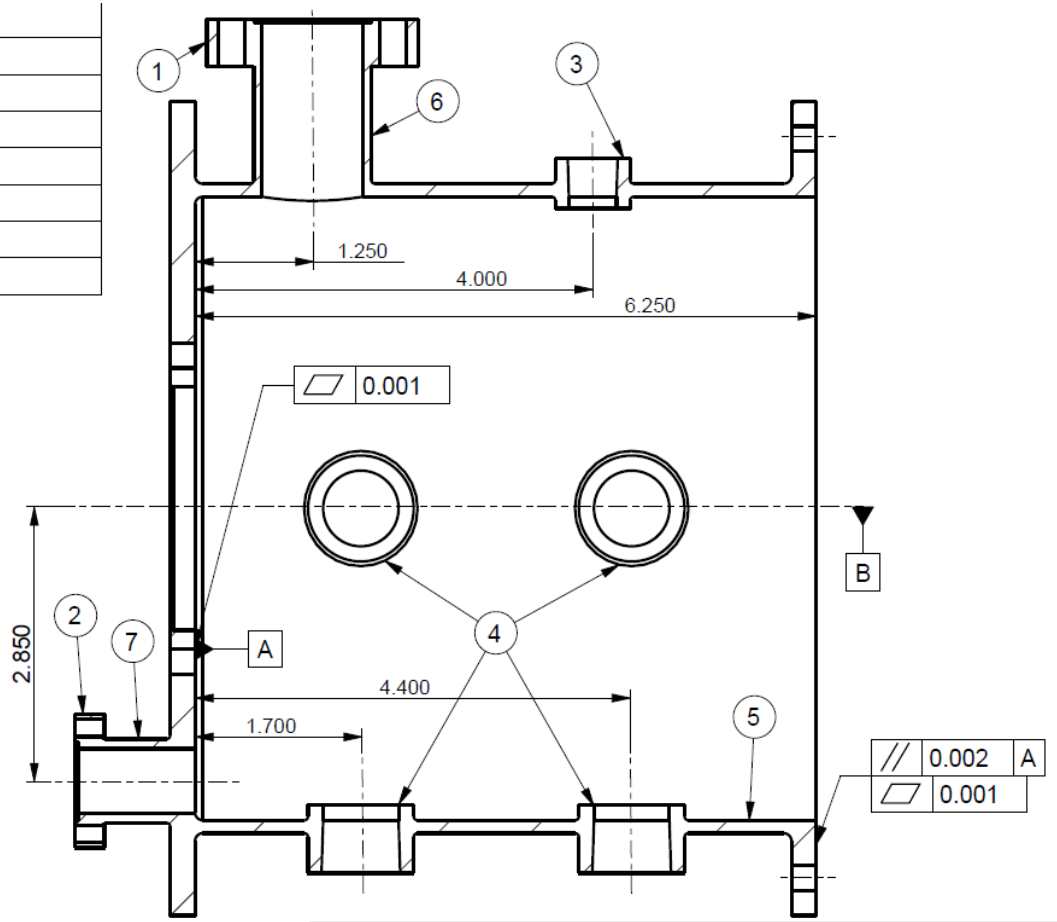

SECTION A-A
SCALE 0.750

UNIVERSITY OF MINNESOTA		
General Tolerances 0.060in (1.5mm)	Outer Housing Cross-section	
Drawn by: B. J. Hathaway Rev: March 10, 2012	Scale: 0.75	DWG: 4/7

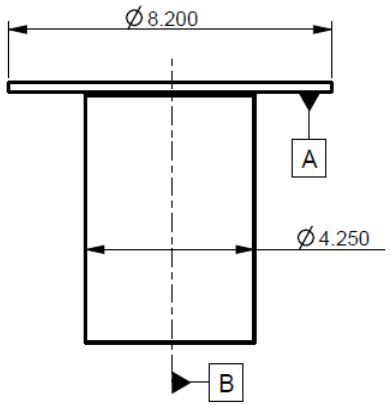

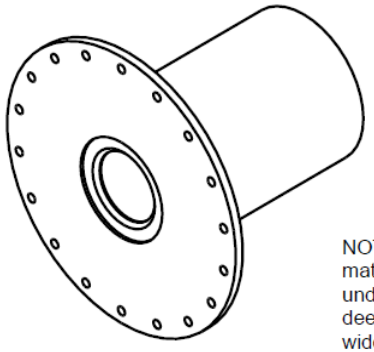

SCALE 0.300

NOTE: All flange mating surfaces undercut 1/16" deep and 3/8" wide centered on the bolt circle

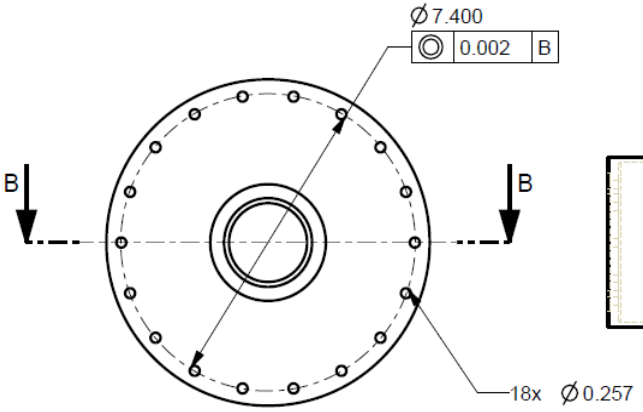

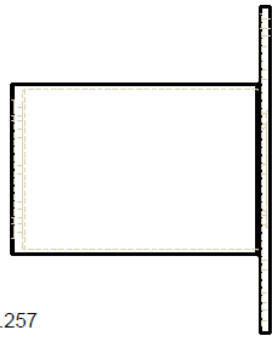

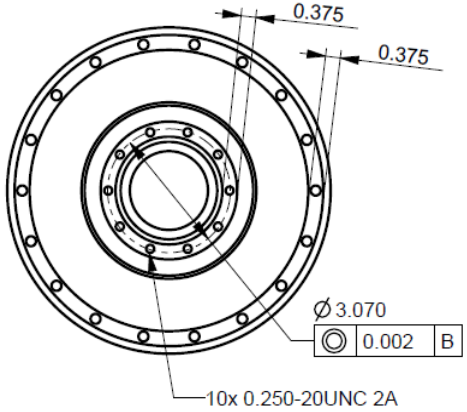

UNIVERSITY OF MINNESOTA		
General Tolerances 0.060in (1.5mm)	Cavity	
Drawn by: B. J. Hathaway Rev: March 10, 2012	Scale: 0.30	DWG: 5/7

#	Feature	Description
1	Cavity Wall	4.250" OD, 4.000" ID

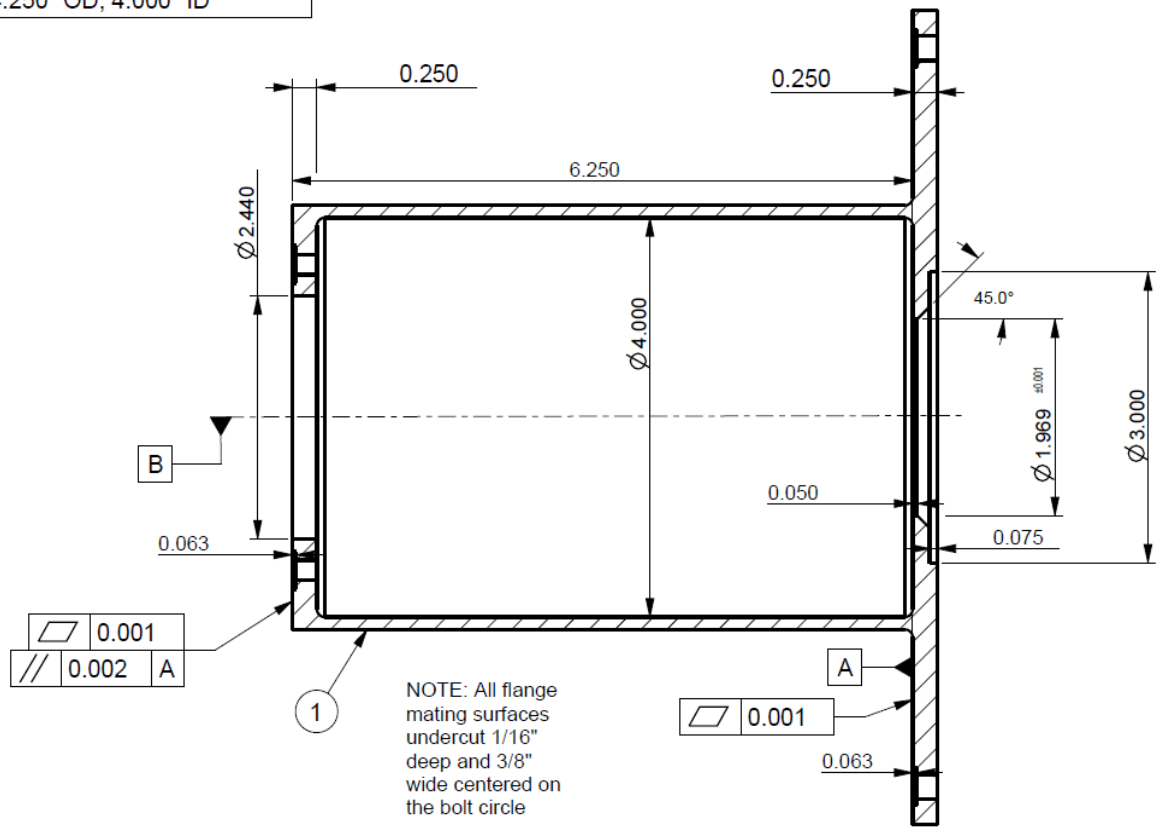

NOTE: Flatness tolerance on datum plane "A" may be relaxed outside of regions that will be in direct contact when assembled. (Within diameter of 6.24" about datum axis "B".)

SECTION B-B
SCALE 0.750

UNIVERSITY OF MINNESOTA		
General Tolerances 0.060in (1.5mm)	Cavity Cross-section	
Drawn by: B. J. Hathaway Rev: March 10, 2012	Scale: 0.75	DWG: 6/7

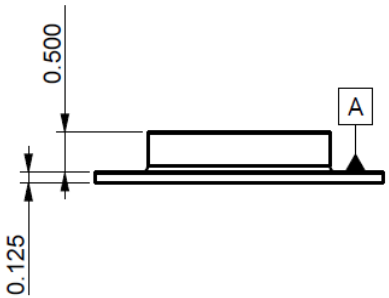

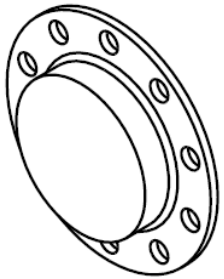

SCALE 0.600

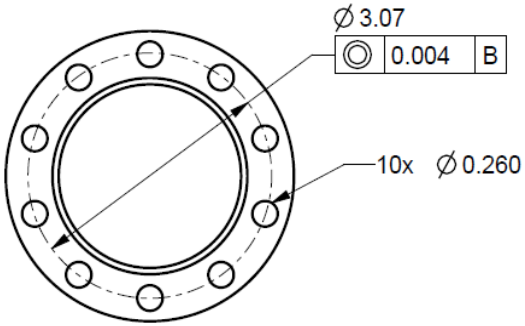

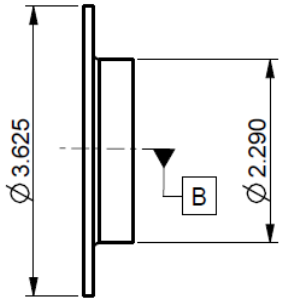

UNIVERSITY OF MINNESOTA		
General Tolerances 0.060in (1.5mm)	Endcap	
Drawn by: B. J. Hathaway Rev: March 10, 2012	Scale: 0.60	DWG: 7/7

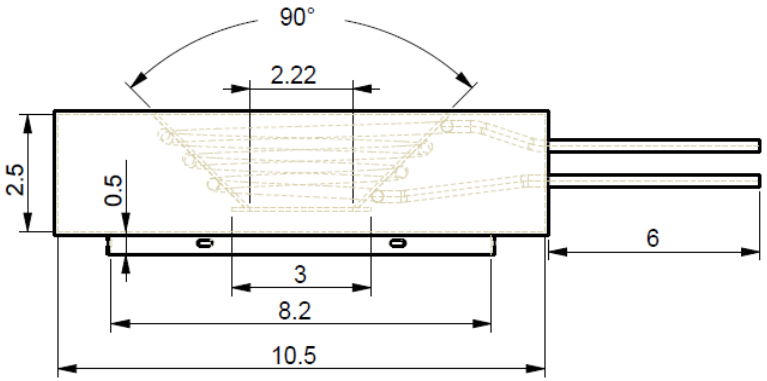

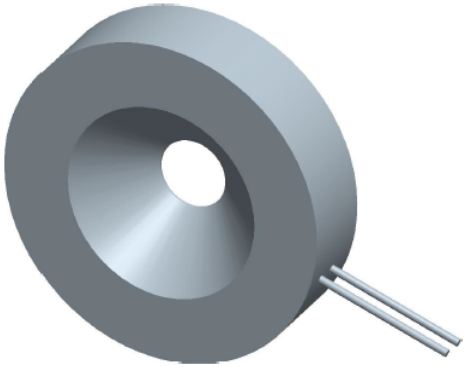

SCALE 0.250

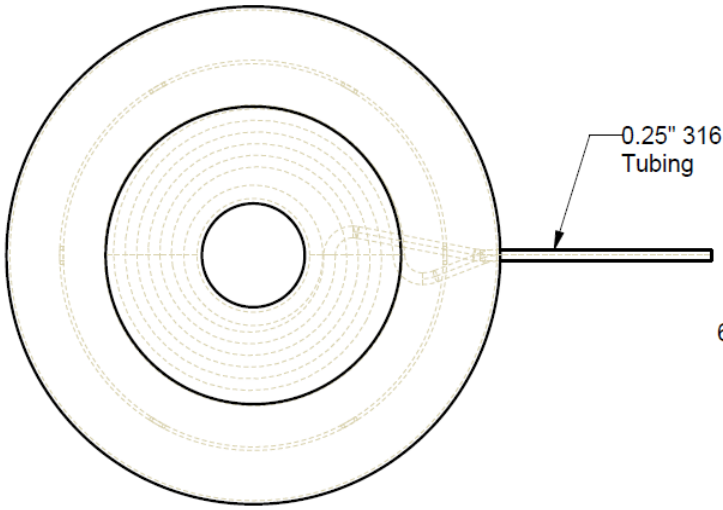

SCALE 0.350

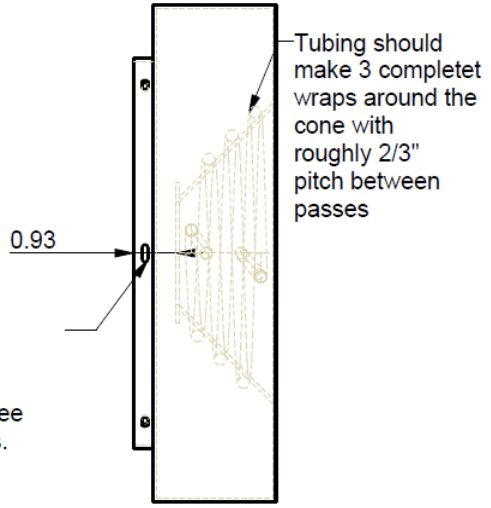

For heat transfer purposes, the cone portion of the front shield MUST be made from at least 16 Guage (1/16") stainless steel sheet. The remaining surfaces may be thinner if manufacturablility allows.

UNIVERSITY OF MINNESOTA		
General Tolerances 0.060in (1.5mm)	Front Shield w/ Cooling	
Drawn by: B. J. Hathaway Rev: August 20, 2012	Scale:	DWG: 1/2

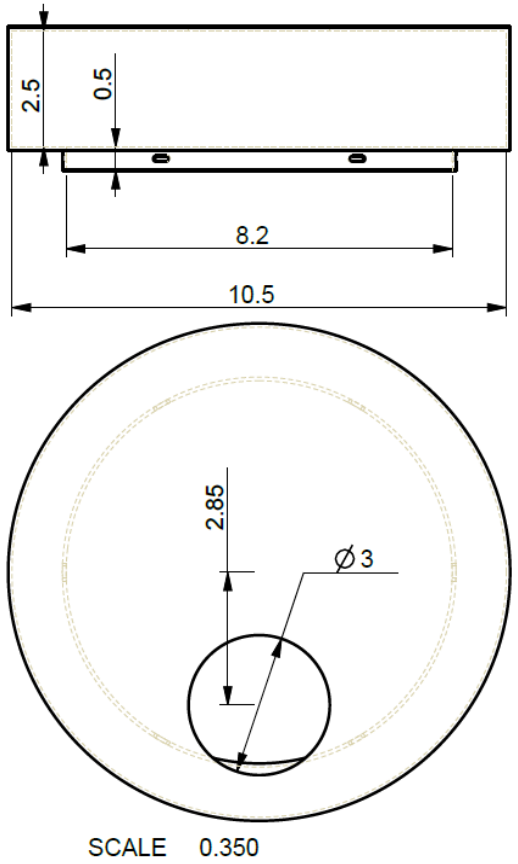

SCALE 0.350

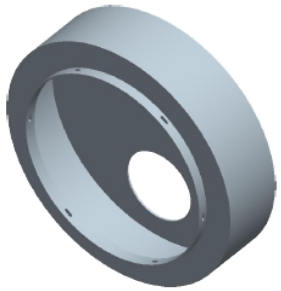

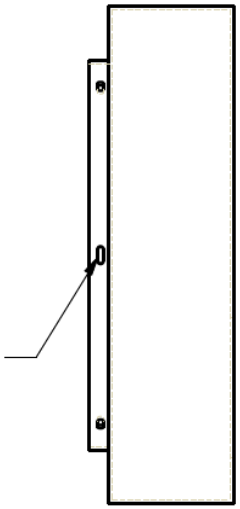

6x 0.125" Width Slotted Hole spaced in even 60 degree increments.

The rear shield only exists to hold insulation in place and is not load bearing, thus the thinnest manufacturable guage of sheet metal may be used.

UNIVERSITY OF MINNESOTA		
General Tolerances 0.060in (1.5mm)	Rear Shield	
Drawn by: B. J. Hathaway Rev: August 20, 2012	Scale:	DWG: 2/2

Appendix D: Experimental uncertainty analysis

This appendix covers the propagation of uncertainty form the raw experimental measurements to the final calculated performance indicators of specific yield, solar efficiency, and cold gas efficiency. The base measured values involved in the calculated performance indicators include N_2 and CO_2 volumetric flow rate, volume (or mole) fractions of N_2, CO, H_2, CO_2, CH_4, mass flow rate of feedstock, and LHV of feedstock. The mass flow controllers are all MKS series 1176 and calibrated to an uncertainty of ±1% of the indicated setpoint. The volume fractions of gasses are determined from a RLGA-8800 series Raman laser gas analyzer with ±0.25% total uncertainty for all gases except CH_4, which is certain to ±0.06%. The feed delivery rate is calibrated to a relative uncertainty of ±2% of the target delivery rate, while the feedstock LHV was calculated by an outside laboratory (Huffman Labs) to a relative uncertainty of ±0.5%.

Table D.1 contains the measured values and associated measurement uncertainties for these terms as averaged over the period of steady operation. This period begins when the CO volume fraction reaches the approximately steady value of 20% and ends when the yield rates drop off after the feed system became blocked.

Table D.1 Base measured values averaged over the steady operation period and associated measurement uncertainty within a 95% CI.

Measurand	Value	Uncertainty, w_i
Injector N_2 Flow, $\dot{V}_{N_2,\mathrm{inj}}$	3570 SCCM	±36 SCCM
Hopper N_2 Flow, $\dot{V}_{N_2,\mathrm{hop}}$	100 SCCM	±1 SCCM
Dilution N_2 Flow, $\dot{V}_{N_2,\mathrm{dil}}$	1990 SCCM	±20 SCCM
Injector CO_2 Flow, $\dot{V}_{CO_2,\mathrm{inj}}$	2000 SCCM	±20 SCCM
N_2 Volume Fraction, y_{N_2}	39.19%	±0.25%
H_2 Volume Fraction, y_{H_2}	7.57%	±0.29%
CO Volume Fraction, y_{CO}	23.72%	±0.30%
CO_2 Volume Fraction, y_{CO_2}	24.27%	±0.30%
CH_4 Volume Fraction, y_{CH_4}	4.30%	±0.6%
Feed Delivery Rate, $\dot{m}_{\mathrm{feed}}$	6.92 g/min	±0.14 g/min
Feed Heating Value, $\mathrm{LHV}_{\mathrm{feed}}$	15950 kJ/kg	±80 kJ/kg

In Table D.1, the total uncertainties, w_i, take into account both random uncertainty due to variation during the averaging period and the systematic uncertainty inherent to the measurement equipment as described previously. The total uncertainty is calculated by

$$w_i = \left[B_i^2 + P_i^2\right]^{1/2} \tag{D.1}$$

where B_i is the systematic uncertainty and P_i is the random uncertainty. The random uncertainty is calculated from the standard deviation of the measured data points, σ_x, the number of data points n, and the value of $t = 1.96$ obtained from the student's *t*-distribution for a 95% confidence interval and more than 30 data points according to

$$P_i = t\frac{\sigma_x}{\sqrt{n}} \tag{D.2}$$

Uncertainty is propagated in the calculated terms according to the following equation for a general calculated term R based on uncertain terms x_i,

$$w_R = \left[\sum_i \left(w_{x_i}\frac{\partial R}{\partial x_i}\right)^2\right]^{1/2} \tag{D.3}$$

The specific yield of useful syngas is calculated according to

$$S_Y = \frac{\dot{m}_{\text{gas}}}{\dot{m}_{\text{feed}}} = \frac{\dot{V}_{\text{CO}}\cdot\rho_{\text{CO}} + \dot{V}_{\text{H}_2}\cdot\rho_{\text{H}_2} + \dot{V}_{\text{CH}_4}\cdot\rho_{\text{CH}_4}}{\dot{m}_{\text{feed}}} \tag{D.4}$$

Substituting X_S for R in eq. (D.1) yields the equation for uncertainty in specific yield.

$$\begin{aligned} w_{S_Y} = \Bigg[&\left(w_{\dot{m}_{\text{feed}}}\cdot\frac{S_Y}{\dot{m}_{\text{feed}}}\right)^2 + \left(w_{\dot{V}_{\text{CO}}}\cdot\frac{\rho_{\text{CO}}}{\dot{m}_{\text{feed}}}\right)^2 + \left(w_{\dot{V}_{\text{H}_2}}\cdot\frac{\rho_{\text{H}_2}}{\dot{m}_{\text{feed}}}\right)^2 \\ &+ \left(w_{\dot{V}_{\text{CH}_4}}\cdot\frac{\rho_{\text{CH}_4}}{\dot{m}_{\text{feed}}}\right)^2\Bigg]^{1/2} \end{aligned} \tag{D.5}$$

The volume flow rate of gas species i is calculated based on the measured volume fractions and the volume flow rate of nitrogen reported from the mass flow controllers.

$$\dot{V}_i = \dot{V}_{\text{N}_2}\cdot\frac{y_i}{y_{\text{N}_2}} \tag{D.6}$$

with the uncertainty in the gas flow of species i found from

$$w_{\dot{V}_i} = \dot{V}_i\cdot\left[\left(\frac{w_{\dot{V}_{\text{N}_2}}}{\dot{V}_{\text{N}_2}}\right)^2 + \left(\frac{w_{y_i}}{y_i}\right)^2 + \left(\frac{w_{y_{\text{N}_2}}}{y_{\text{N}_2}}\right)^2\right]^{1/2} \tag{D.7}$$

and the total nitrogen flow rate

$$\dot{V}_{\text{N}_2} = \dot{V}_{\text{N}_2,\text{inj}} + \dot{V}_{\text{N}_2,\text{hop}} + \dot{V}_{\text{N}_2,\text{dil}} \tag{D.8}$$

with associated uncertainty

$$w_{\dot{V}_{\mathrm{N_2}}} = \left(w_{\dot{V}_{\mathrm{N_2,inj}}}^2 + w_{\dot{V}_{\mathrm{N_2,hop}}}^2 + w_{\dot{V}_{\mathrm{N_2,dil}}}^2 \right)^{1/2} \tag{D.9}$$

The mass flow controllers report flow rates at standard conditions (1 atm and 273.15 K) regardless of actual ambient conditions, so all density terms may be calculated directly from the ideal gas law and are considered sufficiently certain to not contribute to propagated uncertainty.

The definition of solar efficiency used here is

$$\begin{aligned} \eta_{\mathrm{solar}} &= \frac{\sum_{\mathrm{i}} \dot{m}_i \cdot \mathrm{LHV}_i}{\dot{Q}_{\mathrm{solar}} + \dot{m}_{\mathrm{feed}} \cdot \mathrm{LHV}_{\mathrm{feed}}} \\ &= \frac{\dot{V}_{\mathrm{CO}} \cdot \rho_{\mathrm{CO}} \cdot \mathrm{LHV}_{\mathrm{CO}} + \dot{V}_{\mathrm{H_2}} \cdot \rho_{\mathrm{H_2}} \cdot \mathrm{LHV}_{\mathrm{H_2}} + \dot{V}_{\mathrm{CH_4}} \cdot \rho_{\mathrm{CH_4}} \cdot \mathrm{LHV}_{\mathrm{CH_4}}}{\dot{Q}_{\mathrm{solar}} + \dot{m}_{\mathrm{feed}} \cdot \mathrm{LHV}_{\mathrm{feed}}} \end{aligned} \tag{D.10}$$

Applying eq. (D.3) yields the propagated uncertainty of

$$\begin{aligned} w_{\eta_{\mathrm{solar}}} = \Bigg[& \left(w_{\dot{m}_{\mathrm{feed}}} \cdot \frac{\eta_{\mathrm{solar}}}{\frac{\dot{Q}_{\mathrm{solar}}}{\mathrm{LHV}_{\mathrm{feed}}} + \dot{m}_{\mathrm{feed}}} \right)^2 + \left(w_{\mathrm{LHV}_{\mathrm{feed}}} \cdot \frac{\eta_{\mathrm{solar}}}{\frac{\dot{Q}_{\mathrm{solar}}}{\dot{m}_{\mathrm{feed}}} + \mathrm{LHV}_{\mathrm{feed}}} \right)^2 \\ & + \left(w_{\dot{Q}_{\mathrm{solar}}} \cdot \frac{\eta_{\mathrm{solar}}}{\dot{Q}_{\mathrm{solar}} + \dot{m}_{\mathrm{feed}} \cdot \mathrm{LHV}_{\mathrm{feed}}} \right)^2 \\ & + \left(w_{\dot{V}_{\mathrm{CO}}} \cdot \frac{\rho_{\mathrm{CO}} \cdot \mathrm{LHV}_{\mathrm{CO}}}{\dot{Q}_{\mathrm{solar}} + \dot{m}_{\mathrm{feed}} \cdot \mathrm{LHV}_{\mathrm{feed}}} \right)^2 \\ & + \left(w_{\dot{V}_{\mathrm{H_2}}} \cdot \frac{\rho_{\mathrm{H_2}} \cdot \mathrm{LHV}_{\mathrm{H_2}}}{\dot{Q}_{\mathrm{solar}} + \dot{m}_{\mathrm{feed}} \cdot \mathrm{LHV}_{\mathrm{feed}}} \right)^2 \\ & + \left(w_{\dot{V}_{\mathrm{CH_4}}} \cdot \frac{\rho_{\mathrm{CH_4}} \cdot \mathrm{LHV}_{\mathrm{CH_4}}}{\dot{Q}_{\mathrm{solar}} + \dot{m}_{\mathrm{feed}} \cdot \mathrm{LHV}_{\mathrm{feed}}} \right)^2 \Bigg]^{1/2} \end{aligned} \tag{D.11}$$

where the LHV for each gas is obtained from published data with sufficient certainty to not contribute to propagated uncertainty.

The solar power input in this term is obtained as described in Appendix B by integrating the measured grayscale intensity of light reflected from a Lambertian target placed in the focal region over the area of the aperture of the reactor multiplied by the calibration constant to convert intensity to flux.

$$\dot{Q}_{\mathrm{solar}} = C_{\mathrm{flux}} \cdot \int_0^{2\pi} \int_0^{d_{\mathrm{ap}}/2} I(r, \theta) \cdot r \cdot \mathrm{d}r \, \mathrm{d}\theta \tag{D.12}$$

with the propagated uncertainty for the final integrated value of

$$w_{\dot{Q}_{\text{solar}}} = \left[\left(w_{C_{\text{flux}}} \int_0^{2\pi} \int_0^{d_{\text{ap}}/2} I(r,\theta) \cdot r \cdot \mathrm{d}r \, \mathrm{d}\theta \right)^2 + \left(w_I \cdot C_{\text{flux}} \cdot \frac{\pi d_{\text{ap}}^2}{4} \right)^2 + \left(w_{d_{\text{ap}}} \cdot \frac{2}{d_{ap}} \cdot C_{\text{flux}} \cdot \int_0^{2\pi} \int_0^{d_{\text{ap}}/2} I(r,\theta) \cdot r \cdot \mathrm{d}r \, \mathrm{d}\theta \right)^2 \right]^{1/2} \tag{D.13}$$

where the calibration constant has a relative uncertainty of ±12.7% [89]. The certainty of the calibration constant is dominant in this term due to the relativley high accuracy of grayscale intensity measurement and high degree of machining accuracy, resulting in a relative uncertainty in the incident power of $\frac{w_{\dot{Q}_{\text{solar}}}}{\dot{Q}_{\text{solar}}} = 12.8\%$.

The cold gas efficiency is given by

$$\eta_{\text{CG}} = \frac{\sum_{\text{i}} \dot{m}_i \cdot \text{LHV}_i}{\dot{m}_{\text{feed}} \cdot \text{LHV}_{\text{feed}}} = \frac{\dot{V}_{\text{CO}} \cdot \rho_{\text{CO}} \cdot \text{LHV}_{\text{CO}} + \dot{V}_{\text{H}_2} \cdot \rho_{\text{H}_2} \cdot \text{LHV}_{\text{H}_2} + \dot{V}_{\text{CH}_4} \cdot \rho_{\text{CH}_4} \cdot \text{LHV}_{\text{CH}_4}}{\dot{m}_{\text{feed}} \cdot \text{LHV}_{\text{feed}}} \tag{D.14}$$

where the propagated uncertainty using eq. (D.1) is

$$w_{\eta_{\text{CG}}} = \left[\left(w_{\dot{m}_{\text{feed}}} \cdot \frac{\eta_{\text{CG}}}{\dot{m}_{\text{feed}}} \right)^2 + \left(w_{\text{LHV}_{\text{feed}}} \cdot \frac{\eta_{\text{CG}}}{\text{LHV}_{\text{feed}}} \right)^2 + \left(w_{\dot{V}_{\text{CO}}} \cdot \frac{\rho_{\text{CO}} \cdot \text{LHV}_{\text{CO}}}{\dot{m}_{\text{feed}} \cdot \text{LHV}_{\text{feed}}} \right)^2 + \left(w_{\dot{V}_{\text{H}_2}} \cdot \frac{\rho_{\text{H}_2} \cdot \text{LHV}_{\text{H}_2}}{\dot{m}_{\text{feed}} \cdot \text{LHV}_{\text{feed}}} \right)^2 + \left(w_{\dot{V}_{\text{CH}_4}} \cdot \frac{\rho_{\text{CH}_4} \cdot \text{LHV}_{\text{CH}_4}}{\dot{m}_{\text{feed}} \cdot \text{LHV}_{\text{feed}}} \right)^2 \right]^{1/2} \tag{D.15}$$

Solving eqs. (D.4) through (D.15) based on the measured values given in Table D.1 allows us to obtain the final calculated values and uncertainties of the key performance parameters as listed in Table D.2.

Table D.2 Calculated values and associated measurement uncertainty within a 95% CI.

Calculated Term	Value	Uncertainty, w_i
Specific Yield, S_Y	70.3%	±1.7%
Solar Efficiency, η_{solar}	32%	±2.3%
Cold Gas Efficiency, η_{CG}	70.5%	±1.7%

Appendix E: Computational source codes

Index

cav2mat.f90 - Cavity simulation output to MATLAB output conversion

flux_interfacing.c - UDF for interfacing FLUENT with cavity simulations

GenOptFit.f90 - Reacting tablet pyrolysis/gasification simulation for optimization

sub_adpcavsim.f0 - Parallel adiabatic cavity MCRT radiative simulation subroutine

sub_cav2flu.f90 - Cavity simulation output to FLUENT UDF interface

sub_cavsim.f90 - Cavity MCRT radiative simulation subroutine

sub_pcavsim.f90 - Parallel cavity MCRT radiative simulation subroutine

sub_lib.f90 - Library of general subroutines used by other files

Current filename is listed at the top of each page. All programs are written in either the FORTRAN90 or C languages and with compiler-specific nuances favored towards the GNU Compiler Collection. The “flux_interfacing.c” file contains notation specific to FLUENT UDF compilation.

```
program cav2mat
!-------------------------------------------------------------------------------
!  A program to run Monte-Carlo Ray Tracing radiative transfer simulations and
!  output the results to a MATLAB m-file for quick data analysis.
!
!  Syntax: cav2mat mode isoval Dx100 Lx100 Csuns imatl (Nrays)
!
!  Inputs:  mode     - 1 for isothermal, 2 for adiabatic, 3 for constant flux
!                      or 4 for specified heat transfer coefficient
!           isoval   - Isothermal, constant flux, or convection value
!           Dx100    - Cavity diameter / aperture diameter ratio x 100
!           Lx100    - Cavity length / diameter aspect ratio x 100
!           Csuns    - Concentration of incident sunlight (1 [sun] = 1 [kW/m^2])
!           imatl    - Material index (0-black, 1-inco, 2-alumina, 3-grey)
!           Nrays    - OPTIONAL Number of rays. Defaults to 100 million.
!
!  Output: <mode><isoval>_<Dx100>_<Lx100>_<Csuns>_<matname>_<nrays?>_<T/q?>.m
!          Matlab M-file that loads the parameter values and flux/temperature
!          arrays into memory for processing.
!
!  Notes:  This program uses the parallelized versions of the isothermal and
!          adiabatic cavity solvers.  All preparation and data generation steps
!          are carried out on process 0, ray tracing is done by all processes.
!
!  Brandon Jay Hathaway
!  Last Rev: September 7, 2011
!-------------------------------------------------------------------------------
!   use mpi
   implicit none
   include 'mpif.h'
   integer        :: Nrays, mode, imatl
   real(8)        :: D, L, Csuns, isoval, avgval
   real(8)        :: dTcond, dxcond=6.25d-3, kcond=28d0, Tinf = 1200d0
   real(8)        :: lasterr
   real(8)        :: drm=0.01d0, dzm=0.01d0, dap=0.05d0, dr, dphi, dz
   real(8)        :: eta_abs, qavg, sdev, maxerr, thresh, Tavg, t0, urf=0.9d0
   integer        :: nphi=16, nr, nz, nmin=1, nbins=20, maxiter=3000
   integer        :: is, ir, iz, iphi, ophi, iargc, iproc, ierr, iter, ibin, ih=1
   integer        :: ipass, passes, nsurfs, nincrease=0, istep=0
   character(1)   :: outvar
   character(11)  :: outform
   character(16)  :: clarg1, clarg2, clarg3, clarg4, clarg5, clarg6, clarg7
   character(40)  :: modename, paramlist
   real(8), dimension(:), allocatable     :: r,phi,z
   real(8), dimension(:,:), allocatable   :: bins
   integer, dimension(:,:), allocatable   :: f
   real(8), dimension(:,:,:), allocatable :: T,qnet,distval,Tlast,qset,qdiff,h
   real(8), parameter                     :: c_sb = 5.6704d-8
   real(8), parameter                     :: c_pi = 3.1415926535898d0
   real(8), dimension(7)                     :: h_vect = real((/600., 700., 1000., 2000.,
3000., 4000., 5000./),8)
   logical                                :: verbose = .true., rough = .true.
   logical                                :: distout = .true., sumout = .true.
   !!!!!!  DIAGNOSTIC DECLARATIONS
   integer :: errcount !, iser, izer, iphier
   real(8) :: erravg
   logical :: errtrip = .true.

   !!! PROCESS INITIALIZATION
   ! Initialize MPI and determine process ranks
   call MPI_INIT(ierr)
   t0 = MPI_WTIME()
   call MPI_COMM_RANK(MPI_COMM_WORLD, iproc, ierr)
   ! Obtain parameters from supplied command line arguments
   if( iargc() .ge. 6 ) then
      call getarg(1,clarg1)
      call getarg(2,clarg2)
      call getarg(3,clarg3)
      call getarg(4,clarg4)
      call getarg(5,clarg5)
      call getarg(6,clarg6)
```

```
      read(clarg1,*) mode
      read(clarg2,*) isoval
      read(clarg3,*) D
      D=D/100d0
      read(clarg4,*) L
      L=L/100d0
      read(clarg5,*) Csuns
      read(clarg6,*) imatl
      if( iargc() .eq. 7 ) then
         call getarg(7,clarg7)
         read(clarg7,*) Nrays
      elseif( iargc() .eq. 6 ) then
         Nrays = 100000000
         if((iproc .eq. 0).and. verbose) print *,' Default to 100 million rays.'
      endif
   else
      print *,' Incorrect number of command line arguments supplied. ',iargc()
      stop
   endif
   ! Set up computational grid and allocate arrays
   allocate(bins(4,nbins))
   allocate(f(4,nbins))
   call gridspit(D,L,drm,dzm,dap,nr,nz)
   allocate(T(3,nz,nphi))
   allocate(distval(3,nz,nphi))
   allocate(Tlast(3,nz,nphi))
   allocate(qnet(3,nz,nphi))
   allocate(qset(3,nz,nphi))
   allocate(h(3,nz,nphi))
   allocate(qdiff(3,nz,nphi))
   allocate(r(0:nr))
   allocate(phi(0:nphi))
   allocate(z(0:nz))
   call gridspace(D,L,dap,nr,nphi,nz,dr,dphi,dz,r,phi,z)
   nsurfs = nphi * nz + (nr-3)*nphi*2 + 4 + 8
   !!! SIMULATION CALLS
   ! All processes carry out the ray-tracing subroutine
   if(mode .eq. 1)then
      modename ='Tcav'//trim(clarg2)//''
      ! Standard isothermal analysis
      T = isoval
      call pcavsim(T,D,L,Csuns,imatl,Nrays,nr,nphi,nz,                          &
                   qnet,eta_abs,qavg,sdev)
      if((iproc .eq. 0).and. verbose) print *,' Simulation complete'
   elseif(mode .eq. 2)then
      modename ='Adiabatic'
      ! Adiabatic cavity analysis  Tlast = initial guess of cavity temperature.
      Tlast = 2280d+0  ! Make this a function of Csuns.
      call adpcavsim(Tlast,D,L,Csuns,imatl,Nrays,nr,nphi,nz,T,Tavg,sdev)
      ! Call the analysis again to use corrected Tlast for improved accuracy.
      call adpcavsim(Tlast,D,L,Csuns,imatl,Nrays,nr,nphi,nz,T,Tavg,sdev)
      eta_abs = 0d0
      if((iproc .eq. 0).and. verbose) print *,' Simulation complete'
   elseif(mode .eq. 3) then
      modename ='qnet'//trim(clarg2)//''
      ! Specified net flux analysis
      qset    = isoval
      qdiff   = 0d0
      ! Initial temperature estimate via average flux of isothermal simulations.
      T       = 194.4d0 * ( 17132d0 - qset ) ** (0.253d0) ! Based on inconel
      ! Call and re-call simulation until error is within threshold (or i > 50)
      thresh  = 0.01d0 * isoval
      maxerr  = thresh + 1d0
      iter    = 0
      do while ((maxerr .gt. thresh).and.(iter.lt.maxiter))
         if(iter .eq. 20) urf = 7d-1
         if(iter .eq. 40) urf = 5d-1
         if(iter .eq. 90) urf = 2d-1
!         if(iter .eq. 180) urf = 5d-1
         ! Call parallel cavity simulation subroutine
         call pcavsim(T,D,L,Csuns,imatl,Nrays,nr,nphi,nz,                       &
```

```
                 qnet,eta_abs,qavg,sdev)
         Tlast = T
         ! NOTE: only process 0 recieves rational output from the subroutine
         !       so broadcast the new temperature array to all processes before
         !       the loop returns to the subroutine call again.
         iter  = iter + 1
         if(iproc .eq. 0)then
            errcount = 0
            errtrip  = .true.
            ! Fixed flux temperature adjustment for cylinder end elements
            do is=1,2
               if(is==1) nmin=4
               if(is==2) nmin=1
               do ir=nmin,nr
                  ophi = 1
                  if(ir==1) ophi = 4
                  if(ir==2) ophi = 2
                  do iphi=ophi,nphi,ophi
                     qdiff(is,ir,iphi) = qnet(is,ir,iphi) - qset(is,ir,iphi)
                     if(dsqrt(qdiff(is,ir,iphi)**2) > thresh)then
                        T(is,ir,iphi) =(urf*qdiff(is,ir,iphi) &
                                       /(c_sb)+T(is,ir,iphi)**4.d+0)**(0.25d0)
                        errcount = errcount + 1
                     end if
                  end do
               end do
            end do
            ! Fixed flux temperature adjustment for cylinder wall elements
            do iz=1,nz
               do iphi=1,nphi
                  qdiff(3,iz,iphi) = qnet(3,iz,iphi) - qset(3,iz,iphi)
                  if(dsqrt(qdiff(3,iz,iphi)**2)>=thresh)then
                     T(3,iz,iphi)  = (urf*qdiff(3,iz,iphi)    &
                                     /(c_sb)+T(3,iz,iphi)**4.d+0)**(0.25d0)
                     errcount = errcount + 1
                     errtrip = .false.
                  endif
               enddo
            enddo
            ! Calc maximum error and continue if above threshold
            maxerr = maxval(dsqrt(qdiff**2.d+0))
            if(verbose) print *,' Simulation iteration complete: iter = ',iter
            if(verbose) print *,' Current max-error: ',maxerr
            if(verbose) print *,' Number of high-error surfaces: ',errcount
            erravg  =  sum(sqrt(qdiff(:,:,:)**2),mask=logical(sqrt(qdiff(:,:,:)**2)  .gt.
0.d0 ))/real(nsurfs,8)
            if(verbose) print *,' Average error on surfaces  : ',erravg
            if(verbose)  print  *,'  Non-symmetric  cylinder  err  :  ',maxval(qnet(3,10,:))-
minval(qnet(3,10,:))
            open(99, file='convergance-relax.csv', position='APPEND')
            write(99,999) iter, maxerr, errcount, erravg
            close(99)
         endif ! irpoc == 0 limiter
         ! Broadcast new temperatures to all processes and continue solving.
         call MPI_BCAST(T, size(T), MPI_REAL8, 0, MPI_COMM_WORLD, ierr)
         call MPI_BCAST(maxerr, 1, MPI_REAL8, 0, MPI_COMM_WORLD, ierr)
      enddo
      if((iproc .eq. 0).and. verbose) print *,' Specified flux converged.'
      ! Compute resultant average temperature (weighted by number of surfaces, not area).
      Tavg = sum(Tlast)/real(nsurfs,8)
   elseif(mode .eq. 4) then
      modename ='h'//trim(clarg2)//''
      ! Specified heat transfer coefficient analysis
!      h       = isoval ! Comment out and form array instead for varied 'h'
      qset    = 15600d0! Net flux est. based on avg for 1250K cavity w/ D=L=2
      qdiff   = 0d0
      ! Initial temperature estimate
      T       = 1240d0
      ! Call and re-call simulation until error is within threshold (or i > 250)
      thresh  = 0.04d0 * 15600d0 ! Threshold 1% of estimated avg flux
      iter    = 0
```

```
  do while (ih .le. 7)
     if(ih .ge. 2) urf = 0.5d0/real(ih,8)
     maxerr  = thresh + 1d0
     lasterr = maxerr + 1d0
     h = min(h_vect(ih),isoval)
     ih = ih + 1
     do while ((maxerr .gt. thresh).and.(iter.lt.maxiter))
        if((iter .eq. 20).and.(urf .gt. 7d-1)) urf = 7d-1
        if((iter .eq. 40).and.(urf .gt. 5d-1)) urf = 5d-1
        if((iter .eq. 80).and.(urf .gt. 2d-1)) urf = 2d-1
        if(iter .eq. (150 + istep))then
           urf = 0.80d0 * urf
           istep = istep + 10
        endif
        ! Use progressivley more rays as the proper solution is approached.
        ! Also, high values of 'h' result in numerical error so these values
        ! are also slowly scaled up to aid in convergence.
        if(((maxerr .gt. 200d0*thresh).or.(iter .eq. 0 )).and. rough)then
           Nrays = 1000000
           h     = min(isoval,600d0)
        elseif(iter .lt. 70)then
           Nrays = 10000000
           h     = min(isoval,650d0)
           rough = .false.
        else
           Nrays = 100000000
           if((iproc .eq. 0).and. verbose) print *,'---> h = ',h(1,1,1)
           rough = .false.
        endif

        ! Clamp down on the URF by reducing it by 25% if two consecutive
        ! increases in max error occurr
        if (maxerr .gt. lasterr)then
           nincrease = nincrease + 1
        else
           nincrease = 0
        endif
        if (nincrease .ge. 3)then
           urf = urf * 0.90d0
           if((iproc .eq. 0).and. verbose) print *,' DROPPING URF '
        endif
        if(urf .lt. 0.005d0)then
           urf = 0.005d0
           if((iproc .eq. 0).and. verbose) print *,' URF Bottomed out '
        endif

        ! Call parallel cavity simulation subroutine
        call pcavsim(T,D,L,Csuns,imatl,Nrays,nr,nphi,nz,                    &
                  qnet,eta_abs,qavg,sdev)
        Tlast = T
        ! NOTE: only process 0 recieves rational output from the subroutine
        !       so broadcast the new temperature array to all processes before
        !       the loop returns to the subroutine call again.
        iter  = iter + 1
        lasterr = maxerr
        if(iproc .eq. 0)then
           errcount = 0
           errtrip  = .true.
           ! Fixed flux temperature adjustment for cylinder end elements
           ! Currently configured to establish adiabatic ends
           do is=1,2
              if(is==1) nmin=4
              if(is==2) nmin=1
              do ir=nmin,nr
                 ophi = 1
                 if(ir==1) ophi = 4
                 if(ir==2) ophi = 2
                 do iphi=ophi,nphi,ophi
!                    qdiff(is,ir,iphi) = qnet(is,ir,iphi) - qset(is,ir,iphi)
                    qdiff(is,ir,iphi) = qnet(is,ir,iphi)      ! Adiabatic ends
                    if(dsqrt(qdiff(is,ir,iphi)**2) > thresh)then
```

```
                           T(is,ir,iphi)                      =(1d0                      -
urf)*T(is,ir,iphi)+urf*(qdiff(is,ir,iphi) &
                                      /(c_sb)+T(is,ir,iphi)**4.d+0)**(0.25d0)
   !                        T(is,ir,iphi) =(urf*qdiff(is,ir,iphi) &
   !                                       /(c_sb)+T(is,ir,iphi)**4.d+0)**(0.25d0)
                           errcount = errcount + 1
                        end if
                     end do
                  end do
               end do
               ! Fixed flux temperature adjustment for cylinder wall elements
               do iz=1,nz
                  do iphi=1,nphi
                     ! The desired wall flux is calculated from convection and Tinf
                     dTcond = qset(3,iz,iphi) * dxcond / kcond
                     qset(3,iz,iphi)  = h(3,iz,iphi) * ( (T(3,iz,iphi)-dTcond) - Tinf )
                     qdiff(3,iz,iphi) = qnet(3,iz,iphi) - qset(3,iz,iphi)
                     ! If above threshold, the temp is adjusted so re-radiation
                     ! accounts for the net flux difference
!                     qdiff(3,iz,iphi) = 0d0
!                     T(3,iz,iphi) = Tinf
                     if(dsqrt(qdiff(3,iz,iphi)**2)>=thresh)then
                        T(3,iz,iphi)    =  (1d0  -  urf)*T(3,iz,iphi)+urf*(qdiff(3,iz,iphi)
&
                                          /(c_sb)+T(3,iz,iphi)**4.d+0)**(0.25d0)
   !                       T(3,iz,iphi)  = (urf*qdiff(3,iz,iphi)    &
   !                                        /(c_sb)+T(3,iz,iphi)**4.d+0)**(0.25d0)
                       errcount = errcount + 1
                       errtrip = .false.
                     endif
                  enddo
               enddo
               ! Calc maximum error and continue if above threshold
               maxerr = maxval(dsqrt(qdiff**2.d+0))
               if(verbose) print *,'Simulation iteration complete: iter = ',iter
               if(verbose) print *,' Current max-error: ',maxerr
               if(verbose) print *,' Solution relaxed at         omega = ',urf
               if(verbose) print *,' Number of high-error surfaces: ',errcount
               erravg = sum(sqrt(qdiff(:,:,:)**2),mask=logical(sqrt(qdiff(:,:,:)**2) .gt.
0.d0 ))/real(nsurfs,8)
               if(verbose) print *,' Average error on surfaces  : ',erravg
   !                           if(verbose)  print  *,'  Non-symmetric  cylinder  err  :
',maxval(qnet(3,10,:))-minval(qnet(3,10,:))
               open(99, file='convergance-history.csv', position='APPEND')
               write(99,999) iter, maxerr, errcount, erravg
               close(99)
            endif ! irpoc == 0 limiter
            ! Broadcast new temperatures to all processes and continue solving.
            call MPI_BCAST(T, size(T), MPI_REAL8, 0, MPI_COMM_WORLD, ierr)
            call MPI_BCAST(maxerr, 1, MPI_REAL8, 0, MPI_COMM_WORLD, ierr)
            ! Force high  fidelity finishing runs for smooth distributions
            if((maxerr .lt. thresh).and.(iter .lt. 70))then
               maxerr = thresh + 1d0
               iter = 70
               if((iproc .eq. 0).and. verbose) print *,'CONVERGED WHILE COARSE! Skipping
to iter = 70'
            endif
         enddo
      enddo
      if((iproc .eq. 0).and. verbose) print *,' Specified conv coeff converged.'
      ! Compute resultant average temperature (weighted by number of surfaces, not area).
      Tavg = sum(Tlast)/real(nsurfs,8)
   else
      print *,' Unknown simulation mode specified:',mode
      stop
   endif

   !!! DATA OUTPUT
   ! Process 0 calculates distributions and prints data to the output file
   if(iproc .eq. 0)then
      if(distout) then
```

```
passes = 1
if(mode .eq. 4) passes = 2
do ipass = 1,passes
   ! Calculate flux or temperature frequency distribution
   if((mode .eq. 1).or.((ipass .eq. 1).and.(mode .eq. 4))) then
      distval = qnet
      avgval  = qavg
      outvar  = 'q'
      outform = '(1X,EN11.2)'
   elseif(((mode .gt. 1).and.(mode .lt. 4)).or.(ipass .eq. 2)) then
      distval = T
      avgval  = Tavg
      outvar  = 'T'
      outform = '(1X,F7.1)'
   endif
   call freqdist(distval, nr, nz, nbins, f, bins)
   ! Set up naming for output file
   ! <mode><isoval>_<Dx100>_<Lx100>_<Csuns>_<matl>_<Nrays?>_<T/qnet?>.m
   paramlist = ''//trim(clarg3)//'_'//trim(clarg4)//'_'//trim(clarg5)//'_'
   if(imatl == 0) paramlist = ''//trim(paramlist)//'black'
   if(imatl == 1) paramlist = ''//trim(paramlist)//'inco'
   if(imatl == 2) paramlist = ''//trim(paramlist)//'alumina'
   if(imatl == 3) paramlist = ''//trim(paramlist)//'grey'
   if(iargc() == 7) paramlist = ''//trim(paramlist)//'_'//trim(clarg7)//''
   if(mode == 4) paramlist = ''//trim(paramlist)//'_'//trim(outvar)//''
   ! Prepare the output file
   open(10,file=''//trim(modename)//'_'//trim(paramlist)//'.m')
   ! Write the run parameters to file
   write(10,98) outvar, outvar, outvar, outvar, outvar, outvar
   write(10,99) ''//trim(modename)//'_'//trim(paramlist)//''
   write(10,100)
   write(10,101) D
   write(10,102) L
   write(10,107) Csuns
   write(10,111) Nrays
   ! Write the absorption efficiency and average/sdev flux or temperature
   write(10,112) eta_abs
   write(10,113,advance='no') outvar
   write(10,outform,advance='no') avgval
   write(10,196)
   write(10,114) sdev
   ! Write position vectors to file (position of centroids of surfaces)
   write(10,103,advance='no')
   do iz=1,nz
      write(10,106,advance='no') (z(iz)+z(iz-1))/2d+0
   end do
   write(10,199)
   write(10,104,advance='no')
   do ir=1,nr
      write(10,106,advance='no') sqrt((r(ir)**2+r(ir-1)**2)/2d+0)
   end do
   write(10,199)
   write(10,105,advance='no')
   do iphi=1,nphi
      write(10,106,advance='no') (phi(iphi)+phi(iphi-1))/2d+0
   end do
   write(10,199)
   ! Cylinder wall output variable
   write(10,121) outvar
   do iz=1,nz
      write(10,197,advance='no')
      do iphi=1,nphi
         write(10,outform,advance='no') distval(3,iz,iphi)
      end do
      write(10,198)
   end do
   write(10,199)
   ! Ring output variable (aperture end)
   write(10,122) outvar, nr
   do ir=4,nr
      write(10,197,advance='no')
```

```
            do iphi=1,nphi
               write(10,outform,advance='no') distval(1,ir,iphi)
            end do
            write(10,198)
         end do
         write(10,199)
         ! Disk output variable (far end)
         write(10,123) outvar
         do ir=1,nr
            write(10,197,advance='no')
            if(ir==1)then
               do iphi=4,nphi,4
                  write(10,outform,advance='no') distval(2,ir,iphi)
                  write(10,outform,advance='no') distval(2,ir,iphi)
                  write(10,outform,advance='no') distval(2,ir,iphi)
                  write(10,outform,advance='no') distval(2,ir,iphi)
               end do
            elseif(ir==2)then
               do iphi=2,nphi,2
                  write(10,outform,advance='no') distval(2,ir,iphi)
                  write(10,outform,advance='no') distval(2,ir,iphi)
               end do
            else
               do iphi=1,nphi
                  write(10,outform,advance='no') distval(2,ir,iphi)
               end do
            end if
            write(10,198)
         end do
         write(10,199)
         ! Global and surface output variable frequency distributions
         write(10,124) outvar
         do is=1,4
            write(10,197,advance='no')
            do ibin = 1,nbins
               write(10,131,advance='no') f(is,ibin)
            end do
            write(10,198)
         end do
         write(10,199)
         ! Global and surface output variable frequency distribution bin limits
         write(10,125) outvar
         do is=1,4
            write(10,197,advance='no')
            do ibin = 1,nbins
               write(10,outform,advance='no') bins(is,ibin)
            end do
            write(10,198)
         end do
         write(10,199)
         write(10,201)
         close(10)
      end do ! ipass loop (for outputting both flux and temps)
   endif ! distribution output routine
   if(sumout)then
      open(20, file='parametric_sweep.csv', position='APPEND')
      write(20,300) imatl, isoval, D, L, eta_abs, qavg
      close(20)
   endif ! summary output routine
endif ! End process 0 output portion

! Finalize and close MPI
if((iproc .eq. 0).and.verbose) write(*,200) MPI_WTIME()-t0
call MPI_FINALIZE(ierr)

! Format codes
98 format('function [r,z,phi,eta_abs,',A1,'avg,',A1,'_ring,',A1,'_disk,'    &
           ,A1,'_cyl,',A1,'_bin,f',A1,',nrays] ...')
99 format('          = ',A42)
100 format('% Output file from cav2mat data generation program.')
101 format('D   = ',F5.2,';')
```

```
   102 format('L   = ',F5.2,';')
   103 format('z   = [ ')
   104 format('r   = [ ')
   105 format('phi = [ ')
   106 format(1X,F6.4)
   107 format('Csuns = ',F6.0,';')
   111 format('nrays = ',I10,';')
   112 format('eta_abs = ',F5.3,';')
   113 format('',A1,'avg = ')
   114 format('sdev = ',F8.2,';')
   121 format('',A1,'_cyl(:,:) = [')
   122 format('',A1,'_ring(4:',I2,',:) = [')
   123 format('',A1,'_disk(:,:) = [')
   124 format('f',A1,'(:,:) = [')
   125 format('',A1,'_bin(:,:) = [')
   131 format(1X,I4)     ! Integer value of form "xxxx" for flux dist counts
   196 format(';')
   197 format('[ ')
   198 format(' ]')
   199 format(' ];')
   200 format(' Time Elapsed: t = ',F7.1,' [sec]')
   201 format('end')
   300 format(' ',I4,', ',F8.0,', ',F7.2,', ',F7.2,', ',F7.3,', ',F9.0)
   999 format(' ',I6,', ',F8.0,', ',I5,', ',F8.0)
end program cav2mat

subroutine freqdist(v, nr, nz, nbins, fv, vbin)
   implicit none
   integer, intent(in)                         :: nr, nz, nbins
   real(8), dimension(3,nz,16), intent(in)   :: v
   real(8), dimension(3,nz,16)               :: vi ! edit-ready data copy
   real(8), dimension(4)                       :: dv
   integer                                     :: oz, zm, ophi, isurf, iz, iphi
   integer                                     :: ibin, ibint, i
   integer, dimension(4,nbins), intent(out)  :: fv
   real(8), dimension(4,nbins), intent(out)  :: vbin
   vi        = v     ! copy input array to modifiable internal variable
   vi(1,1,1) = 0d0   ! Set aperture value to zero to avoid skewed results
   fv        = 0     ! Initialize distribution
   ! Set global bin width and bin limits
   dv(4) = ( maxval(vi,mask=logical(vi**2 .gt. epsilon(0d0),1)) -              &
             minval(vi,mask=logical(vi**2 .gt. epsilon(0d0),1)))/dble(nbins)
   vbin(4,:) = minval(vi,mask=logical(vi**2 .gt. epsilon(0d0),1))              &
               + dv(4) * (/ (dble(i),i=1,nbins) /)
   ! Loop over every surface element
   do isurf=1,3
      ! Set surface specific bin width and bin limits
      dv(isurf) = (maxval(vi(isurf,:,:),                                       &
                   mask=logical(vi(isurf,:,:)**2 .gt. epsilon(0d0),1))        &
                   - minval(vi(isurf,:,:),                                     &
                   mask=logical(vi(isurf,:,:)**2 .gt. epsilon(0d0),1)))       &
                   /dble(nbins)
      vbin(isurf,:) = minval(vi(isurf,:,:),                                    &
                   mask=logical(vi(isurf,:,:)**2 .gt. epsilon(0d0),1))        &
                   + dv(isurf) * (/ (dble(i),i=1,nbins) /)
      ! Set loop limits for either 'z' or 'r' based on surface
      oz = 1
      zm = nz
      if(isurf==1)then
         oz = 4
         zm = nr
      elseif(isurf==2)then
         zm = nr
      endif
      ! Loop through radial or axial positions
      do iz=oz,zm
         ! Set angular position skip for coarse inner disk elements
         ophi = 1
         if((isurf==2).and.(iz==1)) ophi = 4
         if((isurf==2).and.(iz==2)) ophi = 2
         ! Loop through angular positions
```

```
         do iphi=ophi,16,ophi
            ! Determine surface specific bin index
            ibin  = ceiling( (vi(isurf,iz,iphi)-                                &
                    minval(vi(isurf,:,:), mask=logical(                        &
                    vi(isurf,:,:)**2 .gt. epsilon(0d0),1)))/dv(isurf))
            if(ibin.LT.1)      ibin  = 1
            if(ibin.GT.nbins)  ibin  = nbins
            ! Determine global bin index
            ibint = ceiling( (vi(isurf,iz,iphi)-minval(vi(:,:,:),              &
                    mask=logical(vi**2 .gt. epsilon(0d0),1)))/dv(4))
            if(ibint.LT.1)     ibint = 1
            if(ibint.GT.nbins) ibint = nbins
            ! Accumulate flux intensity frequency distributions
            fv(isurf,ibin) = fv(isurf,ibin) + 1
            fv(4,ibint)    = fv(4,ibint) + 1
         end do
      end do
   end do
end subroutine freqdist
```

```
/*****************************************************************************
   flux_interfacing.c

   This UDF file contains user defined functions to allow the coupling of a
   Monte Carlo ray tracing algorithm to a FLUENT simulation.  Specifically,
   these functions will allow a cylindrical cavity, split into six surfaces, to
   be simulated.  The first two functions are simple compare/count functions
   to aid the main UDFs.  The next DEFINE_ADJUST UDF is what actually gathers
   temperatures, calls the MC ray tracing simulation, and sets the resulting
   heat flux on the surface.  After that come the DEFINE_PROFILE UDFs which
   either just report the current surface id and property id to be used by the
   DEFINE_ADJUST UDF, or set an initial value of the boundary flux to help start
   the simulation with a fixed value and avoid nonlinear instabilities.

   The last UDFs cover the reaction chemistry/thermodynamics/kinetics requred
   to simulate the pyrolysis of biomass (cellulose) and gasification of char.

   Brandon Jay Hathaway
   Latest Revision: June 5, 2012
*****************************************************************************/

#include "udf.h"
#include "sg.h"

/* Constants utilized in establishing the reaction rates. */
#define E_a_pyr 238 /* [kJ/mol] */
#define k_0_pyr 1.96E11 /* [1/s] */
#define E_a_gas 158 /* [kJ/mol] */
#define k_0_gas 2.5E4 /* [1/s] */
#define alpha_23 0.93 /* Volatile fraction of cellulose */
#define alpha_24 0.07 /* Char fraction of cellulose */
#define R_ig 8.314E-3 /* Ideal gas constant [kJ/mol-K] */

/* End of definitions */

int iterskip = 100; /* Set the Monte Carlo flux BC iteration skip interval */

/* In order to use a FORTRAN subroutine it must first be declared as an EXTERN */
extern void cav2flu_(int *, real *, real *, real *, real *, real *);

/* Minimum integer value function. */
int minint(int a, int b)
{
   if( a >= b)
   {
      return b;
   }
   else
   {
      return a;
   }
}

/* Function to count faces in a face thread becaue the existing macro lies. */
int count_faces(Thread *th)
{
   int holdval = 0;
   face_t f;
   begin_f_loop(f,th)
   {
      if(f > holdval)
      {
         holdval = f;
      }
   }
   end_f_loop(f,th)
   holdval = holdval + 1 * minint(holdval,1);
   return holdval;
}

DEFINE_ADJUST(cav2flu_fluxset, domain)
```

```
{
   int current_iter = (nres == 0) ? (0) : ((int) count2[nres - 1]);
   int iprop_frnt[2], iprop_back[2], iprop_cyl[2];
   int izone_frnt[2], izone_back[2], izone_cyl[2];
   int i, gtotfaces, f_offset = 0;
   real *t_loc, *r_loc, *p_loc, *z_loc, *qnet_loc;
   #if PARALLEL
      int buffsize=0;
   #endif
   #if !PARALLEL
      int node_last = -1;
   #endif
   #if !RP_NODE
      FILE  *fid;
      real *temp, *r, *p, *z, *qnet;
   #endif
   #if !RP_HOST
      face_t f;
      int nfaces_frnt[2], nfaces_back[2], nfaces_cyl[2], totfaces, iprop_loop;
      Thread *th_frnt1, *th_frnt2, *th_back1, *th_back2, *th_cyl1, *th_cyl2,
             *th_loop;
      real FC[3];
   #endif
   #if RP_HOST
      int *nbuff, j;
      nbuff    = (int *)malloc((node_last+1)*sizeof(*nbuff));
      r_loc    = 0;
      p_loc    = 0;
      z_loc    = 0;
      t_loc    = 0;
      qnet_loc = 0;
   #endif

   /* Every nth iteration, read temps and adjust BCs */
   if ((current_iter % iterskip) == 0)
   {
      /* Only host or serial process reads the property and zone IDs */
      #if !RP_NODE
         fid = fopen("f_id_frnt1.txt", "r");
         fscanf(fid,"%d, %d",&iprop_frnt[0], &izone_frnt[0]);
         fclose(fid);
         fid = fopen("f_id_back1.txt", "r");
         fscanf(fid,"%d, %d",&iprop_back[0], &izone_back[0]);
         fclose(fid);
         fid = fopen("f_id_cyl1.txt", "r");
         fscanf(fid,"%d, %d",&iprop_cyl[0], &izone_cyl[0]);
         fclose(fid);
         fid = fopen("f_id_frnt2.txt", "r");
         fscanf(fid,"%d, %d",&iprop_frnt[1], &izone_frnt[1]);
         fclose(fid);
         fid = fopen("f_id_back2.txt", "r");
         fscanf(fid,"%d, %d",&iprop_back[1], &izone_back[1]);
         fclose(fid);
         fid = fopen("f_id_cyl2.txt", "r");
         fscanf(fid,"%d, %d",&iprop_cyl[1], &izone_cyl[1]);
         fclose(fid);
      #endif
      /* Host process shares property and zone id's to all nodes */
      host_to_node_int(iprop_frnt,2);
      host_to_node_int(iprop_back,2);
      host_to_node_int(iprop_cyl,2);
      host_to_node_int(izone_frnt,2);
      host_to_node_int(izone_back,2);
      host_to_node_int(izone_cyl,2);

      /* Number of faces in each zone are calculated and the corresponding
      arrays for temperature, position, and heat flux are created. */
      #if !RP_HOST
         /* Thread pointers assigned based on read-in zone indexes. */
         th_frnt1 = Lookup_Thread(domain, izone_frnt[0]);
         th_frnt2 = Lookup_Thread(domain, izone_frnt[1]);
```

```
th_back1 = Lookup_Thread(domain, izone_back[0]);
th_back2 = Lookup_Thread(domain, izone_back[1]);
th_cyl1 = Lookup_Thread(domain, izone_cyl[0]);
th_cyl2 = Lookup_Thread(domain, izone_cyl[1]);
/* Number of faces for each thread counted. */
nfaces_frnt[0] = count_faces(th_frnt1);
nfaces_frnt[1] = count_faces(th_frnt2);
nfaces_back[0] = count_faces(th_back1);
nfaces_back[1] = count_faces(th_back2);
nfaces_cyl[0] = count_faces(th_cyl1);
nfaces_cyl[1] = count_faces(th_cyl2);

/* Allocate arrays for temp, position, and flux. */
totfaces = nfaces_frnt[0]+nfaces_back[0]+nfaces_cyl[0]+
           nfaces_frnt[1]+nfaces_back[1]+nfaces_cyl[1];
#if PARALLEL
   gtotfaces = PRF_GISUM1(totfaces);
#endif
#if !PARALLEL
   gtotfaces = totfaces;
#endif
t_loc    = (real *)malloc(totfaces*sizeof(*t_loc));
r_loc    = (real *)malloc(totfaces*sizeof(*r_loc));
p_loc    = (real *)malloc(totfaces*sizeof(*p_loc));
z_loc    = (real *)malloc(totfaces*sizeof(*z_loc));
qnet_loc = (real *)malloc(totfaces*sizeof(*qnet_loc));
/* Fill allocated arrays */
for ( i = 1; i <= 6; i++)
{
   if (i == 1)
   {
      th_loop    = th_frnt1;
      f_offset   = 0;
   }
   else if (i==2)
   {
      th_loop    = th_frnt2;
      f_offset   = nfaces_frnt[0];
   }
   else if (i==3)
   {
      th_loop    = th_back1;
      f_offset   = f_offset + nfaces_frnt[1];
   }
   else if (i==4)
   {
      th_loop    = th_back2;
      f_offset   = f_offset + nfaces_back[0];
   }
   else if (i==5)
   {
      th_loop    = th_cyl1;
      f_offset   = f_offset + nfaces_back[1];
   }
   else if (i==6)
   {
      th_loop    = th_cyl2;
      f_offset   = f_offset + nfaces_cyl[0];
   }
   else
   {
      th_loop   =  0;
      f_offset  =  0;
      Error("Unreal face thread loop index.\n");
   }
   begin_f_loop(f,th_loop)
   {
      t_loc[f+f_offset] = F_T(f,th_loop);
      F_CENTROID(FC,f,th_loop);
      z_loc[f+f_offset] = FC[2];
      r_loc[f+f_offset]=sqrt(FC[0]*FC[0]+FC[1]*FC[1]);
```

```
         if(FC[0] < 0)
         {
            p_loc[f+f_offset]=atan(FC[1]/FC[0])+M_PI;
         }
         else if (FC[1]<0)
         {
            p_loc[f+f_offset]=atan(FC[1]/FC[0])+2*M_PI;
         }
         else if (FC[1]>=0)
         {
            p_loc[f+f_offset]=atan(FC[1]/FC[0]);
         }
         else
         {
            p_loc[f+f_offset]=0.0;
            Error("NODE %d: Polar angle assignment error on loop %d.\n"
                  ,myid,i);
         }
      }
      end_f_loop(f,th_loop)
   } /* Face thread loop */
#endif

/* Send the grand total number of faces to the host. */
node_to_host_int_1(gtotfaces);

/* For parallel processes, the host uses the sum of faces
   for all boundaries to allocate appropriate sized master arrays. For
   serial runs, the master arrays are assigned the local array values. */
#if !RP_NODE
   temp = (real *)malloc(gtotfaces*sizeof(*temp));
   r    = (real *)malloc(gtotfaces*sizeof(*r));
   p    = (real *)malloc(gtotfaces*sizeof(*p));
   z    = (real *)malloc(gtotfaces*sizeof(*z));
   qnet = (real *)malloc(gtotfaces*sizeof(*qnet));
   #if !PARALLEL
      for(i=0; i<gtotfaces; i++)
      {
         temp[i] = t_loc[i];
         r[i]    = r_loc[i];
         p[i]    = p_loc[i];
         z[i]    = z_loc[i];
      }
   #endif
#endif

/* Build the global rpz-T arrays by sending local arrays up to Node-0
   then on to the host. Serial processes will skip the node loop. */
#if RP_NODE
   buffsize = totfaces;
#endif
for(i=0; i<=node_last; i++)
{
   #if RP_NODE
      if( i > 0 )
      {
         if(myid == i)
         {
            PRF_CSEND_INT(0,&buffsize,1,i);
            PRF_CSEND_REAL(0,t_loc,buffsize,i);
            PRF_CSEND_REAL(0,r_loc,buffsize,i);
            PRF_CSEND_REAL(0,p_loc,buffsize,i);
            PRF_CSEND_REAL(0,z_loc,buffsize,i);
         }
         if(I_AM_NODE_ZERO_P)
         {
            PRF_CRECV_INT(i,&buffsize,1,i);
            t_loc = (real *)realloc(t_loc, buffsize*sizeof(*t_loc));
            r_loc = (real *)realloc(r_loc, buffsize*sizeof(*r_loc));
            p_loc = (real *)realloc(p_loc, buffsize*sizeof(*p_loc));
            z_loc = (real *)realloc(z_loc, buffsize*sizeof(*z_loc));
```

```
            PRF_CRECV_REAL(i,t_loc,buffsize,i);
            PRF_CRECV_REAL(i,r_loc,buffsize,i);
            PRF_CRECV_REAL(i,p_loc,buffsize,i);
            PRF_CRECV_REAL(i,z_loc,buffsize,i);
         }
      }
   #endif
   node_to_host_int_1(buffsize);
   #if RP_HOST
      nbuff[i] = buffsize;
      if( i == 0 )
      {
        t_loc = (real *)malloc(buffsize*sizeof(*t_loc));
        r_loc = (real *)malloc(buffsize*sizeof(*r_loc));
        p_loc = (real *)malloc(buffsize*sizeof(*p_loc));
        z_loc = (real *)malloc(buffsize*sizeof(*z_loc));
      }
      else
      {
         t_loc = (real *)realloc(t_loc, buffsize*sizeof(*t_loc));
         r_loc = (real *)realloc(r_loc, buffsize*sizeof(*r_loc));
         p_loc = (real *)realloc(p_loc, buffsize*sizeof(*p_loc));
         z_loc = (real *)realloc(z_loc, buffsize*sizeof(*z_loc));
      }
   #endif
   node_to_host_real(t_loc,buffsize);
   node_to_host_real(r_loc,buffsize);
   node_to_host_real(p_loc,buffsize);
   node_to_host_real(z_loc,buffsize);
   #if RP_HOST
      for(j=0; j<buffsize; j++)
      {
         temp[j+f_offset]=t_loc[j];
         r[j+f_offset]=r_loc[j];
         p[j+f_offset]=p_loc[j];
         z[j+f_offset]=z_loc[j];
      }
      f_offset = f_offset + buffsize;
   #endif
}

/* Call the Cavity Monte Carlo Simulation through the interface function
  'cav2flu', a precompiled FORTRAN object. Only HOST or SERIAL process. */
#if !RP_NODE
   cav2flu_(&gtotfaces, r, p, z, temp, qnet);
#endif

/* Host dishes out the net fluxes, one nodes worth of values at a time,
   to node zero.  Nodes are run through last to first and node zero pushes
   the value to the appropriate node after obtaining it from the host. */
for(i=node_last; i>=0; i--)
{
   #if RP_HOST
      buffsize = nbuff[i];
      PRF_CSEND_INT(0,&buffsize,1,myid);
      f_offset = 0;
      for(j=0; j<i; j++)
      {
         f_offset = f_offset + nbuff[j];
      }
      if(i == node_last)
      {
         qnet_loc = (real *)malloc(buffsize*sizeof(*qnet_loc));
      }
      else
      {
         qnet_loc = (real *)realloc(qnet_loc, buffsize*sizeof(*qnet_loc));
      }
      for(j=buffsize; j>0; j--)
      {
         qnet_loc[j-1] = qnet[f_offset + j-1];
```

```
      }
      PRF_CSEND_REAL(0,qnet_loc,buffsize,myid);
   #endif
   #if RP_NODE
      if(I_AM_NODE_ZERO_P)
      {
         PRF_CRECV_INT(node_host,&buffsize,1,node_host);
         qnet_loc = (real *)realloc(qnet_loc, buffsize*sizeof(*qnet_loc));
         PRF_CRECV_REAL(node_host,qnet_loc,buffsize,node_host);
      }
      if(i > 0)
      {
         if(I_AM_NODE_ZERO_P)
         {
            PRF_CSEND_REAL(i,qnet_loc,buffsize,0);
         }
         if(myid == i)
         {
            PRF_CRECV_REAL(0,qnet_loc,buffsize,0);
         }
      }
   #endif
}
#if !PARALLEL
   for(i=0; i<gtotfaces; i++)
   {
      qnet_loc[i] = qnet[i];
   }
#endif

/* Each node or serial process runs through the various face loops and
   assigns the new net flux value to the corresponding faces. */
#if !RP_HOST
   for(i=1; i<=6; i++)
   {
      if (i == 1)
      {
         th_loop    = th_frnt1;
         f_offset   = 0;
         iprop_loop = iprop_frnt[0];
      }
      else if (i==2)
      {
         th_loop    = th_frnt2;
         f_offset   = nfaces_frnt[0];
         iprop_loop = iprop_frnt[1];
      }
      else if (i==3)
      {
         th_loop    = th_back1;
         f_offset   = f_offset + nfaces_frnt[1];
         iprop_loop = iprop_back[0];
      }
      else if (i==4)
      {
         th_loop    = th_back2;
         f_offset   = f_offset + nfaces_back[0];
         iprop_loop = iprop_back[1];
      }
      else if (i==5)
      {
         th_loop    = th_cyl1;
         f_offset   = f_offset + nfaces_back[1];
         iprop_loop = iprop_cyl[0];
      }
      else if (i==6)
      {
         th_loop    = th_cyl2;
         f_offset   = f_offset + nfaces_cyl[0];
         iprop_loop = iprop_cyl[1];
      }
```

```
            else
            {
               th_loop   =  0;
               f_offset  =  0;
               iprop_loop = 0;
               Error("Unreal face thread loop index.\n");
            }
            begin_f_loop(f,th_loop)
            {
               F_PROFILE(f,th_loop,iprop_loop) = qnet_loc[f+f_offset];
            }
            end_f_loop(f,th_loop)
         }
         Message0("CAVSIM: New MC simulation profile calculated and loaded.\n");
      #endif

      /* Free allocated arrays to avoid memory leaks. */
      #if !RP_NODE
         free(temp);
         free(r);
         free(p);
         free(z);
         free(qnet);
         temp = 0;
         r = 0;
         p = 0;
         z = 0;
         qnet = 0;
      #endif
      #if RP_HOST
         free(nbuff);
         nbuff = 0;
      #endif
      free(t_loc);
      free(r_loc);
      free(p_loc);
      free(z_loc);
      free(qnet_loc);
      t_loc = 0;
      r_loc = 0;
      p_loc = 0;
      z_loc = 0;
      qnet_loc = 0;
   } /* Iteration skip loop. */
}

/* The below Flux Setnget UDFs are used to set a defined net flux profile
   boundary condition (BC), then get the BC's corresponding zone and property
   ID value for use by the cav2flu_fluxset UDF to adjust the BC value. */
DEFINE_PROFILE(flux_setnget_cyl1,t,i)
{
   int zoneid  = THREAD_ID(t);
   FILE  *fid;
   #if PARALLEL
      if(I_AM_NODE_ZERO_P)
      {
         /* Write property and zone identifiers to file */
         fid = fopen("f_id_cyl1.txt", "w");
         fprintf(fid, "%d, %d\n", i, zoneid);
         fclose(fid);
      }
   #endif
   #if !PARALLEL
      /* Write property and zone identifiers to file */
      fid = fopen("f_id_cyl1.txt", "w");
      fprintf(fid, "%d, %d\n", i, zoneid);
      fclose(fid);
   #endif
   /* Set no flux distribution. */
   /* New distro will come from DEFINE_ADJUST macro. */
}
```

```
DEFINE_PROFILE(flux_setnget_cyl2,t,i)
{
   int zoneid  = THREAD_ID(t);
   FILE  *fid;
   #if PARALLEL
      if(I_AM_NODE_ZERO_P)
      {
         /* Write property and zone identifiers to file */
         fid = fopen("f_id_cyl2.txt", "w");
         fprintf(fid, "%d, %d\n", i, zoneid);
         fclose(fid);
      }
   #endif
   #if !PARALLEL
      /* Write property and zone identifiers to file */
      fid = fopen("f_id_cyl2.txt", "w");
      fprintf(fid, "%d, %d\n", i, zoneid);
      fclose(fid);
   #endif
   /* Set no flux distribution. */
   /* New distro will come from DEFINE_ADJUST macro. */
}

DEFINE_PROFILE(flux_setnget_frnt1,t,i)
{
   int zoneid  = THREAD_ID(t);
   FILE  *fid;
   #if PARALLEL
      if(I_AM_NODE_ZERO_P)
      {
         /* Write property and zone identifiers to file */
         fid = fopen("f_id_frnt1.txt", "w");
         fprintf(fid, "%d, %d\n", i, zoneid);
         fclose(fid);
      }
   #endif
   #if !PARALLEL
      /* Write property and zone identifiers to file */
      fid = fopen("f_id_frnt1.txt", "w");
      fprintf(fid, "%d, %d\n", i, zoneid);
      fclose(fid);
   #endif
   /* Set no flux distribution. */
   /* New distro will come from DEFINE_ADJUST macro. */
}

DEFINE_PROFILE(flux_setnget_frnt2,t,i)
{
   int zoneid  = THREAD_ID(t);
   FILE  *fid;
   #if PARALLEL
      if(I_AM_NODE_ZERO_P)
      {
         /* Write property and zone identifiers to file */
         fid = fopen("f_id_frnt2.txt", "w");
         fprintf(fid, "%d, %d\n", i, zoneid);
         fclose(fid);
      }
   #endif
   #if !PARALLEL
      /* Write property and zone identifiers to file */
      fid = fopen("f_id_frnt2.txt", "w");
      fprintf(fid, "%d, %d\n", i, zoneid);
      fclose(fid);
   #endif
   /* Set no flux distribution. */
   /* New distro will come from DEFINE_ADJUST macro. */
}

DEFINE_PROFILE(flux_setnget_back1,t,i)
```

```
{
   int zoneid  = THREAD_ID(t);
   FILE  *fid;
   #if PARALLEL
      if(I_AM_NODE_ZERO_P)
      {
         /* Write property and zone identifiers to file */
         fid = fopen("f_id_back1.txt", "w");
         fprintf(fid, "%d, %d\n", i, zoneid);
         fclose(fid);
      }
   #endif
   #if !PARALLEL
      /* Write property and zone identifiers to file */
      fid = fopen("f_id_back1.txt", "w");
      fprintf(fid, "%d, %d\n", i, zoneid);
      fclose(fid);
   #endif
   /* Set no flux distribution. */
   /* New distro will come from DEFINE_ADJUST macro. */
}

DEFINE_PROFILE(flux_setnget_back2,t,i)
{
   int zoneid  = THREAD_ID(t);
   FILE  *fid;
   #if PARALLEL
      if(I_AM_NODE_ZERO_P)
      {
         /* Write property and zone identifiers to file */
         fid = fopen("f_id_back2.txt", "w");
         fprintf(fid, "%d, %d\n", i, zoneid);
         fclose(fid);
      }
   #endif
   #if !PARALLEL
      /* Write property and zone identifiers to file */
      fid = fopen("f_id_back2.txt", "w");
      fprintf(fid, "%d, %d\n", i, zoneid);
      fclose(fid);
   #endif
   /* Set no flux distribution. */
   /* New distro will come from DEFINE_ADJUST macro. */
}

/* The below Flux Init UDF's represent the isothermal MC Ray Tracing net flux
   values which can be used for initial stablilization of the simulation. */
DEFINE_PROFILE(flux_init_frnt,t,i)
{
   #if !RP_HOST
      face_t f;
      /* Initial specified flux for first iterations [W/m^2] */
      begin_f_loop(f,t)
      {
         F_PROFILE(f,t,i) = 1000.0;
      }
      end_f_loop(f,t)
   #endif
}

DEFINE_PROFILE(flux_init_back,t,i)
{
   #if !RP_HOST
      face_t f;
      /* Initial specified flux for first iterations [W/m^2] */
      begin_f_loop(f,t)
      {
         F_PROFILE(f,t,i) = 5000.0;
      }
      end_f_loop(f,t)
   #endif
```

```
}

DEFINE_PROFILE(flux_init_cyl,t,i)
{
   #if !RP_HOST
      face_t f;
      real FC[3];

      /* Set the estimated flux distribution for first iterations [W/m^2] */
      /* The current values below are fit for a cavity of parameters D=2 L=2*/
      begin_f_loop(f,t)
      {
         F_CENTROID(FC,f,t);
         if(FC[2] < 0.035)
         {
            F_PROFILE(f,t,i) = 1000.0;
         }
         else if( (FC[2] > 0.035) && (FC[2] < 0.2) )
         {
            F_PROFILE(f,t,i) = 10420000.0*FC[2] - 118300000.0*pow(FC[2],2.0) + \
                               534000000.0*pow(FC[2],3.0) -                    \
                               851300000.0*pow(FC[2],4.0) - 240600.0;
         }
         else
         {
            F_PROFILE(f,t,i) = 3000.0;
         }
      }
      end_f_loop(f,t)
   #endif
}

DEFINE_HET_RXN_RATE(cell_pyr,c,t,r,mw,yi,rr,rr_t)
{
   /* Determine the temperature of the current cell, then calculate the */
   /* reaction rate according to the kinetics established by Hathaway et al. */
   /* mw[i][0] = molecular weight of phase 'i' */
   #if !RP_HOST
      int current_iter = (nres == 0) ? (0) : ((int) count2[nres - 1]);
      Thread **pt = THREAD_SUB_THREADS(t);
/*      Thread *ts  = pt[0]; Salt subthread */
/*      Thread *tg  = pt[1];  Gas subthread */
      Thread *tf  = pt[2]; /* Feedstock subthread */
/*      Thread *tc  = pt[3]; Char subthread */
      real T_feed = C_T(c,tf); /* Feedstock temperature */
      real rho_feed = C_R(c,tf); /* Feedstock density */
      real MW_feed = mw[2][0];
      real f_v_feed = C_VOF(c,tf);

      int skipint=20;

      if(Data_Valid_P())
      {
         *rr = k_0_pyr*exp(-E_a_pyr/(T_feed*R_ig))*rho_feed*f_v_feed/MW_feed;
         /* Debugging block follows */
         if ( ((current_iter % skipint) == 0) && (c == 20) )
         {
            Message0("PYROLYSIS: Current T_Feed is: %f. \n",T_feed);
            Message0("PYROLYSIS: Current f_v_feed is: %f. \n",f_v_feed);
            Message0("PYROLYSIS: Current reaction rate is: %e. \n",*rr);
         }
         /* End debugging block */
      }
   #endif
}

DEFINE_HET_RXN_RATE(c_gasif,c,t,r,mw,yi,rr,rr_t)
{
   /* Determine the temperature of the current cell, then calculate the */
   /* reaction rate according to the kinetics established by Hathaway et al. */
   /* mw[i][0] = molecular weight of phase 'i' */
```

```
   /* yi[i][0] = MASS fraction of phase i  */
   #if !RP_HOST
      int current_iter = (nres == 0) ? (0) : ((int) count2[nres - 1]);
      Thread **pt = THREAD_SUB_THREADS(t);
/*      Thread *ts  = pt[0]; Salt subthread */
/*      Thread *tg  = pt[1];  Gas subthread */
/*      Thread *tf  = pt[2]; Feedstock subthread */
      Thread *tc  = pt[3]; /* Char subthread */
      real T_c = C_T(c,tc); /* Char temperature */
      real rho_c = C_R(c,tc); /* Char density */
      real MW_c = mw[3][0];
      real f_v_c = C_VOF(c,tc);

      int skipint=20;

      if(Data_Valid_P())
      {
         *rr = k_0_gas*exp(-E_a_gas/(T_c*R_ig))*rho_c*pow(f_v_c,(2.0/3.0))/MW_c;
         /* Debugging block follows */
         if ( ((current_iter % skipint) == 0) && (c == 20) )
         {
            Message0("GASIF: Current T_c is: %f. \n",T_c);
            Message0("GASIF: Current f_v_c is: %f. \n",f_v_c);
            Message0("GASIF: Current reaction rate is: %e. \n",*rr);
         }
         /* End debugging block */
      }
   #endif
}
```

```
PROGRAM GenOptFit
IMPLICIT NONE
!!!
! Syntax:
! GenOptFit.F90 <inputfile>
!       WHERE: inputfile       = the name of the file containing the following imput
parameters:
!              runID         = string up to 32 characters long describing the run
!              Tinfinity     = temperature of salt / air
!              yh2o          = effective steam molar ratio
!                 hconv           = convective heat transfer coefficient around particle
[W/m^2-K] ~150 salt, ~20 air
!              Eapyr         = Pyrolysis activation energy [kJ/mol] ~238 uncat, ~220 cat
!               lnar           = ln(Ar), the natural log of the frequency factor of the
pyrolysis reaction
!              tabsize       = tablet size (either 8mm or 10mm)
!              tshift        = time shift for curve fitting
!
! Info:
!   This program explicitly solves for the transient heating of a
! cylindrical tablet of material immersed in a convective environment
! via finite-volume methods.  The solid is modeled as a series
! of cylindrical ring sections concentrically aligned and stacked.
!
! The product gas for the pyrolysis reaction is of the following composition:
!       H2  -   38%col
!       CO  -   40%vol
!       CO2 -   11%vol
!       CH4 -   11%vol
!
!!!
!!!
! CONSTANT PARAMETERS
REAL, PARAMETER :: ks=0.56, kc=140. &               ! Thermal conductivity in [W/m-k]
                ,rhog=0.7615,rhos=1300.,rhoc=2200. &! Density in [kg/m**3]
                ,cps=1400.,cpc=711. &               ! Specific Heat in [J/kg-K]
                ,T0=300.,tf=120. &                  ! Initial Temp [K] and final time [s]
                ,fc0=0.0 &                          ! Initial solid vol frac [-]
                ,xcs=0.07,vgs=1.220 &                   ! Carbon and gas yields per unit
cellulose [g/g], [m^3/kg@22C]
                ,vgc=2.015, Eagas=1. &                   ! Gas yield per unit carbon via
gasification [m^3/kg], gasification Ea (not used now)
                ,convlimit=0.5                          ! Extent of conversion at which to
report the current reaction rate.
               !,yh2o=0.7642                         ! Steam concentration [mol/total mol]
Currently passed from call.
!!!
! VARIABLES
REAL :: kpb,cpg,htot,dHp,rdotp,rdotg,Ceff,dHg,fcmax,mpertab,rconv,convext=0.,avetemp &
        ,yh2o,Tinf,hconv,Eapyr,ar, wssefit=0., vdotuse, datavdotnsum=0., wrmsfit &
        ,fs0,r0,l0, tshift
REAL, DIMENSION(3) :: keff
!!!
! NUMBER OF FINITE VOLUMES. IF CHANGED, ENSURE
! THE OUTPUT FORMAT STRINGS ARE ADJUSTED LIKEWISE!
INTEGER, PARAMETER :: Nr=10, Nz=5
!!!
! Counters, step and block sizes, file labels, etc.
REAL :: dt,dr,dz,Fosr,Fogr,Fosz,Fogz,FoMax,rem=0,tlapse
INTEGER :: it,ir,iz,iblock, Nt,Nblocks,bsize,check=0,limithit=0,Ntsug,pplane,lastpct=0
INTEGER :: clock_0, clock_1, clock_rate, clock_max, IARGC,io,lines,iread
CHARACTER(32) :: tmpstr, runid, inputfile, tabsize
REAL :: trash1, trash2
!!!
! Time / Space Vectors and State arrays. Block index vector.
REAL, DIMENSION(:), ALLOCATABLE     :: time,z,r,vdot, datatime, datavdotn
REAL, DIMENSION(2)                  :: tvhold    !Time and volume yield carryover vector
REAL, DIMENSION(:,:,:), ALLOCATABLE :: T,u,fs,fc,eps,statehold
INTEGER, DIMENSION(:), ALLOCATABLE  :: bndx
! LOGICAL                            ::
    !!!
```

```
    ! PRE-RUN
    ! Snag command argument specified terms.
    IF ( IARGC() == 1 ) THEN
        PRINT *,'Arguments Recieved'
        CALL getarg(1,tmpstr)
        READ(tmpstr,*) inputfile
    ELSE
        PRINT *,' Incorrect number of arguments supplied',IARGC()
        STOP
    ENDIF
    ! Read input file for run parameters.
    OPEN(40,FILE=''//TRIM(inputfile)//'')
    READ(40,*),runid
    READ(40,*),Tinf
    READ(40,*),yh2o
    READ(40,*),hconv
    READ(40,*),Eapyr
    READ(40,*),ar
    ar = EXP(ar)
    READ(40,*),tabsize
    READ(40,*),tshift
    CLOSE(40)
    ! Configure geometry
    ! 7.77mm Dia cellulose tablets use: r0=0.00385, l0=0.00320, fs0=0.7670
    ! 10.2mm Dia cellulose tablets use: r0=0.00512, l0=0.00471, fs0=0.7543
    IF ( TRIM(tabsize) == '8mm' ) THEN
        fs0 = 0.7670
        r0  = 0.00385
        l0  = 0.00320
    ELSE IF ( TRIM(tabsize) == '10mm' ) THEN
        fs0 = 0.7543
        r0  = 0.00512
        l0  = 0.00471
    ENDIF
    ! Grab the data from the curve-to-be-fit file: "fit-data.dat". (Tab Delimited)
    ! Store the real data time as "datatime" and the normalized gas flows [L/min-g]
    ! as "datavdotn". Ensure the source data is the USEFUL gas flowrate
    OPEN(20,FILE='/h/hatha050/Gasification/rxnmod/fitdat/'//TRIM(runid)//'.dat')
    DO iread = 1, 6000
        READ(20,*,IOSTAT = io ),trash1,trash2
        IF (io < 0) exit
        lines = iread
    END DO
    ALLOCATE(datatime(lines))
    ALLOCATE(datavdotn(lines))
    REWIND(20)
    DO iread = 1, lines
        READ(20,*,IOSTAT = io ),datatime(iread),datavdotn(iread)
    ENDDO
    PRINT *,'Data file loaded. Lines read = ',lines
    CLOSE(20)
    ! Establish maximum possible carbon volume fraction
    fcmax=rhos*fs0*xcs/rhoc+fc0
    mpertab=3.14159*r0**2.*l0*(fs0*rhos+fc0*rhoc)*1000     ! mass of simulated tablet in
grams
    ! Establish desired number of timesteps based on total and grid sizes
    Ntsug=0.10*(tf/120.)*CEILING(2.5E6*(MAX(0.003855/r0,
0.003199/l0)*REAL(Nr)/20.*REAL(Nz)/8.)**2.)
    PRINT *,''
    PRINT *,'Suggested number of time steps: ',Ntsug
    PRINT *,'Using suggested value.'     ! Comment out and adjust below for user selected
Nt
    !READ *,Nt                           ! User selection code
    Nt=Ntsug                            ! Using suggested value code
    ! Establish the Temperature, velocity, solid cellulose
    ! and carbon volume fractions, and total porosity arrays
    ALLOCATE(r(Nr))
    ALLOCATE(z(Nz))
    dt=tf/(real(Nt)-1)
    dr=r0/(real(Nr)-0.5)
    dz=l0/(2.*real(Nz))
```

```
! Set array block size, in number of steps. Each array
! should cover ~0.25 seconds of behavior.
bsize=CEILING(0.25/dt)
! Verify blocks can hold 2 steps, but are not too large.
IF (bsize < 2) THEN
    PRINT *,'Block size is less than 2 steps! EXITING'
    STOP
ELSE IF (bsize > 20000) THEN
    PRINT *,'Block size too large. Imminent stack overflow! EXITING'
    STOP
END IF
! Set the number of blocks required to fit all time steps
Nblocks=CEILING(real(Nt)/real(bsize))
! Create block index vector. Indexes final time step for
! each array block.
ALLOCATE(bndx(Nblocks))
DO iblock=1,Nblocks
    IF (iblock*bsize < Nt) THEN
        bndx(iblock)=iblock*bsize
    ELSE
        bndx(iblock)=Nt
    ENDIF
ENDDO
! Establish the radial and axial coordinate vectors
DO ir=1,Nr
    r(ir)=(ir-1)*dr
END DO
DO iz=1,Nz
    z(iz)=(real(iz)-0.5)*dz
END DO
! Allocate state carrover arrays. The final timestep in a
! block will be stored here, and the first step in the next block
! is loaded from here. (Blocks used to avoid memory stack overflows)
! statehold(X,n,m) where X is (1-Temperature, 2-Outer edge velocity,
! 3-Cellulose vol frac, 4-Carbon vol frac, 5-porosity) then n and m are
! the r-position index value.
ALLOCATE(statehold(5,Nr,Nz))
! Utilize fourier number criterion to assess numerical stability
! The maximum fourier number in either the radial or axial direction
Fosr=(kpb(real(1200),ks,fs0,kc,fc0)/(rhos*cps))*dt/(dr*dr)
Fogr=(kpb(real(1200),ks,0.,kc,0.)/(rhog*cpg(real(1200))))*dt/(dr*dr)
Fosz=(kpb(real(1200),ks,fs0,kc,fc0)/(rhos*cps))*dt/(dz*dz)
Fogz=(kpb(real(1200),ks,0.,kc,0.)/(rhog*cpg(real(1200))))*dt/(dz*dz)
! OUTPUT the status of the current solution method.
PRINT *,''
PRINT *,'Stability Characteristics (Fo < 0.25) :'
PRINT *,' Fully Solid Radial Fourier number  = ',Fosr
PRINT *,' Fully Porous Radial Fourier number = ',Fogr
PRINT *,' Fully Solid Axial Fourier number  = ',Fosz
PRINT *,' Fully Porous Axial Fourier number = ',Fogz
FoMax = MAX ( Fosr, Fosz, Fogr, Fogz )
IF (FoMax > 0.25) THEN
    PRINT *,' CAUTION: Fourier Number exceeds stability criteron!'
    PRINT *,' !!!!!!!!!!!!!!BRACE FOR OSCILLATIONS!!!!!!!!!!!!!!!'
    IF (FoMax == Fogr) THEN
        PRINT *,' Oscillations due to hypertransport in radial direction.'
    ELSE IF (FoMax == Fogz) THEN
        PRINT *,' Oscillations due to hypertransport in axial direction.'
    ELSE
        PRINT *,' Fully solid hypertransport detected (this shouldnt be).'
        PRINT *,' Verify solid conductivities and recompile.'
    ENDIF
ENDIF
PRINT *,''
PRINT *,'Step characteristics:'
PRINT *,'   delta-t = ',dt
PRINT *,'   delta-r = ',dr
PRINT *,'   delta-z = ',dz
PRINT *,'   Time Steps   = ',Nt
PRINT *,'   Radial Steps = ',Nr
PRINT *,'   Axial Steps  = ',Nz
```

```
      PRINT *,''
      PRINT *,'Block processing characteristics:'
      PRINT *,'   Block Size (steps) = ',bsize
      PRINT *,'   Number of Blocks   = ',Nblocks
      PRINT *,''
!     PRINT *,'Which axial plane do you want to plot temperature and comp. data from?'
!     PRINT *,'1 - Middle symmetry plane, 8 - Top boundary plane'
!     READ  *,pplane
      PRINT *,'Temp and composition data will be from the tablet mid-plane.'
      pplane = 1
      !!!!!!!!!!!!!!!!!!!!!!!!!!!!!!!!!!!!!!!!!!!!!!!!!!!!!!!!!!!!!!!!!!!
      ! Print reaction conditions and prepare for primary calculations
      !
      iread = 1
      limithit = 0
      lastpct = 0.
      OPEN(1,FILE='run-info.txt',POSITION='APPEND')
      IF ( lines < 3 ) WRITE (1,313)
      313 FORMAT('NO FIT-DATA LOADED')
      WRITE (1,312)
      312 FORMAT(' ')
      WRITE (1,223) Tinf
      223 FORMAT('        T_inf  = ',F5.0)
      WRITE (1,224) yh2o
      224 FORMAT('        yh2o   = ',F5.3)
      WRITE (1,222) Eapyr
      222 FORMAT('        Ea_pyr = ',F4.0)
      WRITE (1,225) hconv
      225 FORMAT('        h_conv = ',F5.1)
      WRITE (1,226) LOG(ar)
      226 FORMAT('        LN(Ar) = ',F5.1)
      CLOSE(1)
      PRINT *,''
      PRINT *,'Reaction conditions:'
      PRINT *,'   Tablet =   ',TRIM(tabsize)
      PRINT *,'   T_salt =',Tinf
      PRINT *,'   y_H2O  =',yh2o
      PRINT *,'   h_conv =',hconv
      PRINT *,'   Ea_pyr =',Eapyr
      PRINT *,'   LN(Ar) =',LOG(ar)
      PRINT *,''
      PRINT *,'Continuing with computation . . . '
      PRINT *,''
      ! "Start the timer" by storing the initial system clock value.
      CALL SYSTEM_CLOCK( clock_0, clock_rate, clock_max)
      ! Initialize first block of time and state arrays
      ALLOCATE(T(bndx(1),Nr,Nz))
      ALLOCATE(u(bndx(1),Nr,Nz))
      ALLOCATE(fs(bndx(1),Nr,Nz))
      ALLOCATE(fc(bndx(1),Nr,Nz))
      ALLOCATE(eps(bndx(1),Nr,Nz))
      ALLOCATE(time(bndx(1)))
      ALLOCATE(vdot(bndx(1)))
      ! Set initial time and temperature conditions
      T(1,:,:)=T0
      u(1,:,:)=0.
      vdot(1)=0.
      fs(1,:,:)=fs0
      fc(1,:,:)=fc0
      eps(1,:,:)=1.-fs0-fc0
      time(1)=0.
      ! Reset the block processing counter
      iblock=1
      ! Open the output files for data dumping
      OPEN(1,FILE=''//TRIM(runid)//'_temp.txt')
!      OPEN(2,FILE=''//TRIM(runid)//'_uouter.txt')
!      OPEN(3,FILE=''//TRIM(runid)//'_fsolidcell.txt')
!      OPEN(4,FILE=''//TRIM(runid)//'_fcarbon.txt')
      OPEN(7,FILE=''//TRIM(runid)//'_porosity.txt')
!      OPEN(8,FILE=''//TRIM(runid)//'_vdot.txt')
      OPEN(9,FILE=''//TRIM(runid)//'_vdotUSE.txt')
```

```
    ! List the output formats for data dumping
    ! NOTE: CHANGE the number 50 in the format
    ! strings if you change the number of
    ! spatial divisions!
    100 FORMAT(7X,10(1X,F6.4))
    101 FORMAT((1X,F6.2  ,10(1X,F6.1)))
!    200 FORMAT(7X,50(1X,F8.4))
!    201 FORMAT((1X,F6.2  ,50(1X,F8.4)))
!    300 FORMAT(7X,50(1X,F6.4))
!    301 FORMAT((1X,F6.2  ,50(1X,F6.4)))
!    400 FORMAT(7X,50(1X,F6.4))
!    401 FORMAT((1X,F6.2  ,50(1X,F6.4)))
    500 FORMAT(7X,10(1X,F6.4))
    501 FORMAT((1X,F6.2  ,10(1X,F6.4)))
    600 FORMAT(1X,F6.2,1X,F8.4)
   !!!
   !!!
   ! PRIMARY CALCULATIONS
   !!!
   ! Explicitly establish the temporal variation of temperature
   ! (Explicit => Changes in temperature are determined only from the
   !  temperatures of the volume of interest and neighboring
   !  volumes using the previous time step.)
   timeloop: DO it=1,(Nt-1)
        ! Advance the time vector
        time(it+1)=it*dt
        !! First Calculate the midplane z-layer behaviors
        ! Set the nonlinear term values for the core
        keff(:)=kpb(T(it,1,1),ks,fs(it,1,1),kc,fc(it,1,1))
        Ceff=rhog*cpg(T(it,1,1))*eps(it,1,1)+fs(it,1,1)*cps*rhos+fc(it,1,1)*cpc*rhoc
        ! Set the new temperature of the core volume.
        T(it+1,1,1)=T(it,1,1)+dt/Ceff*( keff(2)*(4./(dr**2.))*(T(it,2,1)-T(it,1,1)) &
            +keff(2)*1./(dz**2.)*(T(it,1,2)-T(it,1,1)) &
            -u(it,1,1)*rhog*cpg(T(it,1,1))*(4./dr+1./dz)*eps(it,1,1)*(T(it,1,1)-T0) &
            -rdotp(ar,Eapyr,T(it,1,1),fs(it,1,1),rhos)*dHp(T(it,1,1)) &
            -rdotg(fcmax,Eagas,T(it,1,1),fc(it,1,1),rhoc,yh2o)*dHg(T(it,1,1)) )
        ! Determine the change in volume fractions of cellulose and carbon
        fs(it+1,1,1)=fs(it,1,1)-dt*rdotp(ar,Eapyr,T(it,1,1),fs(it,1,1),rhos)/rhos
        ! Control structure introduced to prevent the volume fraction of cellulose
        ! from dropping below zero.  It uses the remainng fraction prior to hitting
        ! zero to determine how much the carbon volume fraction increases.
        IF (fs(it+1,1,1) <= 0) THEN
            fs(it+1,1,1)=0
            rem=fs(it,1,1)
            fc(it+1,1,1)=fc(it,1,1)+rem*rhos*xcs/rhoc &
                -dt*rdotg(fcmax,Eagas,T(it,1,1),fc(it,1,1),rhoc,yh2o)/rhoc
        ELSE
            fc(it+1,1,1)=fc(it,1,1)+dt*rdotp(ar,Eapyr,T(it,1,1),fs(it,1,1),rhos) &
                *xcs/rhoc-dt*rdotg(fcmax,Eagas,T(it,1,1),fc(it,1,1),rhoc,yh2o)/rhoc
        END IF
        IF (fc(it+1,1,1) < 0) THEN
            fc(it+1,1,1)=0
        END IF
        eps(it+1,1,1)=(1.-fs(it+1,1,1)-fc(it+1,1,1))
        ! Set the gas velocities during this time step

u(it+1,1,1)=(1./eps(it+1,1,1))*(rdotp(ar,Eapyr,T(it+1,1,1),fs(it+1,1,1),rhos)*(vgs-
1./rhos+xcs/rhoc) &
                +rdotg(fcmax,Eagas,T(it+1,1,1),fc(it+1,1,1),rhoc,yh2o)*(vgc-
1./rhoc) )*dr*dz/( 4.*dz+dr)
        ! Moving from the core outwards through ring volumes at the midplane level
        rloop: DO ir=2,(Nr-1)
            ! Set the nonlinear term values
            keff(1)=kpb(T(it,ir-1,1),ks,fs(it,ir-1,1),kc,fc(it,ir-1,1))
            keff(2)=kpb(T(it,ir,1),ks,fs(it,ir,1),kc,fc(it,ir,1))

Ceff=rhog*cpg(T(it,ir,1))*eps(it,ir,1)+fs(it,ir,1)*cps*rhos+fc(it,ir,1)*cpc*rhoc
            ! Set the new temperature values of the non-core and non-boundary volumes.
            T(it+1,ir,1)=T(it,ir,1)+dt/Ceff*( &
                1./(dr**2.)*(keff(1)*(1.-dr/(2.*r(ir)))*(T(it,ir-1,1)-T(it,ir,1)) &
                +keff(2)*(1.+dr/(2.*r(ir)))*(T(it,ir+1,1)-T(it,ir,1))) &
```

```
                +keff(2)*1./(dz**2.)*(T(it,ir,2)-T(it,ir,1)) &
                -
u(it,ir,1)*rhog*cpg(T(it,ir,1))*(1./dr+1./(2.*r(ir))+1./dz)*eps(it,ir,1)*(T(it,ir,1)-T0)
&
                +u(it,ir-1,1)*rhog*cpg(T(it,ir-1,1))*(1./dr-1./(2.*r(ir)))*eps(it,ir-
1,1)*(T(it,ir-1,1)-T0) &
                -rdotp(ar,Eapyr,T(it,ir,1),fs(it,ir,1),rhos)*dHp(T(it,ir,1)) &
                -rdotg(fcmax,Eagas,T(it,ir,1),fc(it,ir,1),rhoc,yh2o)*dHg(T(it,ir,1)))
            ! Set the new volume fractions
            fs(it+1,ir,1)=fs(it,ir,1)-dt*rdotp(ar,Eapyr,T(it,ir,1),fs(it,ir,1),rhos)/rhos
            IF (fs(it+1,ir,1) <= 0) THEN
                fs(it+1,ir,1)=0
                rem=fs(it,ir,1)
                fc(it+1,ir,1)=fc(it,ir,1)+rem*rhos*xcs/rhoc-
dt*rdotg(fcmax,Eagas,T(it,ir,1),fc(it,ir,1),rhoc,yh2o)/rhoc
            ELSE

fc(it+1,ir,1)=fc(it,ir,1)+dt*rdotp(ar,Eapyr,T(it,ir,1),fs(it,ir,1),rhos)*xcs/rhoc &
                    -dt*rdotg(fcmax,Eagas,T(it,ir,1),fc(it,ir,1),rhoc,yh2o)/rhoc
            END IF
            IF (fc(it+1,ir,1) <= 0) THEN
                fc(it+1,ir,1)=0
            ENDIF
            eps(it+1,ir,1)=(1.-fs(it+1,ir,1)-fc(it+1,ir,1))
            ! Set the gas velocities during this time step
            u(it+1,ir,1)=u(it+1,ir-1,1)*eps(it+1,ir-1,1)/eps(it+1,ir,1)*        dz*(1./dr-
1/(2.*r(ir)))/(1.+dz*(1/dr+1/(2.*r(ir)))) &
                +
(1./eps(it+1,ir,1))*(        rdotp(ar,Eapyr,T(it+1,ir,1),fs(it+1,ir,1),rhos)*(        vgs-
1./rhos+xcs/rhoc ) &
                +      rdotg(fcmax,Eagas,T(it+1,ir,1),fc(it+1,ir,1),rhoc,yh2o)*(      vgc-
1./rhoc ) ) &
                *dr*dz/(dr+dz*(1.+dr/(2.*r(ir))))
        ENDDO rloop
        ! Finishing with the exterior boundary volume of the midplane level
        ! Set the nonlinear term values
        keff(1)=kpb(T(it,Nr-1,1),ks,fs(it,Nr-1,1),kc,fc(it,Nr-1,1))
        keff(2)=kpb(T(it,Nr,1),ks,fs(it,Nr,1),kc,fc(it,Nr,1))
        Ceff=rhog*cpg(T(it,Nr,1))*eps(it,Nr,1)+fs(it,Nr,1)*cps*rhos+fc(it,Nr,1)*cpc*rhoc
        ! Set the new value of the boundary midplane volume temperature
        T(it+1,Nr,1)=T(it,Nr,1)+dt/Ceff*( &
                 keff(1)*1./(dr**2.)*( 1-dr/(2.*r(Nr)))*(T(it,Nr-1,1)-T(it,Nr,1)) &
                +keff(2)*1./(dz**2.)*(T(it,Nr,2)-T(it,Nr,1)) &
                -u(it,Nr,1)*rhog*cpg(T(it,Nr,1))*(1./dr+1./(2.*r(Nr))
+1./dz)*eps(it,Nr,1)*(T(it,Nr,1)-T0) &
                +u(it,Nr-1,1)*rhog*cpg(T(it,Nr-1,1))*(1./dr-1./(2.*r(Nr)))*eps(it,Nr-
1,1)*(T(it,Nr-1,1)-T0) &
                -rdotp(ar,Eapyr,T(it,Nr,1),fs(it,Nr,1),rhos)*dHp(T(it,Nr,1)) &
                -rdotg(fcmax,Eagas,T(it,Nr,1),fc(it,Nr,1),rhoc,yh2o)*dHg(T(it,Nr,1)) &
                +htot(hconv,T(it,Nr,1),Tinf)*r0/(r(Nr)*dr)*(Tinf-T(it,Nr,1)) )
        ! Set the new volume fractions of the boundary midplane volume
        fs(it+1,Nr,1)=fs(it,Nr,1)-dt*rdotp(ar,Eapyr,T(it,Nr,1),fs(it,Nr,1),rhos)/rhos
        IF (fs(it+1,Nr,1) <= 0) THEN
            fs(it+1,Nr,1)=0
            rem=fs(it,Nr,1)
            fc(it+1,Nr,1)=fc(it,Nr,1)+rem*rhos*xcs/rhoc &
                -dt*rdotg(fcmax,Eagas,T(it,Nr,1),fc(it,Nr,1),rhoc,yh2o)/rhoc
        ELSE
            fc(it+1,Nr,1)=fc(it,Nr,1)+dt*rdotp(ar,Eapyr,T(it,Nr,1),fs(it,Nr,1),rhos) &
            *xcs/rhoc-dt*rdotg(fcmax,Eagas,T(it,Nr,1),fc(it,Nr,1),rhoc,yh2o)/rhoc
        END IF
        IF (fc(it+1,Nr,1) <=0) THEN
            fc(it+1,Nr,1) = 0
        ENDIF
        eps(it+1,Nr,1)=(1.-fs(it+1,Nr,1)-fc(it+1,Nr,1))
        ! Set the gas velocities during this time step
        u(it+1,Nr,1)=u(it+1,Nr-1,1)*eps(it+1,Nr-1,1)/eps(it+1,Nr,1)*dz*(1./dr-
1/(2.*r(Nr)))/(1.+dz*(1/dr+1/(2.*r(Nr)))) &
            +
(1./eps(it+1,Nr,1))*(        rdotp(ar,Eapyr,T(it+1,Nr,1),fs(it+1,Nr,1),rhos)*(        vgs-
1./rhos+xcs/rhoc ) &
```

```
            +        rdotg(fcmax,Eagas,T(it+1,Nr,1),fc(it+1,Nr,1),rhoc,yh2o)*(        vgc-
1./rhoc ) )*dr*dz/(dr+dz*(1.+dr/(2.*r(Nr))))
        !! Work through the non-midplane nor top-boundary z-layers
        zloop: DO iz=2,(Nz-1)
            ! Set the nonlinear term values for the general core volumes
            keff(2)=kpb(T(it,1,iz),ks,fs(it,1,iz),kc,fc(it,1,iz))
            keff(3)=kpb(T(it,1,iz-1),ks,fs(it,1,iz-1),kc,fc(it,1,iz-1))

Ceff=rhog*cpg(T(it,1,iz))*eps(it,1,iz)+fs(it,1,iz)*cps*rhos+fc(it,1,iz)*cpc*rhoc
            ! Set the new temperature of the core volume.
            T(it+1,1,iz)=T(it,1,iz)+dt/Ceff*( &
                 keff(2)*(4./(dr**2.))*(T(it,2,iz)-T(it,1,iz)) &
                +keff(2)*1./(dz**2.)*(T(it,1,iz+1)-T(it,1,iz)) &
                +keff(3)*1./(dz**2.)*(T(it,1,iz-1)-T(it,1,iz)) &
                -u(it,1,iz)*rhog*cpg(T(it,1,iz))*(4./dr+1./dz)*eps(it,1,iz)*(T(it,1,iz)-
T0) &
                +u(it,1,iz-1)*rhog*cpg(T(it,1,iz-1))*(1./dz)*eps(it,1,iz-1)*(T(it,1,iz-
1)-T0) &
                -rdotp(ar,Eapyr,T(it,1,iz),fs(it,1,iz),rhos)*dHp(T(it,1,iz)) &
                -rdotg(fcmax,Eagas,T(it,1,iz),fc(it,1,iz),rhoc,yh2o)*dHg(T(it,1,iz)) )
            ! Determine the change in volume fractions of cellulose and carbon
            fs(it+1,1,iz)=fs(it,1,iz)-dt*rdotp(ar,Eapyr,T(it,1,iz),fs(it,1,iz),rhos)/rhos
            ! Control structure introduced to prevent the volume fraction of cellulose
            ! from dropping below zero.  It uses the remainng fraction prior to hitting
            ! zero to determine how much the carbon volume fraction increases.
            IF (fs(it+1,1,iz) <= 0) THEN
                fs(it+1,1,iz)=0
                rem=fs(it,1,iz)
                fc(it+1,1,iz)=fc(it,1,iz)+rem*rhos*xcs/rhoc &
                    -dt*rdotg(fcmax,Eagas,T(it,1,iz),fc(it,1,iz),rhoc,yh2o)/rhoc
            ELSE
                fc(it+1,1,iz)=fc(it,1,iz)+dt*rdotp(ar,Eapyr,T(it,1,iz),fs(it,1,iz),rhos)
&
                    *xcs/rhoc-dt*rdotg(fcmax,Eagas,T(it,1,iz),fc(it,1,iz),rhoc,yh2o)/rhoc
            END IF
            IF (fc(it+1,1,iz) < 0) THEN
                fc(it+1,1,iz)=0
            END IF
            eps(it+1,1,iz)=(1.-fs(it+1,1,iz)-fc(it+1,1,iz))
            ! Set the gas velocities during this time step
            u(it+1,1,iz)=u(it+1,1,iz-1)*eps(it+1,1,iz-1)/eps(it+1,1,iz)*dr/(4.*dz+dr) &
                 +
(1./eps(it+1,1,iz))*(                rdotp(ar,Eapyr,T(it+1,1,iz),fs(it+1,1,iz),rhos)*(vgs-
1./rhos+xcs/rhoc) &
                 +           rdotg(fcmax,Eagas,T(it+1,1,iz),fc(it+1,1,iz),rhoc,yh2o)*(vgc-
1./rhoc) )*dr*dz/( 4.*dz+dr)
            ! Moving from the core outwards through ring volumes
            rloopiz: DO ir=2,(Nr-1)
                ! Set the nonlinear term values
                keff(1)=kpb(T(it,ir-1,iz),ks,fs(it,ir-1,iz),kc,fc(it,ir-1,iz))
                keff(2)=kpb(T(it,ir,iz),ks,fs(it,ir,iz),kc,fc(it,ir,iz))
                keff(3)=kpb(T(it,ir,iz-1),ks,fs(it,ir,iz-1),kc,fc(it,ir,iz-1))

Ceff=rhog*cpg(T(it,ir,iz))*eps(it,ir,iz)+fs(it,ir,iz)*cps*rhos+fc(it,ir,iz)*cpc*rhoc
                ! Set the new temperature values of the non-core and non-boundary volumes.
                T(it+1,ir,iz)=T(it,ir,iz)+dt/Ceff*( &
                     1./(dr**2.)*(keff(1)*(1.-dr/(2.*r(ir)))*(T(it,ir-1,iz)-T(it,ir,iz))
&
                    +keff(2)*(1.+dr/(2.*r(ir)))*(T(it,ir+1,iz)-T(it,ir,iz))) &
                    +keff(2)*1./(dz**2.)*(T(it,ir,iz+1)-T(it,ir,iz)) &
                    +keff(3)*1./(dz**2.)*(T(it,ir,iz-1)-T(it,ir,iz)) &
                    -
u(it,ir,iz)*rhog*cpg(T(it,ir,iz))*(1./dr+1./(2.*r(ir))+1./dz)*eps(it,ir,iz)*(T(it,ir,iz)-
T0) &
                    +u(it,ir-1,iz)*rhog*cpg(T(it,ir-1,iz))*(1./dr-
1./(2.*r(ir)))*eps(it,ir-1,iz)*(T(it,ir-1,iz)-T0) &
                    +u(it,ir,iz-1)*rhog*cpg(T(it,ir,iz-1))*(1./dz)*eps(it,ir,iz-
1)*(T(it,ir,iz-1)-T0) &
                    -rdotp(ar,Eapyr,T(it,ir,iz),fs(it,ir,iz),rhos)*dHp(T(it,ir,iz)) &
                    -
rdotg(fcmax,Eagas,T(it,ir,iz),fc(it,ir,iz),rhoc,yh2o)*dHg(T(it,ir,iz)))
```

```
                ! Set the new volume fractions
                fs(it+1,ir,iz)=fs(it,ir,iz)-
dt*rdotp(ar,Eapyr,T(it,ir,iz),fs(it,ir,iz),rhos)/rhos
                IF (fs(it+1,ir,iz) <= 0) THEN
                    fs(it+1,ir,iz)=0
                    rem=fs(it,ir,iz)
                    fc(it+1,ir,iz)=fc(it,ir,iz)+rem*rhos*xcs/rhoc &
                        -dt*rdotg(fcmax,Eagas,T(it,ir,iz),fc(it,ir,iz),rhoc,yh2o)/rhoc
                ELSE

fc(it+1,ir,iz)=fc(it,ir,iz)+dt*rdotp(ar,Eapyr,T(it,ir,iz),fs(it,ir,iz),rhos)*xcs/rhoc &
                        -dt*rdotg(fcmax,Eagas,T(it,ir,iz),fc(it,ir,iz),rhoc,yh2o)/rhoc
                END IF
                IF (fc(it+1,ir,iz) <= 0) THEN
                    fc(it+1,ir,iz)=0
                ENDIF
                eps(it+1,ir,iz)=(1.-fs(it+1,ir,iz)-fc(it+1,ir,iz))
                ! Set the gas velocities during this time step
                u(it+1,ir,iz)=u(it+1,ir-1,iz)*eps(it+1,ir-1,iz)/eps(it+1,ir,iz) &
                    *dz*(1./dr-1/(2.*r(ir)))/(1.+dz*(1/dr+1/(2.*r(ir)))) &
                    +                                        u(it+1,ir,iz-1)*eps(it+1,ir,iz-
1)/eps(it+1,ir,iz)*1./(1.+dz*(1./dr+1/(2.*r(ir)))) &
                    +
(1./eps(it+1,ir,iz))*(      rdotp(ar,Eapyr,T(it+1,ir,iz),fs(it+1,ir,iz),rhos)*(      vgs-
1./rhos+xcs/rhoc ) &
                    +   rdotg(fcmax,Eagas,T(it+1,ir,iz),fc(it+1,ir,iz),rhoc,yh2o)*(   vgc-
1./rhoc ) ) &
                    *dr*dz/(dr+dz*(1.+dr/(2.*r(ir))))
            ENDDO rloopiz
            ! Finishing with the exterior boundary volume
            ! Set the nonlinear term values
            keff(1)=kpb(T(it,Nr-1,iz),ks,fs(it,Nr-1,iz),kc,fc(it,Nr-1,iz))
            keff(2)=kpb(T(it,Nr,iz),ks,fs(it,Nr,iz),kc,fc(it,Nr,iz))
            keff(3)=kpb(T(it,Nr,iz-1),ks,fs(it,Nr,iz-1),kc,fc(it,Nr,iz-1))

Ceff=rhog*cpg(T(it,Nr,iz))*eps(it,Nr,iz)+fs(it,Nr,iz)*cps*rhos+fc(it,Nr,iz)*cpc*rhoc
            ! Set the new value of the boundary volume temperature
            T(it+1,Nr,iz)=T(it,Nr,iz)+dt/Ceff*( &
                     keff(1)*1./(dr**2.)*( 1-dr/(2.*r(Nr)))*(T(it,Nr-1,iz)-T(it,Nr,iz)) &
                    +keff(2)*1./(dz**2.)*(T(it,Nr,iz+1)-T(it,Nr,iz)) &
                    +keff(3)*1./(dz**2.)*(T(it,Nr,iz-1)-T(it,Nr,iz)) &
                    -u(it,Nr,iz)*rhog*cpg(T(it,Nr,iz))*(1./dr+1./(2.*r(Nr))
+1./dz)*eps(it,Nr,iz)*(T(it,Nr,iz)-T0) &
                    +u(it,Nr-1,iz)*rhog*cpg(T(it,Nr-1,iz))*(1./dr-
1./(2.*r(Nr)))*eps(it,Nr-1,iz)*(T(it,Nr-1,iz)-T0) &
                    +u(it,Nr,iz-1)*rhog*cpg(T(it,Nr,iz-1))*(1./dz)*eps(it,Nr,iz-
1)*(T(it,Nr,iz-1)-T0) &
                    -rdotp(ar,Eapyr,T(it,Nr,iz),fs(it,Nr,iz),rhos)*dHp(T(it,Nr,iz)) &
                    -
rdotg(fcmax,Eagas,T(it,Nr,iz),fc(it,Nr,iz),rhoc,yh2o)*dHg(T(it,Nr,iz)) &
                    +htot(hconv,T(it,Nr,iz),Tinf)*r0/(r(Nr)*dr)*(Tinf-T(it,Nr,iz)) )
            ! Set the new volume fractions of the boundary volume
            fs(it+1,Nr,iz)=fs(it,Nr,iz)-
dt*rdotp(ar,Eapyr,T(it,Nr,iz),fs(it,Nr,iz),rhos)/rhos
            IF (fs(it+1,Nr,iz) <= 0) THEN
                fs(it+1,Nr,iz)=0
                rem=fs(it,Nr,iz)
                fc(it+1,Nr,iz)=fc(it,Nr,iz)+rem*rhos*xcs/rhoc &
                    -dt*rdotg(fcmax,Eagas,T(it,Nr,iz),fc(it,Nr,iz),rhoc,yh2o)/rhoc
            ELSE

fc(it+1,Nr,iz)=fc(it,Nr,iz)+dt*rdotp(ar,Eapyr,T(it,Nr,iz),fs(it,Nr,iz),rhos) &
                *xcs/rhoc-dt*rdotg(fcmax,Eagas,T(it,Nr,iz),fc(it,Nr,iz),rhoc,yh2o)/rhoc
            END IF
            IF (fc(it+1,Nr,iz) <=0) THEN
                fc(it+1,Nr,iz) = 0
            ENDIF
            eps(it+1,Nr,iz)=(1.-fs(it+1,Nr,iz)-fc(it+1,Nr,iz))
            ! Set the gas velocities during this time step
            u(it+1,Nr,iz)=u(it+1,Nr-1,iz)*eps(it+1,Nr-1,iz)/eps(it+1,Nr,iz) &
                *dz*(1./dr-1/(2.*r(Nr)))/(1.+dz*(1/dr+1/(2.*r(Nr)))) &
```

```
                +                                        u(it+1,Nr,iz-1)*eps(it+1,Nr,iz-
1)/eps(it+1,Nr,iz)*1./(1.+dz*(1./dr+1/(2.*r(ir)))) &
                +
(1./eps(it+1,Nr,iz))*(      rdotp(ar,Eapyr,T(it+1,Nr,iz),fs(it+1,Nr,iz),rhos)*(      vgs-
1./rhos+xcs/rhoc ) &
                +     rdotg(fcmax,Eagas,T(it+1,Nr,iz),fc(it+1,Nr,iz),rhoc,yh2o)*(     vgc-
1./rhoc ) ) &
                *dr*dz/(dr+dz*(1.+dr/(2.*r(Nr))))
        ENDDO zloop
        ! Work with the top-boundary z-layer
        ! Set the nonlinear term values for the top core volume
        keff(2)=kpb(T(it,1,Nz),ks,fs(it,1,Nz),kc,fc(it,1,Nz))
        keff(3)=kpb(T(it,1,Nz-1),ks,fs(it,1,Nz-1),kc,fc(it,1,Nz-1))
        Ceff=rhog*cpg(T(it,1,Nz))*eps(it,1,Nz)+fs(it,1,Nz)*cps*rhos+fc(it,1,Nz)*cpc*rhoc
        ! Set the new temperature of the core volume.
        T(it+1,1,Nz)=T(it,1,Nz)+dt/Ceff*( &
             keff(2)*(4./(dr**2.))*(T(it,2,Nz)-T(it,1,Nz)) &
            +keff(3)*1./(dz**2.)*(T(it,1,Nz-1)-T(it,1,Nz)) &
            -u(it,1,Nz)*rhog*cpg(T(it,1,Nz))*(4./dr+1./dz)*eps(it,1,Nz)*(T(it,1,Nz)-T0) &
            +u(it,1,Nz-1)*rhog*cpg(T(it,1,Nz-1))*(1./dz)*eps(it,1,Nz-1)*(T(it,1,Nz-1)-T0)
&
            -rdotp(ar,Eapyr,T(it,1,Nz),fs(it,1,Nz),rhos)*dHp(T(it,1,Nz)) &
            -rdotg(fcmax,Eagas,T(it,1,Nz),fc(it,1,Nz),rhoc,yh2o)*dHg(T(it,1,Nz)) &
            +htot(hconv,T(it,1,Nz),Tinf)*(1./dz)*(Tinf-T(it,1,Nz)))
        ! Determine the change in volume fractions of cellulose and carbon
        fs(it+1,1,Nz)=fs(it,1,Nz)-dt*rdotp(ar,Eapyr,T(it,1,Nz),fs(it,1,Nz),rhos)/rhos
        ! Control structure introduced to prevent the volume fraction of cellulose
        ! from dropping below zero.  It uses the remainng fraction prior to hitting
        ! zero to determine how much the carbon volume fraction increases.
        IF (fs(it+1,1,Nz) <= 0) THEN
            fs(it+1,1,Nz)=0
            rem=fs(it,1,Nz)
            fc(it+1,1,Nz)=fc(it,1,Nz)+rem*rhos*xcs/rhoc &
                -dt*rdotg(fcmax,Eagas,T(it,1,Nz),fc(it,1,Nz),rhoc,yh2o)/rhoc
        ELSE
            fc(it+1,1,Nz)=fc(it,1,Nz)+dt*rdotp(ar,Eapyr,T(it,1,Nz),fs(it,1,Nz),rhos) &
                *xcs/rhoc-dt*rdotg(fcmax,Eagas,T(it,1,Nz),fc(it,1,Nz),rhoc,yh2o)/rhoc
        END IF
        IF (fc(it+1,1,Nz) < 0) THEN
            fc(it+1,1,Nz)=0
        END IF
        eps(it+1,1,Nz)=(1.-fs(it+1,1,Nz)-fc(it+1,1,Nz))
        ! Set the gas velocities during this time step
        u(it+1,1,Nz)=u(it+1,1,Nz-1)*eps(it+1,1,Nz-1)/eps(it+1,1,Nz)*dr/(4.*dz+dr) &
             +
(1./eps(it+1,1,Nz))*(               rdotp(ar,Eapyr,T(it+1,1,Nz),fs(it+1,1,Nz),rhos)*(vgs-
1./rhos+xcs/rhoc) &
             +              rdotg(fcmax,Eagas,T(it+1,1,Nz),fc(it+1,1,Nz),rhoc,yh2o)*(vgc-
1./rhoc) )*dr*dz/( 4.*dz+dr)
        ! Moving from the core outwards through ring volumes
        rlooptop: DO ir=2,(Nr-1)
            ! Set the nonlinear term values
            keff(1)=kpb(T(it,ir-1,Nz),ks,fs(it,ir-1,Nz),kc,fc(it,ir-1,Nz))
            keff(2)=kpb(T(it,ir,Nz),ks,fs(it,ir,Nz),kc,fc(it,ir,Nz))
            keff(3)=kpb(T(it,ir,Nz-1),ks,fs(it,ir,Nz-1),kc,fc(it,ir,Nz-1))

Ceff=rhog*cpg(T(it,ir,Nz))*eps(it,ir,Nz)+fs(it,ir,Nz)*cps*rhos+fc(it,ir,Nz)*cpc*rhoc
            ! Set the new temperature values of the non-core and non-boundary volumes.
            T(it+1,ir,Nz)=T(it,ir,Nz)+dt/Ceff*(                 1./(dr**2.)*(keff(1)*(1.-
dr/(2.*r(ir)))*(T(it,ir-1,Nz)-T(it,ir,Nz)) &
                +keff(2)*(1.+dr/(2.*r(ir)))*(T(it,ir+1,Nz)-T(it,ir,Nz))) &
                +keff(3)*1./(dz**2.)*(T(it,ir,Nz-1)-T(it,ir,Nz)) &
                -
u(it,ir,Nz)*rhog*cpg(T(it,ir,Nz))*(1./dr+1./(2.*r(ir))+1./dz)*eps(it,ir,Nz)*(T(it,ir,Nz)-
T0) &
                +u(it,ir-1,Nz)*rhog*cpg(T(it,ir-1,Nz))*(1./dr-1./(2.*r(ir)))*eps(it,ir-
1,Nz)*(T(it,ir-1,Nz)-T0) &
                +u(it,ir,Nz-1)*rhog*cpg(T(it,ir,Nz-1))*(1./dz)*eps(it,ir,Nz-
1)*(T(it,ir,Nz-1)-T0) &
                -rdotp(ar,Eapyr,T(it,ir,Nz),fs(it,ir,Nz),rhos)*dHp(T(it,ir,Nz)) &
                -rdotg(fcmax,Eagas,T(it,ir,Nz),fc(it,ir,Nz),rhoc,yh2o)*dHg(T(it,ir,Nz)) &
```

```
                +htot(hconv,T(it,ir,Nz),Tinf)*(1./dz)*(Tinf-T(it,ir,Nz)) )
            ! Set the new volume fractions
            fs(it+1,ir,Nz)=fs(it,ir,Nz)-
dt*rdotp(ar,Eapyr,T(it,ir,Nz),fs(it,ir,Nz),rhos)/rhos
            IF (fs(it+1,ir,Nz) <= 0) THEN
                fs(it+1,ir,Nz)=0
                rem=fs(it,ir,Nz)
                fc(it+1,ir,Nz)=fc(it,ir,Nz)+rem*rhos*xcs/rhoc &
                    -dt*rdotg(fcmax,Eagas,T(it,ir,Nz),fc(it,ir,Nz),rhoc,yh2o)/rhoc
            ELSE

fc(it+1,ir,Nz)=fc(it,ir,Nz)+dt*rdotp(ar,Eapyr,T(it,ir,Nz),fs(it,ir,Nz),rhos)*xcs/rhoc &
                    -dt*rdotg(fcmax,Eagas,T(it,ir,Nz),fc(it,ir,Nz),rhoc,yh2o)/rhoc
            END IF
            IF (fc(it+1,ir,Nz) <= 0) THEN
                fc(it+1,ir,Nz)=0
            ENDIF
            eps(it+1,ir,Nz)=(1.-fs(it+1,ir,Nz)-fc(it+1,ir,Nz))
            ! Set the gas velocities during this time step
            u(it+1,ir,Nz)=u(it+1,ir-1,Nz)*eps(it+1,ir-1,Nz)/eps(it+1,ir,Nz) &
                *dz*(1./dr-1/(2.*r(ir)))/(1.+dz*(1/dr+1/(2.*r(ir)))) &
                +                                       u(it+1,ir,Nz-1)*eps(it+1,ir,Nz-
1)/eps(it+1,ir,Nz)*1./(1.+dz*(1./dr+1/(2.*r(ir)))) &
                +
(1./eps(it+1,ir,Nz))*(      rdotp(ar,Eapyr,T(it+1,ir,Nz),fs(it+1,ir,Nz),rhos)*(      vgs-
1./rhos+xcs/rhoc ) &
                +     rdotg(fcmax,Eagas,T(it+1,ir,Nz),fc(it+1,ir,Nz),rhoc,yh2o)*(     vgc-
1./rhoc ) ) &
                *dr*dz/(dr+dz*(1.+dr/(2.*r(ir))))
        ENDDO rlooptop
        ! Finishing with the exterior boundary volume
        ! Set the nonlinear term values
        keff(1)=kpb(T(it,Nr-1,Nz),ks,fs(it,Nr-1,Nz),kc,fc(it,Nr-1,Nz))
        keff(2)=kpb(T(it,Nr,iz),ks,fs(it,Nr,iz),kc,fc(it,Nr,iz))
        keff(3)=kpb(T(it,Nr,Nz-1),ks,fs(it,Nr,Nz-1),kc,fc(it,Nr,Nz-1))

Ceff=rhog*cpg(T(it,Nr,Nz))*eps(it,Nr,Nz)+fs(it,Nr,Nz)*cps*rhos+fc(it,Nr,Nz)*cpc*rhoc
        ! Set the new value of the boundary volume temperature

        T(it+1,Nr,Nz)=T(it,Nr,Nz)+dt/Ceff*( &
                +keff(1)*1./(dr**2.)*( 1-dr/(2.*r(Nr)))*(T(it,Nr-1,Nz)-T(it,Nr,Nz)) &
                +keff(3)*1./(dz**2.)*(T(it,Nr,Nz-1)-T(it,Nr,Nz)) &
                -u(it,Nr,Nz)*rhog*cpg(T(it,Nr,Nz))*(1./dr+1./(2.*r(Nr))
+1./dz)*eps(it,Nr,Nz)*(T(it,Nr,Nz)-T0) &
                +u(it,Nr-1,Nz)*rhog*cpg(T(it,Nr-1,Nz))*(1./dr-1./(2.*r(Nr)))*eps(it,Nr-
1,Nz)*(T(it,Nr-1,Nz)-T0) &
                +u(it,Nr,Nz-1)*rhog*cpg(T(it,Nr,Nz-1))*(1./dz)*eps(it,Nr,Nz-
1)*(T(it,Nr,Nz-1)-T0) &
                -rdotp(ar,Eapyr,T(it,Nr,Nz),fs(it,Nr,Nz),rhos)*dHp(T(it,Nr,Nz)) &
                -rdotg(fcmax,Eagas,T(it,Nr,Nz),fc(it,Nr,Nz),rhoc,yh2o)*dHg(T(it,Nr,Nz)) &
                +htot(hconv,T(it,Nr,Nz),Tinf)*(r0/(r(Nr)*dr)+ 1./dz)*(Tinf-T(it,Nr,Nz)))
        ! Set the new volume fractions of the boundary volume
        fs(it+1,Nr,Nz)=fs(it,Nr,Nz)-dt*rdotp(ar,Eapyr,T(it,Nr,Nz),fs(it,Nr,Nz),rhos)/rhos
        IF (fs(it+1,Nr,Nz) <= 0) THEN
            fs(it+1,Nr,Nz)=0
            rem=fs(it,Nr,Nz)
            fc(it+1,Nr,Nz)=fc(it,Nr,Nz)+rem*rhos*xcs/rhoc &
                -dt*rdotg(fcmax,Eagas,T(it,Nr,Nz),fc(it,Nr,Nz),rhoc,yh2o)/rhoc
        ELSE
            fc(it+1,Nr,Nz)=fc(it,Nr,Nz)+dt*rdotp(ar,Eapyr,T(it,Nr,Nz),fs(it,Nr,Nz),rhos)
&
            *xcs/rhoc-dt*rdotg(fcmax,Eagas,T(it,Nr,Nz),fc(it,Nr,Nz),rhoc,yh2o)/rhoc
        END IF
        IF (fc(it+1,Nr,Nz) <=0) THEN
            fc(it+1,Nr,Nz) = 0
        ENDIF
        eps(it+1,Nr,Nz)=(1.-fs(it+1,Nr,Nz)-fc(it+1,Nr,Nz))
        ! Set the gas velocities at the upper outer boundary
        u(it+1,Nr,Nz)=u(it+1,Nr-1,Nz)*eps(it+1,Nr-1,Nz)/eps(it+1,Nr,Nz)*dz*(1./dr-
1/(2.*r(Nr)))/(1.+dz*(1/dr+1/(2.*r(Nr)))) &
```

```
            +                                                u(it+1,Nr,Nz-1)*eps(it+1,Nr,Nz-
1)/eps(it+1,Nr,Nz)*1./(1.+dz*(1./dr+1/(2.*r(ir)))) &
            +
(1./eps(it+1,Nr,Nz))*(      rdotp(ar,Eapyr,T(it+1,Nr,Nz),fs(it+1,Nr,Nz),rhos)*(      vgs-
1./rhos+xcs/rhoc ) &
            +       rdotg(fcmax,Eagas,T(it+1,Nr,Nz),fc(it+1,Nr,Nz),rhoc,yh2o)*(       vgc-
1./rhoc ) )*dr*dz/(dr+dz*(1.+dr/(2.*r(Nr))))
        !
        ! The entire tablet has been iterated over. Set final timestep data:
        ! Gas yield rate in liters/minute-g
        vdot(it+1)=(2.*3.14159*1000*60*( SUM(u(it+1,Nr,:)*eps(it+1,Nr,:))*r0*dz*2. &
            +
SUM(u(it+1,2:Nr,Nz)*r(2:Nr)*eps(it+1,2:Nr,Nz))*dr*2.+(dr**2./4.)*u(it+1,1,Nz)*eps(it+1,1,
Nz) ))/(mpertab)
        ! Conversion rate in 1/sec
        rconv = vdot(it+1) / (60*vgs)
        ! extent of conversion
        convext = convext + rconv * dt
        IF ( (convext .GT. convlimit) .AND. (limithit .EQ. 0) ) THEN
            limithit = 1
            avetemp = SUM(T(it+1,:,:))/(Nr*Nz)
            OPEN(10,FILE='run-info.txt',POSITION='APPEND')
            WRITE (10,668),convext,avetemp,rconv/(1.-convext)
            668 FORMAT('        R_cc(X=',F4.2,' Tavg=',F5.0,')= ',E8.2,' sec^-1')
            CLOSE(10)
        ENDIF
        ! USEFUL volume flow rate in STD l/m-g for data compairison. (STD meaning 1 atm,
0C)
        vdotuse = vdot(it+1) * ( 1. - 0.11 ) / 1.1096
        ! Calculate weighted root mean square error at each data time position.
        IF ( ( (time(it+1)-tshift) .GT. datatime(iread) ) .AND. (iread .LE. lines ) )
THEN
            wssefit = wssefit + datavdotn(iread) * (vdotuse-datavdotn(iread))**2.
            datavdotnsum = datavdotnsum + datavdotn(iread)
            iread = iread + 1
        ENDIF
        !!!
        ! Oscillation Observer: Detect explicit instability oscillations and report to
the user / output files.
        IF ((T(it+1,Nr,Nz) > Tinf) .AND. (check==0)) THEN
            check = 1
            PRINT *, '!!!!!!!!!!!!!!!!!!!!!!!!!!!!!!!!!!!!!!!!!!!!!!!!!!!'
            WRITE (*,666) time(it+1)
            666 FORMAT(' !! CHAOTIC OSCILLATIONS AT time=',F6.2,' SECONDS !!')
            PRINT *, '!!!!!!!!!!!!!!!!!!!!!!!!!!!!!!!!!!!!!!!!!!!!!!!!!!!'
            Fosz=(keff(2)/Ceff)*(dt/(dz*dz))
            PRINT *,''
            PRINT *,'Outer layer axial fourier number = ',Fosz
            OPEN(10,FILE='run-info.txt',POSITION='APPEND')
            WRITE (10,999)
            999 FORMAT('OSCILLATIONS WERE DETECTED')
            CLOSE(10)
        ENDIF
        !!!
        ! DATA DUMP / ARRAY BLOCK ADVANCING
        ! When a timestep index point is reached, dump data and reinit arrays
        IF ( (it+1) == bndx(iblock) ) THEN
            ! Display extent of conversion on screen
            IF ( CEILING(convext*10.) .GT. lastpct ) THEN
                lastpct = CEILING(convext*10.)
                WRITE(*,667),lastpct
                667 FORMAT('Status: ',I2,'0% conversion')
            ENDIF
            ! Retain final block step values
            statehold(1,:,:)=T(it+1,:,:)
            statehold(2,:,:)=u(it+1,:,:)
            statehold(3,:,:)=fs(it+1,:,:)
            statehold(4,:,:)=fc(it+1,:,:)
            statehold(5,:,:)=eps(it+1,:,:)
            tvhold(1)=time(it+1)
            tvhold(2)=vdot(it+1)
```

```
            !!!
            ! Write out the index point(s) of each block.
            IF (iblock == 1) THEN
                ! Write out the position labels above the first record
                WRITE(1,100) r
!                WRITE(2,200) r
!                WRITE(3,300) r
!                WRITE(4,400) r
                WRITE(7,500) r
                ! Print the initial and index (final) rows from the first block (tablet
plane# pplane)
                WRITE(1,101) time(1),T(1,:,pplane)
                WRITE(1,101) time(bndx(iblock)),T(bndx(iblock),:,pplane)
!                WRITE(2,201) time(1),u(1,:,pplane)
!                WRITE(2,201) time(bndx(iblock)),u(bndx(iblock),:,pplane)
!                WRITE(3,301) time(1),fs(1,:,pplane)
!                WRITE(3,301) time(bndx(iblock)),fs(bndx(iblock),:,pplane)
!                WRITE(4,401) time(1),fc(1,:,pplane)
!                WRITE(4,401) time(bndx(iblock)),fc(bndx(iblock),:,pplane)
                WRITE(7,501) time(1),eps(1,:,pplane)
                WRITE(7,501) time(bndx(iblock)),eps(bndx(iblock),:,pplane)
!                WRITE(8,600) time(1),vdot(1)
!                WRITE(8,600) time(bndx(iblock)),vdot(bndx(iblock))
                WRITE(9,600) time(1),0.0
                WRITE(9,600) time(bndx(iblock)),vdotuse
            ELSE
                !  Print  the  index  (final)  row  from  all  other  blocks  (tablet  plane#
pplane)
                WRITE(1,101) time(bndx(iblock)),T(bndx(iblock),:,pplane)
!                WRITE(2,201) time(bndx(iblock)),u(bndx(iblock),:,pplane)
!                WRITE(3,301) time(bndx(iblock)),fs(bndx(iblock),:,pplane)
!                WRITE(4,401) time(bndx(iblock)),fc(bndx(iblock),:,pplane)
                WRITE(7,501) time(bndx(iblock)),eps(bndx(iblock),:,pplane)
!                WRITE(8,600) time(bndx(iblock)),vdot(bndx(iblock))
                WRITE(9,600) time(bndx(iblock)),vdotuse
            ENDIF
            ! CLEAR ALLOCATED ARRAYS
            DEALLOCATE(T,u,fc,fs,eps,vdot,time)
!             IF( (convext .GT. 0.998) .AND. ( tvhold(1) .GT. 60. ) ) exit timeloop
!                  ! If neither the final step nor 99.8% conversion has been reached,
reallocate the arrays
            IF (bndx(iblock) /= Nt) THEN
                ALLOCATE(T(bndx(iblock):bndx(iblock+1),Nr,Nz))
                ALLOCATE(u(bndx(iblock):bndx(iblock+1),Nr,Nz))
                ALLOCATE(fs(bndx(iblock):bndx(iblock+1),Nr,Nz))
                ALLOCATE(fc(bndx(iblock):bndx(iblock+1),Nr,Nz))
                ALLOCATE(eps(bndx(iblock):bndx(iblock+1),Nr,Nz))
                ALLOCATE(time(bndx(iblock):bndx(iblock+1)))
                ALLOCATE(vdot(bndx(iblock):bndx(iblock+1)))
                ! Assign initial block step values
                T(it+1,:,:)=statehold(1,:,:)
                u(it+1,:,:)=statehold(2,:,:)
                fs(it+1,:,:)=statehold(3,:,:)
                fc(it+1,:,:)=statehold(4,:,:)
                eps(it+1,:,:)=statehold(5,:,:)
                time(it+1)=tvhold(1)
                vdot(it+1)=tvhold(2)
                ! Advance the block counter
                iblock=iblock+1
            ENDIF
        ENDIF
       !
       !!! End of time loop of primary calculations
    ENDDO timeloop
    CLOSE(1)
    CLOSE(2)
    CLOSE(3)
    CLOSE(4)
    CLOSE(7)
    CLOSE(8)
    CLOSE(9)
```

```
    wrmsfit = SQRT( (1./datavdotnsum)*wssefit )
    ! END PRIMARY CALCULATIONS
    !!!
    ! Determine the time elapsed during the long boring primary calculations and report
to terminal.
    ! (Simply divide the difference in clock times from start to end by the clockrate.)
    CALL SYSTEM_CLOCK( clock_1, clock_rate, clock_max )
    tlapse = REAL(clock_1-clock_0)/REAL(clock_rate)
    WRITE (*,333), TRIM(runid)
    333 FORMAT('Completed run ',A)
    PRINT *,' Elapsed time (seconds)        = ',tlapse
    PRINT *,' Weighted RMS deviation of fit = ',wrmsfit
    OPEN(1,FILE='WRMSD.err')
    WRITE (1,311) wrmsfit
    311 FORMAT('WRMSD_fit = ',E24.16)
    CLOSE(1)
END PROGRAM GenOptFit
!!!
! EMBEDDED FUCNTIONS
! Functions for determining 1.a-b) Reaction rates a.)pyrolysis and b.)gasification
!                           2.) Heat of reaction
!                           3.) Gas specific heat
!                           4.) Gas thermal conductivity
!                           5.) Radiation / convection hx coeff
! Most are based on polynomial fits to temperature-dependend behavior
!!!
REAL function rdotp(ar,Ea,T,fs,rhos)
    implicit none
    ! Inputs:   Temperature in Kelvin, volume fraction and density of cellulose
    ! Output:   Volumetric reaction rate [kg/m**3-s]
    !
    REAL, intent(in) :: T,fs,rhos,Ea,ar
    REAL :: Er,R
        Er=Ea*1000. ! [J/mol]
        R=8.31447 ! [J/mol-K]
        rdotp=ar*exp(-Er/(R*T))*fs*rhos
end function rdotp

REAL function rdotg(fcmax,Ea,T,fc,rhoc,yh2o)
    implicit none
    ! Inputs:   Temperature in Kelvin, volume fraction and density of carbon
    ! Output:   Volumetric reaction rate [kg/m**3-s]
    !
!!!!!!!!!!!!!!!!MODEL 1:
!    REAL, intent(in) :: fcmax,T,fc,rhoc,Ea,yh2o
!    REAL :: Er,R,k0,shapefact
!        shapefact=1.32E7  ! [1/m]
!        Er=Ea*1000.       ! [J/mol]
!        R=8.31447         ! [J/mol-K]
!        k0=0.5           ! [m/s]
!        IF (fc==0) THEN
!                                  rdotg=k0*exp(-Er/(R*T))*yh2o*shapefact*fc*rhoc*sqrt(1-
log((fc+0.000001)/fcmax))
!        ELSE
!            rdotg=k0*exp(-Er/(R*T))*yh2o*shapefact*fc*rhoc*sqrt(1-log(fc/fcmax))
!        ENDIF
!!!!!!!!!!!!!!!!MODEL 2: Umehara, 1983
        REAL, intent(in) :: fcmax,Ea,T,fc,rhoc,yh2o
        REAL :: k1,k2,k3,ph2o,ph2,ptot,erchk
        REAL, PARAMETER :: E1=1.64*10**5, dH2=-1.70*10**5          ! J/mol
        REAL, PARAMETER :: R=8.31447                               ! J / K-mol
        erchk=Ea
        k1=1.02*10**2*exp(-E1/(R*T))                               ! kg/kg-s-Pa
        k2=1.02*10**2*exp(-dH2/(R*T))                              ! Pa^-1
        k3=1.18*10**(-3)                                           ! Pa^-1
        ptot  = 3447.+98066.5                                      ! Pa
        ph2o  = yh2o*ptot
        ph2   = 0.*ptot
        rdotg = (fc/(fc+1.0E-9)) * rhoc * fcmax * k1 * ph2o / ( 1 + k2*ph2 + k3*ph2o ) !
s^-1
!!!!!!!!!!!!!!!!REACTION OFF
```

```
!        rdotg=0
end function rdotg

REAL function dHp(T)
    implicit none
    ! Inputs:   Temperature in [Kelvin]
    ! Output:   Enthalpy of reaction [J/kg] based on 300 [K] enthalpy reference
    ! Note: The enthalpy was fit to a function with +/-0.10% avg error
    REAL, intent(in) :: T
    REAL :: a,b,c,d
        a=-5.61E-5
        b=4.09E-1
        c=-4.90E1
        d=3.2E5
        dHp=a*T**3+b*T**2+c*T+d
end function dHp

REAL function dHg(T)
    implicit none
    ! Inputs:   Temperature in [Kelvin]
    ! Output:   Enthalpy of reaction [J/kg] based on 300 [K] enthalpy reference
    ! Note: The enthalpy was fit to a function with +/-0.xx% avg error
    REAL, intent(in) :: T
    REAL :: a,b,c,d
        a=1.59E-5
        b=-1.89E-1
        c=1.45E3
        d=1.05E7
        dHg=a*T**3+b*T**2+c*T+d
end function dHg

REAL function cpg(T)
    implicit none
    ! Input:    Temperature in [Kelvin]
    ! Output:   Constant-pressure specific heat for gas blend in [J/kg-K]
    ! Note: The specific heat was averaged by mass. +/-0.03% avg error
    REAL, intent(in) :: T
    REAL :: a,b,c,d
        a=-5.49E-8
        b=3.31E-5
        c=4.22E-1
        d=1.344E3
        cpg=a*T**3+b*T**2+c*T+d
end function cpg

REAL function kpb(T,ks,fs,kc,fc)
    implicit none
    ! Effective conductivity of a packed bed (or packed tablet). Adapted from
    ! Yagi and Kunii, A.I.Ch.E. Journal, Vol.3, No.3, p.373-381
    ! Inputs:   ks = Thermal conductivity of solid cellulose
    !           kc = Thermal conductivity of carbon
    !           fs = Volume (and area) fraction of solid cellulose
    !           fc = Volume (and area) fraction of carbon
    !           T  = Temperature in [Kelvin]
    !
    ! Output:   Effective Thermal conductivity of the tablet in [W/m-K]
    REAL, intent(in) :: ks,kc,fs,fc,T
    REAL :: a,b,c,d,kg,kse,epsse,Dp,N,phi,gam,hrs,hrv,usdx,uvdx
    ! First establishing the thermal conductivity of the gas blend based on
    ! the temperature supplied.
    ! Note: The thermal conductivity was averaged by volume. -/+0.12% avg error
        a=4.086E-11
        b=-1.070E-7
        c=2.686E-4
        d=1.151E-2
        kg=a*T**3.0+b*T**2.0+c*T+d
    ! Next we establish the solid properties based on the amount of carbon and
    ! cellulose remaining.
        kse   =(fs*ks+fc*kc+0.0000000001)/(fs+fc+0.00001)
!           epsse =(fs*0.9+fc*0.95+0.0000000001)/(fs+fc+0.00001) ! VERIFY EMISSIVITY OF
THESE MATERIALS
```

```
        epsse = 0.92
    ! Now we set up the geometric properties of the cellulose tablets (ADJUST FOR
ACTIVATED CARBON)
        Dp  = 0.00005                   ! 50 micrometer nominal diameter
        N   = 1./Dp                     ! Solid spheres per unit length
        phi = 0.178*(1.-fs-fc)-0.029      ! Gas film thickness parameter (see Yagi and
Kunii 1957)
        gam = (fs+fc)**(1.0/3.0)        ! Ratio of solid diameter to packing diameter
    ! Next we set up the radiative heat transfer coefficients from solid to solid
    ! and from void to void.
        hrs = 0.1952*(epsse/(2.-epsse))*(T/100.)**3.0
        hrv         =         (0.1952/(         1.+(1.-fs-fc)/(2.*(fs+fc+0.000001))*(1.-
epsse)/epsse))*(T/100.)**3.0
    ! We now put together overall heat transfer coefficient/thickness products for the
solid and void portions
        usdx = 1./(N*(gam*Dp/kse+1./(kg/(phi*Dp)+hrs)))
        uvdx = hrv/N
    ! Finally we assemble it all together into the effective conducivity (eq.9 from the
article)
        kpb = usdx * (fs+fc) + uvdx * (1.-fs-fc)
end function kpb

!REAL function kg(T)
!    implicit none
!    ! Input:    Temperature in [Kelvin]
!    ! Output:   Thermal conductivity for gas blend in [W/m-K]
!    ! Note: The thermal conductivity was averaged by volume. -/+0.12% avg error
!    REAL, intent(in) :: T
!    REAL :: a,b,c,d
!        a=4.086E-11
!        b=-1.070E-7
!        c=2.686E-4
!        d=1.151E-2
!        kg=a*T**3+b*T**2+c*T+d
!end function kg

REAL function htot(hconv,T,Tsalt)
    implicit none
    ! INPUT:    Salt Temperature, Interface Temperature [K]
    ! OUTPUT:   Overall heat transfer coefficient from salt to biomass [W/m**2-K]
    ! on radiative and stagnant convective heat transfer. For radiation
    ! calculations, surface 1 is taken as the cellulose cylinder and surface
    ! 2 is the cylindrical crucible wall.
    REAL, intent(in) :: hconv,T,Tsalt
    REAL :: sigma,eps1,eps2,A1,A2,F12,hrad
!        hconv=150      ! [w/m**2*k] typical value for salt
        sigma=5.67E-8  ! [w/m**2*K**4]
        eps1=0.95
        eps2=0.7
        A1=0.5
        A2=3.5
        F12=1
        hrad=sigma*(T**2+Tsalt**2)*(T+Tsalt)/((1-eps1)/eps1+1/F12+(1-eps2)*A1/(eps2*A2) )
        htot=hconv+hrad
end function htot
```

```
subroutine adpcavsim(Tguess, D, L, Csuns, imatl, Nrayin, Nr, Nphi, Nz,          &
                     T, Tavg, sdev)
!-------------------------------------------------------------------------------
! Syntax:
! adpcavsim(Tguess,D,L,Csuns,imatl,Nrays,Nr,Nphi,Nz,T,Tavg,sdev)
!     INPUTS:   Tguess(3,Nz,16) = Estimated temperature array for all cells
!               D         = The [cavity] / [aperture] diameter aspect ratio
!               L         = The cavity [length]/[diameter] aspect ratio
!               Csuns     = Solar concentration in suns [1 sun = 1000 W/m^2]
!               imatl     = Material index
!                           (0=black, 1=inco, 2=Al2O3, 3=grey(constant))
!               Nrays     = Number of ray bundles to be launched
!               Nr        = Number of radial spatial divisions (MINIMUM 3!)
!               Nphi      = Number of angular divisions (ALWAYS USE 16!)
!               Nz        = Number of axial spatial divisions
!
!     OUTPUTS:  T(3,Nz,16)= Temperature array for all cells
!               Tavg      = Average surface temperature in cavity (mu)
!               sdev      = Standard deviation of surface temperature (sigma)
! Info:
!   !!! THIS IS A PARALLEL PROGRAM.
!   !!! ONLY THE RANK 0 PROCESS RECIEVES PROPER OUTPUT VALUES !!!
!   This subroutine simulates radiative exchange between an adiabatic
!   emitting cylindrical cavity with 5cm aperture and the planned solar
!   simulator using Monte Carlo ray tracing methods.  The program is passed
!   the solar concentration, dimensionless geometry ratios, material,
!   number of rays and discritization parameters prior to execution.
!   This subroutine requires a guess of the temperatures before running
!   and should be executed multiple times to ensure the accuracy of the result
!   due to solution dependency on the guess temperature.
!
! Note: The grid spacing Nr and Nz can be calculated in the calling program via:
!       Nr     = ceiling(dap*(D-1.0)/(2.0*drmax)) + 3
!       Nphi   = 16
!       Nz     = ceiling(dap*D*L/dzmax)
!-------------------------------------------------------------------------------
!   use mpi
   implicit none
   include 'mpif.h'
   ! Declarations.  All units in SI base [kg,m,s] values unless otherwise noted.
   integer, intent(in)  :: imatl, Nrayin      ! Material index and ray count
   integer, intent(in)  :: Nr, Nphi, Nz       ! Number of grid elements
   integer, parameter   :: Ns = 3             ! Number of surfaces
   real(8), parameter   :: dap  = 5d-2        ! Aperture diameter
   real(8), parameter   :: c_pi = 3.141592653589793d+0
   real(8), parameter   :: c_sb = 5.670400d-8    ! [W/m^2-K^4]
   real(8), intent(in)  :: D, L, Csuns        ! Geometry ratios and concentration
   real(8), intent(out) :: Tavg, sdev         ! Averaged properties
   integer         :: irstart = 1, Nsdev, diphi = 1
   integer         :: isurf, ir, iphi, iz, iloop
   integer         :: iproc, nprocs, ierror
   integer(8)      :: Nri, Nrays
   real(8)         :: dr, dphi, dz, emissavg, eps, dTg, qap, qray = 0d0
   real(8)         :: sdevsum, area_ap, dTsqsum = 0d0
   logical         :: verbose = .false.
   integer(8), dimension(Ns,Nz,Nphi) :: Ne, Nei
   real(8), dimension(0:Nr)          :: r
   real(8), dimension(0:Nphi)        :: phi
   real(8), dimension(0:Nz)          :: z
   integer, dimension(Ns,Nz,Nphi)    :: faces
   real(8), dimension(Ns,Nz,Nphi)    :: area
   real(8), dimension(Ns,Nz,Nphi), intent(inout) :: Tguess ! Temp estimate
   real(8), dimension(Ns,Nz,Nphi), intent(out)   :: T     ! Element temperatures

   ! Query MPI system size, assign rank.
   call MPI_COMM_SIZE(MPI_COMM_WORLD, nprocs, ierror)
   call MPI_COMM_RANK(MPI_COMM_WORLD, iproc, ierror)
   ! Program execution banner
   if(verbose .and. (iproc .eq. 0))then
      print *,' '
      print *,' --- SUBROUTINE: adabatic parallel cavsim -----'
```

```
   print *,' Utilizing ',nprocs,' process(es).'
end if

! Discritize grid for all processes
call gridspace(D,L,dap,Nr,Nphi,Nz,dr,dphi,dz,r,phi,z)

! Initialize emission count array for all processes
Nei  = int(0,8)

! Carry out setup calculations on the primary process only
if( iproc .eq. 0 ) then
   ! Initialize overall emission count and area arrays
   Ne   = int(0,8)
   area = 0d+0

   ! Calculate total emissive power from aperture
   area_ap = c_pi*(dap/2d+0)**2
   qap         = Csuns*1000d+0 * area_ap

   ! Surface areas
   do isurf = 1,Ns
      if ( isurf <= 2 ) then
         ! Surfaces 1 or 2: circular ends of cavity.
         if ( isurf == 1 ) irstart = 4 ! Surface 1 omits 3 aperture rows
         if ( isurf == 2 ) irstart = 1
         do ir = irstart,Nr
            if ( ir == 1 ) diphi = 4  ! Four segment core circle
            if ( ir == 2 ) diphi = 2  ! Eight segment transition ring
            if ( ir >= 3 ) diphi = 1  ! Standard 16 segment ring sections
            do iphi = diphi,Nphi,diphi
               area(isurf, ir, iphi) = &
                  (r(ir)**2-r(ir-1)**2)*(phi(iphi)-phi(iphi-diphi))/2d+0
            end do
         end do
      else if ( isurf == 3 ) then
         ! Surface 3: Cylindrical wall of cavity
         area(isurf,:,:) = dz*dphi*r(Nr)
      end if
   end do

   ! Report power statistics
   if(verbose .and. (iproc .eq. 0))then
      print *,' '
      print *,' Power incident at aperture [W]: ',nint(qap)
   end if

   ! Reduce ray limit (adabatic solving results in the generation of ~52x
   ! as many rays as are launched from the aperture).
   Nrays = ceiling(real(Nrayin,8)/52d0,8)
   ! Assign rays
   Nri  = nint(real(Nrays,8)/real(nprocs,8),8)
   ! Correct power per ray according to actual assigned rays
   qray = qap / (real(Nri,8)*real(nprocs,8))

endif ! process 0 limiter

! Broadcast calculated ray launch bundle size, 'Nri', to all processes.
call MPI_BCAST(Nri, 1, MPI_INTEGER8, 0, MPI_COMM_WORLD, ierror)

! Execute tracing of all Nri rays yielding Nei re-emissions for each process.
call adraytrace(Nri, Nei)

! Sum up the ray-tracing counts from each process
call MPI_REDUCE(Nei, Ne, size(Ne), MPI_INTEGER8, MPI_SUM, 0,                &
                MPI_COMM_WORLD, ierror)

! The following work is performed by the rank 0 process only.
if(iproc .eq. 0) then
   ! Report ray emission and absorption statistics
   if(verbose)then
      print *,' Number of intended rays : ',Nrays
```

```
         print *,' Power per ray [W/ray]   : ',qray
         print *,' Number of assigned rays : ',Nri*int(nprocs,8)
         print *,' Re-emission rays        : ',sum(Ne)
         print *,' '
         print *,' ----------Emission summary-----------'
         print *,' Rays from the wall     : ',sum(Ne(3,:,:))
         print *,' Rays from the back end : ',sum(Ne(2,:,:))
         print *,' Rays from the front end: ',sum(Ne(1,4:Nr,:))
         print *,' '
      end if

      ! Calculate Temperature field
      faces  = 0
      eps    = 1.d+0  ! Maximum std dev between guess and calc'd temp.
      iloop  = 0
      dTg    = eps + 1d+0
      do while( (dTg .gt. eps) .or. (iloop .lt. 5) )
         dTsqsum = 0d0
         iloop = iloop + 1
         do isurf = 1,Ns
            do iz = 1,Nz
               do iphi = 1,Nphi
                  if( area(isurf,iz,iphi) .gt. 10d0*tiny(1d0) )then
                     T(isurf,iz,iphi) = ( (real(Ne(isurf,iz,iphi),8)*qray)/    &
                                          (c_sb*emissavg(Tguess(isurf,iz,iphi),&
                                           imatl)*area(isurf,iz,iphi))         &
                                           )**(1d0/4d0)
                     faces(isurf,iz,iphi) = 1
                     dTsqsum = dTsqsum + ( T(isurf,iz,iphi) -                  &
                               Tguess(isurf,iz,iphi) )**2
                  else
                     T(isurf,iz,iphi) = 0d0
                     faces(isurf,iz,iphi) = 0
                  end if
               enddo
            enddo
         enddo
         dTg    = sqrt( dTsqsum / real(sum(faces),8) )
         Tguess = T
      end do
      sdevsum = 0d+0
      Nsdev   = 0
      Tavg    = sum( T * area )/sum(area)
      do isurf=1, Ns
         do iz=1, Nz
            do iphi=1, Nphi
               if((isurf==1).and.(iz==1).and.(iphi==1))then
               ! Skip aperture.
               else if(area(isurf,iz,iphi) > 10d+0*tiny(0d+0))then
                  sdevsum = sdevsum + (T(isurf,iz,iphi)-Tavg)**2
                  Nsdev   = Nsdev + 1
               end if
            end do
         end do
      end do
      sdev    = sqrt(sdevsum/real(Nsdev,8))
      if(verbose)then
         print *,' ------------Performance Stats--------------'
         print *,' Average wall temperature     : ',nint(Tavg)
         print *,' Standard deviation of temp   : ',nint(sdev)
         print *,' '
      end if
   endif ! Rank 0 only if loop.
   return
contains
   subroutine adraytrace(Nri, Nei)
      !  Adiabatic rayracing routine contained within adpcavsim subroutine.
      !     Nrays = Number of rays to be launched from aperture
      !     Ne    = Array of surface re-emission rays
      use randdp
      implicit none
```

```
integer(8),                         intent(in)  :: Nri
integer(8), dimension(Ns,Nz,Nphi), intent(out) :: Nei
integer(1)     :: ierr = int(0,1)
integer(2)     :: csurf
integer        :: iseed, iray, ira, iza, iphia, band
integer        :: primes
real(8)        :: psi, theta, ro, randn, emiss
logical        :: solar = .false., sameray = .false.
integer(2), dimension(2):: isint
real(8), dimension(3)   :: Pp, Pc, t1, t2, midlam, s, c1, c2
real(8), dimension(2)   :: Rlam, dist
real(8), dimension(2,3) :: Pint
real(8), dimension(3,3) :: normal

! Initialize random number generator. A prime seed is reccomended.
iseed = primes(iproc + 1)
call sdprnd(iseed)

! Set up problem geometry and ref. wavelengths from each discrete band.
c1          = (/0.d0, 0.d0, 0.d0/)           ! Disc center, aperture end
c2          = (/0.d0, 0.d0, real(dap*D*L,8)/)! Disc center, closed end
normal(1,:) = (/0.d0, 0.d0, 1.d0 /)
normal(2,:) = (/0.d0, 0.d0, -1.d0/)
normal(3,:) = (/0.d0, 0.d0, 0.d0/)
ro          = dap*D/2d+0
midlam      = (/0.5d0, 2.0d0, 5.5d0/) ! Wavelengths [micron] from bands.

! Launch and trace all rays
do iray = 1, int(Nri,4)
   call bandset(5777d+0, 0, Rlam) ! Set bands, blackbody @ Tsolar
   solar = .true.
   ! Set emission wavelength band
   randn = dprand()
   if(randn < Rlam(1))then
      band = 1
   else if(randn < Rlam(2))then
      band = 2
   else if(randn >= Rlam(2))then
      band = 3
   end if
   ! Set emission location
   Pp(1) = sqrt(dprand()*(dap/2d+0)**2)
   Pp(2) = dprand()*2d+0*c_pi
   Pp(3) = 0d+0
   call pol2car(Pp,Pc)

   ! Launch new ray and follow to its extinction
   sameray = .true.
   csurf = int(1,2)
   do while(sameray)
      ! Set emission/reflection direction
      psi = dprand() * 2d+0 * c_pi
      if(solar)then
         ! Constant below calculated for cone angle of 37 deg.
         theta = asin( sqrt( dprand()/2.761047960d+0 ) )
         solar = .false. ! Use diffuse reflection hereafter
      else
         theta = asin( sqrt( dprand() ) )
      end if
      if(csurf==int(3,2)) then
         normal(csurf,1)=-Pc(1)/ro
         normal(csurf,2)=-Pc(2)/ro
      end if
      call tripod(normal(csurf,:), t1, t2)
      s = cos(theta) * normal(csurf,:) + sin(theta)                    &
          * ( cos(psi) * t1 + sin(psi) * t2 )

      ! Check for intesection location
      call int_line_cylinder(Pc,s,c1,c2,ro,isint,Pint,ierr)
      if(ierr<int(0,1)) print *,' Intersect detect error: ',ierr
```

```
! Assign ray location to new intersection point
dist(1) = sqrt(sum((Pc-Pint(1,:))**2))
dist(2) = sqrt(sum((Pc-Pint(2,:))**2))
if(dist(1)>dist(2)) then
   Pc    = Pint(1,:)
   csurf = isint(1)
else if(dist(2)>dist(1)) then
   Pc    = Pint(2,:)
   csurf = isint(2)
else
   print *,' Negligible ray length. ',                              &
            'Maintaining Pc and csurf.'
end if

! Check for loss out aperture
if((csurf==int(1,2)).AND.                                           &
   (sqrt(Pc(1)**2+Pc(2)**2)<dap/2d+0))then
   sameray   = .false.
end if

! Check for absorption
if(dprand()<=emiss(midlam(band),imatl)) then
   ! Translate absorbed position to absorption matrix value
   call car2pol(Pc,Pp)
   if(csurf<=int(2,2)) then
   ! Ray ends at one of the discs at the cylindrical cavity ends
      if((Pp(1) < dap/2d+0).and.(csurf==int(1,2)))then
      ! Ignore aperture loss
      else
      ! Detect surface absorption
         if(Pp(1)<=r(1))then
            ira = 1
            iphia = 4*ceiling(Pp(2)/(4d+0*dphi))
         else if(Pp(1)<=r(2))then
            ira = 2
            iphia = 2*ceiling(Pp(2)/(2d+0*dphi))
         else if(Pp(1)<=r(3))then
            ira = 3
            iphia = ceiling(Pp(2)/dphi)
         else
            ira = ceiling((Pp(1)-dap/2d+0)/dr)+3
            iphia = ceiling(Pp(2)/dphi)
         end if
         if(ira .gt. Nr) then
            print *,' Dimensional Bounds exceeded: r=',Pp(1)
            ira = Nr
         endif
         if(iphia .gt. Nphi) then
            print *,' Dimensional Bounds exceeded: phi=',Pp(2)
            iphia = Nphi
         endif
         Nei(csurf,ira,iphia) = Nei(csurf,ira,iphia) + int(1,8)
         ! Set re-emission wavelength band
         call bandset(Tguess(csurf,ira,iphia), imatl, Rlam)
         randn = dprand()
         if(randn < Rlam(1))then
            band = 1
         else if(randn < Rlam(2))then
            band = 2
         else if(randn >= Rlam(2))then
            band = 3
         end if
      end if
   else if(csurf==int(3,2)) then
   ! Ray ends at the circumferential cylinder cavity wall
      iza   = ceiling(Pp(3)/dz)
      iphia = ceiling(Pp(2)/dphi)
      if(iza .gt. Nz) then
         if(Pp(3) .gt. z(Nz)*1.0001d0) print *,'OOB: z=',Pp(3)
         iza = Nz
      endif
```

```
                  if(iphia .gt. Nphi) then
                     print *,' Dimensional Bounds exceeded: phi=',Pp(2)
                     iphia = Nphi
                  endif
                  Nei(csurf,iza,iphia) = Nei(csurf,iza,iphia) + int(1,8)
                  ! Set re-emission wavelength band
                  call bandset(Tguess(csurf,iza,iphia), imatl, Rlam)
                  randn = dprand()
                  if(randn < Rlam(1))then
                     band = 1
                  else if(randn < Rlam(2))then
                     band = 2
                  else if(randn >= Rlam(2))then
                     band = 3
                  end if
               end if ! Surface to re-emission array count loop
            end if  ! Absoption detection loop
            ! If ray isn't lost out aperture, set new direction and continue
         end do
         ! End ray-tracing loop
      end do
      ! End ray emission loop
      return
   end subroutine adraytrace
end subroutine adpcavsim
```

sub_cav2flu.f90

```
subroutine cav2flu(nfaces_total,r_in,phi_in,z_in,T_in,qnet_out)
!-------------------------------------------------------------------------------
!     A subroutine calling the Monte-Carlo Ray Tracing radiative simulations
!  based on the cylinder wall face temperatures obtained from a FLUENT linked
!  UDF that generates a set of arrays with face centroids and temperatures.
!  Grid-to-grid correlation accomplished by two stage averaging.  First
!  averaging the values in grid areas that have multiple corresponding faces
!  then averaging the values around unassigned faces into that unassigned face.
!  The resulting net flux values for the cylinder wall are then returned as a
!  array that is interpreted by the FLUENT UDF to define the wall fluxes.
!
!  Syntax: cav2flu (nfaces_total, r_in, phi_in, z_in, T_in, qnet_out)
!
!  Inputs:  nfaces_total - The number of FLUENT cell faces considered.
!           r_in    - r-coordinate of cell face centroid
!           phi_in  - phi-coordinate of cell face centroid
!           z_in    - z-coordinate of cell face centroid.
!           T_in    - Temperature of the face.
!
!  Output:  qnet_out - Net heat flux through the face.
!
!  Notes:  This program is not yet parallelized and may be modified for
!          parallel operation in order to speed later analyses.  The current
!          holdup is the inability to use typical MPI calls within the fluent
!          MPI environment.
!
!  Brandon Jay Hathaway
!  Latest Revision: June 26, 2012
!-------------------------------------------------------------------------------
   implicit none
   integer,                           intent(in)  :: nfaces_total
   real(8), dimension(nfaces_total), intent(in)  :: r_in, phi_in, z_in, T_in
   real(8), dimension(nfaces_total), intent(out) :: qnet_out
   integer, parameter   :: Nrays=10000000, imatl=1, nphi=16
   real(8), parameter   :: drm=1d-2, dzm=1d-2, dap=5d-2, Csun=1530d+0
   real(8)     :: D, L, dr, dphi, dz
   integer     :: nr, nz, i, ii, j, jj, ir, iz, iphi, ineg, ipos, jneg, jpos, nsum
   integer     :: nfaces_ring=0, nfaces_disk=0, nfaces_cyl=0, nfaces_err=0
   integer     :: check_ring, check_disk, check_cyl
   real(8)     :: eta_abs, qnetavg, sdev, Tavg
   real(8), dimension(:), allocatable  :: rc_ring, phic_ring, zc_ring, Tin_ring,
qnet_ring
   real(8), dimension(:), allocatable  :: rc_disk, phic_disk, zc_disk, Tin_disk,
qnet_disk
   real(8), dimension(:), allocatable  :: rc_cyl, phic_cyl, zc_cyl, Tin_cyl, qnet_cyl
   real(8), dimension(:), allocatable  :: r, phi, z
   integer, dimension(nfaces_total)    :: f_wallid
   integer, dimension(:,:), allocatable   :: fcorr_ring
   integer, dimension(:,:), allocatable   :: fcorr_disk
   integer, dimension(:,:), allocatable   :: fcorr_cyl
   integer, dimension(:,:), allocatable   :: acorr_ring, acorr_disk, acorr_cyl
   real(8), dimension(:,:), allocatable   :: Tring, Tdisk, Tcyl
   real(8), dimension(:,:,:), allocatable :: T,qnet

   ! Pull cavity geometry from centroid location extremes.
   D = maxval(r_in)*2d+0/dap
   L = (maxval(z_in)-minval(z_in)) / (D*dap)

   ! Take the raw property vectors and translate them into surface specific
   ! property vectors.
   f_wallid = 0
   do j = 1, 2
      nfaces_ring = 0
      nfaces_disk = 0
      nfaces_cyl  = 0
      do i = 1, nfaces_total
         if(z_in(i) .lt. (minval(z_in) + 0.0001d+0))then
            nfaces_ring = nfaces_ring + 1
            if(j .eq. 2)then
               f_wallid(i)            = 1
               rc_ring(nfaces_ring)   = r_in(i)
```

```
            phic_ring(nfaces_ring) = phi_in(i)
            zc_ring(nfaces_ring)   = z_in(i)
            Tin_ring(nfaces_ring)  = T_in(i)
         endif
      elseif(z_in(i) .gt. (maxval(z_in) - 0.0001d+0))then
         nfaces_disk = nfaces_disk + 1
         if(j .eq. 2)then
            f_wallid(i)            = 2
            rc_disk(nfaces_disk)   = r_in(i)
            phic_disk(nfaces_disk) = phi_in(i)
            zc_disk(nfaces_disk)   = z_in(i)
            Tin_disk(nfaces_disk)  = T_in(i)
         endif
      elseif(r_in(i) .gt. (maxval(r_in) - 0.0001d+0))then
         nfaces_cyl = nfaces_cyl + 1
         if(j .eq. 2)then
            f_wallid(i)           = 3
            rc_cyl(nfaces_cyl)    = r_in(i)
            phic_cyl(nfaces_cyl)  = phi_in(i)
            zc_cyl(nfaces_cyl)    = z_in(i)
            Tin_cyl(nfaces_cyl)   = T_in(i)
         endif
      else
         if(j .eq. 1)then
            print *,' Centroid not on expected surfaces. Index =',i
            nfaces_err = nfaces_err + 1
         endif
      endif
   enddo
   if(j .eq. 1)then
      allocate(rc_ring(nfaces_ring))
      allocate(phic_ring(nfaces_ring))
      allocate(zc_ring(nfaces_ring))
      allocate(Tin_ring(nfaces_ring))
      allocate(qnet_ring(nfaces_ring))
      allocate(fcorr_ring(nfaces_ring,2))
      allocate(rc_disk(nfaces_disk))
      allocate(phic_disk(nfaces_disk))
      allocate(zc_disk(nfaces_disk))
      allocate(Tin_disk(nfaces_disk))
      allocate(qnet_disk(nfaces_disk))
      allocate(fcorr_disk(nfaces_disk,2))
      allocate(rc_cyl(nfaces_cyl))
      allocate(phic_cyl(nfaces_cyl))
      allocate(zc_cyl(nfaces_cyl))
      allocate(Tin_cyl(nfaces_cyl))
      allocate(qnet_cyl(nfaces_cyl))
      allocate(fcorr_cyl(nfaces_cyl,2))
   endif
enddo

! Allocate sizes and set initial values
call gridspit(D,L,drm,dzm,dap,nr,nz)
allocate(T(3,nz,nphi))
T     = 0d0
allocate(qnet(3,nz,nphi))
qnet  = 0d0
allocate(Tring(4:nr,nphi))
allocate(Tdisk(nr,nphi))
allocate(Tcyl(nz,nphi))
Tring = 0d0
Tdisk = 0d0
Tcyl  = 0d0
allocate(acorr_ring(4:nr,nphi))
allocate(acorr_disk(nr,nphi))
allocate(acorr_cyl(nz,nphi))
acorr_ring = 0
acorr_disk = 0
acorr_cyl  = 0
allocate(r(0:nr))
allocate(phi(0:nphi))
```

```
allocate(z(0:nz))
! Generate grid and position vectors
call gridspace(D,L,dap,nr,nphi,nz,dr,dphi,dz,r,phi,z)

! Set-up face correlation list and array of correlation numbers
! fcorr_<zone> = list of r, phi, or z indices corresponding to face centroids
! acorr_<zone> = array counting number of face centroids with same indexes
! Starting with the cavity aperture end
do i = 1, nfaces_ring
   iphi = ceiling(phic_ring(i)/dphi)
   ir = 3 + ceiling( (rc_ring(i)-r(3))/dr )
   if(ir .gt. nr) print *,' Ray overbound - r =',rc_ring(i)
   if(iphi .gt. nphi) print *,' Ray overbound - phi =',phic_ring(i)
   fcorr_ring(i,1) = ir
   fcorr_ring(i,2) = iphi
   acorr_ring(ir, iphi) = acorr_ring(ir, iphi) + 1
   Tring(ir, iphi)  = Tring(ir,iphi) + Tin_ring(i)
enddo
! far cavity end
do i = 1, nfaces_disk
   iphi = ceiling(phic_disk(i)/dphi)
   if(rc_disk(i) .lt. r(1))then
      ir   = 1
      iphi = ceiling(real(iphi)/4.0)*4
   elseif(rc_disk(i) .lt. r(2))then
      ir   = 2
      iphi = ceiling(real(iphi)/2.0)*2
   elseif(rc_disk(i) .lt. r(3))then
      ir = 3
   else
      ir = 3 + ceiling( (rc_disk(i)-r(3))/dr )
   endif
   if(ir .gt. nr) print *,' Ray overbound - r =',rc_disk(i)
   if(iphi .gt. nphi) print *,' Ray overbound - phi =',phic_disk(i)
   fcorr_disk(i,1) = ir
   fcorr_disk(i,2) = iphi
   acorr_disk(ir, iphi) = acorr_disk(ir, iphi) + 1
   Tdisk(ir, iphi)  = Tdisk(ir,iphi) + Tin_disk(i)
enddo
! cavity cylindrical wall
do i = 1, nfaces_cyl
   iz   = ceiling(zc_cyl(i)/dz)
   iphi = ceiling(phic_cyl(i)/dphi)
   if(iz .gt. nz) print *,' Ray overbound - Z =',zc_cyl(i)
   if(iphi .gt. nphi) print *,' Ray overbound - phi =',phic_cyl(i)
   fcorr_cyl(i,1) = iz
   fcorr_cyl(i,2) = iphi
   acorr_cyl(iz, iphi) = acorr_cyl(iz, iphi) + 1
   Tcyl(iz, iphi)  = Tcyl(iz,iphi) + Tin_cyl(i)
enddo

! Divide cylinder temperature array by number of included face temperatures
where( acorr_ring .gt. 0 )
   Tring = Tring / real(acorr_ring,8)
end where
where( acorr_disk .gt. 0 )
   Tdisk = Tdisk / real(acorr_disk,8)
end where
where( acorr_cyl .gt. 0 )
   Tcyl = Tcyl / real(acorr_cyl,8)
end where
! Find unassigned temperatures and take average of neighboring assigned
! temperatures to determine missing value. Repeat loop as needed to remove
! all zero temperatures
! ring
do while(minval(Tring) .lt. 1d+0)
   do i = 4, nr
      do j = 1, nphi
         if(Tring(i,j) .lt. 10d+0*tiny(0d+0) )then
            nsum = 0
            Tavg = 0d0
```

```
            ineg = max(i-1, 4)
            ipos = min(i+1, nr)
            jneg = max(j-1, 1)
            jpos = min(j+1, nphi)
            do ii = ineg, ipos
               do jj = jneg, jpos
                  if(Tring(ii,jj) .gt. 10d+0*tiny(0d+0) )then
                     Tavg = Tavg + Tring(ii,jj)
                     nsum = nsum + 1
                  endif
               enddo
            enddo
            if(nsum .gt. 0) Tring(i,j) = Tavg/real(nsum,8)
         endif
      enddo
   enddo
enddo
! disk
do while(minval(Tdisk) .lt. 1d+0)
   do i = 1, nr
      do j = 1, nphi
         if(Tdisk(i,j) .lt. 10d+0*tiny(0d+0) )then
            nsum = 0
            Tavg = 0d0
            ineg = max(i-1, 1)
            ipos = min(i+1, nr)
            jneg = max(j-1, 1)
            jpos = min(j+1, nphi)
            do ii = ineg, ipos
               do jj = jneg, jpos
                  if(Tdisk(ii,jj) .gt. 10d+0*tiny(0d+0) )then
                     Tavg = Tavg + Tdisk(ii,jj)
                     nsum = nsum + 1
                  endif
               enddo
            enddo
            if(nsum .gt. 0) Tdisk(i,j) = Tavg/real(nsum,8)
         endif
      enddo
   enddo
enddo
! cylinder
do while(minval(Tcyl) .lt. 1d+0)
   do i = 1, nz
      do j = 1, nphi
         if(Tcyl(i,j) .lt. 10d+0*tiny(0d+0) )then
            nsum = 0
            Tavg = 0d0
            ineg = max(i-1, 1)
            ipos = min(i+1, nz)
            jneg = max(j-1, 1)
            jpos = min(j+1, nphi)
            do ii = ineg, ipos
               do jj = jneg, jpos
                  if(Tcyl(ii,jj) .gt. 10d+0*tiny(0d+0) )then
                     Tavg = Tavg + Tcyl(ii,jj)
                     nsum = nsum + 1
                  endif
               enddo
            enddo
            if(nsum .gt. 0) Tcyl(i,j) = Tavg/real(nsum,8)
         endif
      enddo
   enddo
enddo
! Assign temperatures to the combined array to be sent to the cavsim routine.
T(1,4:nr,:) = Tring(4:nr,:)
T(2,:,:) = Tdisk(:,:)
T(3,:,:) = Tcyl(:,:)

! Call MC Subroutine
```

```
   call cavsim(T,D,L,Csun,imatl,Nrays,nr,nphi,nz,                              &
               qnet,eta_abs,qnetavg,sdev)

   ! Assign net flux values to each face acording to the net flux value in its
   ! corresponding cavsim grid location and write resultant net flux values
   ! for each face to surface specific arrays in face index order.
   do i = 1, nfaces_ring
      qnet_ring(i) = qnet(1,fcorr_ring(i,1),fcorr_ring(i,2))
   enddo
   do i = 1, nfaces_disk
      qnet_disk(i) = qnet(2,fcorr_disk(i,1),fcorr_disk(i,2))
   enddo
   do i = 1, nfaces_cyl
      qnet_cyl(i) = qnet(3,fcorr_cyl(i,1),fcorr_cyl(i,2))
   enddo

   ! Take the surface specific net flux vectors and arrange into their correct
   ! positions in the global flux vector to ship out.
   check_ring = 0
   check_disk = 0
   check_cyl  = 0
   do i = 1 , nfaces_total
      if (f_wallid(i) .eq. 1)then
         check_ring  = check_ring + 1
         qnet_out(i) = qnet_ring(check_ring)
      elseif(f_wallid(i) .eq. 2)then
         check_disk  = check_disk + 1
         qnet_out(i) = qnet_disk(check_disk)
      elseif(f_wallid(i) .eq. 3)then
         check_cyl   = check_cyl + 1
         qnet_out(i) = qnet_cyl(check_cyl)
      else
         print *,' Bad wall-id assigned. Should have errd earlier as well.'
      endif
   enddo
   if( (check_ring .ne. nfaces_ring) .OR. (check_disk .ne. nfaces_disk) .OR.
(check_cyl .ne. nfaces_cyl) ) then
      print *,' Number of assigned face fluxes do not match number of face temps.'
   endif
   ! qnet_out is now filled with net fluxes in the same order that the temps and
   ! positions were brought in.  It will be used by the UDF to assign new BC values.
end subroutine cav2flu
```

```
subroutine cavsim(T, D, L, Csuns, imatl, Nrays, Nr, Nphi, Nz,                  &
                  qnet, eta_abs, qnetavg, sdev)
!-------------------------------------------------------------------------------
! Syntax:
! cavsim(T,D,L,Csuns,imatl,Nrays,Nr,Nphi,Nz,qnet,eta_abs,qnetavg,sdev)
!     INPUTS:   T(3,Nz,16)= Temperature array for all cells
!               D         = The [cavity] / [aperture] diameter aspect ratio
!               L         = The cavity [length]/[diameter] aspect ratio
!               Csuns     = Solar concentration in suns [1 sun = 1000 W/m^2]
!               imatl     = Material index
!                           (0=black, 1=inco, 2=Al2O3, 3=grey(constant))
!               Nrays     = Number of ray bundles to be launched
!               Nr        = Number of radial spatial divisions (MINIMUM 3!)
!               Nphi      = Number of angular divisions (ALWAYS USE 16!)
!               Nz        = Number of axial spatial divisions
!
!     OUTPUTS:  qnet(3,Nz,16) = Net heat flux for all cells (aperture at 1,1,1)
!               eta_abs       = Absorption efficiency (q_net/q_solar)
!               qnetavg       = Average net heat flux in cavity (mu)
!               sdev          = Standard deviation of surface flux (sigma)
! Info:
!   This subroutine simulates radiative exchange between a specified
!   temperature cylindrical cavity with 5cm aperture and the planned solar
!   simulator using Monte Carlo ray tracing methods.  The program is passed
!   the temperature distribution, dimensionless geometry ratios, material,
!   number of rays and discritization parameters prior to execution.
!
! Note: The grid spacing Nr and Nz can be calculated in the calling program via:
!       Nr     = ceiling(dap*(D-1.0)/(2.0*drmax)) + 3
!       Nphi   = 16
!       Nz     = ceiling(dap*D*L/dzmax)
!-------------------------------------------------------------------------------
   use randdp
!   use fsl_types,    only: k_r8, k_i1, k_i2, k_i4
!   use fsl_geometry, only: int_line_cylinder
   implicit none

   ! Declarations.  All units in SI base [kg,m,s] values unless otherwise noted.
   integer, intent(in)  :: imatl, Nrays      ! Material index and ray count
   integer, intent(in)  :: Nr, Nphi, Nz      ! Number of grid elements
   integer, parameter   :: Ns = 3            ! Number of surfaces
   real(8), parameter   :: dap  = 5d-2       ! Aperture diameter
   real(8), parameter   :: c_pi = 3.141592653589793d+0
   real(8), parameter   :: c_stef_boltz = 5.670400d-8    ! [W/m^2-K^4]
   real(8), intent(in)  :: D, L, Csuns       ! Geometry ratios and concentration
   real(8), intent(out) :: eta_abs, qnetavg, sdev     ! Averaged properties
   integer(1)     :: ierr = int(0,1)
   integer(2)     :: csurf
   integer        :: irstart = 1, Nsdev, band = 1, diphi = 1
   integer        :: iray, iseed, isurf, ir, iz, iphi, ira, iza, iphia
   integer        :: clock_0, clock_1, clock_rate, clock_max
   real(8)        :: dr, dphi, dz, psi, theta, ro, emiss, emissavg, qesum, qray
   real(8)        :: tlapse, rand, sdevsum
   logical        :: sameray = .false., solar = .false.
   logical        :: verbose = .false.
   integer(2), dimension(2)          :: isint
   real(8), dimension(2)             :: Rlam, dist
   real(8), dimension(3)             :: Pp, t1, t2, midlam, Pc, s, c1, c2
   real(8), dimension(2,3)           :: Pint
   real(8), dimension(3,3)           :: normal
   integer(8), dimension(Ns,Nz,Nphi) :: Ne, Na
   real(8), dimension(0:Nr)          :: r
   real(8), dimension(0:Nphi)        :: phi
   real(8), dimension(0:Nz)          :: z
   real(8), dimension(Ns,Nz,Nphi)    :: qe, area
   real(8), dimension(Ns,Nz,Nphi), intent(in)   :: T     ! Element temperatures
   real(8), dimension(Ns,Nz,Nphi), intent(out)  :: qnet  ! Element net fluxes

   ! Program execution banner
   if(verbose)then
      print *,' '
```

```
   print *,' ----------- SUBROUTINE: ideal_cavsim -------------'
end if
! "Start the timer" by storing the initial system clock value.
call system_clock(clock_0, clock_rate, clock_max)

! Input data
normal(1,:) = (/0.d0, 0.d0, 1.d0 /)
normal(2,:) = (/0.d0, 0.d0, -1.d0/)
normal(3,:) = (/0.d0, 0.d0, 0.d0/)
c1          = (/0.d0, 0.d0, 0.d0/)           ! Disc center on aperture end
c2          = (/0.d0, 0.d0, real(dap*D*L,8)/)! Disc center on closed end
midlam      = (/0.5d0, 2.0d0, 5.5d0/) ! Wavelengths [micron] from each band

! Initialize cell value arrays
Ne   = int(0,8)
Na   = int(0,8)
qe   = 0d+0
qnet = 0d+0
area = 0d+0
! Initialize standard deviation calculation terms
sdevsum = 0d+0
Nsdev   = 0

! Initialize random number generator. A prime seed is reccomended.
iseed = 59
call sdprnd(iseed)

! Discritize grid
call gridspace(D,L,dap,Nr,Nphi,Nz,dr,dphi,dz,r,phi,z)
ro    = dap*D/2d+0

! Sum up total emissive power from all emitting elements.
qesum = 0d+0
! Aperture emission
area(1,1,1) = c_pi*(dap/2d+0)**2
qe(1,1,1)   = Csuns*1000d+0* area(1,1,1)
qesum = qe(1,1,1)
! Surface emission
do isurf = 1,Ns
   if ( isurf <= 2 ) then
      ! Surfaces 1 or 2: circular ends of cavity.
      if ( isurf == 1 ) irstart = 4 ! Surface 1 omits 3 aperture rows
      if ( isurf == 2 ) irstart = 1
      do ir = irstart,Nr
         if ( ir == 1 ) diphi = 4  ! Four segment core circle
         if ( ir == 2 ) diphi = 2  ! Eight segment transition ring
         if ( ir >= 3 ) diphi = 1  ! Standard 16 segment ring sections
         do iphi = diphi,Nphi,diphi
            area(isurf, ir, iphi) = &
               (r(ir)**2-r(ir-1)**2)*(phi(iphi)-phi(iphi-diphi))/2d+0
            qe(isurf,ir,iphi) = emissavg(T(isurf,ir,iphi),imatl) &
                                *area(isurf,ir,iphi)*c_stef_boltz &
                                *T(isurf,ir,iphi)**4
            qesum = qesum + qe(isurf,ir,iphi)
         end do
      end do
   else if ( isurf == 3 ) then
      ! Surface 3: Cylindrical wall of cavity
      area(isurf,:,:) = dz*dphi*r(Nr)
      do iz = 1,Nz
         do iphi = 1,Nphi
            qe(isurf,iz,iphi) = emissavg(T(isurf,iz,iphi),imatl) &
                                *area(isurf,iz,iphi)*c_stef_boltz &
                                *T(isurf,iz,iphi)**4
            qesum = qesum + qe(isurf,iz,iphi)
         end do
      end do
   else
      ! Unexpected surface
      print *,' Error: unexpected surface index. isurf=  ',isurf
   end if
```

```
end do ! Finished summing all power values

! Assign rays
qray = qesum / real(Nrays,8)
Ne=nint(qe/qray,8)
! Correct power per ray according to actual assigned rays
qray = qesum / real(sum(Ne),8)

! Report power/ray-launching statistics
if(verbose)then
   print *,' '
   print *,' Power incident at aperture [W]: ',nint(qe(1,1,1))
   print *,' Power emitted from walls   [W]: ',nint(qesum-qe(1,1,1))
   print *,'     Total power of system  [W]: ',nint(qesum)
   print *,' ----------------------------------------'
   print *,' Number of intended rays : ',Nrays
   print *,' Power per ray [W/ray]   : ',qray
   print *,' Number of assigned rays : ',sum(Ne)
   print *,' Ray disparity           : ',sum(Ne)-int(Nrays,8)
   print *,' '
   print *,' ----------Emission summary-----------'
   print *,' Rays from the aperture : ',Ne(1,1,1)
   print *,' Rays from the wall     : ',sum(Ne(3,:,:))
   print *,' Rays from the back end : ',sum(Ne(2,:,:))
   print *,' Rays from the front end: ',sum(Ne(1,4:Nr,:))
   print *,' '
end if

! Launch and trace all rays
do isurf=1, Ns
   do iz = 1, Nz
      do iphi = 1, Nphi
         if((isurf==1).and.(iz==1).and.(iphi==1))then
            call bandset(5777d+0, 0, Rlam) ! Set bands for blackbody @ Tsolar
         else
            call bandset(T(isurf,iz,iphi), imatl, Rlam)
         end if
         do iray = 1, int(Ne(isurf,iz,iphi),4)
            ! Set emission wavelength band
            rand = dprand()
            if(rand < Rlam(1))then
               band = 1
            else if(rand < Rlam(2))then
               band = 2
            else if(rand >= Rlam(2))then
               band = 3
            end if
            ! Set emission location
            if(isurf<=2) then
            ! Launch from cavity ends
               if((isurf==1).and.(iz==1).and.(iphi==1)) then
               ! Set position within aperture for incident solar
                  solar = .true.
                  Pp(1) = sqrt(dprand()*(dap/2d+0)**2)
                  Pp(2) = dprand()*2d+0*c_pi
                  Pp(3) = 0d+0
               else
               ! Set non-aperture position for wall emission
                  Pp(1) = sqrt(dprand()*(r(iz)**2-r(iz-1)**2) + r(iz-1)**2 )
                  if(iz==1) then
                     Pp(2) = dprand() * (phi(iphi)-phi(iphi-4)) + phi(iphi-4)
                  else if(iz==2) then
                     Pp(2) = dprand() * (phi(iphi)-phi(iphi-2)) + phi(iphi-2)
                  else if(iz>=3) then
                     Pp(2) = dprand() * (phi(iphi)-phi(iphi-1)) + phi(iphi-1)
                  else
                     print *,' Unrealistic radius index used in launch loop'
                  end if
                  Pp(3) = real(isurf-1,8)*dap*D*L
               end if
            else if(isurf==3) then
```

```
! Launch from cavity sidewall
   Pp(1) = dap*D/2d+0
   Pp(2) = dprand() * (phi(iphi)-phi(iphi-1)) + phi(iphi-1)
   Pp(3) = dprand() * (z(iz)-z(iz-1)) + z(iz-1)
end if
call pol2car(Pp,Pc)

! Launch new ray and follow to its extinction
sameray = .true.
csurf = int(isurf,2)
do while(sameray)
   ! Set emission/reflection direction
   psi = dprand() * 2d+0 * c_pi
   if(solar)then
      ! Constant below calculated for SolSim cone angle of 37 deg
      theta = asin(sqrt(dprand()/2.761047960d+0))
      solar = .false. ! Use diffuse reflection hereafter
   else
      theta = asin(sqrt(dprand()))
   end if
   if(csurf==int(3,2)) then
      normal(csurf,1)=-Pc(1)/ro
      normal(csurf,2)=-Pc(2)/ro
   end if
   call tripod(normal(csurf,:), t1, t2)
   s = cos(theta) * normal(csurf,:) + sin(theta) &
       * (cos(psi) * t1 + sin(psi) * t2)

   ! Check for intesection location
   call int_line_cylinder(Pc,s,c1,c2,ro,isint,Pint,ierr)
   if(ierr<int(0,1)) print *,' Intersection detect error: ',ierr

   ! Assign ray location to new intersection point
   dist(1) = sqrt(sum((Pc-Pint(1,:))**2))
   dist(2) = sqrt(sum((Pc-Pint(2,:))**2))
   if(dist(1)>dist(2)) then
      Pc    = Pint(1,:)
      csurf = isint(1)
   else if(dist(2)>dist(1)) then
      Pc    = Pint(2,:)
      csurf = isint(2)
   else
      print *,' Negligible ray length. Maintaining Pc and csurf.'
   end if

   ! Check for loss out aperture
   if((csurf==int(1,2)).AND.                                    &
      (sqrt(Pc(1)**2+Pc(2)**2)<dap/2d+0))then
      sameray   = .false.
   end if
   ! Check for absorption
   if(dprand()<=emiss(midlam(band),imatl)) sameray = .false.
   ! If ray isn't absorbed, set new direction and continue
end do
! End ray-tracing loop

! Translate absorbed position to absorption matrix value
call car2pol(Pc,Pp)
if(csurf<=int(2,2)) then
! Ray ends at one of the discs at the cylindrical cavity ends
   if((Pp(1) < dap/2d+0).and.(csurf==int(1,2)))then
   ! Detect aperture loss
      Na(1,1,1) = Na(1,1,1) + int(1,8)
   else
   ! Detect surface absorption
      if(Pp(1)<=r(1))then
         ira = 1
         iphia = 4*ceiling(Pp(2)/(4d+0*dphi))
      else if(Pp(1)<=r(2))then
         ira = 2
         iphia = 2*ceiling(Pp(2)/(2d+0*dphi))
```

```
                  else if(Pp(1)<=r(3))then
                     ira = 3
                     iphia = ceiling(Pp(2)/dphi)
                  else
                     ira = ceiling((Pp(1)-dap/2d+0)/dr)+3
                     iphia = ceiling(Pp(2)/dphi)
                  end if
                  Na(csurf,ira,iphia) = Na(csurf,ira,iphia) + int(1,8)
               end if
            else if(csurf==int(3,2)) then
            ! Ray ends at the circumferential cylinder cavity wall
               iza   = ceiling(Pp(3)/dz)
               iphia = ceiling(Pp(2)/dphi)
               if(iza .gt. Nz) print *,' Ray overbound - Z =',Pp(3)
               Na(csurf,iza,iphia) = Na(csurf,iza,iphia) + int(1,8)
            end if
            ! End absorption accounting if loop
         end do
         ! End ray emission loop for current element
      end do
      ! End loop over angular position phi
   end do
   ! End loop over radial or axial positions, z or r
end do
! End loop over all surfaces
if(verbose)then
   print *,' ---------Absorption summary----------'
   print *,' Rays out the aperture  : ',Na(1,1,1)
   print *,' Rays on the wall       : ',sum(Na(3,:,:))
   print *,' Rays on the back end   : ',sum(Na(2,:,:))
   print *,' Rays on the front end  : ',sum(Na(1,4:Nr,:))
   print *,' Unlaunched rays        : ',sum(Ne)-sum(Na)
   print *,' '
end if

! Calculate performance statistics
where(area > 10d+0*tiny(0d+0) )
   qnet = (real(Na-Ne,8 )) * qray / area ! Net flux into surface [W/m^2]
elsewhere
   qnet = 0d+0
end where
qnetavg =real(sum(Na)-Na(1,1,1)-(sum(Ne)-Ne(1,1,1)),8)*qray/                &
         (sum(area)-area(1,1,1))
eta_abs    = 1d+0-real(Na(1,1,1),8)/real(Ne(1,1,1),8)
do isurf=1, Ns
   do iz=1, Nz
      do iphi=1, Nphi
         if((isurf==1).and.(iz==1).and.(iphi==1))then
         ! Skip aperture.
         else if(area(isurf,iz,iphi) > 10d+0*tiny(0d+0))then
            sdevsum = sdevsum + (qnet(isurf,iz,iphi)-qnetavg)**2
            Nsdev   = Nsdev + 1
         end if
      end do
   end do
end do
sdev    = sqrt(sdevsum/real(Nsdev,8))
if(verbose)then
   print *,' ------------Performance Stats--------------'
   print *,' Cavity absorption efficiency : ',nint(eta_abs*100d+0)
   print *,' Average heat flux into walls : ',nint(qnetavg)
   print *,' Standard deviation of flux   : ',nint(sdev)
   print *,' '
end if

! Report time elapsed during program
call system_clock(clock_1, clock_rate, clock_max)
tlapse = real(clock_1-clock_0,8)/real(clock_rate,8)
if(verbose) print *,' Elapsed time (seconds) = ',tlapse
return
end subroutine cavsim
```

```
subroutine pcavsim(T, D, L, Csuns, imatl, Nrays, Nr, Nphi, Nz,                &
                   qnet, eta_abs, qnetavg, sdev)
!-------------------------------------------------------------------------------
! Syntax:
! pcavsim(T,D,L,Csuns,imatl,Nrays,Nr,Nphi,Nz,qnet,eta_abs,qnetavg,sdev)
!     INPUTS:   T(3,Nz,16)= Temperature array for all cells
!               D         = The [cavity] / [aperture] diameter aspect ratio
!               L         = The cavity [length]/[diameter] aspect ratio
!               Csuns     = Solar concentration in suns [1 sun = 1000 W/m^2]
!               imatl     = Material index
!                           (0=black, 1=inco, 2=Al2O3, 3=grey(constant))
!               Nrays     = Number of ray bundles to be launched
!               Nr        = Number of radial spatial divisions (MINIMUM 3!)
!               Nphi      = Number of angular divisions (ALWAYS USE 16!)
!               Nz        = Number of axial spatial divisions
!
!     OUTPUTS:  qnet(3,Nz,16) = Net heat flux for all cells (aperture at 1,1,1)
!               eta_abs       = Absorption efficiency (q_net/q_solar)
!               qnetavg       = Average net heat flux in cavity (mu)
!               sdev       = Standard deviation of flux (sigma)
! Info:
!   THIS IS A PARALLEL VERSION OF THE SERIAL sub_cavsim.f90 PROGRAM.
!   !!! ONLY THE RANK 0 PROCESS RECIEVES PROPER OUTPUT VALUES !!!
!   This subroutine simulates radiative exchange between a specified
!   temperature cylindrical cavity with 5cm aperture and the planned solar
!   simulator using Monte Carlo ray tracing methods.  The program is passed
!   the temperature distribution, dimensionless geometry ratios, material,
!   number of rays and discritization parameters prior to execution.
!
! Note: The grid spacing Nr and Nz can be calculated in the calling program via:
!       Nr     = ceiling(dap*(D-1.0)/(2.0*drmax)) + 3
!       Nphi   = 16
!       Nz     = ceiling(dap*D*L/dzmax)
!-------------------------------------------------------------------------------
!   use mpi
   implicit none
   include 'mpif.h'
   ! Declarations.  All units in SI base [kg,m,s] values unless otherwise noted.
   integer, intent(in)  :: imatl, Nrays      ! Material index and ray count
   integer, intent(in)  :: Nr, Nphi, Nz      ! Number of grid elements
   integer, parameter   :: Ns = 3            ! Number of surfaces
   real(8), parameter   :: dap  = 5d-2       ! Aperture diameter
   real(8), parameter   :: c_pi = 3.141592653589793d+0
   real(8), parameter   :: c_stef_boltz = 5.670400d-8    ! [W/m^2-K^4]
   real(8), intent(in)  :: D, L, Csuns       ! Geometry ratios and concentration
   real(8), intent(out) :: eta_abs, qnetavg, sdev   ! Averaged properties
   integer        :: irstart = 1, Nsdev, diphi = 1
   integer        :: isurf, ir, iz, iphi
   integer        :: iproc, nprocs, ierror
   real(8)        :: dr, dphi, dz, emissavg, qray = 0d0
   real(8)        :: sdevsum
   logical        :: verbose = .false.
   integer(8), dimension(Ns,Nz,Nphi) :: Ne, Na, Nei, Nai
   real(8), dimension(0:Nr)          :: r
   real(8), dimension(0:Nphi)        :: phi
   real(8), dimension(0:Nz)          :: z
   real(8), dimension(Ns,Nz,Nphi)    :: qe, area
   real(8), dimension(Ns,Nz,Nphi), intent(in)   :: T     ! Element temperatures
   real(8), dimension(Ns,Nz,Nphi), intent(out)  :: qnet  ! Element net fluxes

   ! Query MPI system size, assign rank.
   call MPI_COMM_SIZE(MPI_COMM_WORLD, nprocs, ierror)
   call MPI_COMM_RANK(MPI_COMM_WORLD, iproc, ierror)
   ! Program execution banner
   if(verbose .and. (iproc .eq. 0))then
      print *,' '
      print *,' ----------- SUBROUTINE: ideal_cavsim -------------'
      print *,' Utilizing ',nprocs,' process(es).'
   end if

   ! Discritize grid for all processes
```

```
call gridspace(D,L,dap,Nr,Nphi,Nz,dr,dphi,dz,r,phi,z)

! Initialize cell value arrays for all processes
Nei  = int(0,8)
Nai  = int(0,8)

! Carry out setup calculations on the primary process only
if( iproc .eq. 0 ) then
   ! Set up ray distribution
   Ne   = int(0,8)
   Na   = int(0,8)
   qe   = 0d+0
   qnet = 0d+0
   area = 0d+0

   ! Initialize standard deviation calculation terms
   sdevsum = 0d+0
   Nsdev   = 0

   ! Calculate total emissive power from all emitting elements.
   ! Aperture emission
   area(1,1,1) = c_pi*(dap/2d+0)**2
   qe(1,1,1)   = Csuns*1000d+0* area(1,1,1)
   ! Surface emission
   do isurf = 1,Ns
      if ( isurf <= 2 ) then
         ! Surfaces 1 or 2: circular ends of cavity.
         if ( isurf == 1 ) irstart = 4 ! Surface 1 omits 3 aperture rows
         if ( isurf == 2 ) irstart = 1
         do ir = irstart,Nr
            if ( ir == 1 ) diphi = 4  ! Four segment core circle
            if ( ir == 2 ) diphi = 2  ! Eight segment transition ring
            if ( ir >= 3 ) diphi = 1  ! Standard 16 segment ring sections
            do iphi = diphi,Nphi,diphi
               area(isurf, ir, iphi) = &
                  (r(ir)**2-r(ir-1)**2)*(phi(iphi)-phi(iphi-diphi))/2d+0
               qe(isurf,ir,iphi) = emissavg(T(isurf,ir,iphi),imatl) &
                                   *area(isurf,ir,iphi)*c_stef_boltz &
                                   *T(isurf,ir,iphi)**4
            end do
         end do
      else if ( isurf == 3 ) then
         ! Surface 3: Cylindrical wall of cavity
         area(isurf,:,:) = dz*dphi*r(Nr)
         do iz = 1,Nz
            do iphi = 1,Nphi
               qe(isurf,iz,iphi) = emissavg(T(isurf,iz,iphi),imatl) &
                                   *area(isurf,iz,iphi)*c_stef_boltz &
                                   *T(isurf,iz,iphi)**4
            end do
         end do
      else
         ! Unexpected surface
         print *,' Error: unexpected surface index. isurf=  ',isurf
      end if
   end do ! Finished summing all power values

   ! Report power statistics
   if(verbose .and. (iproc .eq. 0))then
      print *,' '
      print *,' Power incident at aperture [W]: ',nint(qe(1,1,1))
      print *,' Power emitted from walls   [W]: ',nint(sum(qe)-qe(1,1,1))
      print *,'     Total power of system  [W]: ',nint(sum(qe))
      print *,' ------------------------------------------'
   end if

   ! Set goal power per ray
   qray = sum(qe) / real(Nrays,8)
   ! Assign rays
   Nei  = nint(qe/(qray*real(nprocs,8)),8)
   Ne   = Nei * int(nprocs,8)
```

```
      ! Correct power per ray according to actual assigned rays
      qray = sum(qe) / real(sum(Nei)*int(nprocs,8),8)
   endif ! process 0 limiter

   ! Broadcast calculated ray launch array, 'Nei', to all processes.
   call MPI_BCAST(Nei, size(Nei), MPI_INTEGER8, 0, MPI_COMM_WORLD, ierror)

   ! Execute tracing of all Nei rays yielding Nai absorptions for each process.
   call raytrace(Nei, Nai)

   ! Sum up the ray-tracing counts from each process
   call MPI_REDUCE(Nai, Na, size(Na), MPI_INTEGER8, MPI_SUM, 0,                &
                   MPI_COMM_WORLD, ierror)

   ! The following work is performed by the rank 0 process only.
   if(iproc .eq. 0) then
      ! Report ray emission and absorption statistics
      if(verbose)then
         print *,' Number of intended rays : ',Nrays
         print *,' Power per ray [W/ray]   : ',qray
         print *,' Number of assigned rays : ',sum(Ne)
         print *,' Ray disparity           : ',sum(Ne)-int(Nrays,8)
         print *,' '
         print *,' ----------Emission summary-----------'
         print *,' Rays from the aperture : ',Ne(1,1,1)
         print *,' Rays from the wall     : ',sum(Ne(3,:,:))
         print *,' Rays from the back end : ',sum(Ne(2,:,:))
         print *,' Rays from the front end: ',sum(Ne(1,4:Nr,:))
         print *,' '
         print *,' ---------Absorption summary----------'
         print *,' Rays out the aperture  : ',Na(1,1,1)
         print *,' Rays on the wall       : ',sum(Na(3,:,:))
         print *,' Rays on the back end   : ',sum(Na(2,:,:))
         print *,' Rays on the front end  : ',sum(Na(1,4:Nr,:))
         print *,' Unlaunched rays        : ',sum(Ne)-sum(Na)
         print *,' '
      end if

      ! Calculate performance statistics
      where(area > 10d+0*tiny(0d+0) )
         qnet = (real(Na-Ne,8 )) * qray / area ! Net flux into surface [W/m^2]
      elsewhere
         qnet = 0d+0
      end where
      qnetavg =real(sum(Na)-Na(1,1,1)-(sum(Ne)-Ne(1,1,1)),8)*qray/             &
               (sum(area)-area(1,1,1))
      eta_abs    = 1d+0-real(Na(1,1,1),8)/real(Ne(1,1,1),8)
      do isurf=1, Ns
         do iz=1, Nz
            do iphi=1, Nphi
               if((isurf==1).and.(iz==1).and.(iphi==1))then
               ! Skip aperture.
               else if(area(isurf,iz,iphi) > 10d+0*tiny(0d+0))then
                  sdevsum = sdevsum + (qnet(isurf,iz,iphi)-qnetavg)**2
                  Nsdev   = Nsdev + 1
               end if
            end do
         end do
      end do
      sdev    = sqrt(sdevsum/real(Nsdev,8))
      if(verbose)then
         print *,' ------------Performance Stats--------------'
         print *,' Cavity absorption efficiency : ',nint(eta_abs*100d+0)
         print *,' Average heat flux into walls : ',nint(qnetavg)
         print *,' Standard deviation of flux   : ',nint(sdev)
         print *,' '
      end if
   endif ! Rank 0 only if loop.
   return
contains
   subroutine raytrace(Nei, Nai)
```

```
!  Rayracing routine contained within pcavsim subroutine.
!     Nei = Array of surface emission rays
!     Nai = Array of surface absorption rays
use randdp
implicit none
integer(8), dimension(Ns,Nz,Nphi), intent(in)  :: Nei
integer(8), dimension(Ns,Nz,Nphi), intent(out) :: Nai
integer(1)     :: ierr = int(0,1)
integer(2)     :: csurf
integer        :: iseed, iray, ira, iza, iphia, isurf, iz, iphi, band = 1
integer        :: primes
real(8)        :: psi, theta, ro, randn, emiss
logical        :: solar = .false., sameray = .false.
integer(2), dimension(2):: isint
real(8), dimension(3)   :: Pp, Pc, t1, t2, midlam, s, c1, c2
real(8), dimension(2)   :: Rlam, dist
real(8), dimension(2,3) :: Pint
real(8), dimension(3,3) :: normal

! Initialize random number generator. A prime seed is reccomended.
iseed = primes(iproc + 1)
call sdprnd(iseed)

! Set up problem geometry and ref. wavelengths from each discrete band.
c1          = (/0.d0, 0.d0, 0.d0/)           ! Disc center, aperture end
c2          = (/0.d0, 0.d0, real(dap*D*L,8)/)! Disc center, closed end
normal(1,:) = (/0.d0, 0.d0, 1.d0 /)
normal(2,:) = (/0.d0, 0.d0, -1.d0/)
normal(3,:) = (/0.d0, 0.d0, 0.d0/)
ro          = dap*D/2d+0
midlam      = (/0.5d0, 2.0d0, 5.5d0/) ! Wavelengths [micron] from bands.

! Launch and trace all rays
do isurf=1, Ns
   do iz = 1, Nz
      do iphi = 1, Nphi
         if((isurf==1).and.(iz==1).and.(iphi==1))then
            call bandset(5777d+0, 0, Rlam) ! Set bands, blackbody @ Tsolar
         else
            call bandset(T(isurf,iz,iphi), imatl, Rlam)
         end if
         do iray = 1, int(Nei(isurf,iz,iphi),4)
            ! Set emission wavelength band
            randn = dprand()
            if(randn < Rlam(1))then
               band = 1
            else if(randn < Rlam(2))then
               band = 2
            else if(randn >= Rlam(2))then
               band = 3
            end if
            ! Set emission location
            if(isurf<=2) then
            ! Launch from cavity ends
               if((isurf==1).and.(iz==1).and.(iphi==1)) then
               ! Set position within aperture for incident solar
                  solar = .true.
                  Pp(1) = sqrt(dprand()*(dap/2d+0)**2)
                  Pp(2) = dprand()*2d+0*c_pi
                  Pp(3) = 0d+0
               else
               ! Set non-aperture position for wall emission
                  Pp(1) = sqrt(dprand()*(r(iz)**2-r(iz-1)**2) +r(iz-1)**2)
                  if(iz==1) then
                     Pp(2) = dprand()*(phi(iphi)-phi(iphi-4)) +phi(iphi-4)
                  else if(iz==2) then
                     Pp(2) = dprand()*(phi(iphi)-phi(iphi-2)) +phi(iphi-2)
                  else if(iz>=3) then
                     Pp(2) = dprand()*(phi(iphi)-phi(iphi-1)) +phi(iphi-1)
                  else
                     print *,' Unreal radius index used in launch loop'
```

```
      end if
      Pp(3) = real(isurf-1,8)*dap*D*L
   end if
else if(isurf==3) then
! Launch from cavity sidewall
   Pp(1) = dap*D/2d+0
   Pp(2) = dprand() * (phi(iphi)-phi(iphi-1)) + phi(iphi-1)
   Pp(3) = dprand() * (z(iz)-z(iz-1)) + z(iz-1)
end if
call pol2car(Pp,Pc)

! Launch new ray and follow to its extinction
sameray = .true.
csurf = int(isurf,2)
do while(sameray)
   ! Set emission/reflection direction
   psi = dprand() * 2d+0 * c_pi
   if(solar)then
      ! Constant below calculated for cone angle of 37 deg.
      theta = asin(sqrt(dprand()/2.761047960d+0))
      solar = .false. ! Use diffuse reflection hereafter
   else
      theta = asin(sqrt(dprand()))
   end if
   if(csurf==int(3,2)) then
      normal(csurf,1)=-Pc(1)/ro
      normal(csurf,2)=-Pc(2)/ro
   end if
   call tripod(normal(csurf,:), t1, t2)
   s = cos(theta) * normal(csurf,:) + sin(theta) &
       * (cos(psi) * t1 + sin(psi) * t2)

   ! Check for intesection location
   call int_line_cylinder(Pc,s,c1,c2,ro,isint,Pint,ierr)
   if(ierr<int(0,1)) print *,' Intersect detect error: ',ierr

   ! Assign ray location to new intersection point
   dist(1) = sqrt(sum((Pc-Pint(1,:))**2))
   dist(2) = sqrt(sum((Pc-Pint(2,:))**2))
   if(dist(1)>dist(2)) then
      Pc    = Pint(1,:)
      csurf = isint(1)
   else if(dist(2)>dist(1)) then
      Pc    = Pint(2,:)
      csurf = isint(2)
   else
      print *,' Negligible ray length. ',                    &
               'Maintaining Pc and csurf.'
   end if

   ! Check for loss out aperture
   if((csurf==int(1,2)).AND.                                 &
      (sqrt(Pc(1)**2+Pc(2)**2)<dap/2d+0))then
      sameray   = .false.
   end if
   ! Check for absorption
   if(dprand()<=emiss(midlam(band),imatl)) sameray = .false.
   ! If ray isn't absorbed, set new direction and continue
end do
! End ray-tracing loop

! Translate absorbed position to absorption matrix value
call car2pol(Pc,Pp)
if(csurf<=int(2,2)) then
! Ray ends at one of the discs at the cylindrical cavity ends
   if((Pp(1) < dap/2d+0).and.(csurf==int(1,2)))then
   ! Detect aperture loss
      Nai(1,1,1) = Nai(1,1,1) + int(1,8)
   else
   ! Detect surface absorption
      if(Pp(1)<=r(1))then
```

```
                        ira = 1
                        iphia = 4*ceiling(Pp(2)/(4d+0*dphi))
                     else if(Pp(1)<=r(2))then
                        ira = 2
                        iphia = 2*ceiling(Pp(2)/(2d+0*dphi))
                     else if(Pp(1)<=r(3))then
                        ira = 3
                        iphia = ceiling(Pp(2)/dphi)
                     else
                        ira = ceiling((Pp(1)-dap/2d+0)/dr)+3
                        iphia = ceiling(Pp(2)/dphi)
                     end if
                     if(ira .gt. Nr) then
                        print *,' Dimensional Bounds exceeded: r=',Pp(1)
                        ira = Nr
                     endif
                     if(iphia .gt. Nphi) then
                        print *,' Dimensional Bounds exceeded: phi=',Pp(2)
                        iphia = Nphi
                     endif
                     Nai(csurf,ira,iphia) = Nai(csurf,ira,iphia) + int(1,8)
                  end if
               else if(csurf==int(3,2)) then
               ! Ray ends at the circumferential cylinder cavity wall
                  iza   = ceiling(Pp(3)/dz)
                  iphia = ceiling(Pp(2)/dphi)
                  if(iza .gt. Nz) then
                     if(Pp(3) .gt. z(Nz)*1.0001d0) print *,'OOB: z=',Pp(3)
                     iza = Nz
                  endif
                  if(iphia .gt. Nphi) then
                     print *,' Dimensional Bounds exceeded: phi=',Pp(2)
                     iphia = Nphi
                  endif
                  Nai(csurf,iza,iphia) = Nai(csurf,iza,iphia) + int(1,8)
               end if
               ! End absorption accounting if loop
            end do
            ! End ray emission loop for current element
         end do
         ! End loop over angular position phi
      end do
      ! End loop over radial or axial positions, z or r
   end do
   ! End loop over all surfaces
   return
 end subroutine raytrace
end subroutine pcavsim
```

```
subroutine gridspit(D,L,drmax,dzmax,dap,Nr,Nz)
   implicit none
   integer                       :: Nr, Nz
   double precision, intent(in) :: D, L, drmax, dzmax, dap
      Nr     = ceiling(dap*(D-1d0)/(2d0*drmax)) + 3
      Nz     = ceiling(dap*D*L/dzmax)
end subroutine gridspit

subroutine gridspace(D,L,dap,Nr,Nphi,Nz,dr,dphi,dz,r,phi,z)
   ! Sets up the dimension vectors and step sizes to describe the geometry
   ! Input:    Geometric parameters   - D, L, Dap
   !           Number of grid steps   - Nr, Nphi,Nz
   ! Output:   Dimensional step sizes - dr, dphi, dz
   !           Dimension vectors      - r, phi, z
   implicit none
   real(8), intent(in)  :: D, L, dap
   integer, intent(in)  :: Nr, Nphi, Nz
   real(8), intent(out) :: dr, dphi, dz
   real(8), dimension(0:Nr), intent(out)     :: r
   real(8), dimension(0:Nphi), intent(out)   :: phi
   real(8), dimension(0:Nz),   intent(out)   :: z
   real(8), parameter   :: c_pi = 3.1415926535898d+0
   integer              :: i = 0
      dr    = dap*(D-1d+0)/(2d+0*(real(Nr-3,8)))
      dphi  = 2d+0*c_pi/real(Nphi,8)
      dz    = dap*D*L/real(Nz,8)
      r     = (/ 0.000d+0, 0.008d+0, 0.016d+0,                                    &
                        ((real(dap,8)/2.d+0)+real(dr,8)*real(i,8),i=0,Nr-3) /)
      phi   = dphi * (/ (real(i,8),i=0,Nphi) /)
      z     = dz * (/ (real(i,8),i=0,Nz) /)
   return
end subroutine gridspace

subroutine pol2car(Vpolar, Vcartesian)
   implicit none
   ! Translates polar to cartesian coordinates. Angular origin is the X-Axis.
   ! Input: 3-Dimensional polar coordinate vector (r,phi,z)
   ! Output: 3-Dimensional cartesian coordinate vector (x,y,z)
   real(8), dimension(3), intent(in)   :: Vpolar
   real(8), dimension(3), intent(out)  :: Vcartesian
      Vcartesian(1) = Vpolar(1) * cos(Vpolar(2))
      Vcartesian(2) = Vpolar(1) * sin(Vpolar(2))
      Vcartesian(3) = Vpolar(3)
   return
end subroutine pol2car

subroutine car2pol(Vcartesian, Vpolar)
   implicit none
   ! Translates Cartesian coordinates to polar. Angular origin is the X-Axis.
   ! Input: 3-Dimensional polar coordinate vector (r,phi,z)
   ! Output: 3-Dimensional cartesian coordinate vector (x,y,z)
   real(8), dimension(3), intent(out)  :: Vpolar
   real(8), dimension(3), intent(in)   :: Vcartesian
   real(8)                             :: c_pi = 3.141592653589793d+0
      Vpolar(1) = sqrt(Vcartesian(1)**2+Vcartesian(2)**2)
      if(Vcartesian(1)<0d+0)then
         Vpolar(2) = atan(Vcartesian(2)/Vcartesian(1)) + c_pi
      else if(Vcartesian(2)<0d+0)then
         Vpolar(2) = atan(Vcartesian(2)/Vcartesian(1)) + 2d+0*c_pi
      else if(Vcartesian(2)>=0d+0)then
         Vpolar(2) = atan(Vcartesian(2)/Vcartesian(1))
      else
         print *,' Error while translating cartesian vector to polar.'
      end if
      Vpolar(3) = Vcartesian(3)
   return
end subroutine car2pol

subroutine bandset(Temp,matind,Rlam)
   implicit none
   ! Input: Temperature [K] of emitting surface, surface material index
```

```
   ! Output: Random number thresholds for upper limit of wavelength bands 1 & 2
   ! Note: Currently configured for 3 bands: 0-1.0, 1.0-5.0, 5.0-inf micrometers
   real(8), intent(in)                :: Temp    ! Element temperature [K]
   integer, intent(in)                :: matind  ! Material index
   real(8), dimension(2),intent(out)  :: Rlam    ! Bandwidth demarcation levels
   real(8)                            :: bbfrac, emiss, emissavg, check
      if(matind == 0) then
      ! Black surface
         Rlam(1) = bbfrac(1d+0, Temp)
         Rlam(2) = bbfrac(5d+0, Temp)
      else
      ! Spectral surfaces
         Rlam(1) =bbfrac(1d+0, Temp)*emiss(0.5d+0,matind)/emissavg(Temp,matind)
         Rlam(2) =(bbfrac(5d+0, Temp)-bbfrac(1d+0, Temp)) &
                  *emiss(2d+0,matind)/emissavg(Temp,matind) + Rlam(1)
         check   =(1d+0-bbfrac(5d+0, Temp)) &
                  *emiss(5.5d+0,matind)/emissavg(Temp,matind) + Rlam(2)
      !   print *,' Check upper bound. Should approach 1:  ',check
      end if
   return
end subroutine bandset

double precision function emissavg(T, imat)
   implicit none
   ! Input:    Material specification (see function emiss) and temperature
   ! Output:   Average total hemispherical emissivity at temp T for matl' imat
   ! Note:
   real(8), intent(in)  :: T
   integer, intent(in)  :: imat
   real(8)              :: bbfrac, emiss
      emissavg = emiss(0.5d+0,imat)*bbfrac(1d+0,T)+ &
                 emiss(3.0d+0,imat)*(bbfrac(5d+0,T)-bbfrac(1d+0,T))+ &
                 emiss(5.5d+0,imat)*(1d+0-bbfrac(5d+0,T))
   return
end function emissavg

double precision function bbfrac(lambda, T)
   implicit none
   ! Input:    Wavelength (micrometers) and temperature (Kelvin) of emitter
   ! Output:   Fraction of radiation emitted from the Wavelength band 0 - lambda
   ! Note:
   real(8), intent(in)  :: lambda, T
   real(8), parameter   :: c_second_radiation = 14387.75225d+0
   real(8), parameter   :: c_pi      = 3.141592653589793d+0
   integer, parameter   :: n = 11;
   integer              :: i
   real(8)              :: zeta, b
      zeta = c_second_radiation/(lambda * T)
      b = 0d+0
      do i = 1,n
         b = b + dexp(-real(i,8)*zeta)/real(i,8)                                &
             *( zeta**3+3d+0*zeta**2/real(i,8)+6d+0*zeta/real(i,8)**2           &
             + 6d+0/real(i,8)**3 )
      end do
      bbfrac = b*15d+0/c_pi**4
   return
end function bbfrac

double precision function emiss(lambda,imat)
   implicit none
   ! Input:    Wavelength in [micrometer]
   !           Material index ( 0 = black, 1 = Inconel , 2 = Al2O3 , 3 = 0.8)
   !           4 = value read from emissfile.in
   ! Output:   Spectral emissivity [-]
   ! Note: From discritized data of Toloukian and DeWitt
   real(8), intent(in)     :: lambda                  ! Wavelength
   integer, intent(in)     :: imat                    ! Material index
   real(8), dimension(2)   :: lband = real((/ 1.0, 5.0 /),8)  ! Band limits
      if( imat == 0 ) then
         ! NOTE: Solar spectra approximated from blackbody behavior, changing
         ! the value of emissivity for imat=0 here will result in error.
```

```
         emiss = 1d+0
      else if( imat == 1 ) then
      ! Properties of roughened, lightly oxidized inconel
         if( lambda <= lband(1) ) then
            emiss = 0.89d+0
         else if( lambda <= lband(2) ) then
            emiss = 0.52d+0
         else
            emiss = 0.62d+0
         end if
      else if ( imat == 2 ) then
      ! Properties of spray coated alumina on inconel substrate.
         if( lambda <= lband(1) ) then
            emiss = 0.26d+0
         else if( lambda <= lband(2) ) then
            emiss = 0.45d+0
         else
            emiss = 0.9d+0
         end if
      else if ( imat == 3 ) then
      ! Set constant grey emissivity here
         emiss = 0.8d+0
      else
      ! Error checking
         print *,'Undefined material index used. Defaulting to black.'
         emiss = 1d+0
      end if
   return
end function emiss

subroutine tripod(n, t1, t2)
   implicit none
   real(8), dimension(3), intent(in)   :: n
   real(8), dimension(3), intent(out)  :: t1, t2
   real(8), dimension(3)               :: uy, uz
      uy = real((/0., 1., 0./),8)
      uz = real((/0., 0., 1./),8)
      t1 = cross_product(n, uz)
      if (sqrt(sum(t1**2)) <= 10d+0 * tiny(1d+0)) then
         t1 = cross_product(uy, n)
      end if
      t1 = t1/sqrt(sum(t1**2))
      t2 = cross_product(n, t1)
      t2 = t2/sqrt(sum(t2**2))
   return
   contains
   function cross_product(a, b) result(c)
      implicit none
      ! Input: Three dimensional vectors a,b
      ! Output: Three dimensional vector c
      ! Note: Performs a vector cross product of the form  'a x b = c'
      real(8), dimension(3), intent(in)   :: a, b
      real(8), dimension(3)               :: c
         c(1) = a(2)*b(3)-a(3)*b(2)
         c(2) = a(3)*b(1)-a(1)*b(3)
         c(3) = a(1)*b(2)-a(2)*b(1)
      return
   end function cross_product
end subroutine tripod

integer function primes(i)
   implicit none
   integer, intent(in)     :: i
   integer, dimension(256) :: primelist
      primelist =(/ 1087, 1091, 1093, 1097, 1103, 1109, 1117, 1123, 1129, 1151,&
                    1153, 1163, 1171, 1181, 1187, 1193, 1201, 1213, 1217, 1223,&
                    1229, 1231, 1237, 1249, 1259, 1277, 1279, 1283, 1289, 1291,&
                    1297, 1301, 1303, 1307, 1319, 1321, 1327, 1361, 1367, 1373,&
                    1381, 1399, 1409, 1423, 1427, 1429, 1433, 1439, 1447, 1451,&
                    1453, 1459, 1471, 1481, 1483, 1487, 1489, 1493, 1499, 1511,&
                    1523, 1531, 1543, 1549, 1553, 1559, 1567, 1571, 1579, 1583,&
```

```
                  1597, 1601, 1607, 1609, 1613, 1619, 1621, 1627, 1637, 1657,&
                  1663, 1667, 1669, 1693, 1697, 1699, 1709, 1721, 1723, 1733,&
                  1741, 1747, 1753, 1759, 1777, 1783, 1787, 1789, 1801, 1811,&
                  1823, 1831, 1847, 1861, 1867, 1871, 1873, 1877, 1879, 1889,&
                  1901, 1907, 1913, 1931, 1933, 1949, 1951, 1973, 1979, 1987,&
                  1993, 1997, 1999, 2003, 2011, 2017, 2027, 2029, 2039, 2053,&
                  2063, 2069, 2081, 2083, 2087, 2089, 2099, 2111, 2113, 2129,&
                  2131, 2137, 2141, 2143, 2153, 2161, 2179, 2203, 2207, 2213,&
                  2221, 2237, 2239, 2243, 2251, 2267, 2269, 2273, 2281, 2287,&
                  2293, 2297, 2309, 2311, 2333, 2339, 2341, 2347, 2351, 2357,&
                  2371, 2377, 2381, 2383, 2389, 2393, 2399, 2411, 2417, 2423,&
                  2437, 2441, 2447, 2459, 2467, 2473, 2477, 2503, 2521, 2531,&
                  2539, 2543, 2549, 2551, 2557, 2579, 2591, 2593, 2609, 2617,&
                  2621, 2633, 2647, 2657, 2659, 2663, 2671, 2677, 2683, 2687,&
                  2689, 2693, 2699, 2707, 2711, 2713, 2719, 2729, 2731, 2741,&
                  2749, 2753, 2767, 2777, 2789, 2791, 2797, 2801, 2803, 2819,&
                  2833, 2837, 2843, 2851, 2857, 2861, 2879, 2887, 2897, 2903,&
                  2909, 2917, 2927, 2939, 2953, 2957, 2963, 2969, 2971, 2999,&
                  3001, 3011, 3019, 3023, 3037, 3041 /)
     primes = primelist(i)
   return
end function primes
```

Appendix F: Reactor Standard Operating Procedure

Section 1: Reactor Preparation

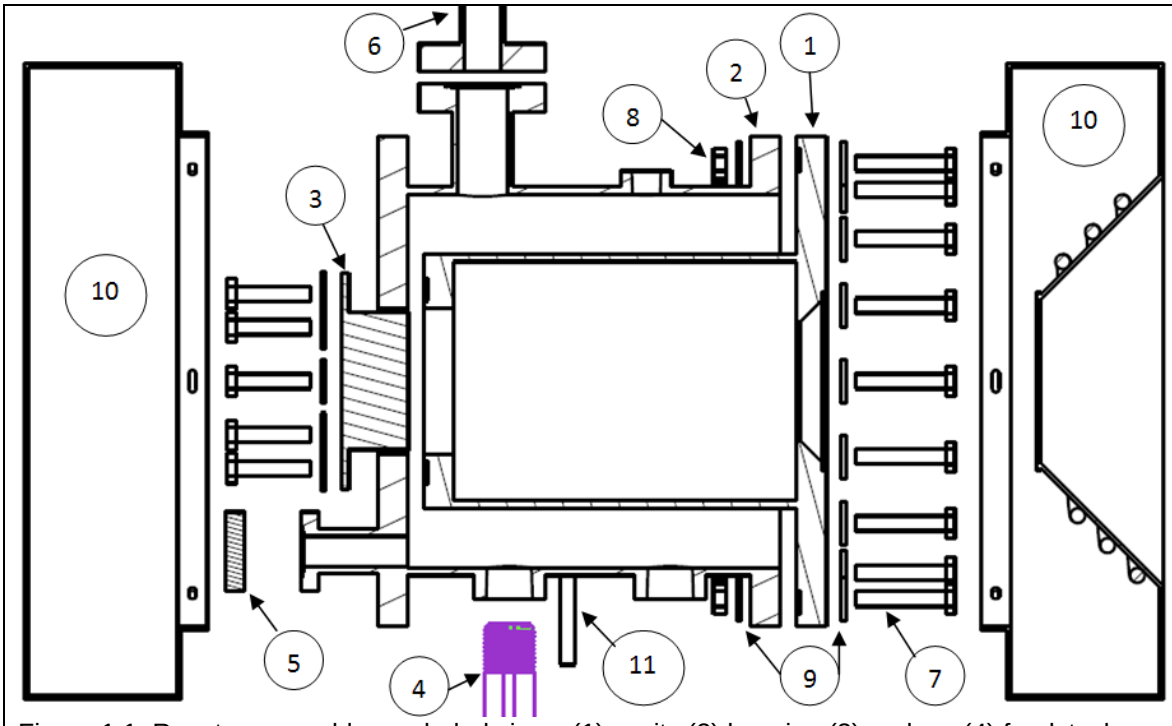

Figure 1.1: Reactor assembly, exploded view. (1) cavity (2) housing (3) endcap (4) feedstock injector (5) drain flange (6) outlet assembly (7) bolt (8) nut (9) washer (10) shields (11) rear mounts.

Proc #	Action	Cautionary Considerations
1.0	Initial Condition: The reactor core components should be cleaned and dried in a disassembled state prior to beginning the reactor prep procedures.	• Ensure the mating faces of the cavity and housing are clean of salt or other buildup.
1.1	Place cavity piece (1) flange-down on a clean, flat, stable surface with four of the front flange bolts protruding through four opposing holes to aid alignment of gaskets/housing. Place gasket material on front and rear mating surfaces of the cavity piece in alignment with the bolt holes. Place housing (2) over cavity piece (1) in alignment with the bolt holes. Place endcap (3) over rear of housing in alignment with bolt holes.	• Ensure gasket material completely covers FLUID-SIDE of mating surfaces outside of the bolt-circle undercut groove. • Ensure gaskets do not shift during assembly (do not slide parts against eachother).
1.2	Feed 10 Inconel bolts (7) through a washer (9), the endcap (3), housing (2) and into the threaded holes of the rear of the cavity (1). Loosely hand-tighten rear bolts (do not apply closing torque!)	• Ensure bolt threads are lubricated with graphite paste or have existing graphite residue on engagement region (end ½").

1.3	Turn assembly over so the cavity aperture end is facing up (drain stem may need to hang over table edge). Feed 18 Inconel bolts (7) through a washer (9), the cavity (1) flange, the housing (2) flange, another washer, and attach a stainless steel nut (8). Hand tighten all fasteners.	• Ensure nut threads are lubricated with graphite paste or have existing graphite residue.
1.4	Using a proper torque sequence (see Fig 1.2 to the right), and using a torque wrench and backing wrench with proper technique: 1. Tighten FIRST the 18 FRONT FLANGE bolts to a torque of 24 in-lbs. 2. Tighten SECOND the 10 REAR bolts to a torque of 24 in-lbs. 3. Return to the FRONT FLANGE bolts and re-tighten all 18 bolts back to 24 in-lbs two times. 4. Return to the REAR bolts and re-tighten all 10 bolts back to 24 in-lbs two times. 5. Continue torquing the front and rear bolts until no further displacement is observed at 24 in-lbs.	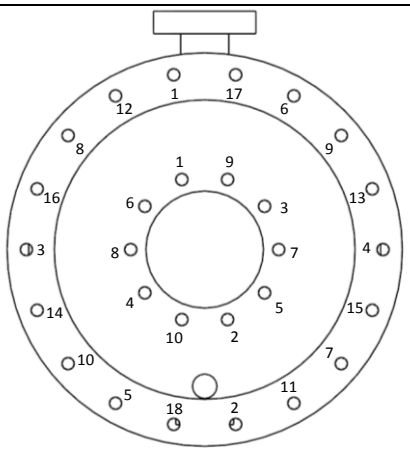 Figure 1.2: Bolt torque sequence.
1.5	Place the reactor aperture-side-down on a stable surface again. Attach the drain flange (5) to the drain stem and the outlet flange (6) to the outlet stem with a copper gasket between the mating surfaces. Seal the drain flange with a ¼" NPT plug.	• Keep in mind that the drain plug must be removed from the hot reactor. Do not tighten the plug beyond what is needed to seal.
1.6	Attach the rear mounting legs (11) to the INNER (or front) side of the REAR flange using the provided mounting holes and stainless steel fasteners.	
1.7	Thread the feed injector (4) into the REAR feedstock delivery port on the bottom of the reactor. Tighten the injector such that the feed-screw tube faces the direction of the feed delivery system (e.g. to the RIGHT if looking at the aperture-end of the reactor).	• Ensure the NPT threads of the injector have been lubricated with graphite paste.

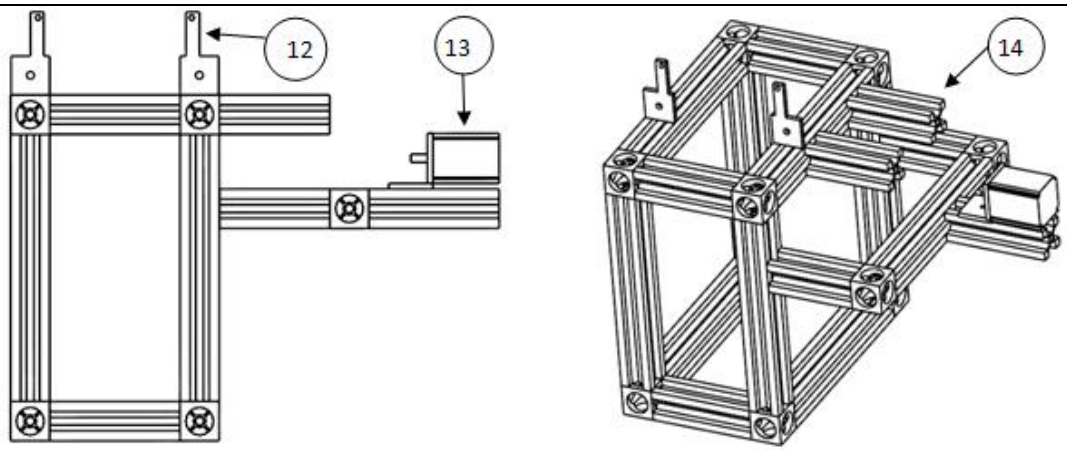

Figure 1.3: Reactor testing frame. (12) Front reactor mounts (13) screw drive motor (14) hopper supports

1.8	Install the front reactor mounts (12) on the testing frame using the FRONT threaded fastener plates. Loosely secure the bolt to the fastener plate such that the mounts still slide along the rail freely.	• Ensure the 90-degree L-bracket at the base of the front reactor mounts extends towards the REAR of the frame.
1.9	Place the reactor on the frame and secure the rear mounts to the REAR threaded fastener plates. Slide the front mounts forward over the front bolts.	• Keep the mount-to-rail connections loose enough to allow the reactor to move freely.
1.10	Slide the reactor to the REAR of the frame and place the cooled front radiation shield (10) over the cavity and housing front flanges. Secure the shield to the housing (2) flange using the 6 holes on the flange. Move the reactor to the FRONT of the frame (being careful to keep the front mounts supporting the front of the reactor in place) and place the rear insulation shield (10) over the rear housing (2) flange and secure using the 6 holes on the flange. Center the reactor and tighten all mounting connections. Place an insulation plug in the aperture.	• Ensure the shields are loosely filled with high temperature insulation material prior to installation. • The insulation within the rear shield should be able to be moved aside to reveal the drain plug. • A broken thread-tap may be blocking one of the holes.
1.11	Install the 5 salt-immersed thermocouples into the reactor using the 1/8” thermocouple fittings in the walls of the housing (2).	
1.12	Wrap a tape heater around the exterior of the reactor housing (2), fully covering the exposed housing wall surfaces.	• Ensure the tape heater DOES NOT overlap itself at any point, as this risks overheating and fire.
1.13	Wrap high temperature insulation around the exterior of the reactor housing. Use sufficient layers of insulation to bring the outer insulation surface up to the outside diameter of the front and rear insulation shields (10).	• Ensure that all electrical connections and sensor leads are able to be accessed after insulation has been put in place.
1.14	Lower the hopper assembly into place between the hopper support struts (14). Adjust the feed	• Ensure the alignment of the two tubes is accurate both

	injector to align with the hopper auger tube if needed. Secure the hopper auger tube to the feed injector auger tube with a ½" Swagelok fitting and Teflon ferrules. Feed the auger shaft assembly into the hopper tube and into the feed injector. Secure the auger shaft assembly to the auger tube again with a ½" Swagelok fitting and Teflon ferrules.	horizontally and vertically. Adjust the hopper support strut positions if vertical movement is needed. • Check for free rotation of the auger shaft after installation to verify alignment.
1.15	Attach the drive coupling between the auger shaft and the screw drive motor (13) and secure the shaft set-screws. Adjust the position of the motor to reduce any misalignment between the two shafts and tighten the motor mount bolt at the base of the motor mount.	
1.16	Connect the cooling coil on the front radiation shield (10) to one of the chilled water circuits on the enclosure wall.	• Use ½" or larger tubing for the connections to the chilled water circuit to ensure design flow.
1.17	Connect the salt-cooling tray and salt spill protection tubing (placed around the feet of the testing stand to freeze a catastrophic salt spill) to another of the chilled water circuits on the enclosure wall.	
1.18	Connect the central condenser tube to the third chilled water circuit on the enclosure wall.	• Ensure counter-flow heat exchange configuration.
1.19	Attach the Lambertian target to the reactor stand such that is it in-plane with the reactor aperture. Connect the target to the #4 cooling system loop.	• Ensure the placement AND orientation of the target is in-plane with the aperture.

Section 2: System Check and Warm-up

ID	Device	Instances
1	Thermocouple	12
2	MFC	4
3	Pressure Sensor	2
4	Motor	1

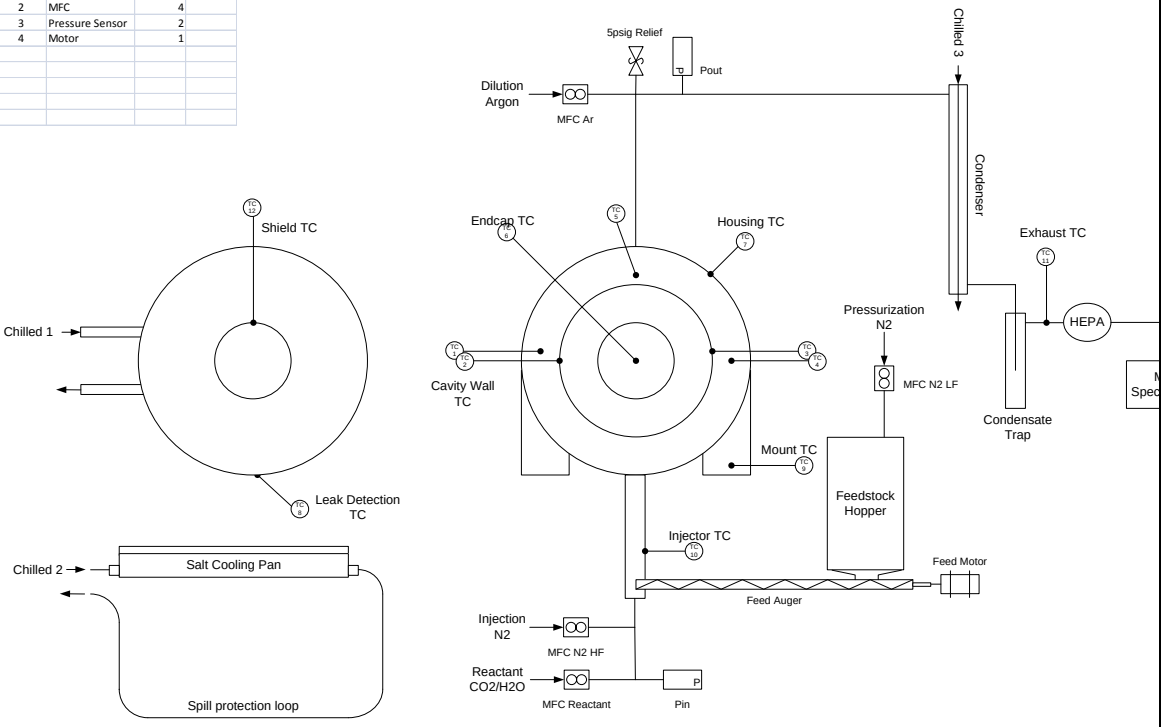

Figure 2.1: Schematic of the reactor system flow pathways, sensor locations, and other devices.

Proc #	Action	Cautionary Considerations
2.0	Initial Condition: The system should be assembled on the test stand as described by Chapter 1.	
2.1	Purge and check the downstream gas cooling/dilution/filtering assembly for leaks by: 1. Cap the ¾" tube fitting on the reactor side of the assembly 2. Apply a small flow of argon (< 1 SLPM) 3. Cap the ¼" tube fitting after the filters and condensate traps but BEFORE the mass spectrometer sampling capillary connection. 4. After 10 PSIG is indicated on the outlet pressure sensor, stop the argon flow and check all joints for leaks with a leak testing fluid, 5. Uncap and re-connect the sampling connections.	• Allow the argon to flow through the assembly for 30 seconds or so to purge air from the system before capping the tubing. • DO NOT allow the pressure to exceed 20 PSIG or the condensate traps may burst.
2.2	Purge and check the reactor and hopper assembly for leaks by: 1. Cap the ¾" reactor outlet	• NOTE: Flange seals will not be accessible at this point, so if excess leakage is noted but not

	2. Apply a small flow of nitrogen (<1 SLPM) into the fuel injector. 3. After 10 PSIG is indicated at the inlet pressure sensor, stop the nitrogen flow and check all joints for leaks with a leak testing fluid 4. Uncap the reactor outlet.	detected, removal of the shields to check the flanges may be required.
2.3	Verify alignment of the horizontal axis of the reactor with the horizontal axis of the solar simulator. Adjust traverse position as needed to achieve alignment. (Proposed method for YAW: Visually align the four reference lines of [1] upper salt thermocouple [2] center of the outlet flange [3] a plumb line hanging over the aperture locating point on the ground and [4] the vertical axis of the center lamp reflector.)	• This gets the reactor YAW correct, but PITCH may still be off. [Need a vertical position reference for PITCH correcting, e.g. wall-to-wall-laser.]
2.4	Fill the cooling system as per cooling assembly SOP. 1. Close the main flow valve to divert flow through the fill indicating spigot. 2. Prime the pumps by adding water until standing water is visible in the filling pipe. 3. One at a time, run each cooling loop pump while adding water to the filling pipe to maintain a visible level until steady flow comes through the spigot. 4. After all cooling loops are full of water, open the main flow valve and turn on all of the pumps, adding water if needed to maintain a visible water level in the fill pipe. 5. Open the chilled water valves to begin cooling the fluid in the heat exchanger.	• Ensure the pumps DO NOT run dry at any time by always adding water while filling the system. TURN OFF the pumps if the water level drops below the fill pipe. • Visually inspect all equipment connected to the cooling system to ensure no water is leaking from any of the connections.
2.5	Connect the pre-heating tape heaters on the reactor to a VARIAC or other power controlling device. Apply maximum heating power to the tape heaters while observing the outer cylinder and inner cylinder temperatures and reducing power if needed.	• Ensure a temperature difference of no greater than 150K occurs at temperatures below 500K, and no greater than 50K at temperature above 500K.
2.6	Fill the steam generator with TAP water, and power on the steam generator and the tape heaters on the steam delivery lines. Once the steam generator indicates a positive pressure buildup, pull the relief valve handle (on TOP of the steam generator) to purge out air from the pressure vessel. Repeat if needed.	• DO NOT use distilled or deionized water, as the steam generator uses a conductivity-based level indicator.
2.7	Once the steam delivery thermocouples indicate that all tubing lines are at least 20 K in excess of the steam saturation temperature, [for 16 PSIG (30	• Determine saturation temperature for the set steam generator pressure if different

	PSIA) steam, 130 C,] open the large silver steam generator valve.	than previously set 16 PSIG.
2.8	Once the reactor thermocouples indicate that both the outer cylinder wall and inner cylinder wall are in excess of the salt melting temperature (T=670K), turn on the flow of nitrogen into the fuel injector. Align the cooling jets to blow on the fuel injector where the solid feed shaft meets the vertical injector shaft. Adjust flow as needed to maintain the measured injector temperature within the range of 130 C – 150 C.	
2.9	Using a metal funnel, add 2.85 kg of crushed salt to the top of the reactor through the reactor outlet passage. Continue to add salt until the salt melt completely covers the inner cavity receiver cylinder wall by at least 1.5cm. (Use a metal dipstick to verify).	• Do not add salt too quickly, such that it backs up the outlet passage. • CAUTION: Salt melt will be bubbling due to agitation gas flow.
2.10	Connect the gas outlet assembly to the reactor outlet port and tighten to seal. Insulate the lower portion of the outlet tubing. Turn on the argon flow at 1 SLPM to keep the outlet line purged.	
2.11	After the reactor temperature has climbed to 800K or slowed in rate of climb, turn off the tape heaters, remove the insulation from the reactor aperture and clear the simulator enclosure in preparation for simulator operation.	
2.12	Initiate the gas sampling recipe on the MS and ensure the capillary selector valve is in the proper position.	• Observe the MS output and verify rational readings of expected gases (CO_2, Ar, N_2)

Section 3: On-simulator Operation

Proc#	Action	Cautionary Considerations
3.0	Initial Condition: The reactor assembly is aligned, full of molten salt, connected to the gas outlet assembly, with an open aperture ready for concentrated light input.	
3.1	Move the traverse table to the left (facing the lamps) using the traverse adjustment hand-wheels so that the Lambertian target is now within the focus of the lamps.	
3.2	Follow the Solar Simulator startup SOP, and turn on the center lamp and verify that the target is positioned properly. Take snapshots of the flux distribution for 1-lamp, 2-lamp, and 3-lamp configurations on the target, and verify that the Region-Of-Interest circle is centered about the peak flux.	• Ensure the filter is in place over the CCD camera before the simulator lamps are turned on.
3.3	Turn off the lamps and close the lamp shutter.	
3.4	Again using the traverse adjustment hand-wheels, move the table to the right such that the reactor is within the focal region. Open the lamp shutter and remove the filter from the CCD camera. Use the camera and Region-Of-Interest circle to fine-tune the position of the reactor. Return the filter to the CCD camera.	• DO NOT stand in front of the exposed lamp array. Make traverse adjustments with the shutter lowered.
3.5	Turn on Lamp #4 (center lamp) and observe the cavity absorber from the CCD camera and monitor cavity and endcap temperature indications to ensure the cavity does not exceed 1300 K.	• Watch for signs of melting in the CCD camera view in addition to watching the thermocouple readings.
3.6	If temperatures are acceptable and a faster heating rate is desired, switch from using the center lamp (#4) to using two opposed outer ring lamps. If continued heating with 2 lamps maintains acceptable observed temperatures, the use of three outer ring lamps may be initiated.	ACCEPTABLE TEMP CRITERIA • No temperature exceeds 1300 K • The difference between the inner cavity wall and outer housing wall temperatures is less than 50 K
3.7	As the observed salt melt temperature approaches 1200K, take the time to look into the enclosure with protective eyewear (welding mask), and look for any signs of leaking water, salt, or overheating materials on or near the traverse stand or simulator array.	• Look for salt dripping from or freezing on the front and rear insulation shields, as the flange gaps just inside the shields are the most likely leaking point.
3.8	After the average salt temperature reaches 1200 K, or once any wall temperatures approach 1280K,	• Observe the stepper motor, lower pressure sensor, and

	initiate the delivery of stream into the feed injection system, and pressurize the feedstock hopper with a nitrogen flow. Turn the Argon dilution flow up to 8 SLPM. Initiate feedstock delivery once gas delivery has been confirmed from the MFC feedback signal.	steam and nitrogen MFC indicators. If there is any indication of clogged flow, stop feedstock delivery, turn off all lamps, and close the shutter. • VERIFY feed-shaft RPM is POSITIVE
3.9	Adjust feedstock flow as required to hold the average salt temperature around 1200K. If not using 3 lamps and temperatures are acceptable, switch to 3 lamps.	
3.10	Upon achieving steady-state operation, continue to run for the desired testing time period.	• Periodically look into the enclosure to check for signs of leakage.
3.11	Following steady testing, turn off all lamps and close the shutter. Enter the enclosure and place an insulating cap over the reactor aperture to encourage uniform cooling.	• NOTE: Reactor is still operating to demonstrate storage potential.
3.12	After the salt temperature drops to below 1180K, terminate the flow of feedstock and steam.	•

Section 4: Normal Shutdown Procedure

Proc#	Action	Cautionary Considerations
4.0	Initial Condition: The reactor assembly is cooling down with lamps off, the aperture covered, and feedstock delivery off.	
4.1	If the outlet stream chemistry is no longer of concern, turn off the MS sampling recipe and turn down the Argon dilution flow to 1 SLPM.	
4.2	Observe cooling to ensure that the difference between the inner and outer cylinder walls is >50K. To increase cooling of the inner cavity, remove the aperture cover. If the temperature difference is still too great (outer wall too cool) the tape heaters may be turned on to slow the rate of cooling of the outer wall.	• Ensure the cavity remains within 50K of the outer wall, and preferably, is hotter than the outer wall to avoid salt leakage from the rear of the reactor.
4.3	Once the salt thermocouples indicate a temperature <800 K, drain the salt from the reactor onto the salt cooling tray. This is done by using an appropriate socket extension and socket driver, through the salt drainage tube, to remove the ¼" NPT plug in the reactor drain flange.	[Cooling tray image] • CAUTION: Hot molten salt can flash-boil any liquid water. Check that the salt cooling tray is free from condensation prior to draining salt!
4.4	After the salt has fully frozen in the salt cooling tray, the cooling water flow through the tray may be terminated. Cooling water through the condenser and Lambertian target may also be turned off at this time. Break up and store salt for later use.	• The flows through the target and condenser are left on until this point to ensure the heat exchanger is experiencing maximum flow and thus maximum heat transfer rates.
4.5	Clear the fuel injector passages from any remaining salt by briefly setting the nitrogen flow to maximum, and then turning off the fuel injector and hopper pressurization gas flows, as well as the Argon dilution gas flow.	
4.6	Once the reactor has cooled to below 500K, cooling flow through the shield may be turned off, and the chilled water valves closed.	• Silver solder should be stable up to 800K, but to be safe cool the shield until the reactor is much cooler.
4.7	Detach gas outlet assembly and remove filter media and take mass measurements. Also use solvents and Kimwipes to remove any residue that may exist from the condenser interior and both condensate traps. Record the mass gain on the wipes.	• Don't forget to mass the wipes BEFORE using them as a reference, and mass them again AFTER all solvent has evaporated.
4.8	Remove insulation from reactor and examine exterior for signs of leakage, corrosion, or deformation. Remove insulation shields and look	

	for same indications.	
4.9	Once reactor has cooled to room temperature (may be overnight), disconnect feedstock delivery motor, shaft, and hopper from feed injector.	• Inspect for signs of salt leakage or feed pyrolysis in the feed tube.
4.10	Disassemble the reactor by reversing steps 1.9-1.1. Wash and inspect all parts for indications of corrosion, deformation, leakage, or other damage.	